Tumour Vessel Structural Analysis and Its Application in Image Analysis

Wang Po
Balliol College

Wolfson Medical Vision Laboratory
Department of Engineering Science
University of Oxford

A thesis submitted for the degree
Doctor of Philosophy
Trinity Term 2010

Tumour Vessel Structural Analysis and its application in Image Analysis

Wang Po

Abstract

submitted for the degree of
Doctor of Philosophy
Trinity Term 2010

Abnormal vascular structure has been identified as one of the major characteristics of tumours. In this thesis, we carry out quantitative analysis on different tumour vascular structures and research the relationship between vascular structure and its transportation efficiency.

We first study segmentation methods to extract the binary vessel representations from microscope images. We found that local phase-hysteresis thresholding is able to segment vessel objects from noisy microscope images. We also study methods to extract the centre lines of segmented vessel objects, a process termed as skeletonization. We modified the conventional thinning method to regularize the extremely asymmetrical structure found in the segmented vessel objects. We found this method is capable to produce vessel skeletons with satisfactory accuracy.

We have developed a software for 3D vessel structural analysis. This software is consisted of four major parts: image segmentation, vessel skeletonization, skeleton modification and structure quantification. This software has implemented local phase-hysteresis thresholding and structure regularization-thinning methods. A GUI was introduced to enable users to alter the skeleton structures based on their subjective judgements. Radius and inter branch length quantification can be conducted based on the segmentation and skeletonization results. The accuracy of segmentation, skeletonization and quantification methods have been tested on several synthesized data sets.

The change of tumour vascular structure after drug treatment was then investigated. We proposed metrics to quantify tumour vascular geometry and statistically analysed the effect of tested drugs on normalizing tumour vascular structure.

Finally, we developed a spatio-temporal model to simulate the delivery of oxygen and 3-^{18}F-fluoro-1-(2-nitro-1-imidazolyl)-2-propanol (Fmiso), which is the hypoxia tracer that gives out PET signal in an Fmiso PET scanning. This model is based on compartmental models, but also considers the spatial diffusion of oxygen and Fmiso. We validated our model on *in vitro* spheroid data and simulated the oxygen and Fmiso distribution on the segmented vessel images.

We contend that the tumour Fmiso distribution (as observed in Fmiso PET imaging) is caused by the abnormal tumour vascular structure which is further aroused from tumour angiogenesis process. We depicted a modelling framework to research the relationships between tumour angiogenesis, vessel structure and Fmiso distribution, which is going to be the focus of our future work.

Acknowledgements

My three-year residency at the University of Oxford has made me realize that a journey is easier when you travel together. I am blessed to get tremendous help, support and encouragement from so many individuals. It is my pleasure to express here my thankfulness to all of them, although saying "thank you" would be never enough.

My most sincere gratitude goes to Prof. Sir. Michael Brady, first of all for providing the opportunity to work in such a fantastic research area, secondly for your continued support, guidance and inspiration, which have helped me grow academically and intellectually. I have learned from you not only scientific truths, but life philosophies that will light up my journey onwards.

I would also like to give my deepest thanks to Dr. Cat Kelly and Prof. Ruth Muschel, for sharing their expertise on biology and providing invaluable comments on my papers and thesis. I would like to thank my colleagues, Wenjia Bai, for numerous discussions on computers and maths; Dr. Naseer Qayum, for providing me the microscope images, and Dr. Ann Harvey, for proofreading my thesis drafts. Of course, I feel grateful for having many other friends who enriched my three years in Oxford with plenty of fun.

Finally, I would like to thank my families, notably, my wife, for your wholehearted support and encouragement, for the joys and pains we share together, for always being proud of me.

Contents

List of Abbreviations

API	Application Programming Interface
ATSM	Diacetyl-bis(N4-methylthiosemicarbazone)
cdf	Cumulative distribution function
CT	Computed Tomography
CPU	Central Processing Unit
CUDA	Compute Unified Device Architecture
dceMRI	Dynamic Contrast Enhanced Magnetic Resonance Imaging
EC	Endothelial Cell
FDG	^{18}F-Flurodeoxyglucose
FMISO	^{18}F-Fluoromisonidazole
fMRI	Functional Magnetic Resonance Imaging
GFP	Green Fluorescent Protein
GPGPU	General-Purpose Computation on Graphics Processing Unit
GPU	Graphics Processing Unit
GUI	Graphical User Interface
ITK	Insight Segmentation and Registration Toolkit
LSR	Least Squares Regression
MIP	Maximum Intensity Projection
MMP	Matrix Metalloproteinase
MR	Magnetic Resonance
MRI	Magnetic Resonance Imaging
MPI	Message Passing Interface
ODE	Ordinary Differential Equation
OpenMP	Open Muti-Processing
PDE	Partial Differential Equation
pdf	Probability density function
PET	Positron Emission Tomography
RF	Radio Frequency
ROI	Region of Interest
SNR	Signal-to-noise Ratio
SPECT	Single Photon Emission Computed Tomography
SSE	Sum of Squared Error
STORM	Stochastic Optical Reconstruction Microscopy
SUV	Standardized Uptake Value
TAC	Time Activity Curve
TAF	Tumour Angiogenic Factor
VBM	Vascular Basement Membrane
VEGF	Vascular Endothelial Growth Factor
VTK	Visualization Toolkit
US	Ultrasound
UV	Ultraviolet

List of Figures

Chapter 1

Introduction

1.1 Cancer

Cancer refers to a family of (approximately 120) diseases that are characterised by uncontrolled cell proliferation. The incidence of cancer is increasing and in 2007 was already responsible for 13% of deaths world wide (Statistics source: WHO).

1.1.1 Causes

Cancer is believed to result from cell mutations. Mutations refer to the phenomenon in which a cell's genetic code has been changed. Mutations may be triggered by radiation, bacteria, viruses, or mutagenic chemicals, which include alcohol and nicotine (Danaei *et al.*, 2005), so a healthy life style helps prevent cancer, at least in early age. Meanwhile, some inherited genes, which are prone to cancerous mutations, have also been identified (Burke *et al.*, 1997). This suggests that cancers may also be caused by inherited genetic predisposition (Liaw *et al.*, 1997).

1.1.2 Clinical Symptoms

Clusters of cells which exhibit abnormal growth are commonly referred to as tumours (Weinberg, 2007). Tumours can be benign or malignant. In benign tumours, the abnormal cellular growth does not lead to the migration of tumour cells to other tissue sites. In malignant tumours, however, the cellular growth is so aggressive that the local tissue

cannot support the tumour cell population and tumour cells may invade other tissues. These malignant tumours pose a threat to the life of the whole organism and are referred to as "cancers" by clinical oncologists and surgeons (Weinberg, 2007).

The clinical symptoms for cancers may vary between organs. For example, patients with brain metastasis typically experience headaches, seizures and vertigo, whereas patients with cancer metastasis to the liver exhibit hepatomegly and jaundice (Figure 1.1).

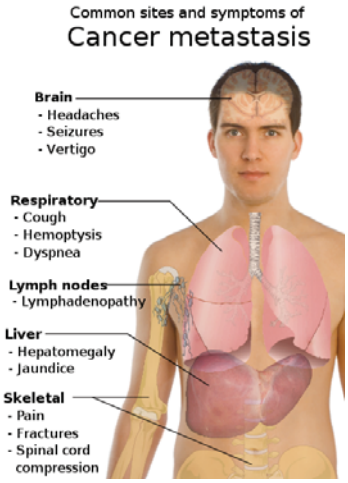

Figure 1.1: Symptoms of cancer metastasis.

1.1.3 Epidemiology

Incidence and mortality rates are strongly associated with cancer types, economic status, and sex. Figure 1.2 summarizes the incidence and mortality rates of different types of cancer in the male and female populations, living in the developed and developing countries. The rates are expressed as absolute numbers of cases per year. It shows for example that lung cancers are the major threat to the male population in both developed countries (second highest incidence rate and highest mortality rate) and developing countries (highest incidence and mortality rates). On the other hand, breast cancers are the primary health threat to the female population in both developed (highest incidence rate and medium mortality rate) and developing countries (highest incidence rate and

medium mortality rate).

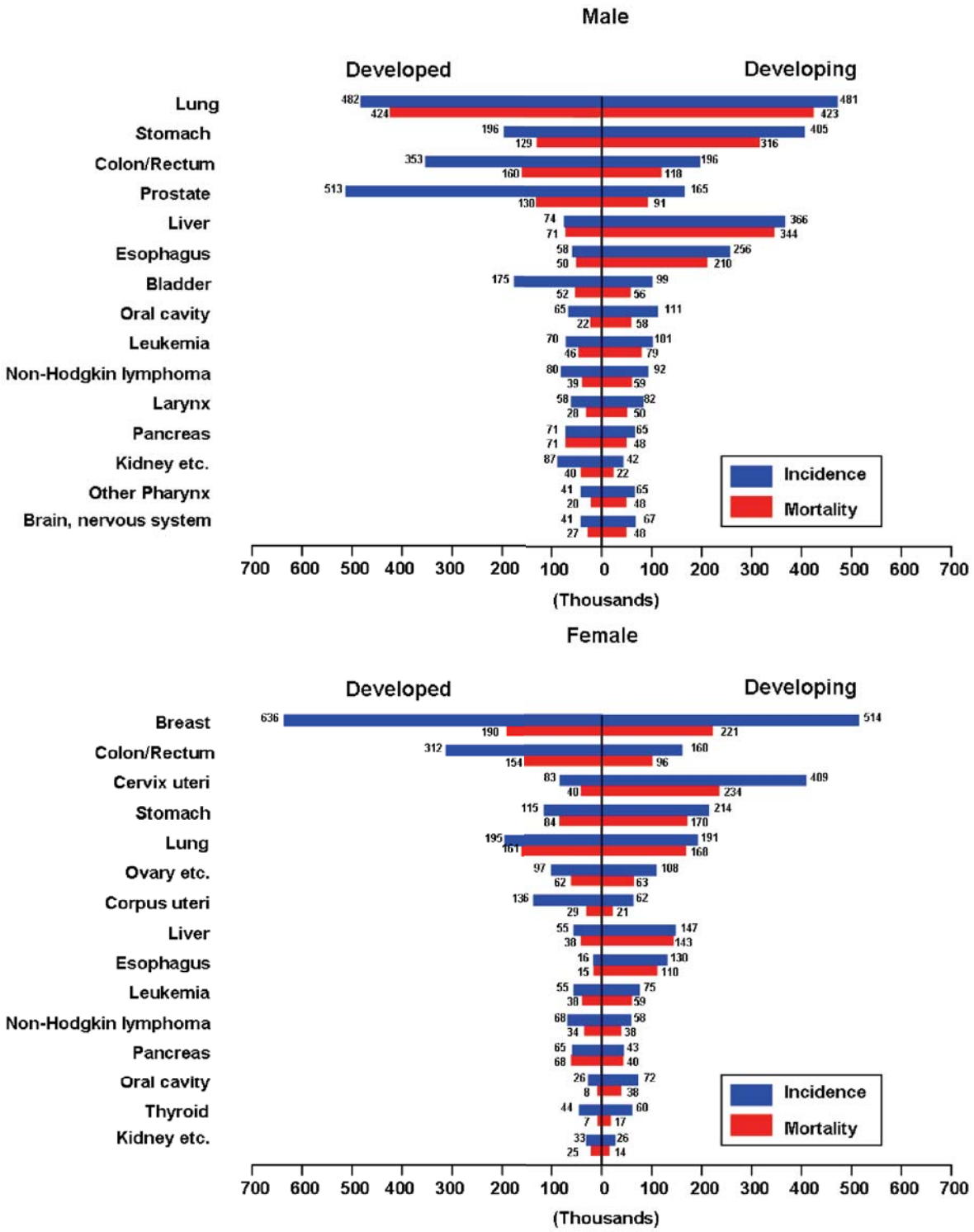

Figure 1.2: Incidence and mortality rates of various types of cancers, reproduced from Parkin *et al.* (2005).

It has been proposed that cancer incidence, mortality and prevalence are also related

to geographical location. Cancer prevalence is a metric that describes the number of people living with occurrences of cancer in a region. Figure 1.3 shows the percentages of cancer incidence, mortality and prevalence cases in each geographical region in relation to the total number of cases world-wide (2004).

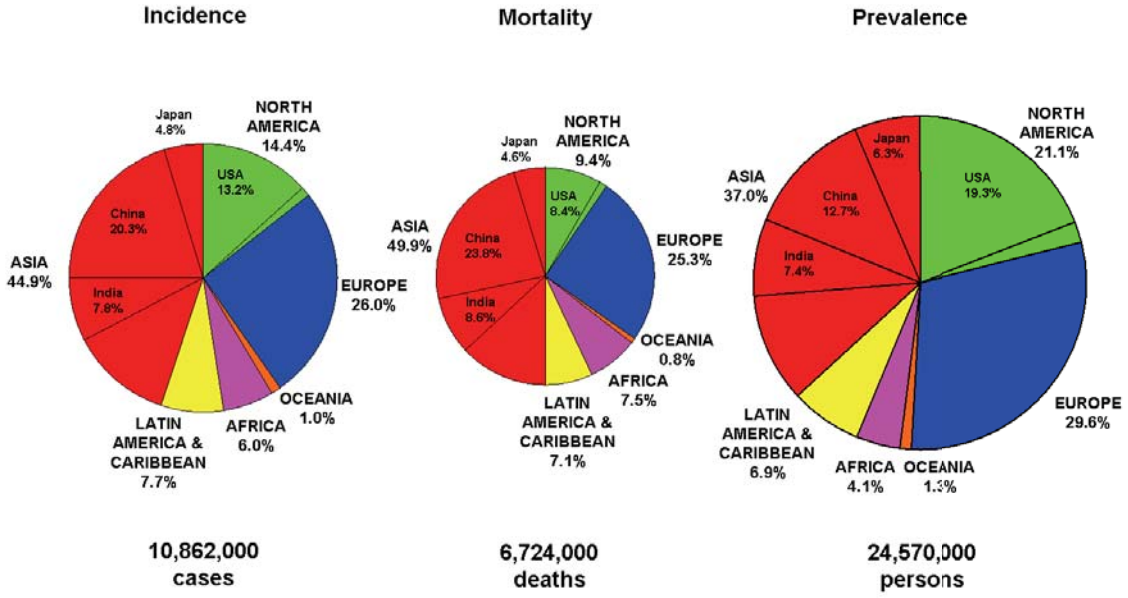

Figure 1.3: Incidence, mortality and prevalence rates of cancer in different area, reproduced from Parkin *et al.* (2005).

1.1.4 Detection of cancer

Laboratory Test

Laboratory tests are based on measuring the concentration of tumour biomarkers in a patient's blood, urine or other bodily fluid. Tumour biomarkers are molecules whose concentrations are altered as a result of cancer. Numerous tumour biomarker molecules have been utilized in detecting different types of cancers (Koepke, 2006). For example, AFP (Alpha-FetoProtein) screening is a useful tool in detecting hepatocellular cancer (Abelev, 1971) while prostate-specific antigen (PSA) has been used to detect prostate cancer (Catalona *et al.*, 1991).

Laboratory tests directly monitor histochemical changes caused by cancer. They provide a precise diagnosis of a cancer's type and site. However, laboratory tests are

cancer-type specific and thus can not be used for generic cancer screening.

Compared with laboratory tests, imaging techniques are not cancer-type specific and are thus increasingly used in cancer screening and management. Depending on the detection method, radiographic imaging techniques may be classified as anatomical imaging, which detects anatomical changes caused by tumour growth, and functional imaging, which detects tumours via functional changes associated with tumour cell activities.

Radiographic Imaging

Radiographic imaging techniques are based on radiation waves which can pass through the human body.

CT

In CT (Computed Tomography), patients are radiated with X-rays, which can be detected by external detectors surrounding the body. Tumour identification is based on exploiting the different X-ray attenuation rates between soft and solid tissues.

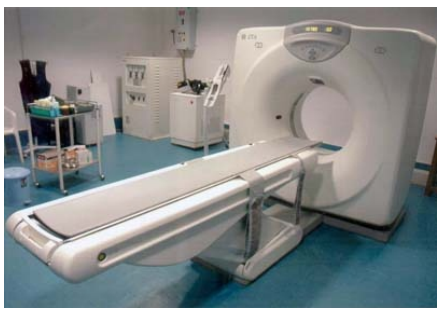

(a) CT scanner

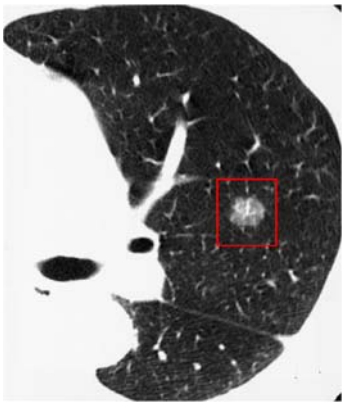

(b) CT image

Figure 1.4: (a) A picture of CT scanner. (b) Type G well differentiated adenocarcinoma in a 49-year-old woman, adapted from Hasegawa *et al.* (2000).

During imaging, a patient lying on a transmission bed is moved through the CT tube where a ring of detectors are installed. Signals recorded by these detectors are reconstructed into 2D or 3D images (Figure 1.4(a)). CT images may indicate the anatomical changes caused by uncontrolled tumour growth. Over proliferated cells normally form

lumps that can, in some cases, be readily differentiated from neighbouring normal tissues (Figure 1.4(b)).

Nuclear Imaging

Nuclear imaging techniques exploit the nuclear properties of either intrinsic or externally administered molecules to generate images. They include MRI (Magnetic Resonance Imaging), SPECT (Single Photon Emission Computed Tomography) and PET (Positron Emission Tomography).

MRI

MRI does not involve ionising radiation or radioactivity, and can be used as either an anatomical or functional imaging modality. The radio wave is generated by the protons that exist in water and the majority of biomolecules inside human bodies. Some of the protons within the body are excited by a radiofrequency wave generated by a rapidly oscillating magnetic field (the radiofrequency, RF, coil). When the RF wave is at a resonant frequency for the protons, they can change their energy state, and, once the RF wave is switched off, they regain their original energy, emitting radio waves (free induction decay). These radio waves are recorded by a RF receiver coil in a frequency-phase representation which can subsequently be used to reconstruct 2D or 3D images. MRI scanners have similar construction as CT scanners shown in Figure 1.4(a), but the detector tube is typically larger than that of a CT scanner because it houses several magnets, in particular the main cylindrical magnet.

MRI is often used to detect tumours in soft tissues because the protons in soft tissues are able to change their energy state more easily than those in solid tissue (*e.g.* bone). In certain cases, tumours can be identified based on their different anatomical appearances or proton densities in MRI image (Figure 1.5).

However, only a relatively few types of tumour can be distinguished based on their magnetic (T1, T2 relaxation rates) properties alone in MR imaging. In fact, many

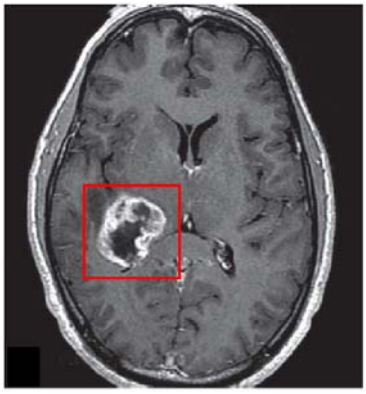

Figure 1.5: T1-weighted axial image in a 55-year-old man with glioblastoma multiforme showing a heterogeneously enhancing mass with irregular central necrosis in the right peritrigonal region, adapted from Jain *et al.* (2008).

tumours cannot be identified solely based on their anatomical abnormalities. Functional imaging techniques are more reliable in detecting these tumours. MRI can be used to image the functional change of tumour tissues either by injecting contrast agents in patients (dceMRI, Taylor *et al.* (1999))or employing specific RF sequences (fMRI Kayser & Logothetis (2010)).

SPECT

Single photon emission computed tomography (SPECT) requires injecting radiolabeled markers into the patient's body. Such markers are designed to accumulate in the tumour area as a result of its altered biological functions. In SPECT, radiolabelled markers have an unstable atomic nucleus and emit γ-ray during their nuclear decay process. γ-waves can pass through the human body and may be recorded by surrounding detectors known as gamma cameras. SPECT is a functional imaging technique which identifies cancers based on their altered cellular activities compared with normal tissues.

PET

PET (Positron Emission Tomography) utilizes a similar mechanism to generate images as SPECT. The difference is that the markers used in PET are labelled with unstable isotopes that do not emit γ-rays directly. Rather, they emit positrons through nuclear

decay which annihilate with electrons and emit two γ-rays in opposite directions. PET detectors record the "coincidences" of these two γ-rays and the annihilation sites can be located as the middle point of the line connecting the coincidently recorded γ-rays (which is termed LOR, line of responses). In this way, the annihilation sites can be more precisely determined by PET than by SPECT. Although some preclinical SPECT systems use collimation to achieve high resolution, clinical PET imaging typically has a higher spatial resolution than SPECT. Figure 1.6 shows a PET image of an adenocarcinoma of the colon. In this case, the tumour area was detected based on its elevated glucose consumption rate.

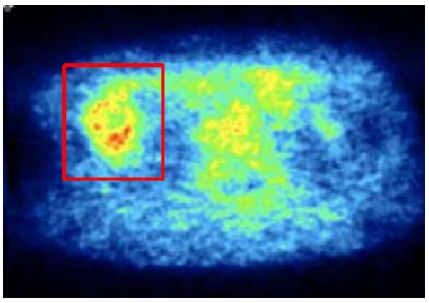

Figure 1.6: FDG-PET scan of a patient with an adenocarcinoma of the colon, adapted from Strauss *et al.* (2007).

1.1.5 Treatment of Cancer

Surgery

Surgery is the one of the primary options for treating localized cancers, such as breast cancer, lung squamous cancer etc. (Souhami & Moxham, 2002). Post surgical rehabilitations include reconstructions after disfiguring procedures, and they form an important part of surgical planning (Macdonald, 2008). However, surgery is often not recommended if the tumour has grown so large as to make resection impossible or metastases have been revealed (Souhami & Moxham, 2002). Meanwhile, it is difficult to identify and remove 100% tumour cells during the surgery, and the "remaining" tumour cells are prone to develop into secondary tumours afterwards (Foster, 1978).

Radiotherapy

Radiotherapy is a strategy that is frequently considered for cancer management. The mechanism is to use targeted radiation to cause DNA damage in both normal and tumour cells. However, most normal cells are differentiated cells which have developed DNA repair mechanisms to remedy the DNA damage. In contrast, tumour cells are similar to undifferentiated cells which lack a DNA repair mechanism. As a result, the DNA damage will be passed down through tumour cell generations. The accumulated DNA damage will ultimately cause tumour cells to die. Radiotherapy is usually combined with surgery to yield optimal management outcome (Souhami & Moxham, 2002).

Chemotherapy

Chemotherapy is a relatively novel cancer management option (Souhami & Moxham, 2002). It functions in a similar way to radiotherapy, but kills tumour cells via cytotoxic agents. These chemicals can hinder cell division processes. Quickly dividing cells, such as tumour cells, are more susceptible to these chemicals so they are more likely to die from the cell division impairment. However, other quickly dividing cells, like those responsible for hair growth, are also killed by these chemicals. Current researches aim to develop cytotoxic agents that can target the biochemical activities of tumour cells exclusively so as to reduce such "side effects".

1.1.6 Tumour Vasculature

Tumour tissues have a very different vascular network from those of normal tissues (Fig 1.7). The malformation of a vascular network is thought to have a role in the alteration of the tumour tissue micro environment and biological function (Jain, 2005).

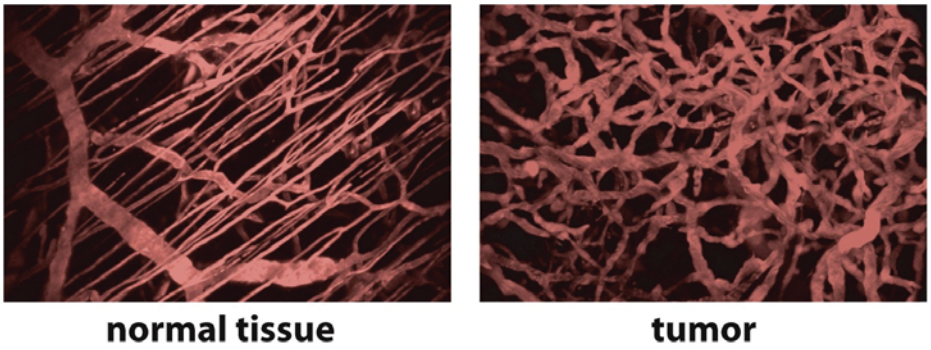

Figure 1.7: Blood vessels in normal tissue (left) and tumour tissue (right). Reprinted from Weinberg (2007), without permission.

The chaotic organization of tumour vasculature is believed to be a consequence of altered angiogenesis in tumour tissues. Angiogenesis is the process of new blood vessel generation. In mature normal tissues, it is often suppressed to maintain the vessel density at an adequate level. In tumour tissues, however, it is activated by signals released from tumour cells (Figure 1.8).

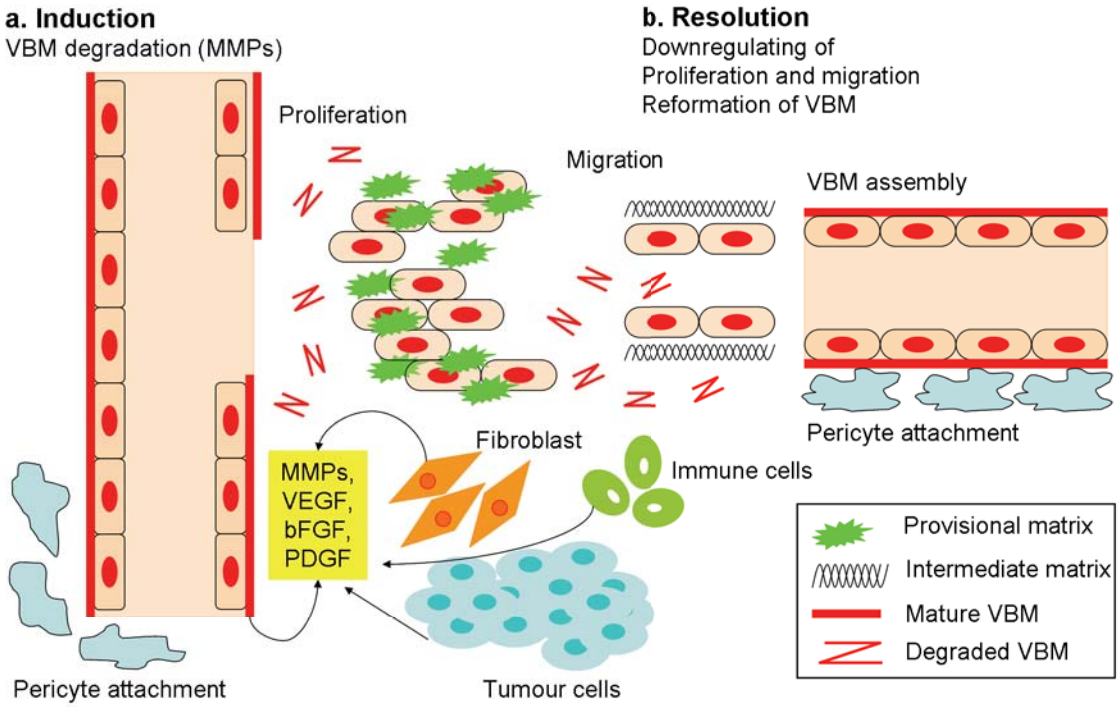

Figure 1.8: Tumour angiogenesis. Reproduced from Kalluri (2003).

Blood vessels are made of endothelial cells (ECs) which are supported both physically and functionally by the vascular basement membrane (VBM). Tumour angiogenesis con-

sists of a series of interlinked events. First, the vascular basement membrane (VBM) is degraded or reformed in response to pro-angiogenic factors, such as growth factors and matrix metalloproteinases (MMPs) produced by the tumour cells. The ECs are then able to proliferate and migrate towards the source of the growth factors, where they become embedded in a provisional matrix (Figure 1.8 **a**). An intermediate and then a new (mature) VBM is formed around the ECs and inserted into the provisional matrix. This generates a new blood vessel segment (Figure 1.8 **b**, Kalluri (2003)).

Usually, the angiogenic process is suppressed by molecules known as antiangiogenic factors such as endostatin, thrombospondins and interleukins (Weinberg, 2007). However, this regulation mechanism is found less effective in tumour tissues with the result being that tumour angiogenesis often produces chaotic and leaky blood vessels, which are less functional. This usually leads to inadequate vascular delivery of oxygen and other nutrients to the tumour tissues.

In functional cancer screening, an agent is often injected into the patient's blood to generate imaging signals. These agents accumulate in tumour cells as a result of their changed biological activities. The recorded images reflect the concentrations of these agents in different tissues of the patient. However, these agents need first to be delivered to the tumour tissue by tumour blood vessels. Thus, in order to accurately evaluate the functional changes of the tissue being scanned, adjustments for the compromised tumour vascular delivery must be made in analysing these images.

Tumour blood vessel dysfunction is also believed to be a major reason underlying the limitations of radio and chemotherapies (Vaupel, 2004; Jain, 2005). Because perfusion of tumour vessels is interrupted in abnormal tumour vessel geometry (Qayum *et al.*, 2009) and leaky tumour vessels give rise to high tumour interstitial pressure which can disrupt blood diffusion into the tumour stroma(Boucher *et al.*, 1990), both effects will compromise tumour vessel's function in delivering oxygen and other chemicals, including radio or chemo agents, to the tumour sites. Additionally, a hypoxic environment is

also adverse to radio therapies, because radiation requires oxygen for maximal fixation of the radical species that cause DNA damage(Vaupel, 2004). Accordingly, vascular normalization therapy has been proposed to normalize tumour vasculature in order to yield optimal responses to radio- and chemo- therapies (Jain, 2005).

1.2 Motivation

In developing drugs for tumour vessel normalization, it is of clinical interest to quantify the structural changes to the tumour vessel network as a result of drug treatment. This quantification involves defining suitable geometrical metrics to measure vessel structures and designing quantitative methods to statistically analyse the changes of vessel structure as a consequences of drug treatment.

Compared with CT and MRI, PET (and SPECT) signals are directly generated by radioactively decaying atoms. It is thus possible to quantify the cellular biochemical processes based on PET imaging. This feature has led to the ever increasing popularity of PET imaging in bench research and in clinical practice. However, the development of mathematical models to quantify a PET signal is complicated by the many co-activating biochemical processes. Simple models (like compartmental models) have been developed to quantify the temporal variances of PET signals (Time Activity Curves). Evidently, the PET signal at a specific location is related to the amount of tracer being delivered to that place. The spatial variation of the PET signal contains information about the geometrical structure of the surrounding vascular network. A model describing both temporal and spatial variations should have greater descriptive power in analyzing the distribution of PET tracers.

This thesis studies the effect of tumour vascular geometry on the delivery and accumulation of PET hypoxic tracers. A provisional distribution of PET tracers could be simulated on a given vascular geometry. By comparing the simulated PET tracer distribution with real tracer distribution, one can separate tumour vascular effects from

tumour cell functional change in analyzing micro PET images. Potentially, this could contribute to a novel framework in processing clinical PET images.

1.3 Thesis Overview

This thesis is organized into 8 chapters. Chapter 1 aims to give the reader a basic appreciation of cancer, its causes, symptoms, epidemiology, detections and therapies. Chapter 1 also expresses the motivation for this research and outlines the thesis structure.

Chapter 2 introduces a number of the molecular imaging techniques that have been recently developed. Molecular imaging refers to a group of imaging techniques which utilize specifically designed contrast agents to target biomolecules of research interest. Thus, molecular imaging techniques produce images of the distribution of contrast agents, which can be translated into maps of cellular functional states based on the biological mechanisms of the interactions between contrast agents and the targeted biomolecules. Molecular imaging encompasses a broad range of imaging modalities such as optical imaging, nuclear imaging and ultra sound imaging; and is becoming a very popular imaging method in both bench research and clinical practices.

Chapter 3 summarises the image analysis techniques we have used and/or developed to analyse tumour vasculature microscope images provided by our collaborators. In order to quantify the changes to the structure of the tumour vasculature, we first extract the blood vessel object from 3D microscope images using segmentation methods. Subsequently, a single voxel wide representation of the vessel objects is extracted to enable quantitative structural evaluations.

Chapter 4 describes a graphical user interface (GUI) we developed for tumour vessel microscope image analysis. In this GUI, tumour vessel skeletons are structured as a hierarchical array data structure. Based on this data structure, a user interactive skeleton modification program is developed to enable user manual correction of the vessel skeleton representations. Several structural metrics have been proposed and a quantification

program has been included in the GUI to conduct quantitative structural analysis on user corrected vessel skeletons.

Chapter 5 depicts and discusses the quantification results based on tumour vessel microscope images provided by our collaborators. Tumour vessels were treated with different vessel normalizing drugs. The structures of drug-treated tumour blood vessels are compared with those of non-treated tumour blood vessels. The quantitative results are found to be consistent with biological conjectures about the effects of the corresponding drugs.

Chapter 6 develops a spatio-temporal model of the *in vivo* delivery of oxygen and a hypoxic tracer, fluorine-18 fluoromisonidazole (Fmiso), through the tumour vascular network. It is developed by augmenting conventional compartmental models with spatial diffusion. The model takes 3D microscope vessel objects obtained by the image segmentation as input and simulates the oxygen and Fmiso distributions over time.

Chapter 7 discusses the techniques we employed in the simulation of the distribution of oxygen and Fmiso during the course of PET scanning, and presents the simulation results. The oxygen distribution is simulated based on the tumour blood vessel map. Fmiso distribution is then simulated based on the blood vessel map and the simulated oxygen distribution map. We find that the time activity curves derived from the spatio-temporal models have similar shapes to those observed in realistic dynamic PET. This supports the reliability of our spatio-temporal modelling and *in silico* simulation.

Finally, Chapter 8 summarises the core findings of this research and suggests possible future research that could be conducted based on the work we present.

Chapter 2

Molecular Imaging

2.1 Introduction

Molecular imaging is an imaging concept that exploits specific molecules as a source of image contrast (Weissleder, 1999). It is based on the utilization of a new generation of contrast agents to explore molecular interactions. The contrast agents are primarily chemicals that bind specifically to the target molecules and emit electromagnetic signals spontaneously or upon excitation by external energy fields.

Molecular imaging produces images of processes that occur at the molecular level. It has become an increasingly important imaging technique both for benchside research and in clinical practice.

2.2 Modalities

Based on the nature of data sampling, molecular imaging techniques can be classified as *in vitro*/*ex vivo* imaging or *in vivo* (Weissleder, 1999). In *in vitro*/*ex vivo* imaging, cell cultures or post-mortem sample tissues are labelled with contrast agents. The images are typically recorded using optical or electron microscopes. In *in vivo* imaging, contrast agents are injected into a living subject. Such agents generally emit high energy electromagnetic radio waves that can pass through the body and be recorded by external detectors. Images are reconstructed from the recorded signals and display on-going cellular activities. Compared with *in vitro*/*ex vivo* imaging, *in vivo* imaging provides

information directly related to the living organism; but it also poses more challenging requirements for imaging technologies and systems.

In terms of image formation mechanisms, molecular imaging modalities include optical, nuclear and ultrasound imaging.

2.2.1 Optical Imaging

Optical molecular imaging normally generates signals in the (near-) visible spectrum of light, which can then be recorded by an optical system. Depending on the photon generation mechanism, optical imaging can be further divided into fluorescence imaging and luminescence imaging.

Fluorescence Imaging

In fluorescence imaging, the contrast agent contains atoms that can absorb energies from radiations of particular frequencies (excitation frequency). This excites the outer electrons to higher energy states. However, electrons at higher energy states are not stable, they will gradually lose energy and return to their normal energy status. As a result, and under certain circumstances, electromagnetic energy of a lower frequency (lower energy than the excitation frequency) is emitted (Figure 2.1). The molecules capable of producing this phenomenon are said to be fluorescent. Green fluorescent protein (GFP) is a frequently used fluorescent contrast agent in this form of optical imaging.

Fluorescent molecules can be excited either by ultraviolet or by near infrared light. Ultraviolet light can produce emissions within the visible spectrum. However, the high energy of ultraviolet light can destroy living cells, so it is generally not considered suitable for *in vivo* imaging. To enable *in vivo* fluorescence imaging, fluorescent dyes have been developed that are excitable by near-infrared light, which is of relatively lower energy and so is more suitable for imaging living subjects. However, the limitation of this is

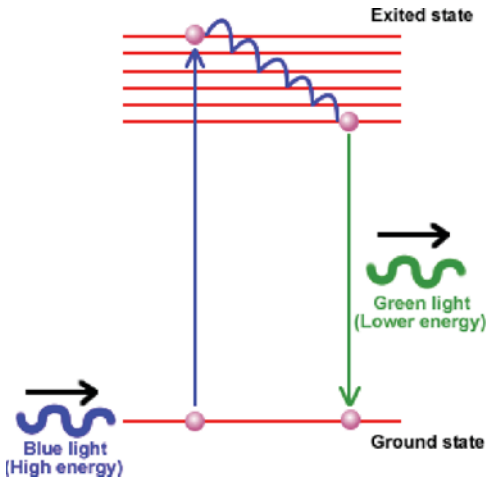

Figure 2.1: Illustration of the mechanism of fluorescence.

that special detectors have to be developed to detect the emissions in the far infrared spectrum.

Luminescence Imaging

In luminescence imaging, the contrast agent is involved in a photo-chemical reaction in which a photon is released as a result of the reduction in the total energy through the atom recombination process. Firefly luciferin (a benzothiazole) is one contrast agent in this category and the corresponding substrate is photinus luciferase (Rudin & Weissleder, 2003).

2.2.2 Nuclear Imaging

As we have seen, in optical molecular imaging the signal is produced by an energy shift of outer electrons. In the case of nuclear molecular imaging, signals are produced as a result of a rearrangement of the atomic nucleus. Two of the most widely used nuclear imaging techniques used in molecular imaging are MRI and PET.

MRI

Some elementary particles are found to have different energy levels in a magnetic field. In quantum theory, this property is characterised as spins. Not every atom has spin, ^{1}H,

^{13}C, ^{14}N and ^{17}O are spin isotopes that exist naturally in many bio-molecules and are most often targeted in biomedical MRI.

Spin atoms can be thought of as magnetic dipoles. Normally, these spin atoms are randomly oriented, that is, they do not give rise to an overall magnetic field. In the presence of a sufficiently strong external magnetic field, the spin atoms will tend to allign with the external magnetic field and produce a magnetic field in the same direction as the external magnetic field (conventionally, this defines the Z axis of a Cartesian coordinate frame). However, due to Newtonian mechanics, these spin atoms do not completely align with the external magnetic field, rather they precess around the external magnetic field vector (Figure 2.2).

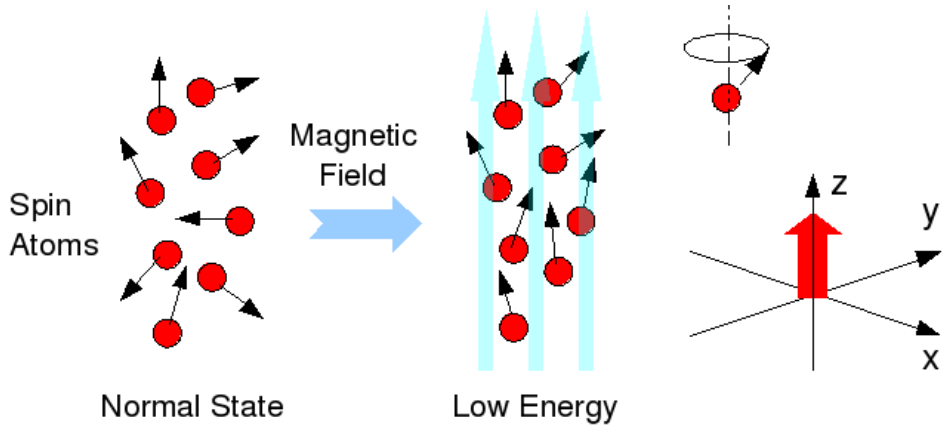

Figure 2.2: Spin atoms in normal environment and in magnetic field.

A radio frequency pulse, when tuned to a specific frequency, can excite spin atoms to a higher energy state. Absorbing energies from the radio pulse, these spin atoms tend to align against the external magnetic field. A 90° pulse is the radio pulse that aligns a number of spin atoms against the external magnetic field so that the premier Z-magnetism is cancelled out. The 90° pulse also resonates the spin precession and produces a magnetic field that rotates in the X-Y plane (Figure 2.3).

When the radio frequency is switched off, the spin atoms experience relaxation processes. First, the spin atom precession will quickly dephase so that the X-Y magnetism

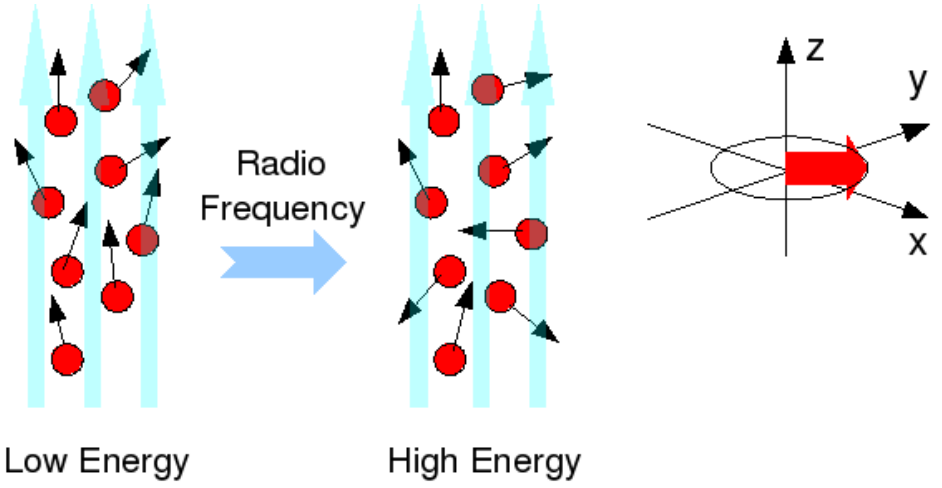

Figure 2.3: Spin atom excitation and relaxation.

will decrease. This process is called T_2 or transverse relaxation. Meanwhile, the excited spins will slowly lose energy and tend to align with the external magnetic field, increasing the magnetism along the Z axis. This process is called T_1 or longitudinal relaxation. Specific detectors are employed in MRI to sense these changes of magnetism. The signal depends on the rates of change of magnetism which is determined by the T_1 or T_2 relaxation rates.

Both T_1 and T_2 relaxations are widely used to produce signal in biomedical MRI. The relaxation rates are related to the lattice structure of the spin atoms. Spin atoms situated in soft tissues have different and very much shorter T_1 or T_2 relaxation rates than those that are situated in solid tissues. In this way, soft tissues can be differentiated from solid tissues, and from each other, in either T_1 or T_2 weighted MR images. However, the difference in the relaxation rates is small, which reduces the MR image contrast. In dynamic contrast enhanced MRI (dce MRI), a contrast agent is designed to accumulate in specific abnormal tissues. These agent molecules are conjugated with spin atoms and will generate MR signals. The image contrast is thus a function of the differences of spin atom densities in the agent molecules and in their surrounding tissues. The reconstructed image then essentially reflects the distribution of contrast agent molecules. This greatly enhances image contrast and can detect tissues with specific physiological abnormalities.

PET

The MR signal originates in a change of nucleus energy status. In contrast, the signal in PET imaging is generated from a change of nuclear structure. It is based on positron decay, which was first discovered by Anderson in 1932. When a nucleus undergoes positron decay, it will produce a new nucleon with one fewer proton and one more neutron, as well as the emission of a positron and a neutrino:

$$ {}^{A}_{Z}X_N \rightarrow {}^{A}_{Z-1}Y_{N+1} + e^+ + \nu, \tag{2.1} $$

where A is the atom's mass number, Z is the atom's atomic number, N is the number of neutrons, e^+ denotes the produced positron, and ν denotes the produced neutrino. Radionuclides that decay via positron emission are proton-rich and move closer to the line of stability, while giving off a positive charge. A neutrino has non-zero mass but interacts only very weakly with other particles. Its presence in the positron decay makes the energy of the positron variable, as opposed to gamma emissions, which have fixed energies for any given radionuclide [1].

A positron has a mass that is similar to that of an electron, but has an opposite charge. In fact, it is the antiparticle or antimatter of an electron. When a pair of antiparticles collide, mass will be transformed into energy, a process which is called annihilation.

According to Einstein's mass-energy equation:

$$ E = mc^2, \tag{2.2} $$

where m is the total mass of the antiparticles, c is the speed of light which equals 2.998 $\times 10^8$ m/s and E is the energy that should be released during the annihilation process.

In the case of a positron and an electron, the annihilation will produce two γ-photons with 511 keV (kilo electron Volt) energy. As the positron and electron are almost at

[1] Gamma emissions are the signal sources in single photon emission computed tomography (SPECT) imaging.

rest when the annihilation occurs, the net momentum is close to zero. According to the law of conservation of momentum, the two photons generated will transverse in (nearly) opposite directions (Figure 2.4):

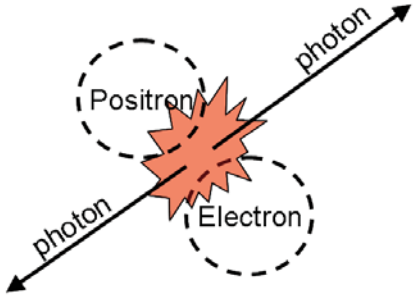

Figure 2.4: Illustration of an annihilation process

The emitted 511 keV γ-ray can pass through most human tissues and be detected by the detectors that form a key part of the PET scanner (however, there is an attenuation effect by the tissue which has to be corrected for in the process of image reconstruction). In PET imaging, a technique called *coincidence detection* is used to detect and record the coincident detection of a pair of γ-photons (termed coincident events) based on energy and timing criteria. Currently, two events are considered coincident if they are detected at times separated by at most 10ns.

Several physiologically active chemicals containing an unstable nucleus are synthesized for PET imaging. They are injected into a living subject intravenously in trace doses (hence the name, tracer) to image the relevant tissues. For example, $[^{13}N]$-Ammonia is an important cardiac PET perfusion agent, $[^{11}C]$acetate and $[^{11}C]$palmitate are used to study cardiac oxygen consumption and fatty acid metabolism, respectively; and $[^{18}F]$ Fluorodeoxyglucose (FDG) has been widely used to imaging glucose metabolism *in vivo*.

2.2.3 Ultrasound Imaging

Optical and nuclear molecular imaging utilize chemical or nuclear reactions as signal sources. In ultrasound imaging, an ultrasound pulse is sent to the targeted tissue. Depending on the tissue's echogenic properties, the ultrasound wave may be absorbed,

refracted or reflected by the tissue. Ultrasound imaging exploits the differences in echogenicity of different tissues to produce *in vivo* images. To enhance image contrast and enable molecular imaging, microbubbles or other acoustically active nanoparticles can be used to highlight the target molecules in the final reconstructed image (Kaufmann & Lindner, 2007).

The microbubbles are usually filled with different gases, and their sizes are typically in the range 1-5μm, which have different resonant properties in the ultrasound field. This enhances the contrast between the microbubble and its surrounding tissues in the final ultrasound (US) image (Voigt, 2009; Kaufmann & Lindner, 2007).

The chemical composition of the microbubble shells can be designed so that it has a high affinity to specific biological molecules. Alternatively, some bio-signal fragments, such as antibodies, glycoproteins, carbohydrates or peptides, can be grafted into the shells of the microbubbles. As a result, such microbubbles attach to specific target biomolecules. Non-bound microbubbles can be quickly washed out before the image is recorded to produce a high signal-to-noise ratio (Voigt, 2009).

2.3 Technology Developments

2.3.1 Imaging Agents

Although many chemicals are fluorescent and can be used as imaging agents in *in vitro*/*ex vivo* optical imaging, imaging agents for *in vivo* imaging have to meet a number of criteria. First, imaging agents should have high affinity for the target molecules in order to give detectable signals for external detectors. Second, such imaging agents should have high specificities, which means that they will not bind to molecules other than the target molecule in the *in vivo* environment. Third, to be useful, imaging agents should have a suitably long life time in the *in vivo* environment. This requires them to have high resistance to the various macrophages and degrading enzymes in the *in vivo* environment. Above all, the imaging agents should be themselves non-cytotoxic and

requires no procedures that may destroy the cells during imaging processes. Figure 2.5 lists the *in vivo* imaging agents for nuclear, optical and ultrasound imaging techniques.

Imaging Technology	Imaging Agent	Clinical Application
Nuclear(SPECT/CT)	^{18}Fluorodeoxyglucose	Tumour cell metabolism
	^{18}Fluorothymidine	Tumour cell metabolism
	Somatostatin analogues	Neuroendocrine tumours
	Metaiodobenzylguanidine	Neuroendocrine tumours
	Arcitumomab	Colorectal, ovarian cancers
	Capromab	Prostate cancer
	Bectumomab	Lymphoma
	Satumomab	Colorectal, ovarian cancers
	Ibritumomab	Lymphoma
	Tc-99m Methoxyisobutylisonitrile	Multidrug-resistant lung cancer
	Bombesin	Many cancers
	Estrogen receptor ligands	Breast cancer
	Folate receptor ligands	Ovarian cancer
	Annexin A5	Apoptosis
MRI	Iron oxide (ferumoxide)	Liver cancer
	Iron oxide (ferumoxtran/ferumoxytol)	Nodal staging
	Integrin $\alpha_v\beta_3$	Agiogenesis
Optical/NIRF	Cathepsin B	Many cancers
	Matrix metalloproteinases	Many cancers
	Targeted fluorochromes (her2neu, annexin A5, etc.)	Many cancers
Ultrasound	Integrin $\alpha_v\beta_3$	Angiogenesis

Figure 2.5: Table of molecular imaging agents applied in cancer detection, reproduced from Jaffer & Weissleder (2005).

Given these strict criteria, multiple technologies have been developed to assist *in vivo* imaging. For example, amplification strategies such as chemical activation and conformational changes; background washout strategies for unbound agents; multivalency and biological trapping strategies have been used to reduce imaging dose, background noise and enhance specificity respectively (Jaffer & Weissleder, 2004).

Meanwhile, other novel technologies, in particular nanotechnology, have been applied in molecular imaging to further improve the accuracy and functionality of molecular imaging.

2.3.2 Nanotechnology

Nanotechnology refers to any technology where the dimensions and tolerances are in the range 0.2 nm to 100 nm (Dowling *et al.*, 2004). Nanomaterials refers to the rapidly evolving branch of nanotechnologies that focuses on developing new materials at nanoscales. It has been observed that materials of such atomic dimensions exhibit dramatically different optical, electronic, and magnetic properties as traditional materials, and this can be exploited in molecular imaging (Jiang *et al.*, 2009). Meanwhile, nanoparticles interact with biological systems at the molecular level and accurately reflect molecular information about the biological system. This feature also enhances the reliability of quantifications of the imaging signal. Finally, the special material design of nanoparticles makes them capable of self-assembly and maintains stability and specificity, which are important in molecular imaging (Wang *et al.*, 2008).

Nanoparticles have been widely used to deliver imaging contrast agents to tissue sites (liposome, polymer) or used as imaging agents directly (quantum dots, upconversion nanoparticles) (Green *et al.*, 2007; Townley *et al.*, 2008).

Liposomes

Natural (endogenous) liposomes are usually formed by phospholipids, which are a class of lipids that have two poles: a hydrophilic pole, which usually consists of a phosphate group; and a hydrophobic pole, which is usually formed by long fatty acid hydrocarbon chains. In a polar environment, such as water, such bipolar molecules can self assemble into a spherical structure (Figure 2.6), with hydrophilic parts contacting with the polar solvent molecule (such as H_2O). This bi-layer spherical structure is called a liposome, and can be used as nanoparticles in molecular imaging. Imaging contrast agents could be loaded in the enclosed volume of liposomes. For targeted delivery, the phosphate groups of phospholipids are usually conjugate with antibodies that target specific signal molecules anchored in the cell membrane. When the liposome is attached to the cell

membrane surface, it fuses with the cell membrane. In this way, the image contrast agents are delivered into the targeted cells.

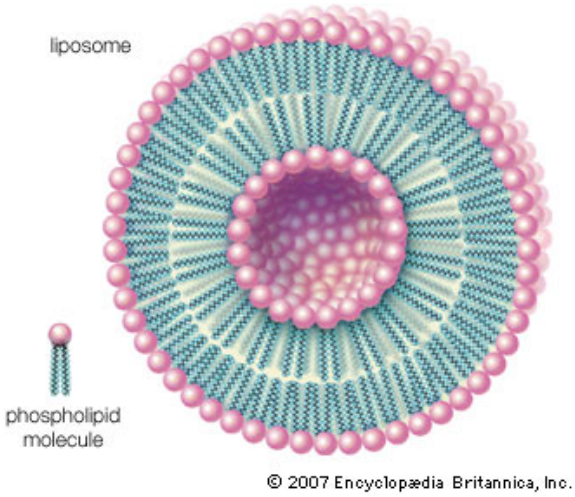

Figure 2.6: Illustration of phospholipid and liposome. Image source: Encyclopedia Britannica.

Polymer

Polymers are a class of macro molecules that are synthesized from monomers. Both natural (albumin, chitosan, heparin, etc.) and synthetic (poly-L-lactide, poly-[Lglutamate],poly-[D,L-lactide-co-glycolide], PEG,etc.) biodegradable polymers have been used to package imaging contrast agent in molecular imaging techniques (Wang *et al.*, 2008). Imaging contrast agents are usually physically dissolved, entrapped, encapsulated in, or covalently attached to the polymer matrix (Rawat *et al.*, 2006). Hydrophilic polymer coating can protect nanoparticles from macrophages and degradative enzymes and increase a nanoparticle's solvency in water (Wang *et al.*, 2008). These nanoparticles thus have a longer lifetime in the plasma and can effectively deliver the imaging contrast agents to the target tissues through the circulatory system.

Quantum Dots

Quantum dots refer to a class of fluorescent semiconductor nanocrystals (Michalet *et al.*, 2005). One striking property of quantum dots is the dramatical change of their fluores-

cence properties as a function of size (Figure.2.7).

Figure 2.7: Fluorescence properties of quantum dots with different sizes. Ten distinguishable emission colours of ZnS-capped CdSe quantum dots were excited with same near-UV lamp. From left to right (blue to red), the emission maxima are located at 443, 473, 481, 500, 518, 543, 565, 587, 610 and 655 nm. Reprinted from Han *et al.* (2001), with permission.

Because of their size-dependent emission property, quantum dots are very useful in multichannel cellular imaging. Targeted cellular molecules can be labelled with quantum dots with different sizes to yield different colours from a single excitation wavelength. It has been found that colloidally prepared II-VI semiconductors, such as CdS and CdSe, and III-V semiconductors like InP can generate a broad emission wavelength range in the visible spectrum (Alivisatos, 1996) and are thus commonly used to synthesize quantum dots for molecular imaging. The sizes of quantum dots can be controlled by changing the concentration of precursors and the crystal growth time (Jiang *et al.*, 2009).

Quantum dots are quite resistant to photobleaching and are suitable for long-period *in vivo* tracking (Jiang *et al.*, 2009). Cytotoxicity is a critical issue in *in vivo* imaging. Although CdTe and CdSe quantum dots have been reported to be cytotoxic (Shiohara *et al.*, 2004; Lovrić *et al.*, 2005), low dose imaging (Michalet *et al.*, 2005) and surface coating (Jiang *et al.*, 2009) can considerably reduce the cytotoxicity of quantum dots. In addition, it has been proposed that quantum dots are more stable for long-period *in vivo* imaging than conventional dye-doped nanoparticles (Gao *et al.*, 2004). For *in vivo* imaging, near-infrared quantum dots have been developed to replace UV quantum dots used in *in vitro*/*ex vivo* imaging (Yong, 2009).

Upconversion Nanoparticles

Upconversion nanoparticles are phosphors that are excited in the near-infrared region and emit light in the visible spectrum region (Jiang *et al.*, 2009). Upconversion nanoparticles are usually LaF_3,, YF_3, Y_2O_3, $LaPO_4$ or $NaYF_4$ crystals embedded with trivalent rare earth ions such as Yb^{3+}, Er^{3+} and Tm^{3+} (Jiang *et al.*, 2009). Such trivalent ions "convert" the near-infrared light "up" to visible light. Specifically, the Yb^{3+} ion absorbs near-infrared light, the absorbed electromagnetic energy is then transferred in the crystal lattice to Er^{3+} or Tm^{3+} ions. Er^{3+} (or Tm^{3+}) accumulates the electromagnetic energies and emits light in the visible spectrum.

Since upconversion nanoparticles can be excited by near-infrared light, this feature makes it suitable to replace ordinary fluorescence molecules that are excited by UV light. Meanwhile, upconversion nanoparticles are also found to have excellent photostablility, chemical stability, low toxicity and are biocompatible (Chatterjee *et al.*, 2008). For these reasons, they have been widely used in *in vivo* optical imaging (Chatterjee *et al.*, 2008; Lim *et al.*, 2006).

2.4 Applications

2.4.1 Histochemical Imaging

In vitro/*ex vivo* optical imaging is a convenient method for researching the histochemical properties of tissues and cells. Numerous studies have been conducted with fluorescence imaging to obtain images of microvessels (Qayum *et al.*, 2009), tumour cells (Voura *et al.*, 2004), actin filaments (Kron & Spudich, 1986), amyloid fibrils (Yagi *et al.*, 2009) and so on.

2.4.2 Imaging Gene expression

Cellular gene expression can be probed by imaging its corresponding protein product. When a particular gene is over-expressed, the concentration of its protein product will

be elevated, yielding a high response to molecular imaging agents. For example, Hilger *et al.* (2004) labelled HER-2 with Cy5.5 coupled anti-HER-2 antibody and research the HER gene expression in tumour cells with fluorescence imaging. Cai *et al.* (2007) evaluated EGFR expression in xenograft-bearing mice by labelling ^{64}Cu to EGFR's antibody, cetuximab, with quantitative PET imaging.

2.4.3 Functional Imaging

Cellular biological activities are usually accompanied by the consumption and production of different chemicals. For instance, neural activities usually lead to a high production of calcium ions. Fluorescent calcium indicator proteins (FCIPs) are a class of fluorescent proteins which have a high affinity to calcium ions. These proteins could be used to monitor the activities of neurons with optical imaging techniques (Hendel *et al.*, 2008).

Tumours cells are characterised by their altered metabolisms. Glucose is the major substrate for cellular metabolism. An ^{18}F labelled glucose analogue, [18F]fluoro-2-deoxy-D-glucose (FDG), has been widely used in PET imaging to assess the activities of various tumour cells (Bradley *et al.*, 2004; Erasmus *et al.*, 1998; Delbeke, 1999). In addition, the tumour microenvironment is usually characterized by a low oxygen concentration (hypoxia). A group of PET imaging agents has been developed to be able to accumulate in this area and monitor the hypoxic regions of the tumour microenvironment. [F-18] fluoromisonidazole (Rasey *et al.*, 2009) and 60 Cu-ATSM (Dehdashti *et al.*, 2003) are two widely applied hypoxia tracers in PET imaging.

2.4.4 Drug Development

Nuclear imaging, quantitative PET imaging in particular, has been widely applied in drug discovery (Rudin & Weissleder, 2003). It is relatively easy to label many candidate drug agents with ^{11}C or ^{18}F (Fischman *et al.*, 2002) and to monitor their biodistributions using PET imaging. Various mathematical models have been developed to calculate

pharmacokinetic parameters of these drug from the temporal variances of PET signal (Guo *et al.*, 2009; Mintun *et al.*, 2004).

2.5 Summary

Molecular imaging is a broad imaging category. Compared with other imaging techniques, molecular imaging directly captures interactions at the molecular level. Thus they are capable of targeting specific marker molecules of various diseases. For this reason, they have quickly gained popularity in biomedical applications. For example, fluorescent imaging has become a primary *in vitro*/*ex vivo* imaging option in biochemical researches and nuclear imaging techniques like PET, SPECT and contrast enhanced MRI, have become an routine clinical imaging modality.

Meanwhile, molecular imaging techniques continue to be the subject of rapid development. For example, special imaging procedures and image reconstruction algorithms have been proposed to enhance the resolution of ordinary fluorescence microscope methods (Rust *et al.*, 2006). This enables optical imaging techniques to monitor interactions on the atomic scale, and empowers biochemical researchers to unravel the mechanisms of life at a finer scale (Figure.2.8).

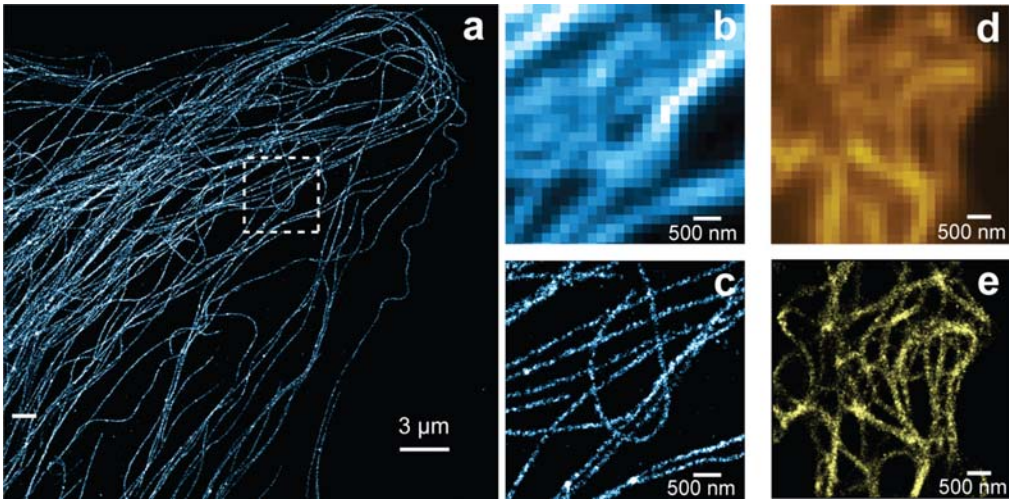

Figure 2.8: Comparison of stochastic optical reconstruction microscopy (STORM) imaging and ordinary microscope images. (a): STORM image of microtubules in BS-C-1 cell; (b) and (c): ordinary microscope and STORM images corresponds to the boxed region in (a); (d) and (e): ordinary microscope and STORM images of vimentin in a BS-C-1 cell, reprinted from Zhuang (2009), with permission.

Chapter 3

Image Processing

3.1 Introduction

Fluorescent microscope imaging techniques are frequently employed in biomedical research to yield pictures on a molecular scale. This chapter discusses the applicabilities of different image analysis methods in processing the tumour vessel microscope images.

3.1.1 Fluorescent Labelling

Fluorescence refers to the phenomenon in which certain chemical molecules emit electromagnetic radiation of a particular wavelength (emission) as a result of absorbing radiation of a different wavelength (excitation). Those chemicals which have the ability to generate fluorescence are said to be "fluorescent", and the specific group of atoms that are responsible for fluorescence are called fluorophores.

In biochemical research, a fluorophore is often conjugated with antibodies which bind specifically with target molecules (antigens). This process is called fluorescent labelling. There are two methods of fluorescent labelling: direct and indirect. In direct labelling, the fluorophore is labelled with an antibody which binds directly with antigens. In indirect labelling, the fluorophore is labelled with an antibody (the secondary antibody) which binds to another antibody (the primary antibody). In turn, this primary antibody binds with the antigens of interest (Figure 3.1):

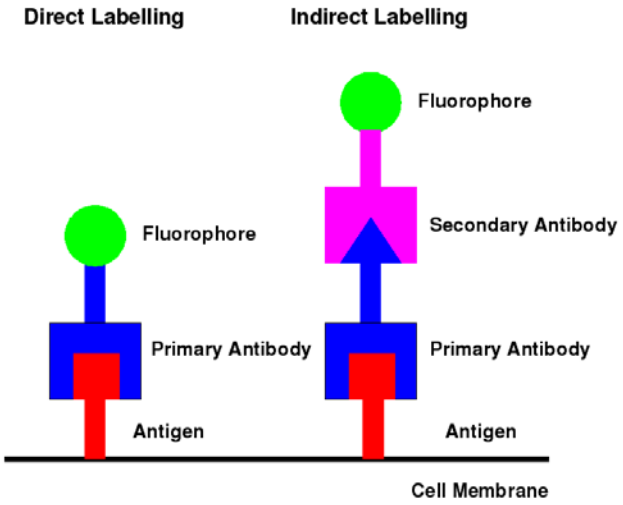

Figure 3.1: Illustration of direct and indirect labelling.

The microscope images of tumour blood vessels used in our research are prepared by labelling CD31, which is a molecule anchored on the membrane of vascular endothelial cells, with antibodies conjugated with RPE. RPE, R-Phycoerythrin, is a widely used fluorophore that can be excited with a 488nm laser and emits radiation with a wavelength of 575nm .

3.1.2 Confocal Microscope

The emission of fluorophores can be detected and recorded with a range of microscope technologies. For example, confocal microscopy is a type of optical microscope which can generate images of cells at a particular depth in the specimen (focal plane). A pinhole is installed in front of the photomultiplier detector (Figure 3.2). It filters out signals emitted from sites other than the focal plane (as contrasted to multiphoton fluorescence microscope where the sectioning is produced by interferences between pulsed laser beams). Since signals from other depths in the specimen are eliminated, images recorded by confocal microscopy are of higher resolution and contrast compared to images obtained through conventional light microscopes. The width of pinhole can be adjusted to set the position of the focal plane at different depths in the specimen. [1] The stack of

[1]The volume resolution is also critically dependent on the optical property of objective lens

2D images recorded at different successive depths can subsequently be constructed into a 3D image of the specimen volume [2].

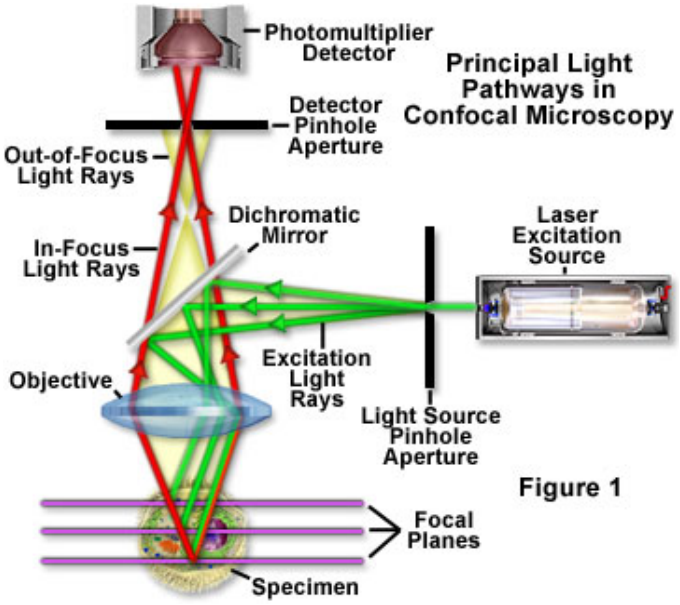

Figure 3.2: Mechanics of confocal microscopy. The fluorescent labelled specimen is radiated with laser of a specific wavelength, the emitted radiance from the specimen is then detected and recorded as an image. A dichromatic mirror is used to filter the excitation laser and the pin hole filters the out-of-focus signal.

3.1.3 Microscope Image Analysis

Microscope images obtained from fluorescence labelling are often found to have relatively high noise levels. This is as a result of the non-specific binding of the fluorescent labelled antibodies with other molecules.

Additionally, if images have to be taken rapidly in order to avoid changes to the *in vivo* physiological conditions, the recorded image can become blurred as a result of the fast motions of experimenters. Besides, depth and low exposure time may also lead to low resolution of microscope images. For this reason, image de-noising and enhancement are critical components of microscope image analysis.

[2]The microscope images analysed in our research were recorded using confocal/multiphoton microscopy (Leica). Confocal/multiphoton stacks of 100 μm were taken at 0.5-μm intervals, using a 20$\times$ lens (each slice corresponds to 600 μm $\times$ 600 μm area and consists of 512 $\times$ 512 pixels). 3D image was constructed from the image stacks and resolution along X, Y and Z axes was made equal to 2.344μm.

In order to perform shape analysis, a binary image in which 1 represents vessel voxels and 0 represents the background is required. The extraction of the object (blood vessel) from its background is called segmentation in conventional image analysis. Most segmentation methods are based on voxel intensities, such as intensity thresholding, clustering methods and methods based on fuzzy sets. However, intensity alone does not provide all the relevant information about the object. More sophisticated methods take the object's spatial connectivities and shapes into consideration; such methods include hysteresis thesholding and level sets. More recently, local phase has been proposed to capture the phase information that is believed to be relevant for feature perception. Local phase-based segmentation methods are discussed in this chapter and segmentation results will be compared with those that result from intensity-based methods.

After segmentation, it is desirable to extract the single voxel-wide centre lines of the blood vessel objects to research their structures. This process is known as skeletonization in the image analysis literature. The majority of skeletonization methods are based on the assumed symmetry of the object's shape, since the object should be (close to) symmetrical about its centre line. Two categories of skeletonization method may be identified: discrete and continuous methods. In discrete methods, the centre line of an object is extracted by eroding the object with equal number of pixels (voxels) from boundaries. In continuous methods, a hypothetical repulsive potential field is generated on the surface of object. The centre line is found at the neutral point inside the object. After extensive experimentation, we found that methods from both skeletonization categories were incapable of extracting the "true" skeletons of vessel objects, due primarily to the irregular surface shapes of real blood vessels. To overcome this difficulty, we propose a vessel surface regularization procedure and we show that it is capable of extracting satisfactory vessel skeletons.

3.2 Image Segmentation

3.2.1 Thresholding

Thresholding is the most basic and straightforward segmentation method. It works by setting an intensity range which defines "object"; all others being labelled as background. The effectiveness of a thresholding method is closely related to the profile of the corresponding image histogram. For images which have identifiable intensity ranges in the histogram, a thresholding method can give quite satisfactory results (Figure 3.3):

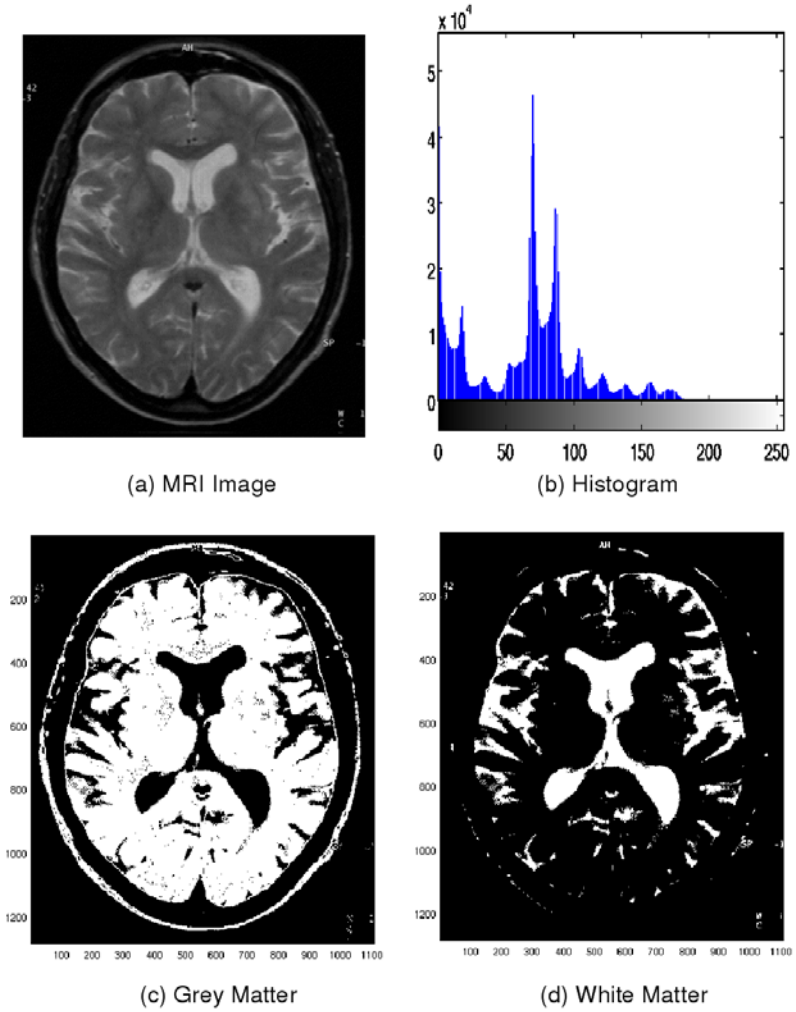

Figure 3.3: (a) Original MR image (2D), reprinted from Fluri *et al.* (2007) with permission. (b) Histogram of original image. (c) Segment of gray matter by setting intensity range between 50 and 100. (d) Segment of white matter by setting intensity range above 100.

However, for images whose histograms do not enable the determination of a range, determining a suitable intensity threshold can be at best problematical, at worst impossible (Figure 3.4).

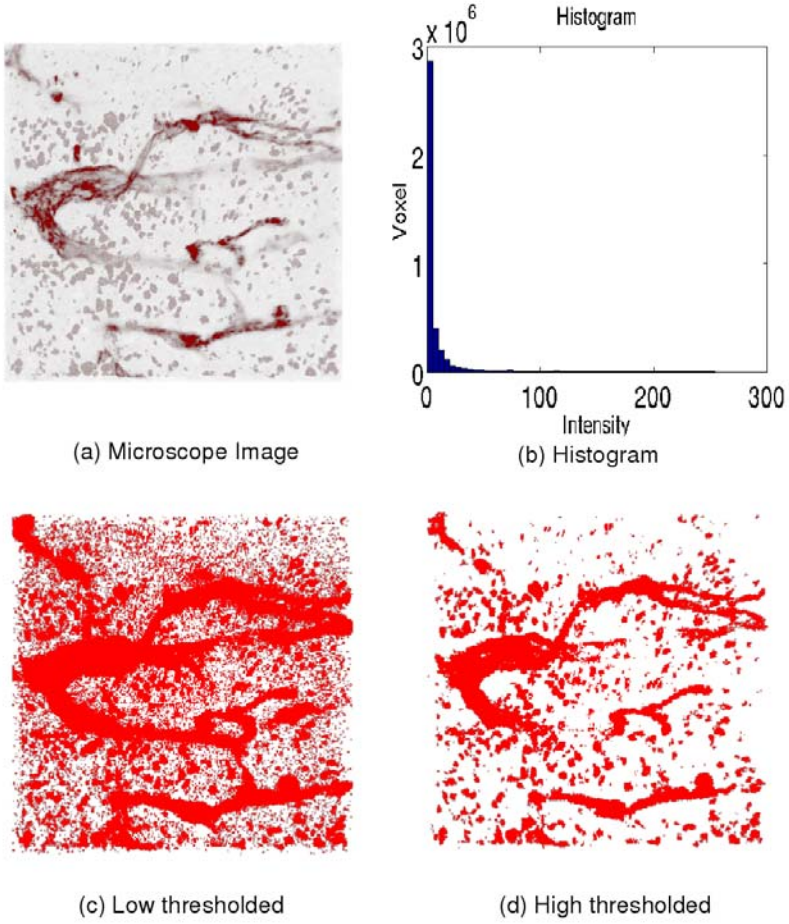

Figure 3.4: (a) Original microscope image (3D), courtesy of Dr.Naseer Qayum, Gray Institute for Radiation Oncology and Biology, University of Oxford. (b) Histogram of original image. (c) Segment of blood vessel by setting intensity range above 5. (d) Segment of blood vessel by setting intensity range above 10.

Simple thresholding classifies the pixels (voxels) based solely on their intensities. This would give a satisfactory result if the threshold can be easily determined, as in Figure 3.3. However, if the image contrast is low, the threshold intensity can be quite difficult to define as shown in Figure 3.4. Further, if intensities in the object region are close to, or even below, the background intensity, they can not be distinguished using simple thresholding Figure 3.4. However, such regions may be identified by considering their

spatial adjacency to the high intensity regions. Thresholding according to voxel intensity-position correlations is known as hysteresis thresholding.

The mechanics of hysteresis thresholding involves defining two thresholds, one higher level and one lower level. The high and low thresholds create three intensity regions, as shown in Figure 3.5(a):

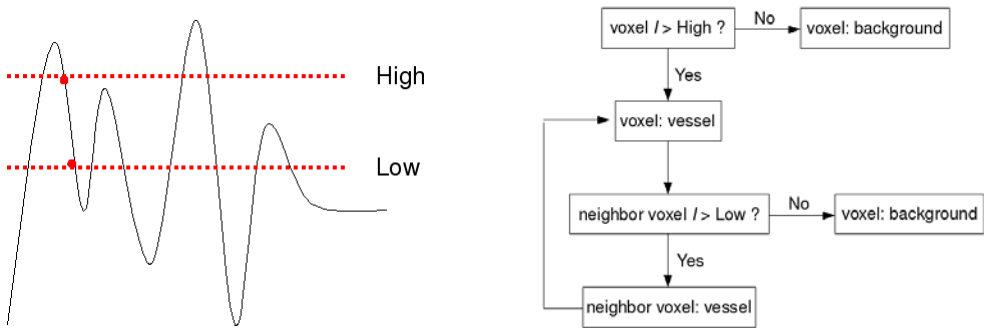

(a) (b)

Figure 3.5: Mechanism of hysteresis thresholding.

Voxels with intensities above the high threshold are accepted as vessel voxels. These voxels are used as seeds in the subsequent region growing algorithm. This algorithm iteratively grows the region by accepting those neighbouring voxels whose intensities are above the low threshold. The algorithm terminates when no more neighbouring voxels can be accepted (Figure 3.5(b)).

Figure 3.6 illustrates the process of hysteresis thresholding. In practice, high and low threshold levels are determined intuitively. The original image (Figure 3.6(a)) was first thresholded at a high intensity level. The segment (Figure 3.6(b)) was then utilized as a set of seeds in the subsequent region growing process which accepts adjacent voxels with intensities above the lower threshold as vessel voxels (Figure 3.6(d)). The effect of applying the lower threshold directly on the original image is illustrated in Figure 3.6(c). The superior performance of hysteresis thresholding over conventional thresholding methods on low contrast images can be evaluated by comparing the segments in Figure 3.6(b), (c) and (d).

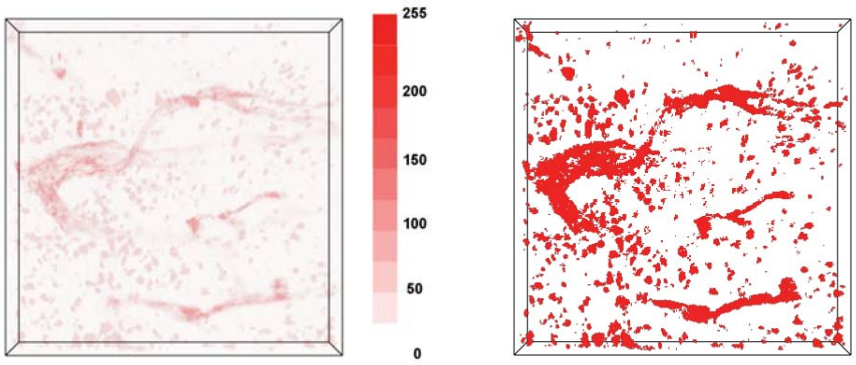

(a) Original Microscope Image (b) High thresholded image

(c) Low thresholded image (d) Final thresholded image

Figure 3.6: Hysteresis thresholding on 3D image with low threshold equals to 3 and high threshold equals to 15 in the 0-255 gray scale.

Fluorescent microscope images are frequently "contaminated" (as we explain below) if multi-channel imaging techniques are used. In multi-channel imaging the specimen tissue is incubated with several types of antibodies labelled with different fluorophores. The emission wavelengths of these fluorophores are different from each other. For example, one fluorophore may emit radiance with a wavelength around 600 nm (in the red channel) while another fluorophore may emit radiance with wavelength around 500 nm (in the green channel). Multi-channel imaging records these signals separately. This technique enables simultaneous imaging distributions of different biomolecules of interest. For this reason, multi-channel imaging is often employed in confocal microscopy.

However, the emission spectra of the fluorophores used in multi-channel imaging may overlap with each other. This results in images from one channel being contaminated by signals from other fluorophores. For example, in the microscope images we have analysed, the CD31 channel has recorded signals from GFPs which label cell membranes. Since the GFP signals are of high intensities, they can't be removed based on their intensity profiles. However, the GFP signal regions are typically small in comparison with the CD31 blood vessel regions, and so we can remove these regions by size thresholding.

In size thresholding we first count voxels contained in each simply connected region after intensity thresholding and then threshold the binary image with a size threshold. This effectively removes regions that are smaller than the specified size. The combination of hysteresis thresholding with size thresholding produces a blood vessel object shown in Figure 3.7

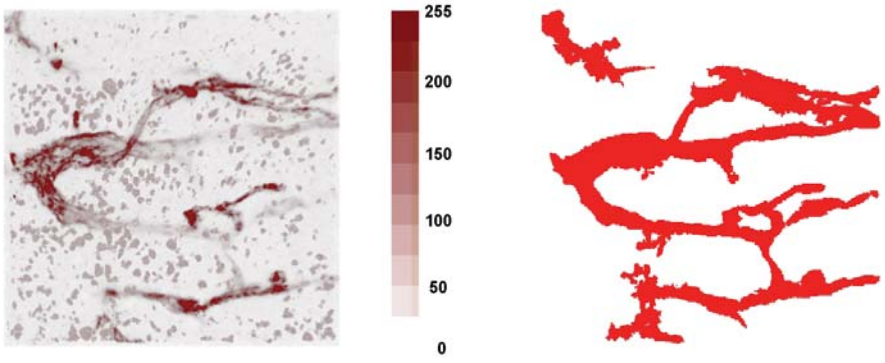

(a) Original Microscope Image (b) Size thresholded image

Figure 3.7: Segmented image was then threhsolded with size range above 1200 voxels.

The combined hysteresis-size thresholding method was found to give satisfactory segmentation results (Figure 3.7). It is computationally efficient and straightforward to implement. However, the high and low thresholds depend on subjective decisions, which can materially affect the accuracy of the segmentation results. For this reason, we have explored alternative segmentation methods. The first of these is the level set method.

3.2.2 Level Sets

The level set method is a PDE-based segmentation technique that converts an image segmentation problem into a functional minimization. It consists of two steps, namely the construction of an appropriate energy model and then functional minimization.

The idea of modelling curves using an energy function(al) was first proposed by Michael Kass, Andrew Witkin and Demetri Terzopoulos (Kass *et al.*, 1988). A snake (also called an active contour) is a closed (i.e. two-connected) parameterized curve whose shape can change arbitrarily in the image field [3]. The snake is defined to possess an energy as expressed in Eq.3.1

$$\begin{aligned} E^*_{snake} &= \int_0^1 E_{snake}(v(s))ds \\ &= \int_0^1 E_{int}(v(s)) + E_{image}(v(s)) + E_{ext}(v(s))ds \\ &= E^*_{int} + E^*_{image} + E^*_{ext}, \end{aligned} \tag{3.1}$$

where $v(s) = (x(s), y(s))$ is the parameterized curve function, E^*_{int} is the "internal" energy of the contour and derives from the geometrical shape of the curve (e.g. curvature), E^*_{image} represents energy derived from the image data and E^*_{ext} expresses a set of constraint conditions that are imposed according to intuitions about the application. In classical active contour models, E^*_{int} is often defined as a weighted sum of the snake's length and the area it encloses. E^*_{image} and E^*_{ext} are usually expressed in the form of regularizers suggested by different researchers to achieve different effects. The energy functional is defined so that it reaches its global minimum when the snake aligns with the boundaries between high and low intensity regions in the image. This effectively segments high intensity (or low intensity) regions from their backgrounds. Thus the image segmentation has been converted to a functional minimization problem to find the function $v_{min}(s)$ which minimises the functional E^*_{snake}.

[3] So named because of the way the contours slither while minimizing their energy (Kass *et al.*, 1988).

The optimization of an energy functional such as that given above can be achieved by solving the corresponding Euler-Lagrange equation. Level sets refer to a mathematical method to solve such partial differential equations (Osher & Sethian, 1988). Essentially, the level set method regulates the path in searching for $v_{min}(s)$. In a level set, the snake is modelled as a moving front of the zero-level set S(t)=$\{X_n|\phi(X_n) = 0\}$ of a level set function $\phi(t, X_n)$, where X_n denotes n-D coordinates. By modelling the evolution of a n-D snake as projections of (n+1)-D snake volume on the zero-level plane, the level sets method effectively ensures that the snake evolves in a constrained and continuous manner (Figure 3.8). This is a valid assumption in the segmentation scenario and narrows considerably the flexibility of snake's evolving behaviour. Also, the level set method removes the constraint of two-connectivity on the energy minimising curve, enabling two curves to merge/split.

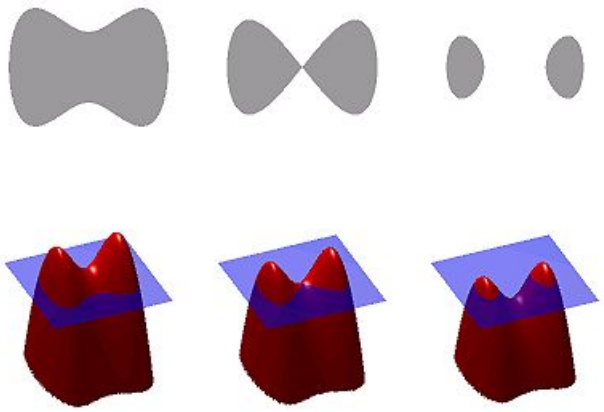

Figure 3.8: Illustration of level set evolution. The evolution of 2D snake (upper) is modelled as zero-plane projections of a 3D volume (lower).

The level set function $\phi(t, X_n)$ is often defined as a signed distance function. For a given distance measure and a set S, any points inside S are given a positive signed distance value to S's boundary, whereas any points outside S are given a negative signed distance value to S's boundary (Figure 3.9).

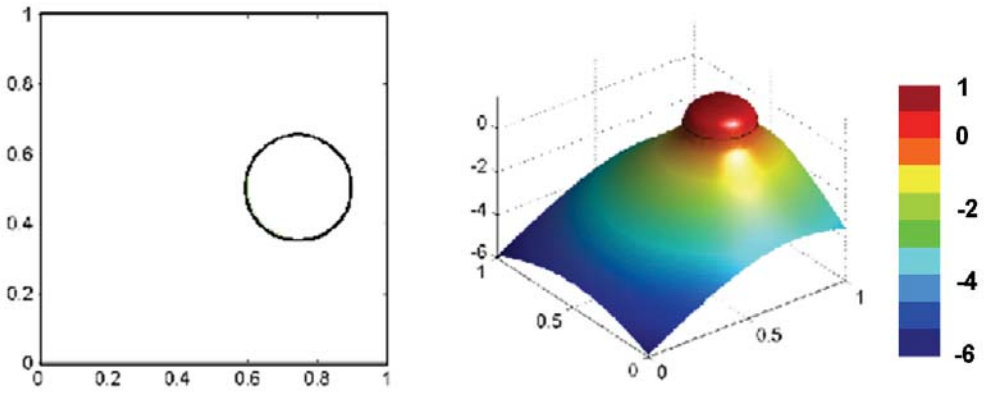

Figure 3.9: A circle in 2D map (left) and its signed distance function in 3D (right).

The equation that regulates the snake's evolution can be expressed as the following level set equation (Osher & Sethian, 1988):

$$\frac{\partial \phi}{\partial t} + F|\nabla \phi| = 0, \tag{3.2}$$

where the speed function F depends on the image data and the level set function ϕ. As it determines convergence speed and iteration errors, it is one of most researched topic in the level set literature.

Level sets methods can either be categorised by the energy models (active contour model) or by speed functions (Chan & Vese, 2001). The speed functions can be classified as edge dependent and independent (Chan & Vese, 2001). Here, we introduce one representative level set method from each class.

Speed function depending on the edges

Usually, to enable the active contour to evolve quickly when it is far from the object's boundary and slowly when it approaches it, images are first filtered with an edge detector before the level set method is applied. The edge detector is normally based on the intensity gradient of the image. A widely used detector is shown in Eq.3.3

$$g = \frac{1}{1 + |\nabla (G_\sigma \otimes I)|^2}, \tag{3.3}$$

where I is the original image, g is the edge enhanced image, G_σ is a Gaussian filter that smoothes the image and $\otimes$ denotes convolution operation. The length of the snake and the area that it encloses are calculated from this edge enhanced image g: (Eq.3.4)

$$\begin{aligned} L_g(\phi) &= \int_\Omega g\delta(\phi)|\nabla\phi|dxdy \\ A_g(\phi) &= \int_\Omega H(-\phi)dxdy, \end{aligned} \tag{3.4}$$

where H is the Heaviside function and δ is the derivative function of H.

Li *et al.* (2005) proposed a regularizer to penalize deviations of ϕ from the signed distance function through the iterations. In the classical active contour model (Eq.3.1) it is a type of external energy. It could be written as Eq.3.5:

$$E^*_{ext}(\phi) = \int_\Omega \frac{1}{2}(|\nabla\phi| - 1)^2 dxdy \tag{3.5}$$

It follows that the snake's energy could be written as (notice there is no image derived energy term):

$$\begin{aligned} E^*_{snake} &= E^*_{int} + \mu E^*_{ext} \\ &= \lambda L_g(\phi) + \nu A_g(\phi) + \mu E^*_{ext} \\ &= \lambda \int_\Omega g\delta(\phi)|\nabla\phi|dxdy + \nu \int_\Omega H(-\phi)dxdy + \mu \int_\Omega \frac{1}{2}(|\nabla\phi| - 1)^2 dxdy \end{aligned} \tag{3.6}$$

The Gateaux derivative of the functional in Eq.3.6 is

$$\frac{\partial E^*_{snake}}{\partial\phi} = -\mu\left[\Delta\phi - div(\frac{\nabla\phi}{|\nabla\phi|})\right] - \lambda\delta(\phi)div(g\frac{\nabla\phi}{|\nabla\phi|}) - \nu g\delta(\phi) \tag{3.7}$$

It follows that the level set equation (Eq.3.2) can be written as Eq.3.8 based on Euler-Lagrange equation:

$$\begin{aligned} \frac{\partial\phi}{\partial t} &= \frac{\partial E^*_{snake}}{\partial\phi} \\ &= -\mu\left[\Delta\phi - div(\frac{\nabla\phi}{|\nabla\phi|})\right] - \lambda\delta(\phi)div(g\frac{\nabla\phi}{|\nabla\phi|}) - \nu g\delta(\phi) \end{aligned} \tag{3.8}$$

In numerical discretization, the Dirac function δ(x) is typically approximated by Eq.3.9 as in (Li *et al.*, 2005):

$$\begin{aligned} \delta_\epsilon &= 0, |x| > \epsilon \\ &\frac{1}{2\epsilon}[1 + cos(\frac{\pi x}{\epsilon})], |x| \leq \epsilon \end{aligned} \tag{3.9}$$

We implemented Chunming Li's active contour formulation on a 2D image slice of our dataset in Matlab® (R2008a) under a Linux environment (Ubuntu hardy) on a desktop with Intel® Core™ 2 duo processor at 2.40GHz. The image was resized to 256 × 256 pixels. The results are summarized in Figure 3.10

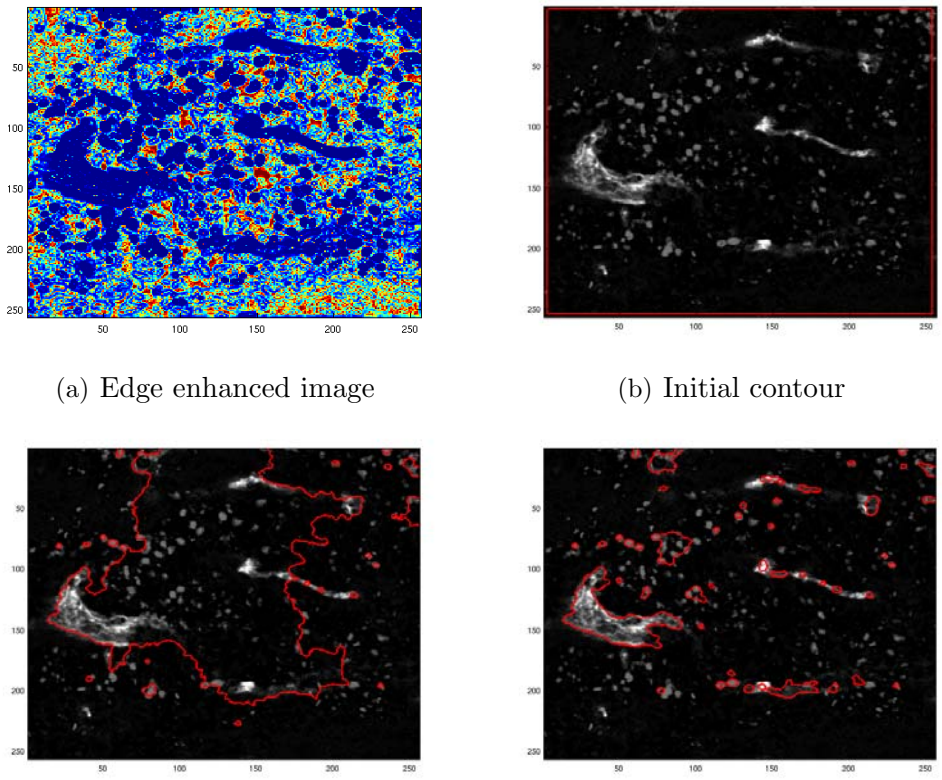

(a) Edge enhanced image (b) Initial contour

(c) Contour after 300 iterations (95.02s) (d) Contour after 600 iterations (193.2s)

Figure 3.10: Segmentation results using level set method according to Li *et al.* (2005), edges in the original image were enhanced by $g = \frac{1}{1+|\nabla G|^2}$, where G is the smoothed image after convolving the original image with Gaussian low pass filter (size = 8, sigma = 0.8). The parameters for level set evolution: $\epsilon = 1.5$, $\mu = 0.002$, $\lambda = 6$, $\alpha = 3$.

We found that the segmentation results depend critically on the chosen values of the parameters in Chunming Li's formula. To appreciate the sensitivity of the segmentation result to the values of the parameters, Figure 3.11 shows results after 600 iterations when we changed one parameter's value at each time.

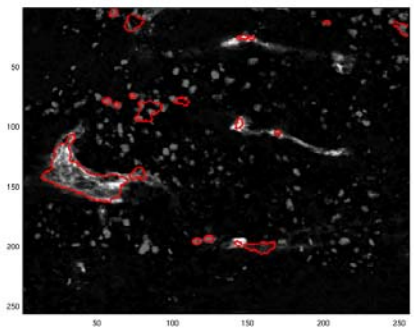

(a) ϵ=0.5, all else equal.

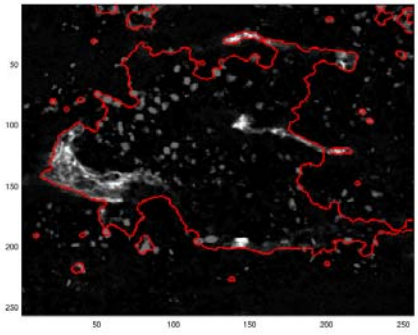

(b) μ=0.02, all else equal

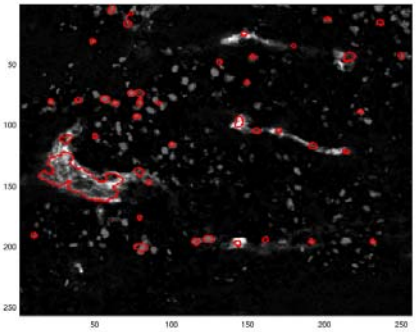

(c) λ=3, all else equal

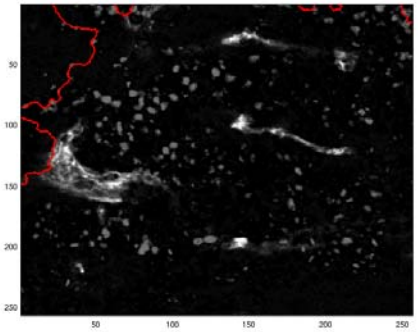

(d) α=1.5, all else equal

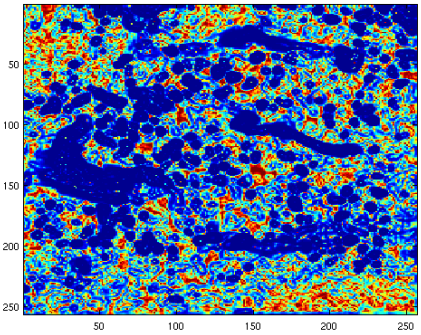

(e) size = 10, sigma = 1, edge image

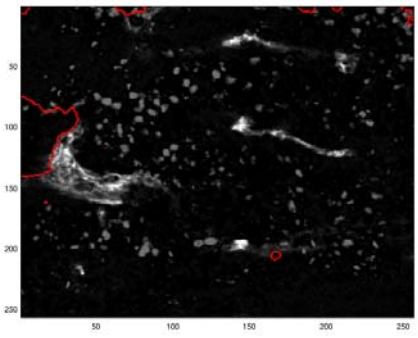

(f) size = 10, sigma = 1, result

Figure 3.11: We started from the parameters used to produce Figure 3.10: $\epsilon = 1.5$, $\mu = 0.002$, $\lambda = 6$, $\alpha = 3$. Gaussian low pass filter size = 8, sigma = 0.8, and changed one parameter's value at a time. (a)-(f) shows segmentation results after 600 iterations.

As Figure 3.11 illustrates, the level set evolution is very sensitive to α and to the edge detector. (Figure 3.11(d)(e)(f)). On the other hand, this level set method is relatively less sensitive to ϵ and λ (Figure 3.11(a)(c)). Since the stabilization condition requires $\mu\Delta t < 0.25$ (Li *et al.*, 2005), where Δt stands for the iteration interval unit, an increase of the μ value implies the decrease of iteration interval which causes the evolution slow down, as observed in Figure 3.11(b).

We also conducted 3D implementation of Chunming Li's method using C/C++. However, we found that the computation becomes extremely slow in this case. It could not produce sensible vessel boundary contours even after 100 iterations, which took half an hour to compute on a desktop with an Intel® Core™ 2 duo processor at 2.40GHz.

Speed function independent of the edges

Since the segmentation results of edge dependent level set methods rely on edge detection, they often fail to segment low contrast images (Chan & Vese, 2001). To overcome this problem, Chan proposed a regularizer which penalizes the mismatch of the snake and the object's boundary. Since it is derived from the image intensity, it corresponds to $E^*_{image} + E^*_{ext}$ in the classical active contour model (Eq.3.10):

$$\begin{aligned} E^*_{image} + E^*_{ext} &= \lambda_1 F_1(\phi) + \lambda_2 F_2(\phi) \\ &= \lambda_1 \int_{inside(\phi)} |I(x,y) - c_1|^2 dxdy + \lambda_2 \int_{outside(\phi)} |I(x,y) - c_2|^2 dxdy, \end{aligned} \tag{3.10}$$

where ϕ is the snake, I is the original image, and c_1, c_2 are the average image intensity values inside and outside the snake respectively. The mechanics of the fitting regularizer is illustrated in Figure 3.12.

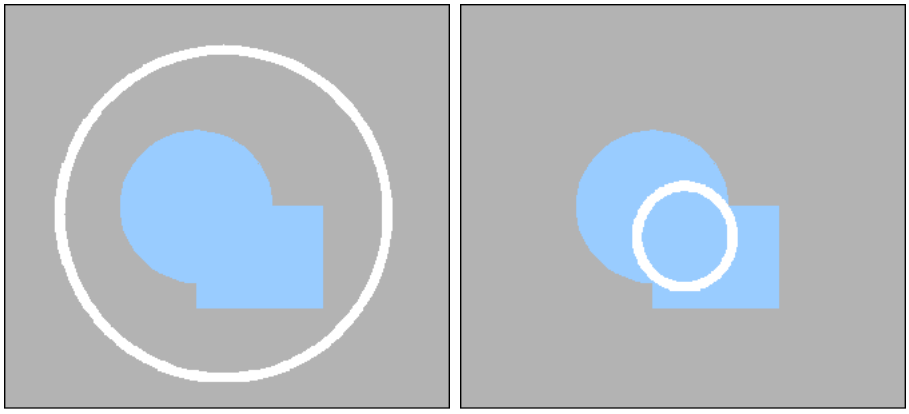

(a) $F_1(\phi)$ >0, $F_2(\phi)$ ≈0, Fitting>0 (b) $F_1(\phi)$ ≈0, $F_2(\phi)$ >0, Fitting>0

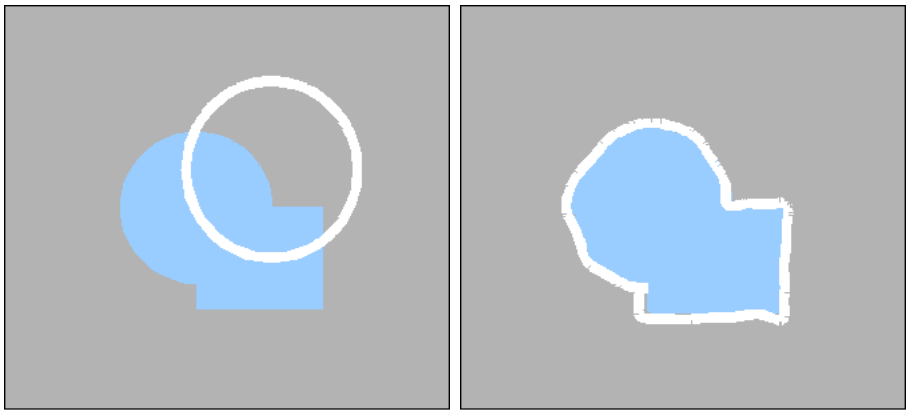

(c) $F_1(\phi)$ >0, $F_2(\phi)$ >0, Fitting> 0 (d) $F_1(\phi)$ ≈0, $F_2(\phi)$ ≈0, Fitting≈0

Figure 3.12: Illustration of the fitting regularizer in detecting object's boundary, reproduced from Chan & Vese (2001).

For example, when the snake is outside the object (Figure 3.12(a)), suppose the object's average intensity value equals p_1 and that the background's average intensity value is p_0, and that the object has a higher average intensity value than its background, i.e. $p_1 > p_0$. Since the pixels outside the snake are all background pixels, it follows that $c_2 = p_0$, $F_2(\phi) = \int_{outside(\phi)} |I(x,y) - c_2|^2 dxdy = 0$. For pixels inside the circle, we have $p_1 > c_1 > p_0$, so $F_1(\phi) = \int_{inside(\phi)} |I(x,y) - c_1|^2 dxdy > 0$. Similarly, it is straightforward to prove that the fitting regularizer term $F_1(\phi) + F_2(\phi) > 0$ if the snake ϕ doesn't match with the object's boundary (Figure.3.12(b)(c)). The fitting regularizer approximates zero when ϕ matches with the object's boundary (Figure 3.12(d)).

The snake's energy was written as (Eq.3.11):

$$\begin{aligned} E^*_{snake} &= E^*_{int} + E^*_{image} + E^*_{ext} \\ &= \mu L(\phi) + \nu A(\phi) + \lambda_1 F_1(\phi) + \lambda_2 F_2(\phi), \end{aligned} \tag{3.11}$$

where $L(\phi)$ is the length of snake ϕ and $A(\phi)$ is the area enclosed by snake ϕ. $\mu \geq 0$,$\nu \geq 0$,$\lambda_1, \lambda_2 > 0$ are fixed weighting parameters for each term. The four terms in Eq.3.11 can be calculated following Eqs.3.12-3.15:

$$\begin{aligned} L(\phi) &= \int_\Omega |\nabla H(\phi)| dxdy, \\ &= \int_\Omega \delta(\phi)|\nabla\phi| dxdy, \end{aligned} \tag{3.12}$$

$$S(\phi) = \int_\Omega H(\phi) dxdy, \tag{3.13}$$

$$\begin{aligned} F_1(\phi) &= \int_{\phi>0} |I(x,y) - c_1|^2 dxdy, \\ &= \int_\Omega |I(x,y) - c_1|^2 H(\phi) dxdy, \end{aligned} \tag{3.14}$$

$$\begin{aligned} F_2(\phi) &= \int_{\phi<0} |I(x,y) - c_2|^2 dxdy, \\ &= \int_\Omega |I(x,y) - c_2|^2 (1 - H(\phi)) dxdy. \end{aligned} \tag{3.15}$$

So E^*_{snake} could by calculated by (Eq.3.16):

$$\begin{aligned} E^*_{snake} &= \mu \int_\Omega \delta(\phi)|\nabla\phi| dxdy, \\ &+ \nu \int_\Omega H(\phi) dxdy, \\ &+ \lambda_1 \int_\Omega |I(x,y) - c_1|^2 H(\phi) dxdy, \\ &+ \lambda_2 \int_\Omega |I(x,y) - c_2|^2 (1 - H(\phi)) dxdy. \end{aligned} \tag{3.16}$$

For any given ϕ, Eq.3.16 was found to attain a minimum value when c_1,c_2 equals the average intensity values of the regions inside and outside the curve respectively. c_1 and c_2 can be calculated as Eq.3.17:

$$
\begin{aligned}
c_1 &= \frac{\int_\Omega u_0(x,y)H(\phi)dxdy}{\int_\Omega H(\phi)dxdy}, \\
c_2 &= \frac{\int_\Omega u_0(x,y)(1-H(\phi))dxdy}{\int_\Omega (1-H(\phi))dxdy}.
\end{aligned} \tag{3.17}
$$

The level set equation can be written as Eq.3.18

$$
\begin{aligned}
\frac{\partial \phi}{\partial t} &= \frac{\partial E^*_{snake}}{\partial \phi} \\
&= \delta\phi \left[\mu \mathrm{div}\left(\frac{\nabla \phi}{|\nabla \phi|} \right) - \nu - \lambda_1 (I - c_1)^2 + \lambda_2 (I - c_2)^2 \right]
\end{aligned} \tag{3.18}
$$

At each iteration, we first calculate the c_1, c_2 values according to Eq.3.17. We then update ϕ according to the level set equation depicted in Eq.3.18 [4].

We implemented Chan's formulation on a 2D image slice of our dataset in Matlab®(R2008a) under a Linux environment (Ubuntu Hardy) on a desktop with an Intel® Core™ 2 duo processor at 2.40GHz. The images were resized to 256 × 256 pixels. The results are summarized in Figure 3.13

[4]Initialized with an arbitrary closed curve with Neumann boundary condistion. We will discuss local phase initialization in section 3.2.3.

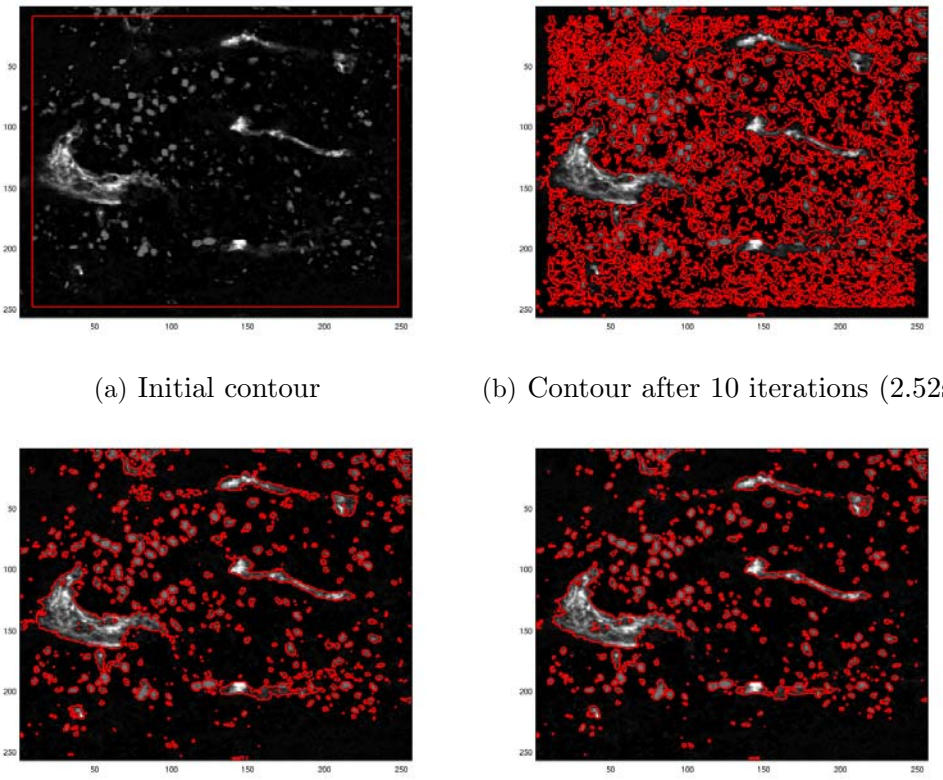

(a) Initial contour (b) Contour after 10 iterations (2.52s)

(c) Contour after 20 iterations (5.12s) (d) Contour after 200 iterations (7.47s)

Figure 3.13: Segmentation results using the level set method according to Chan & Vese (2001). The parameters for level set evolution are: $\epsilon = 1$, $\mu = 0.0255^2$, $\lambda_1 = 1$, $\lambda_2 = 1$, $\nu = 0$, $\Delta t = 0.1$.

We found that Chan's method is more efficient in segmenting our 2D tumour blood vessel images than Chunming Li's method. The edge independent level set method gives more accurate segmentation results after 20 iterations (5.12s) than results after 600 iterations (193.2s) using the edge dependent method. To test the sensitivities of the segmentation results on the values of the parameters, we changed one parameter at a time and applied the method on a 2D image. Figure 3.14 summarizes the segmentation results after 20 iterations:

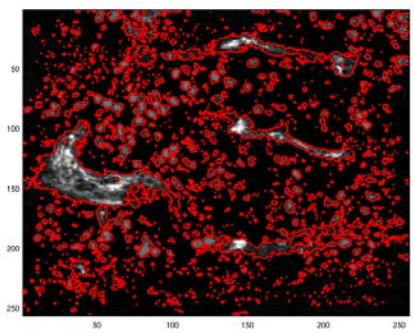

(a) ϵ=0.5, all else equal.

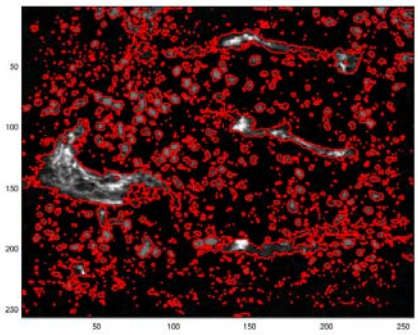

(b) $\mu = 0.255^2$, all else equal

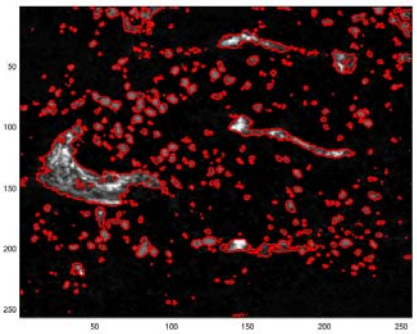

(c) λ_1=0.5, all else equal

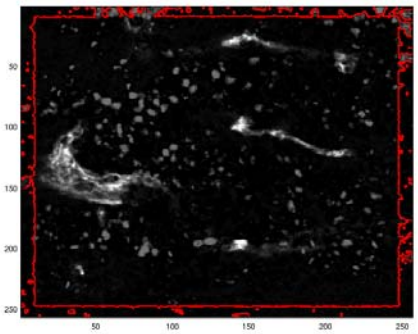

(d) λ_2=0.5, all else equal

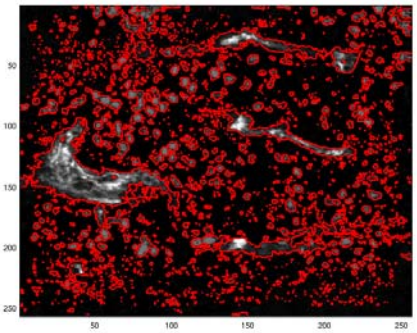

(e) ν=1, all else equal

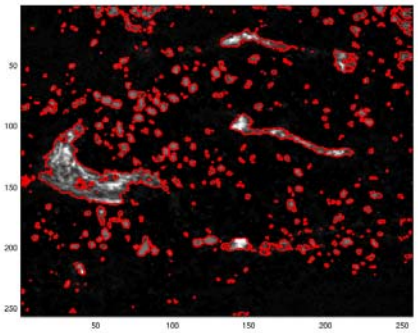

(f) Δt=1, all else equal

Figure 3.14: Segmentation results with changing only one parameter value. (a):ϵ=0.5; (b):$\mu = 0.255^2$; (c):λ_1=0.5; (d):λ_2=0.5; (e):ν=1; (f):Δt=1,all other parameters remain the same with the implementation shown in Figure 3.13.

From Figure 3.14 it can be seen that the edge independent level set method is reasonably stable under changes in the parameter values. Only changes to λ_2 have a detrimental effect on the segmentation result. This is because our initial contour is outside the objects, so the weight of the outside snake average intensity λ_2 is critical in determining

the direction of the snake's evolution.

We have also implemented Chan's method in 3D. Though Chan's method can produce 3D vessel object's boundary in a reasonable time, the segmentation result is found not superior to hysteresis segmentations (As more noise is left and several low intensity parts of vessel object are missed Figure 3.15(b)).

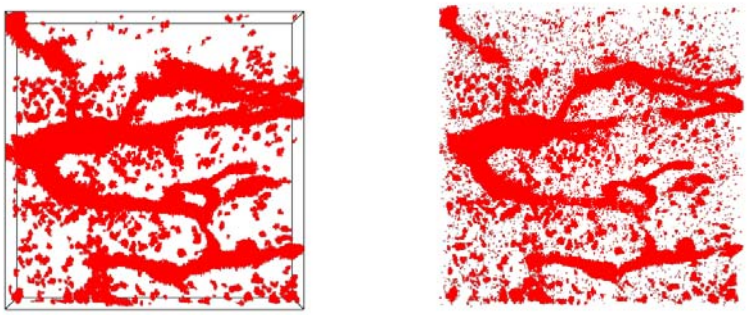

(a) Hysteresis thresholding. (b) Chan's method

Figure 3.15: Segments obtained from hysteresis thresholding (a) and Chan's method (b). In Chan's method we set $\mu = 1.66 \times 10^{-6}$, $\lambda_1 = \lambda_2 = 1$, $\nu = 0$, the result is obtained after 300 iterations (3698 seconds).

3.2.3 Local Phase

Light intensities are important information sources that account for our visual perception. However, the human vision system is not just a camera that simply records intensity information but it also incorporates sophisticated cognitive processes. This can be illustrated by the facts that our perceptions can sometimes deviate from the intensity information (Figure 3.16).

Both Figure 3.16(a) and (b) suggest that phase information also plays an important role in feature perception, as argued by Morrone & Burr (1988).

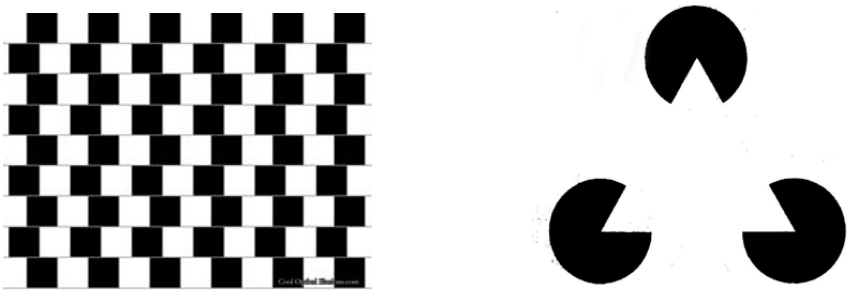

(a) Parallel Lines (b) Hided Triangle

Figure 3.16: Images that cause illusions. (a), carefully arranged black bricks produces the illusion that the lines were not in parallel; (b), three incomplete circles give the impression of the existence of a triangle.

Theories

In signal processing, local phase is defined using the analytical signal. The analytical signal $f_a(t)$ is defined as a signal whose Fourier transform has no negative frequency components. For any real signal $f(t)$, the corresponding analytical signal is defined as in Eq.3.19:

$$F_a(\omega) = F(\omega) + sign(\omega)F(\omega), \tag{3.19}$$

where $F_a(\omega)$ and $F(\omega)$ are Fourier transforms of $f_a(t)$ and $f(t)$. In the signal domain, the following relationship holds:

$$f_a(t) = f(t) + ih \otimes f(t), \tag{3.20}$$

where $\otimes$ represents the convolution operator and h represents the transfer function of the Hilbert transform in the signal domain and equals $-isign(\omega)$ in the Fourier domain. The local phase can then be calculated as

$$\phi(t) = \text{atan}\frac{h \otimes f(t)}{f(t)} \tag{3.21}$$

This can be intuitively illustrated as in Figure 3.17

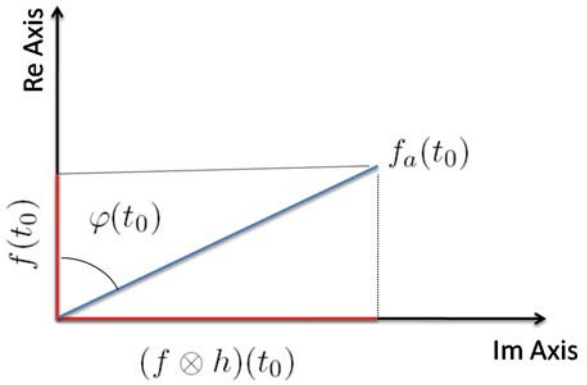

Figure 3.17: 1D Local Phase.

Usually, the local phase value is wrapped in the (-$\pi/2$, $\pi/2$) interval. For sinusoidal signals, local phase has the important properties that it approaches $-\pi/2$ at a local minimum and $\pi/2$ at a local maximum. These properties make local phase a useful metric to detect edges or lines in images, which are approximate sinusoidal signals. However, the analytical signal theory has no direct extension to higher dimensions because the Hilbert transform can not be defined in dimensions greater than one. To overcome this problem, Felsberg & Sommer (2000) proposed the monogenic signal which utilizes the 2D Riesz transform to approximate the effect of the Hilbert transform in 2D. In fact, Eq.3.19 can be rewritten as:

$$F_a(\omega) = F(\omega) + \frac{\omega}{|\omega|}F(\omega) \tag{3.22}$$

Then, based on the definition and L_2 distance in 2D Euclidean space,the 2D monogenic signal in 2D is constructed as:

$$\begin{aligned} F_m(u_1, u_2) &= F(u_1, u_2) + H_1F(u_1, u_2) \\ &\quad + H_2F(u_1, u_2), \end{aligned} \tag{3.23}$$

where

$$H_1 = \frac{u_1}{\sqrt{u_1^2 + u_2^2}}, \tag{3.24}$$

$$H_2 = \frac{u_2}{\sqrt{u_1^2 + u_2^2}}. \tag{3.25}$$

In the signal domain, the complex signal is constructed using quaternions:

$$\begin{aligned} f_m(x,y) &= f(x,y) + i(h_1 \otimes f)(x,y) \\ &\quad + j(h_2 \otimes f)f(x,y), \end{aligned} \tag{3.26}$$

where h_1 and h_2 are the transfer functions of H_1 and H_2. The response of each filter (h_1, h_2) is shown in Figure 3.18

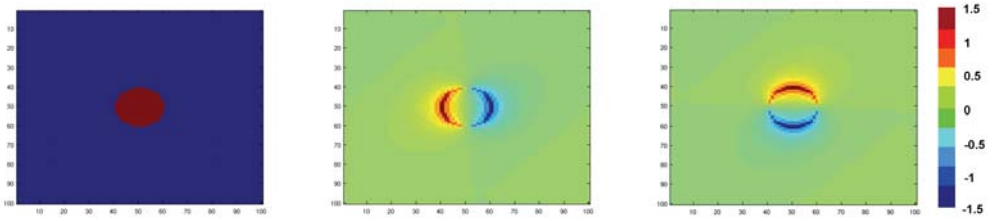

(a) Sphere (b) $f \otimes h_1$ (c) $f \otimes h_2$

Figure 3.18: Responses of 2 orthogonal odd filters in 2D space.

The 2D, the local phase is defined as:

$$\phi(x,y) = \text{atan}\frac{\sqrt{(h_1 \otimes f)^2 + (h_2 \otimes f)^2}}{f} \tag{3.27}$$

The definition of 2D local phase can be intuitively illustrated as in Figure 3.19.

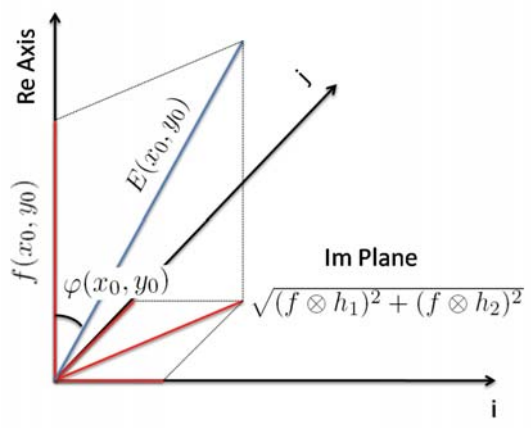

Figure 3.19: 2D Local Phase.

We have extended Felsberg's work to 3D signals. To calculate 3D local phase, the 3D image was convolved with three orthogonal odd filters and the 3D complex signal is constructed as (Eq.3.28):

$$\begin{aligned} f_m(x,y,z) &= f(x,y,z) + i(h_1 \otimes f)(x,y,z) \\ &\quad + j(h_2 \otimes f)(x,y,z) \\ &\quad + k(h_3 \otimes f)(x,y,z), \end{aligned} \tag{3.28}$$

where h_1, h_2 and h_3 are transfer functions of $\frac{u_1}{\sqrt{u_1^2+u_2^2+u_3^2}}$, $\frac{u_2}{\sqrt{u_1^2+u_2^2+u_3^2}}$ and $\frac{u_3}{\sqrt{u_1^2+u_2^2+u_3^2}}$ respectively. The response of each filter (h_1, h_2 and h_3) is shown in Figure 3.20.

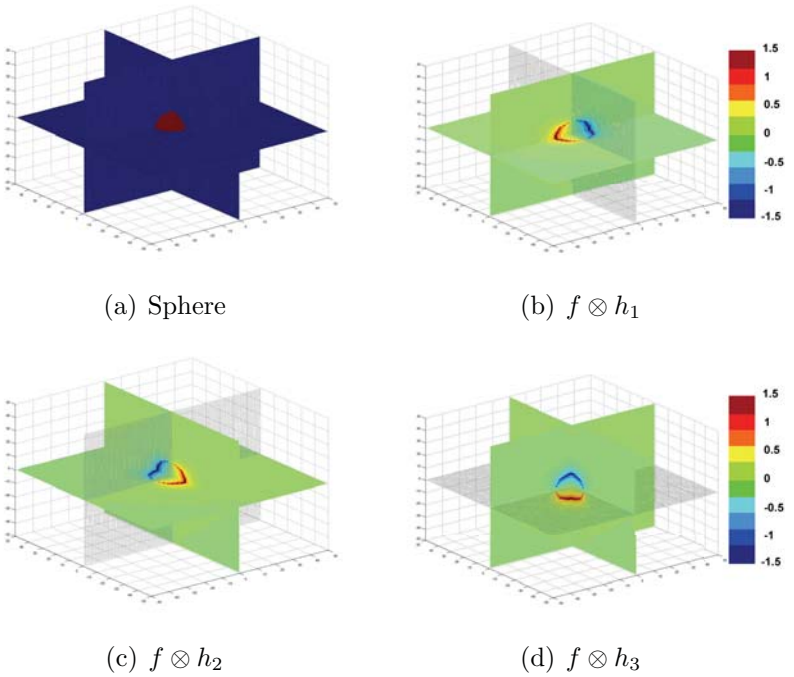

(a) Sphere (b) $f \otimes h_1$

(c) $f \otimes h_2$ (d) $f \otimes h_3$

Figure 3.20: Responses of three orthogonal odd filters in 3D space.

We define the 3D local phase as Eq.3.29:

$$\phi(x, y, z) = atan \frac{\sqrt{(h_1 \otimes f)^2 + (h_2 \otimes f)^2 + (h_3 \otimes f)^2}}{f}. \tag{3.29}$$

Following a similar construction, the definition of 3D local phase can be intuitively illustrated as in Figure 3.21.

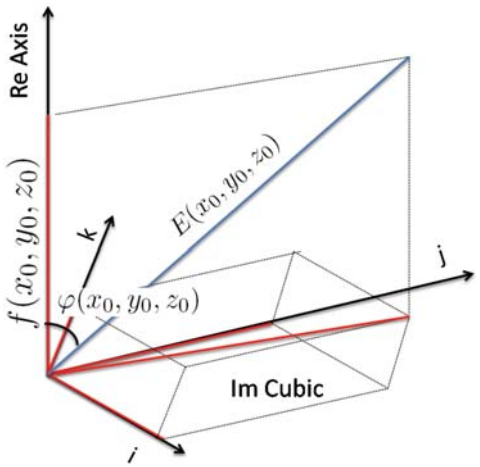

Figure 3.21: 3D Local Phase.

Application in Image Enhancement

In practice, images are often first filtered using a set of multi-scale bandpass filters in order to capture local phase congruency, since this is what conveys local feature information (Felsberg & Sommer, 2000; Kovesi, 1999). In our experiments, we utilized a set of Mellor-Brady (MB) filters (Mellor & Brady, 2005). The fundamental equation of Mellor Brady filter is shown in Eq.3.30:

$$f(r) = \frac{A}{r^{\alpha+\beta}} - \frac{B}{r^{\alpha-\beta}}, \tag{3.30}$$

where $\beta \ll \alpha$, r=$\sqrt{x^2 + y^2}$ in 2D Cartesian coordinate system and A, B are normalization factors.

To study the application of 2D local phase in noisy image enhancement, a binary 2D image of a square was generated, in which pixels inside the square were assigned the value 1, while pixels outside the square were assigned the value 0 (Figure 3.22(a)). Gaussian noise was added to this binary image with mean value and standard deviation equal to 1 (Figure 3.22(b)). We then filtered this noisy image using the MB filter with $\alpha = 1$,$\beta = 0.1$ (Figure 3.22(c)) and calculated the local phase on the filtered image (Figure 3.22(d)). We changed parameters of MB filters (α, β) and obtained local phase images of different scales ($\alpha = 1.5$,$\beta = 0.1$ for Figure 3.22(e) and $\alpha = 2$,$\beta = 0.1$ for Figure 3.22(f)). Finally, we calculated the average image of the multi-scale local phase images, which is shown in Figure 3.22(g).

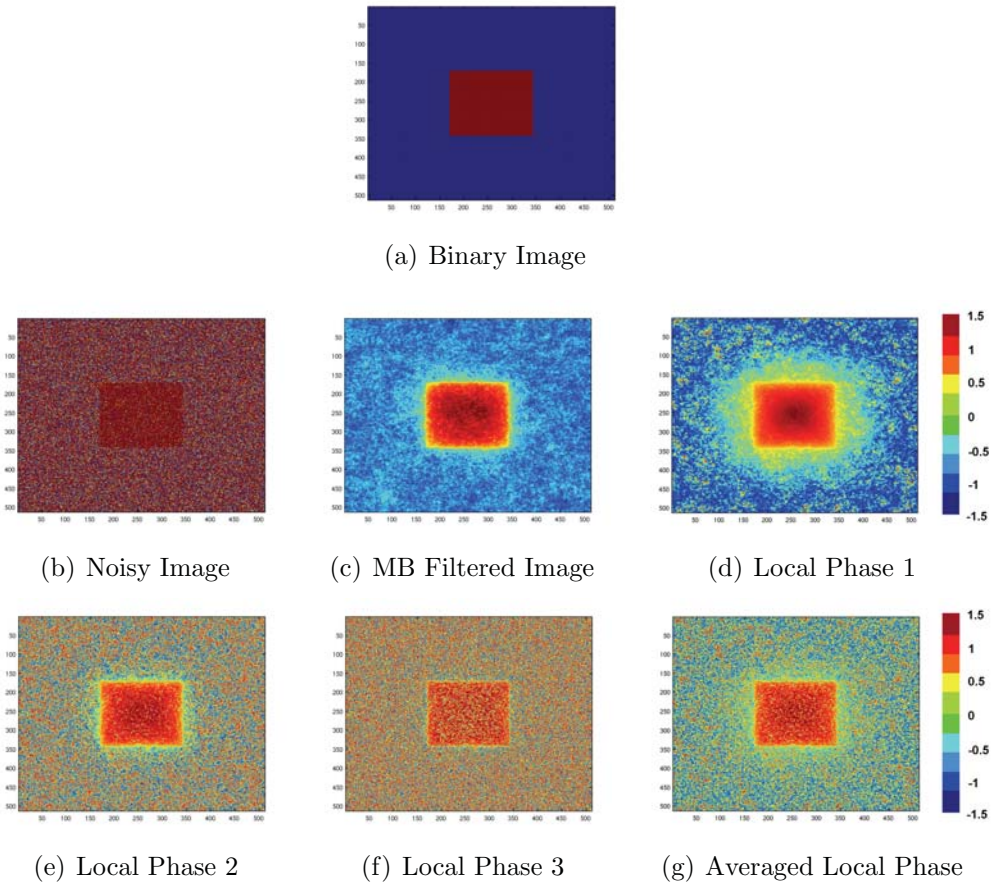

(a) Binary Image

(b) Noisy Image (c) MB Filtered Image (d) Local Phase 1

(e) Local Phase 2 (f) Local Phase 3 (g) Averaged Local Phase

Figure 3.22: Example of 2D local phase calculation.

Comparing Figure 3.22(b) with (g), it can be seen that the contrast between the object and background is enhanced in the average local phase image. Since phase congruency is an intensity-independent feature, applying the phase congruency calculation we can enhance the contrast of noisy images. Since thresholding methods rely on intensities, image contrast enhancement may benefit thresholding methods (Figure 3.23).

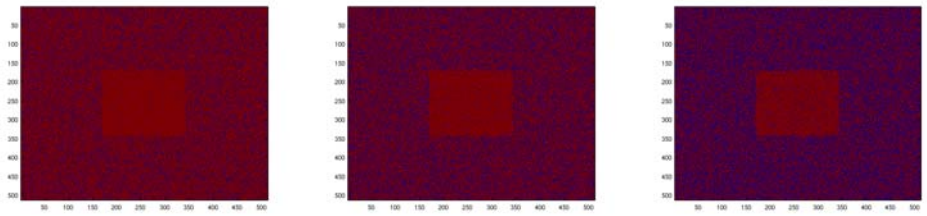

(a) 20% (b) 50% (c) 80%

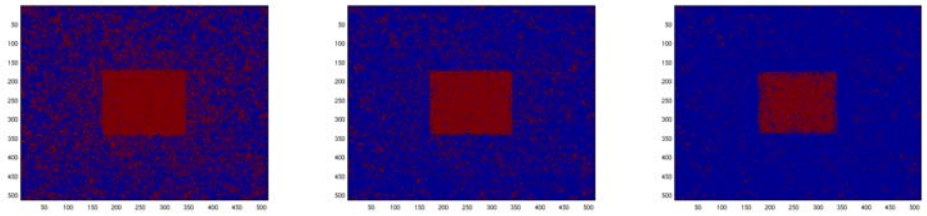

(d) 20% (e) 50% (f) 80%

Figure 3.23: Comparison of threshold on intensity and local phase.(a)-(c): thresholded image of Figure 3.22(b) with thresholding level equals to 20% , 50% and 80% the maximum intensity respectively; (d)-(f): thresholded image of Figure 3.22(f) with thresholding level equals to 20% , 50% and 80% the maximum intensity respectively.

Figure 3.23 illustrates that while it is hard for a thresholding method to segment the object from a noisy image, the segmentation result is greatly improved on the contrast enhanced images. So local phase as an image enhancement tool can be combined with thresholding methods in segmenting noisy images.

In 3D, the MB filter is a matrix with values determined by the distances to the origin (Eq.3.30). Similar to the 2D experiments, we have simulated a 3D cube binary image in which voxels inside the cube were assigned the value 1 and voxels outside the cube were assigned the value 0 (Figure 3.24(a)). Gaussian noise with mean and standard deviation equal to 1 was added to obtain the noisy image (Figure 3.24(b)). As in the 2D case, the addition of noise has significantly reduced the image quality, indeed the original cube is not readily discerned from its background. Figure 3.24(c) shows the noisy image filtered by 3D MB filter with $\alpha = 1$,$\beta = 0.1$. Local phase images were calculated on the noisy image filtered by MB filters of differernt scales. ($\alpha = 2.2$, $\beta = 0.1$ for Figure 3.24(d), $\alpha = 2.5$, $\beta = 0.1$ for Figure 3.24(e) and $\alpha = 2.8$, $\beta = 0.1$ for Figure 3.24(f)). Average local

phase image was shown in Figure 3.24(g).

Contrast enhancement by phase congruency calculation can be appreciated by comparing Figure 3.24(b) with (g). While the cube can hardly be perceived from the noisy image, it is easily seen in the average local phase image.

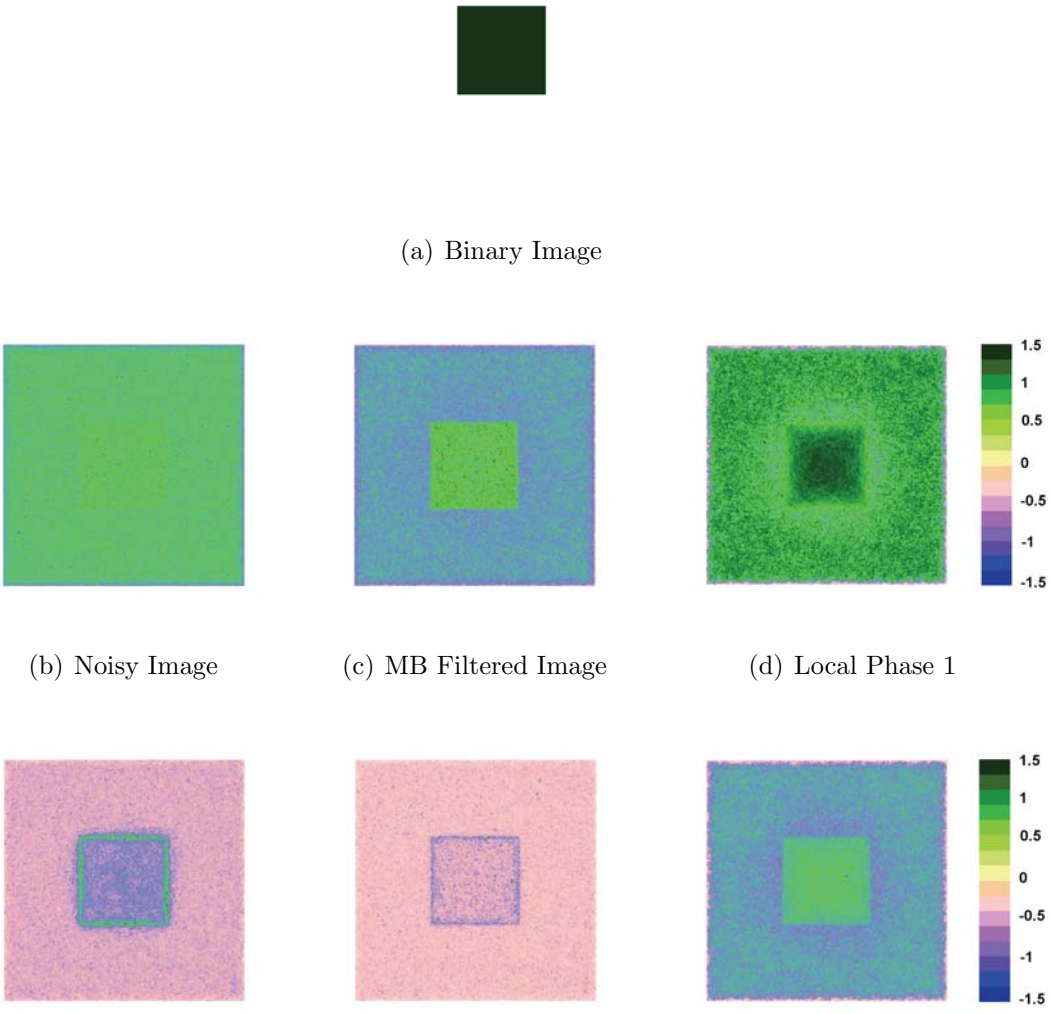

(a) Binary Image

(b) Noisy Image (c) MB Filtered Image (d) Local Phase 1

(e) Local Phase 2 (f) Local Phase 3 (g) Averaged Local Phase

Figure 3.24: Example of 3D local phase calculation. The square, which is barely seen in (b) can be readily perceived after local phase enhancement (g).

A comparison of the segmentation obtained by thresholding the original noisy image and the contrast enhanced image is illustrated in Figure 3.25.

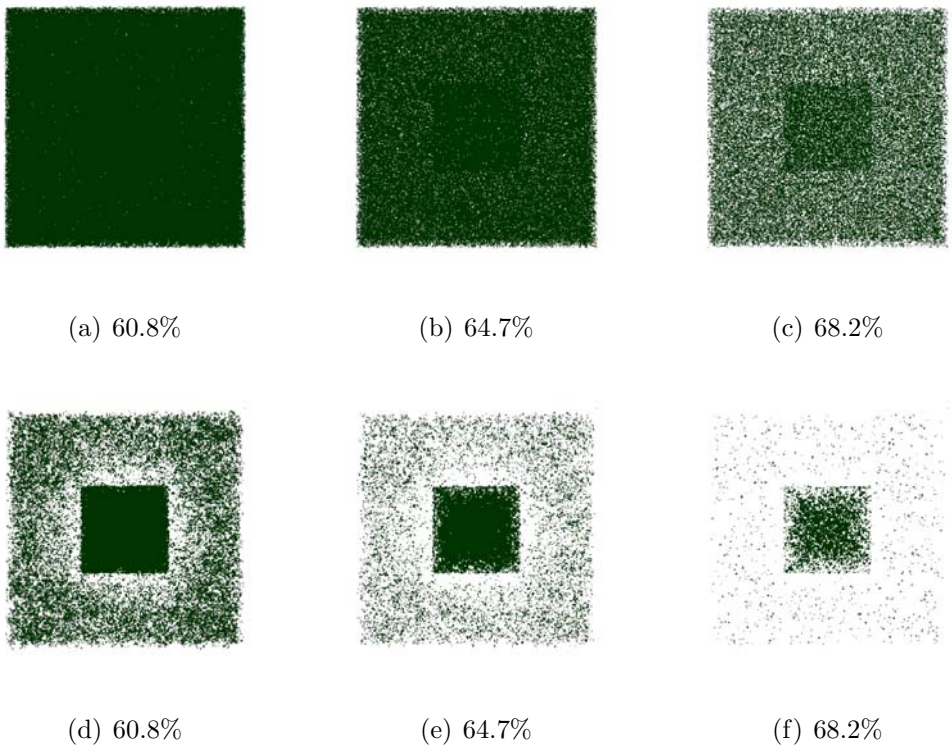

(a) 60.8% (b) 64.7% (c) 68.2%

(d) 60.8% (e) 64.7% (f) 68.2%

Figure 3.25: Comparison of threshold on intensity and local phase.(a)-(c): thresholded image of Figure 3.24(b) with thresholding level equals to 60.8% , 64.7% and 68.2% the maximum intensity respectively (which corresponds to 155, 165 and 175 in 255 grey scale); (d)-(f): thresholded image of Figure 3.24(f) with the same thrsholding.

As in the 2D case, directly thresholding a 3D noisy image produces poor segmentation results (Figure 3.25(a)-(c)). Again, the local phase calculation greatly enhances the image contrast and facilitates thresholding (Figure 3.25(d)-(f)).

Our results show that local phase is an effective tool for image contrast enhancement. Image contrast enhancement of extremely noisy images can greatly improve the segmentation results of thresholding methods.

Application in Level Set Initialization

In the level set method, the initial snake position and shape have to be determined. This can be done either by manual seeding or by using an arbitrary closed curve. Although a manually seeded snake is often close to the object's boundary, thus making level set method converge more quickly, arbitrary initialization has the potential for automation. One often used initializing strategy is to draw a frame near to the image boundary. Points inside the frame are usually assigned the value 1, the frame boundary points are assigned the value 0 while points outside the frame are assigned the value -1 for the initial level set function ϕ. The intialised snake is normally far from the object's boundary in terms of its position and shape. So it requires more iterations in the level set method for the snake to converge to the object's boundary.

Local phase has a value between $-\pi/2$ and $\pi/2$. The zero value fronts is found to be close to the object's boundary in terms of position and shape (Figure 3.26).

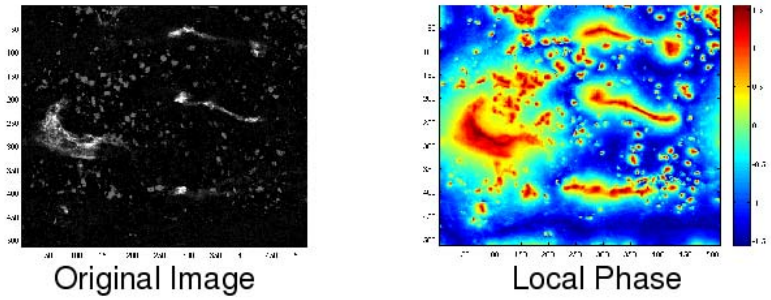

Figure 3.26: Original image and its local phase.

Based on the above observations, we consider that local phase could be used as the initial level set function ϕ in level set methods and we would expect it to accelerate convergence of the snake's evolution. We have compared local phase initialization with arbitrary initialization in Chunming Li's method (Edge dependent speed function), the result is illustrated in Figure 3.27:

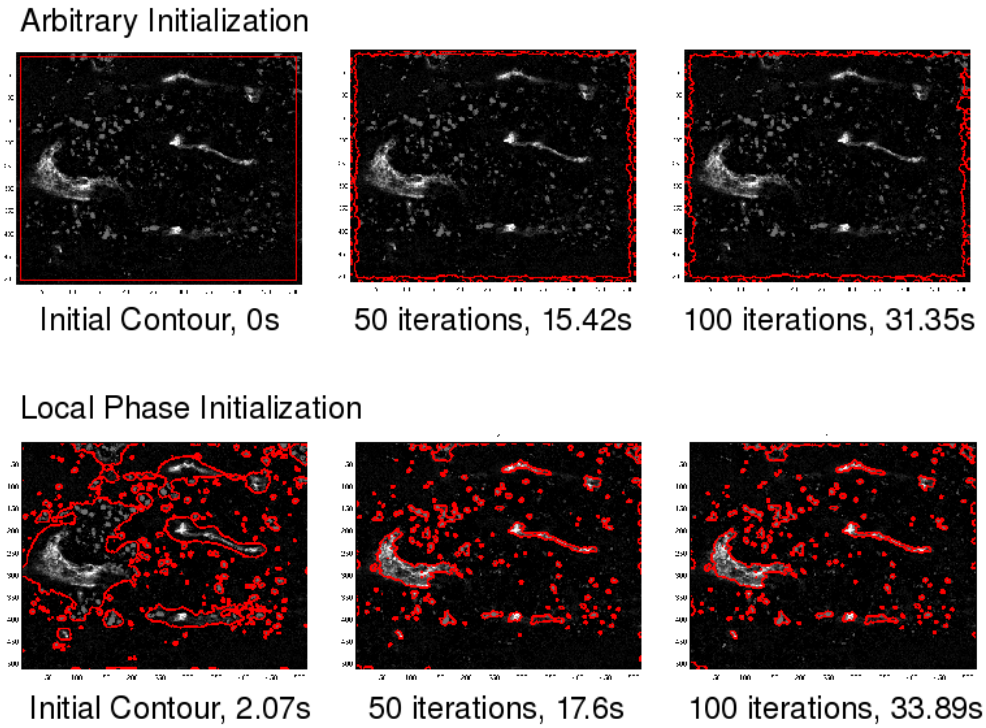

Figure 3.27: Comparison of the contour at each iteration with arbitrary initialization (upper) and local phase initialization (lower). In arbitrary initialization, we set the initial contour 4 pixels apart from image boundary. In local phase initialization, we used local phase values as initial ϕ in level set iteration. The computation time was measured under Matlab® (R2008a) on a desktop with Intel® Core™ 2 duo processor of 2.4GHz. The 2D image was of 256×256 pixels.

From Figure 3.27, Chunming Li's method gave satisfactory vessel's segmentation (because the snake is now alligned with vessel's boundary) after 50 iterations (17.6 seconds including local phase calculation) with local phase initialization. In contrast, Chunming Li's method failed to segment the vessel object after 100 iterations (31.35 seconds) with arbitrary intialization.

Previously, we stated that a 3D implementation of Chunming Li's method is infeasible because of extremely low convergence speed. In extensive experimentation, we found that with local phase initialization, Chunming Li's method produces sensible vessel contours (Figure 3.28):

(a) Initial Contour, 97s (b) 5 iterations, 173s (c) 10 iterations, 251s

(d) 20 iterations, 388s (e) 30 iterations, 505s (f) 40 iterations, 624s

Figure 3.28: Level set evolution initialized with local phase in Chungming Li's method. The computation time was measured under C environment on a desktop with Intel® Core™ 2 duo processor of 2.4GHz. The 3D image was of 256×256×60 voxels.

However, we found that Chunming Li's method is unable to converge to the correct vessel boundaries. Similar results of applying an edge-dependent level set method on 2D low contrast images have been reported in Chan & Vese (2001). We believe this is caused by failure of edge detection in our low contrast image samples.

We have also compared local phase initialization with arbitrary initialization with Chan's method (Edge independent level set) in 2D (Figure 3.29):

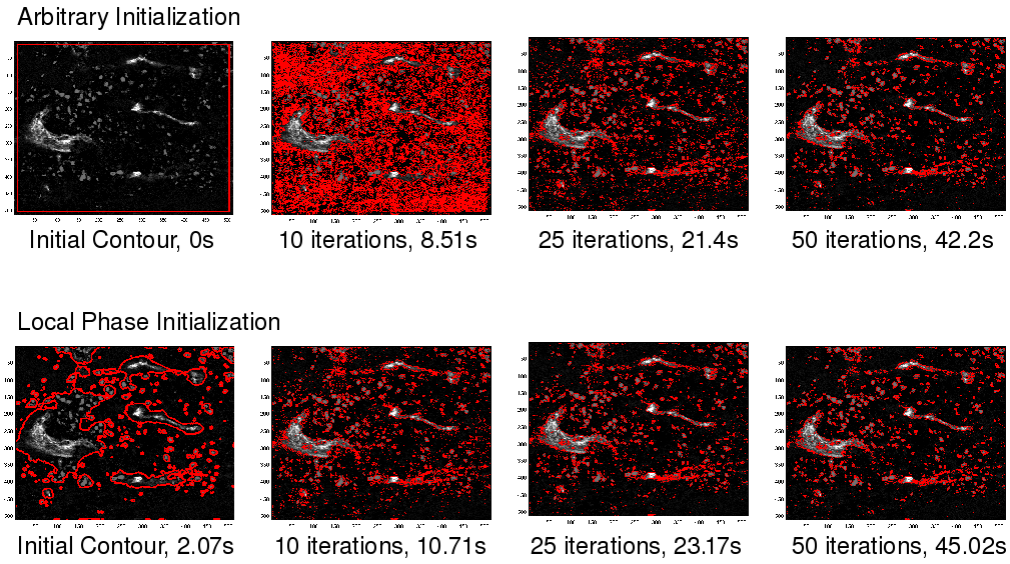

Figure 3.29: Comparison of the contour at each iteration with arbitrary initialization (upper) and local phase initialization (lower). In arbitrary initialization, we set the initial contour 4 pixels apart from image boundary. In local phase initialization, we used local phase values as initial ϕ in level set iteration. The computation time was measured under Matlab® (R2008a) on a desktop with Intel® Core™ 2 duo processor of 2.4GHz. The 2D image was of 256×256 pixels.

From Figure 3.29, Chan's method converged after 10 iterations (10.71 seconds including local phase calculation) with local phase initialization, whereas it took 25 iterations (21.4 seconds) to converge with arbitrary initialization.

We have also compared local phase intialization with arbitrary initialization with Chan's method in 3D (Figure 3.30):

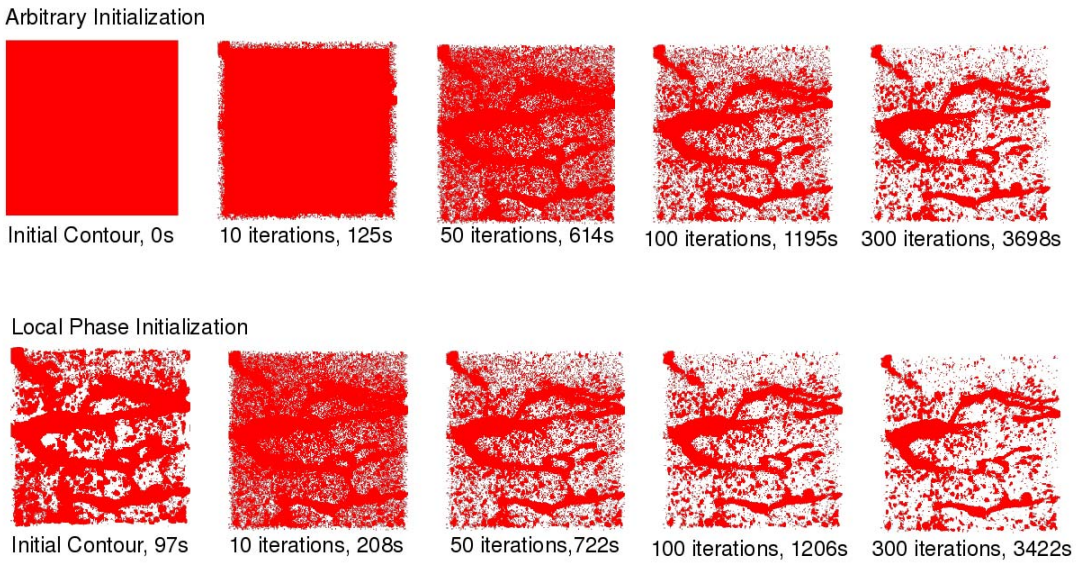

Figure 3.30: Comparison of surface contour at each iteration with arbitrary initialization (upper) and local phase initialization (lower). In arbitrary initialization, we set the initial contour 4 voxels apart from image boundary. In local phase initialization, we used local phase values as initial ϕ in level set iteration. The computation time was measured under C environment on a desktop with Intel® Core™ 2 duo processor of 2.4GHz. The 3D image was of 256×256×60 voxels.

From Figure 3.30, the 3D segmentation result after 50 iterations (722 seconds including local phase calculation) with local phase initialization is comparable with the result after 100 iterations (1195 seconds) with arbitrary initialization in Chan's method.

We conclude that local phase initialization is beneficial in the level set method. Because the local phase zero value front is close to the object's boundary, using it as the initial level set function accelerates convergence in the level set method. Since 3D snake evolution normally demands heavier calculations, local phase initialization show a more significant efficiency improvement in 3D applications.

3.3 Skeletonization

Skeleton is an important concept in shape analysis. Essentially, it is a single-voxel wide abstraction of an elongated shape. Skeleton voxels are equidistant to the shape's boundary. Mathematically, the skeleton is defined as collection of centers of maximal embeddable open balls (in 3D) or disks (in 2D) (Lieutier, 2004). A ball or disk B is said to maximally embeddable in set A if

1. B $\subseteq$ A

2. $\forall$ C $\supseteq$ B, C $\subsetneq$ A

The skeleton S of a shape A is defined as $\{S$: centers of B$\}$. The skeleton preserves the shape's length, connectivity and angles and is more convenient for analysis. It is an ideal shape model for researching the geometrical structure of tumour blood vessels.

The process of acquiring a shape's skeleton is called skeletonization. Many skeletonization algorithms have been proposed in the literature (Cornea *et al.*, 2007). There are two major categories of skeletonization methods, namely continuous and discrete methods. Continuous methods are based on a continuous energy model and calculate the boundary equidistant voxels through energy minimization. In contrast, discrete methods extract the shape's centre line through iterative voxel ablations.

3.3.1 Continuous Methods

Essentially, continuous methods are built from a distance measure. Based on the distance measure, various forms of energy model have been proposed. Such energy models usually produce a potential field inside the object. Skeleton voxels are then determined by finding the minimum potential energy points inside the object (Cornea *et al.*, 2007).

For example, Cornea *et al.* (2005) proposed a generalized potential model. In Cornea's method, boundary voxels were assigned positive unit charges. This generated an electro-

static field inside the object. The repulsive field force generated by boundary voxel C at point P inside the object is expressed as:

$$\vec{F_{PC}} = \frac{\vec{CP}}{r^m}, \tag{3.31}$$

where $\vec{CP}$ is the normalized vector from C to P which determines the force direction, r^m determines force attenuation rate along ditance r (when m=2, it is the Newtonian force). The field force at a point P is the composition of forces generated by all boundary voxels:

$$\vec{F_P} = \sum_i \vec{F_{PC_i}} \tag{3.32}$$

Figure 3.31 illustrates the line of force of the electrostatic field generated in a cow shape:

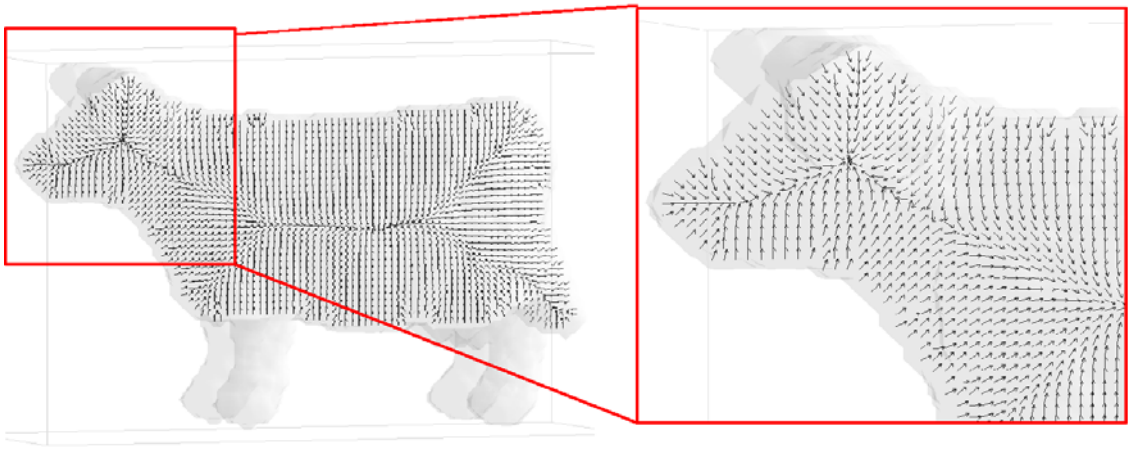

Figure 3.31: Electrostatic potential field generated by the boundary charges, adapted from Cornea *et al.* (2005).

Critical points are defined as those points inside the object where the field strength is (approximately) zero. This results from the symmetry of the object's shape whereby the repulsive forces have cancelled each other. The curve connecting the critical points represents the object's skeleton with highest confidence (where the electrostatic potential is minimum) (Figure 3.32):

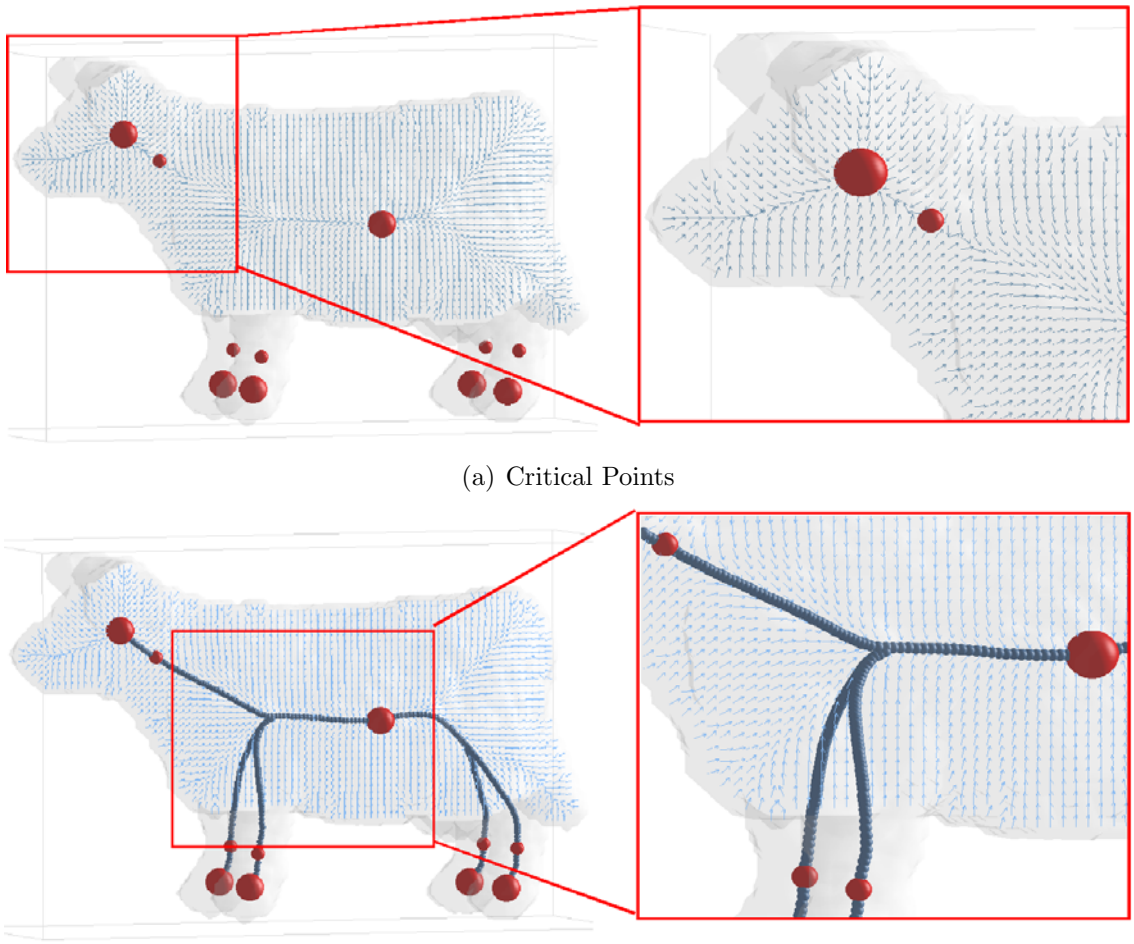

(a) Critical Points

(b) Core Skeleton

Figure 3.32: Crtical points in the potential field and critical skeleton of object, adapted from Cornea *et al.* (2005).

Divergence is a concept in field theory that describes "flow density". Positive values denote outflow of field lines (source), while negative values denote an inflow of field lines (sink). In electrostatic field theory, low divergence points possess low eletrostatic potential. Bearing this in mind, we can threshold on the divergence value to accept low potential points as skeleton voxels. By shifting the threshold level we can produce skeletons forming a "hierarchy" (Cornea *et al.*, 2005). The choice of suitable a divergence threshold is a trade-off between accuracy and redundancy (Figure 3.33).

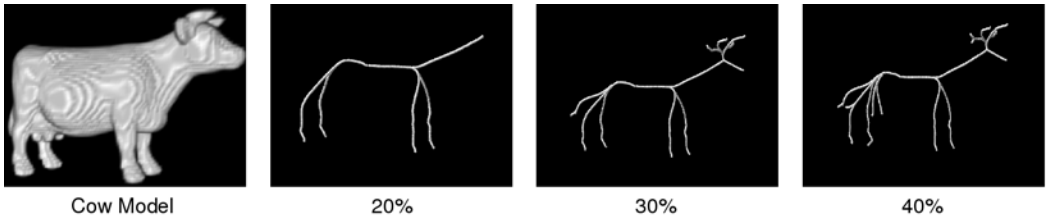

Figure 3.33: Skeleton curves of at different divergence thresholds, reprinted from Cornea *et al.* (2005) with permission.

We have implemented Cornea's method on some simple 3D objects and have obtained the results as shown in Figure 3.34.

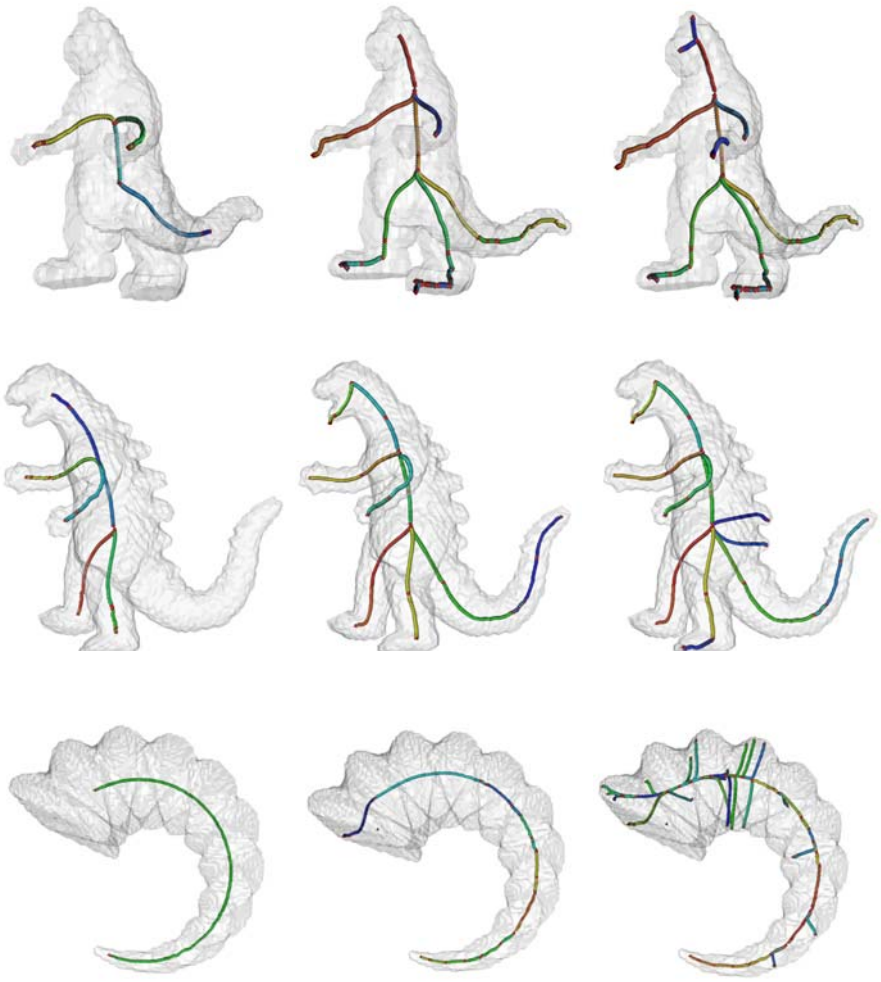

(g) 5% (h) 10% (i) 25%

Figure 3.34: Skeletons obtained by setting threshold equal to bottom 5%, 10%, 25% of divergence values. Skeleton segments of different lengths were labelled with different colours, reproduced from Cornea *et al.* (2005).

Continuous methods are generally computationally intensive. The test volumes are of 50×50×50 voxels on average, and it took between 16 and 40 seconds to process each volume, depending on the specific shapes and volume sizes. With increasing volume size, the processing time increases dramatically. For a 3D vessel image of 256×256×60 voxels it took 1883 and 1770 seconds to process at the 5% and 25% levels respectively (Computation times are measured under C environment on a desktop with Intel® Core™ 2 duo processor of 2.4GHz). The results are shown in Figure 3.35.

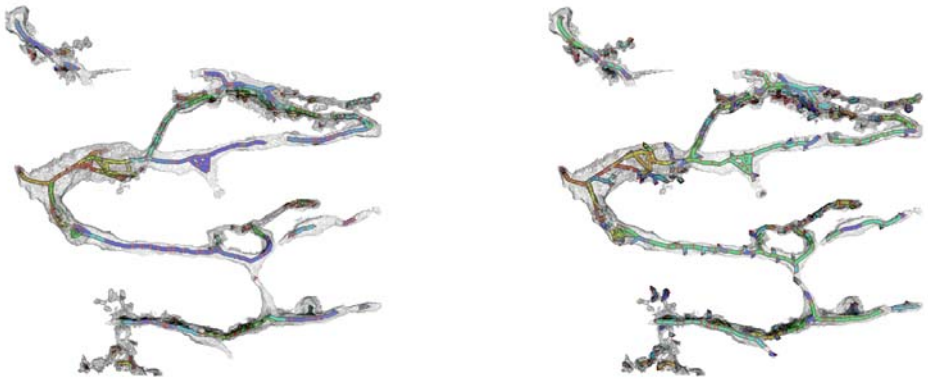

(a) 5% (b) 25%

Figure 3.35: Skeletons obtained by setting threshold equal to 5% and 25% bottom of the local divergence value.

We found that the continuous method failed to extract the centre lines of our blood vessel objects. This is because real blood vessel objects are usually not perfectly symmetrical shapes. This has led to a poorly defined eletrostatic field inside the vessel object, as required in Cornea's method. The skeleton voxels, which are calculated as voxels possessing low electrostatic potential are thus well apart from the centers of the vessel object. Meanwhile, it is hard to regularize the potential field in the continuous model, which makes adaptations infeasible.

3.3.2 Discrete Methods

Discrete methods are based on symmetrical ablation of shape voxels. Thinning is a representative method of this category. Thinning methods extract skeletons by iteratively stripping voxels from the shape's boundary. The iterative thinning process depends on the recognition of a simple point which is first proposed by Morgenthaler in 1981 (Cornea *et al.*, 2007). Basically, simple points are dispensable points, whose removal does not change the shape's topology. Simple points can be determined locally by inspecting their neighbourhood (Cornea *et al.*, 2007). This feature makes thinning methods much faster than their continuous counterparts. Parallel thinning algorithms have been proposed to extract skeletons of 3D objects (Lee *et al.*, 1994) which further enhances the efficacy of thinning methods.

Lee *et al.* (1994)'s method has been implemented by Homann (2007), which is available in ITK (Insight ToolKit) library. This algorithm searches into every shape voxel's 27 neighborhood in parallel and deletes those voxels that are either surface voxels or simple points defined by the Euler table given in Lee *et al.* (1994). The algorithm keeps line ending voxels and terminates when no more voxels can be removed from the object (Homann, 2007).

However, we have found Lee *et al.* (1994)'s method does not extract satisfactory skeletons from extremely irregular shapes, such as the blood vessel objects that are of interest in this thesis (Figure 3.36).

(a) Segmented Vessel Object (b) Extracted Vessel Skeleton

Figure 3.36: 3D thinning applied on the segmented image.

It can be seen that there are several regions that are not completely thinned. This was evidenced by the statistics of neighbour numbers of each skeleton voxel. At each skeleton voxel, the number of its 27-neighbouring skeleton voxel was counted and a histogram has been drawn as Figure 3.37:

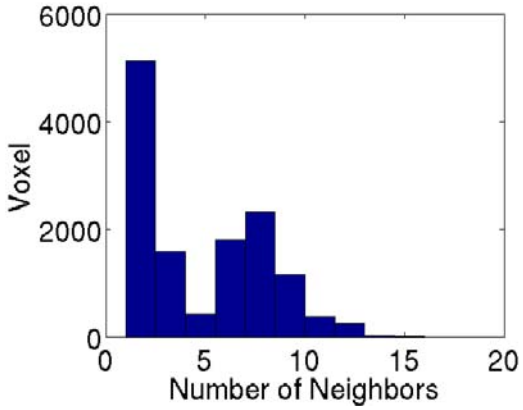

Figure 3.37: Number of neighbors at each voxel.

From the statistics we can see that the uncompleted thinning has led to a large bloated skeleton representation (13032 skeleton voxels), many of which are in fact simple points. The premature termination of the thinning algorithm also results in a large neighbour number for the skeleton voxels (mean 5.07, sd 3.16). This suggests that the skeleton is not yet a single voxel wide line but that additional voxels should be removed.

Although the thinning method failed to extract our blood vessel skeleton either, the discrete manner of its processing makes it amenable to a number of modifications. We have developed a shape regularizing algorithm to adapt the thinning method on our 3D blood vessel objects.

Shape Regularizing

We contend that the irregular shape of the blood vessel object has led to the failure to correctly identify simple points. This has resulted in a redundant representation of vessel object (Figure 3.36). We proposed to dilate the thinned skeleton symmetrically by moving a n × n × n structural element through it. Since the thinned skeleton preserved all topological properties of the original object, this will produce an object of the same topology as the original object, but having more regular (symmetrical) shapes (Figure 3.38).

(a) Original Vessel Object (b) Dilated Skeleton

Figure 3.38: A dilated skeleton.

Now we applied the thinning algorithm on the dilated skeleton object and obtained a new skeleton representation as shown in Figure 3.39.

The extracted skeleton has been found to be closer to the true representation after shape regularization. Since the thinning algorithm preserves all the topological properties

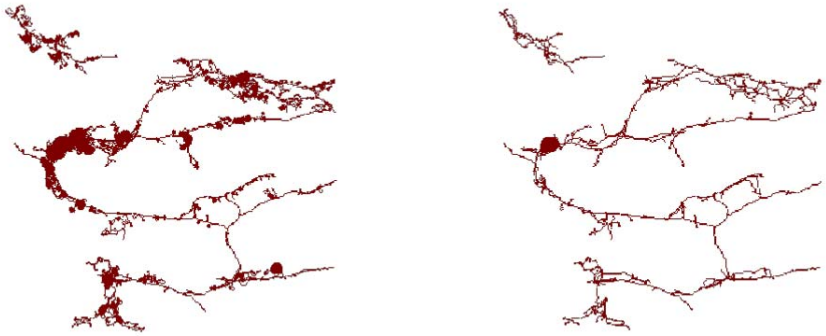

(a) Original Skeleton (b) New Skeleton

Figure 3.39: Thinned image on the dilated vessel skeleton.

of the vessel object, we only care about the width of the extracted skeleton. We can monitor the width of the skeleton by evaluating the number of neighbours of each skeleton voxel. Ideally, in a single voxel wide skeleton, most skeleton voxels should have two neighbours which are their preceding voxels and successing voxels respectively. Line-ending voxels should have only one neighbouring voxel whereas branching voxels can have more than two neighbours. However, line-ending voxels and branching voxels should have relatively low occurrences in our vessel skeleton. The histogram of the thinned skeleton neighbor number after one dilating-thinning cycle is illustrated in Figure 3.40:

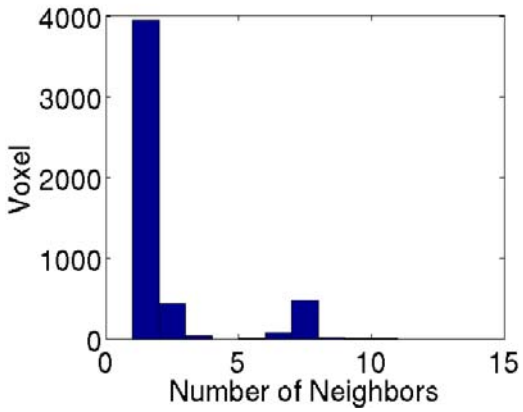

Figure 3.40: Distribution of number of neighbours at each voxel.

As can be seen in Figure 3.40, the skeleton produced by the thinning method after

shape regularising is much thinner (5003 skeleton voxels) than the directly thinned skeleton. The distribution of neighbour numbers of each skeleton voxel has a mean value of 2.75 voxels and standard deviation of 1.91 voxels.

We repeated the dilating-thinning for 3 cycles, and got the thinned skeleton as shown in Figure 3.41:

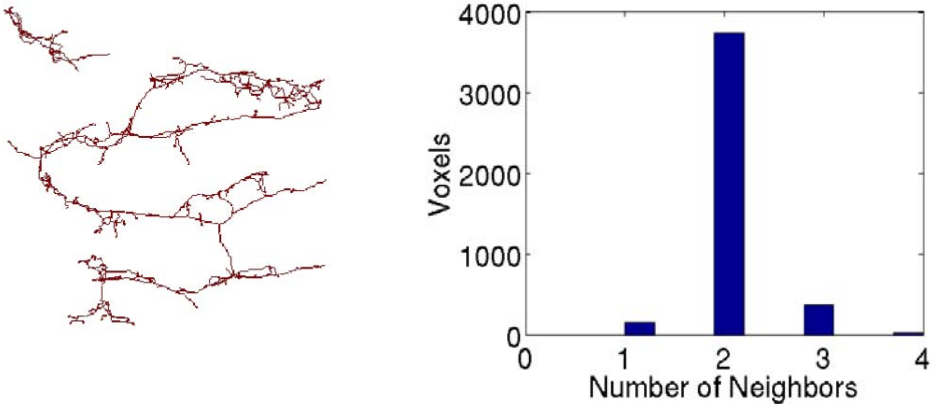

(a) Skeleton (b) Histogram of neighbour number

Figure 3.41: Thinned skeleton after 3 dilating-thinning cycles (a) and histogram of the neighbour numbers (b).

The number of skeleton voxels were finally reduced to 4281 voxels. The distribution of the number of neighbours shows a very high frequency of 2 (mean: 2.06, std: 0.37). The statistics of neighbour numbers suggests that the skeleton showed in Figure 3.41(a) is the single voxel wide skeleton representation of the blood vessel object.

The effectiveness of dilating-thinning method can be reflected by the trend of the reduction of skeleton voxels and the average number of neighbours (Figure 3.42):

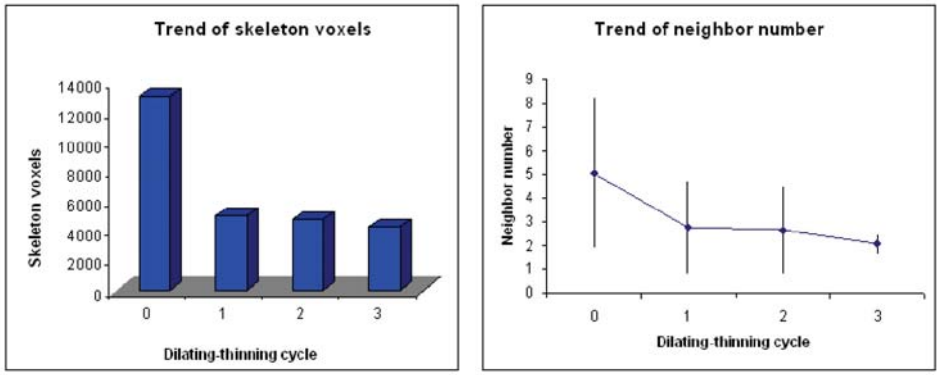

(a) Total Skeleton Voxels (b) Average Neighbor Number

Figure 3.42: Trend of skeleton number and neighbour number through the dilating-thinning cycle

From Figure 3.42 we observe that through the dilating-thinning cycle the total skeleton voxel number decreased from 13032 voxels to 4281 voxels. The average neighbour number decreased from 5.07 to 2.06 with standard deviation decreased from 3.16 to 0.37. This trend indicates that the dilating-thinning method is effective in removing redundant skeleton voxels left by normal morphological thinning operations.

3.4 Conclusion

In this chapter we have discussed different segmentation and skeletonization methods. We found hysteresis thresholding is able to segment the blood vessel object from the microscope images, and is easy to implement and fast in speed. Level set methods are developed from more sophisticated mathematical modelling. However, although they are capable of segmenting the blood vessel object, the accuracy and speed are inferior to the hysteresis thresholding method. Local phase is a useful image attribute and we have showed its applications in processing extremely noisy data set and in level set initialization. We concluded that hysteresis thresholding combined with local phase enhancement is the appropriate method to segment the blood vessel object in our research.

A vessel skeleton is the single representation of vessel object and provides a simplified model to analyse a vessel's structure. We compared one continuous method proposed by

Cornea *et al.* (2005) with the parallel thinning method developed by Lee *et al.* (1994). We found both methods are unable to produce the real vessel skeletons from segmented vessel objects. We contend the irregular shape of realistic tumour blood vessels has led to the failure of both Cornea and Lee's methods. We have proposed a shape regularising - parallel thinning method to extract vessel skeleton from the segmented vessel object, which was found to be effective on our data samples.

Chapter 4

GUI Development

4.1 Introduction

The analysis of vascular structure and function, and the modification of this as a result of therapy, continues to be of major research interest for oncologists. We are interested in studying the structural change to the tumour vasculature in response to vascular normalizing therapy. Various structure analysis algorithms and systems are available (Antiga *et al.*, 2006; Barber *et al.*, 2003). Such systems generally utilize a range of segmentation and skeletonization methods. As we described in the previous chapter, no segmentation and skeletonization method has been found to be universally applicable for different image samples. For this reason, we have developed a vessel analysis system which incorporates the methods we found suitable to process our tumour vessel microscope images. The local phase-(hysteresis) thresholding method and shape regularizing-thinning methods have been included in our software. The level set methods and continuous skeletonization methods are currently not implemented, primarily because of their slow computational speed.

4.2 Overview

The software that we have developed, and whose results on a range of confocal microscope datasets we report later in the thesis, consists of four modules: image segmentation, vessel skeletonization, user interactive skeleton modification, and vessel quantification.

The processing pipeline is shown in Figure 4.1

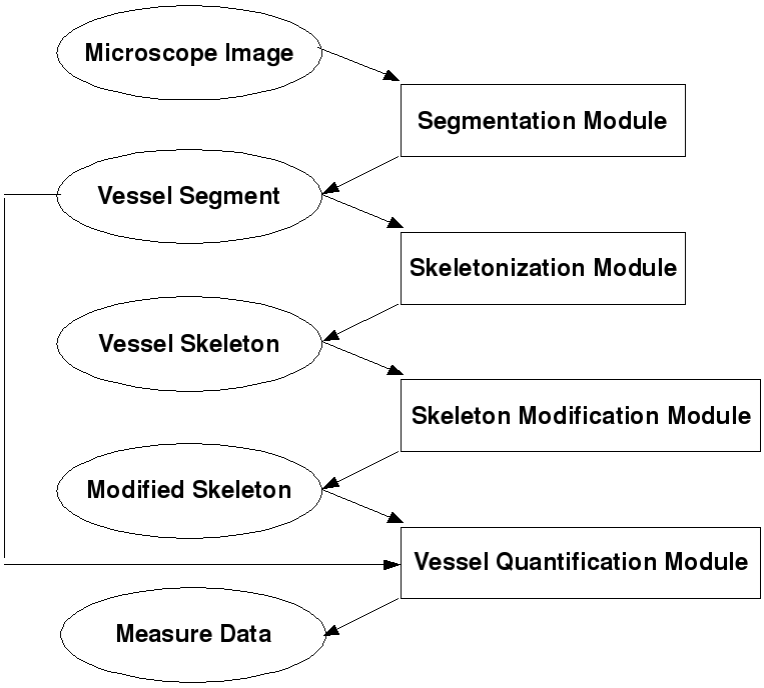

Figure 4.1: Processing pipeline.

The GUI (Graphical User Interface) was developed with the TK/Tcl toolkit under a Linux environment (Ubuntu 8.04) and was coded in Python and C/C++. VTK (Visual Toolkit, Kitware) was used to visualize the 3D images. The VTK rendering window was embedded in the TK GUI window through the Tcl-VTK API (Application Programming Interface). ITK (Insight Segmentation and Registration Toolkit, Kitware) has been used to facilitate image processing. A python-ITK API (WrapITK) has been used to import ITK classes into the python development environment.

4.3 Image Segmentation Module

In the image segmentation module, the local phase and hysteresis thresholding methods are implemented. The GUI is shown in Figure 4.2.

The user can select any directory to load microscope images. After loading the images, the GUI automatically visualizes the image using maximum intensity projection [1]

[1]Mechanics of maximum intensity projection (MIP) will be introduced in detail in Chapter 7.

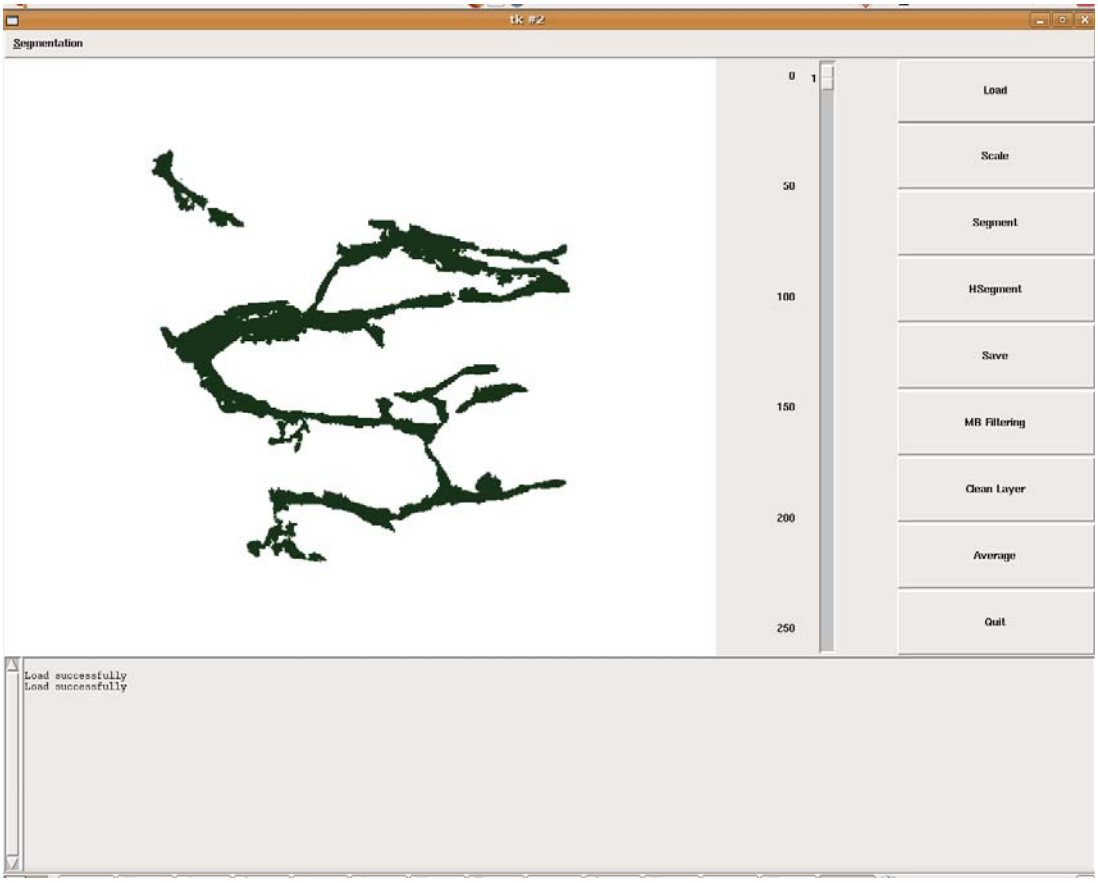

Figure 4.2: GUI for image segmentation.

though other visualization methods are supported. The user can freely scroll the scale bar to determine the minimal scale that is visible. This gives the user an impression of the effects of choosing different threshold levels. The user can click on the 'Segment' button and provide a threshold level in order to perform simple thresholding, or click on the 'HSegment' button and give high and low thresholds to perform hysteresis thresholding. After segmentation, the GUI automatically updates the rendering window with the segmented image. If the segment is not desired, the user can click 'Segment' or 'HSegment' button to provide a new set of parameters to repeat the segmentation process. Finally, the user can save the segmented image in the TIFF format by clicking on the 'Save' button. The GUI will automatically save a copy of the segmented image in a TXT file for visualization, for example in the skeletonization module. The user can also calculate local phase by clicking on the 'MB Filtering' button and give parameters for MB

filtering. The local phase image can be saved in any directory selected by the user. An average local phase image can be calculated from the local phase images computed over a range of scales. In some cases, boundary voxels have been found to have exceptional high local phases because of phase wrapping. In such a case, the user could click on the 'Clean Layer' button to set the boundary voxels' local phases to zero. The user can then perform simple thresholding or hysteresis thresholding on the averaged local phase image.

4.4 Skeletonization Module

In the skeletonization module, the thinning method with shape regularisation is implemented. The system reads the relevant TXT file and visualizes the segmented image as polygonal objects. The user can perform the thinning method by clicking on the 'Thin' button, or by performing shape regularisation by clicking on the 'Blob' button and providing the size of the structuring element. The user can repeat the thinning-dilation cycle until a skeleton that is a single voxel wide is produced Figure 4.3.

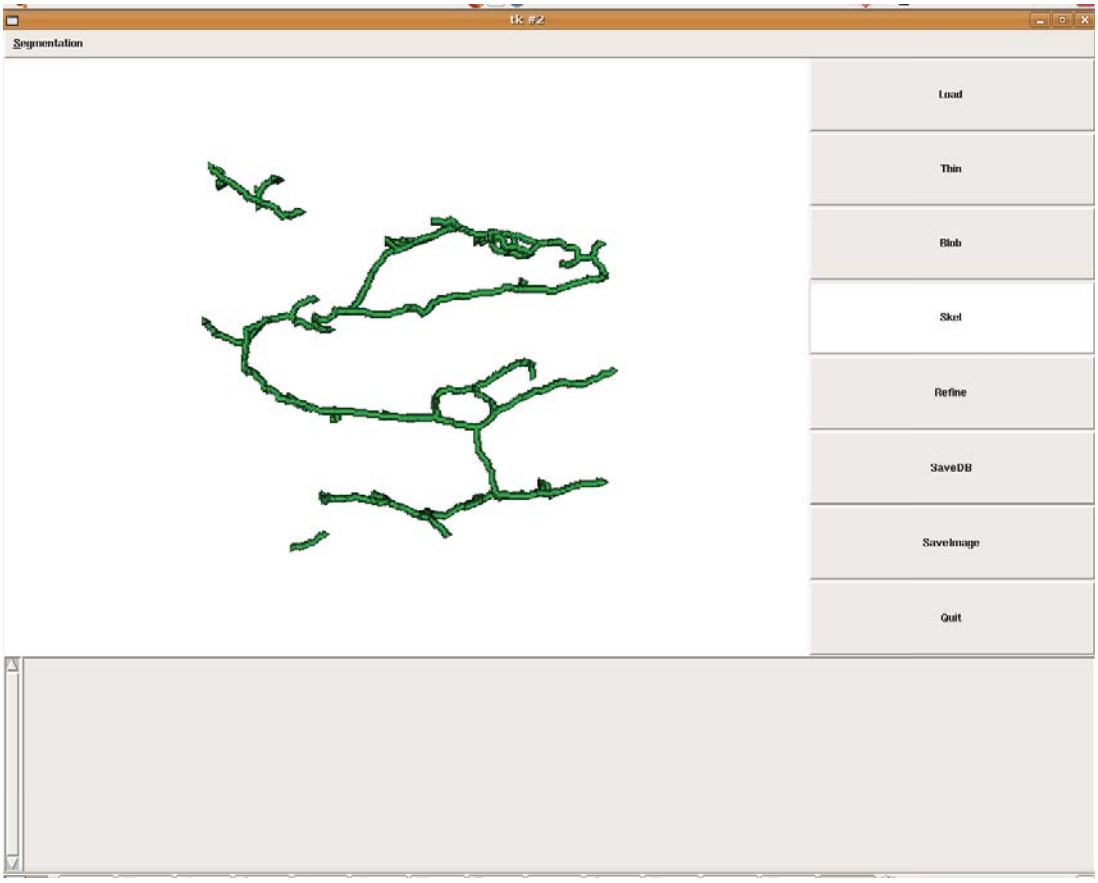

Figure 4.3: GUI for image skeletonization.

The vessel skeleton is represented in the GUI using hierarchical arrays. For each skeleton voxel, we count its 3D neighbouring skeleton voxels in the 27 point neighbourhood. Based on the number of neighbouring skeleton voxels, we classify the skeleton voxels as "tips" (voxels with 1 neighbour), "connecting voxels" (voxels with precisely 2 neighbours) and "branch voxels" (voxels with more than 2 neighbours). A skeleton segment is defined as a sequential link of skeleton voxels beginning and ending with tip voxel (one-neighbour voxel) or branch voxel (multi-neighbour voxel) (Figure 4.4).

To build up this data structure, we trace the skeleton image from one-neighbour voxel. We add this voxel into a void link and remove it from the skeleton image. We then consider its 27-neighbourhood ($(2k+1)^3$, $k=1$). If another one-neighbour voxel is found, we add this voxel to the link and remove it from the image. We continue the tracing algorithm. If a two neighbour voxel is found, we add this voxel into the link,

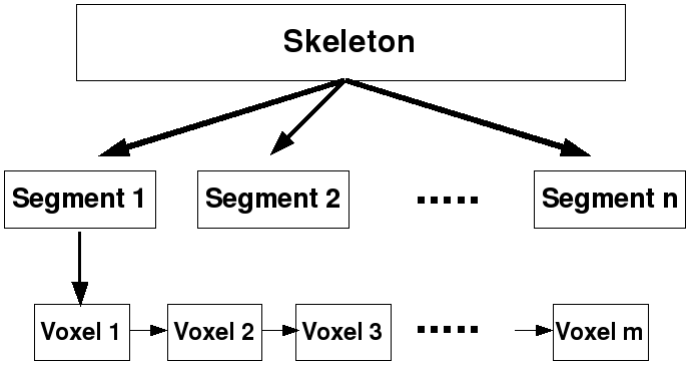

Figure 4.4: Data structure of skeleton representation.

remove it from the image and keep tracing. If a multi-neighbour voxel is found, we add it into the link but keep it in the image because it should be included in other skeleton segments. We then terminate the tracing program and obtain a skeleton segment. If the length of the extracted skeleton segment is above 10 voxels we save this skeleton segment under skeleton data structure, otherwise we discard the segment and start tracing from another one-neighbour voxel. This effectively remove the short skeleton "hairs" left by thinning programs (Gonzalez & Woods, 2002).

If no skeleton voxel is found, we enlarge the search area to the 125-neighbourhood ($(2k+1)^3$, $k=2$) to look for voxels to add to the segment link. If another skeleton voxel is found, we continue the tracing program. If not, we further enlarge the searching area until k rises to 10. This ensures that "tip-tip" segments are joined together if their distance is shorter than 10 voxels (ca.23.44μm in the images we analysed). The extraction algorithm is illustrated in Figure 4.5

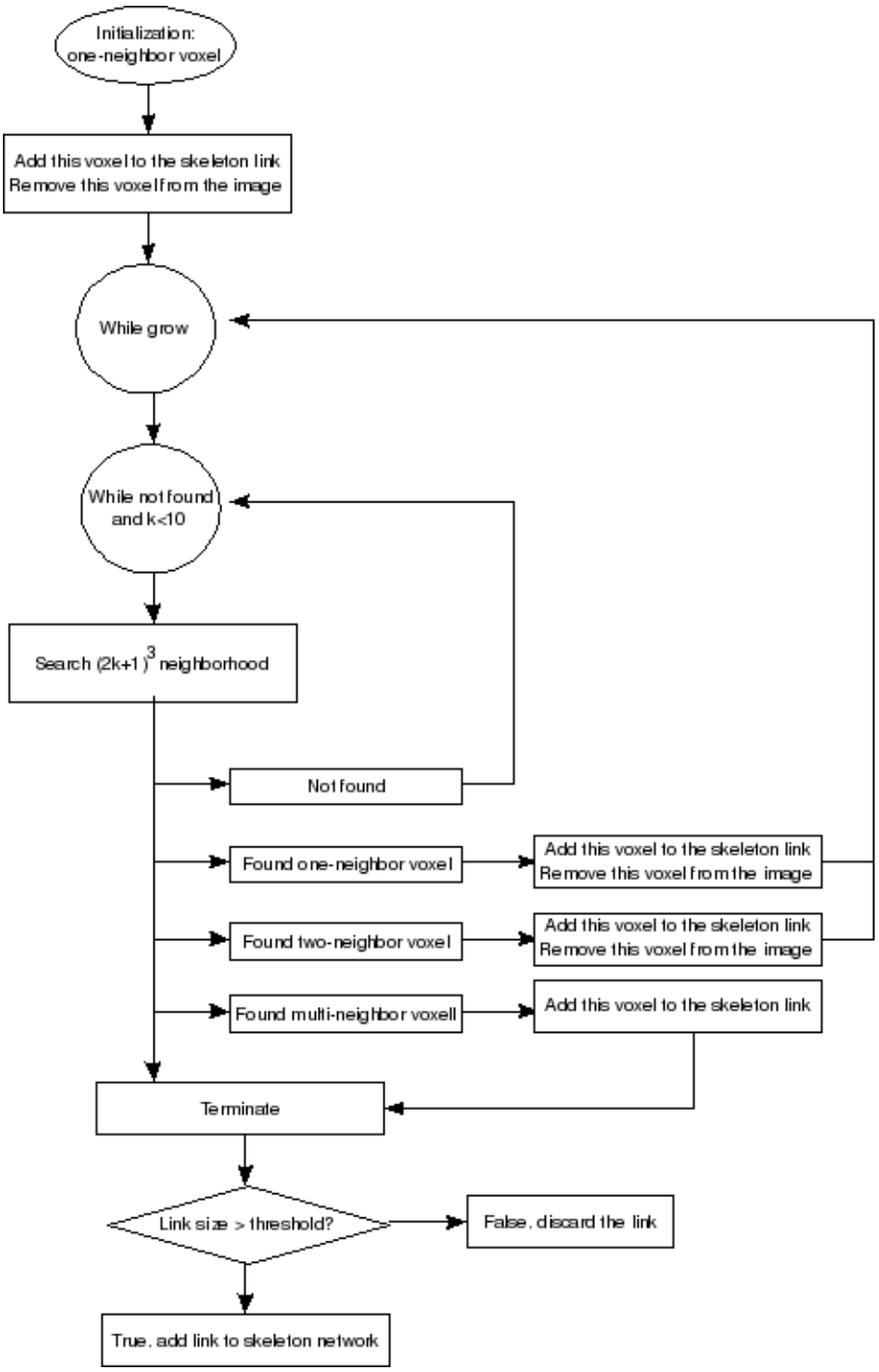

Figure 4.5: Pipeline for our skeleton extraction method.

We have observed that some multi-neighbour voxels are not true branching voxels. They have more than 3 neighbours because they clustered with other connecting voxels. The neighbour number of these false branching voxels needs to be corrected to enable full segment extraction.

Since our tracing program will terminate at these false branching voxels and produce short segment links, we identify the ends of such short segments (less than 3 voxels) as false branching voxels. We reduce the neighbour numbers of these false branching voxels by 1 and relabel the skeleton image with the corrected neighbour numbers. We perform the tracing algorithm on the relabelled skeleton image and update the structured skeleton data.

We also found that the raw skeleton has some redundant rings. The user can click on the 'Refine' button to remove these small skeleton rings that were produced by the morphological thinning operation. A ring is formed when two segments' ends are close to each other (Figure 4.6).

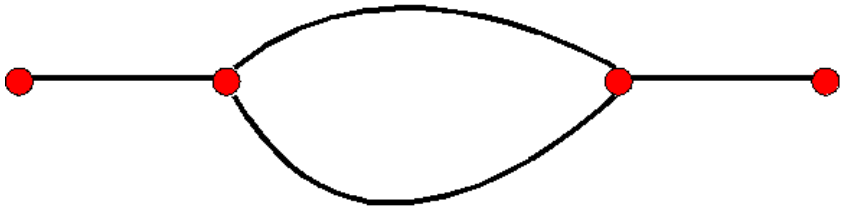

Figure 4.6: Illustration of a ring formation.

The automatic refinement program first searches segments whose ends are close to each other (separated by less than 3 voxels). The longer segment is removed unless its length is longer than 50 voxels, since in that case it represents a possibly true ring structure. Now, we should have a set of voxels which represents a skeleton image as shown in Figure 4.7.

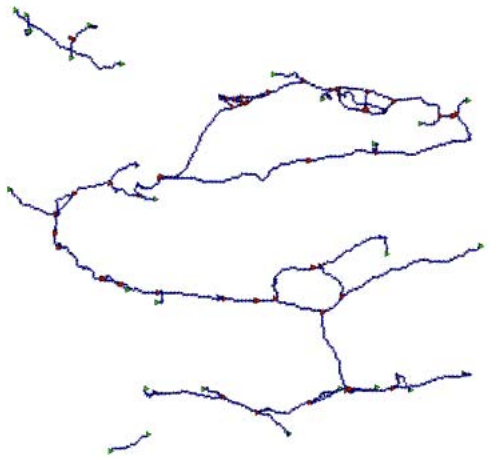

Figure 4.7: Skeleton of the blood vessel.

The user can click on the 'SaveImage' button to save the skeleton as TIFF image or click on the 'SaveDB' button to save the structured data into MySQL databases. MySQL supports remote access, so user can either save the data on the local machine or upload it on a remote server. By clicking on 'SaveDB' button, the user is prompted with the host machine name, user name, user password and database ID to save the structured data under specific database.

4.5 User Interactive Modification

Any fully automatic skeletonization procedure is almost certain to be incapable of producing a faithful representation of vessel skeleton. A user interactive skeleton modification module is introduced to enable manual corrections of an extracted skeleton (Figure 4.8).

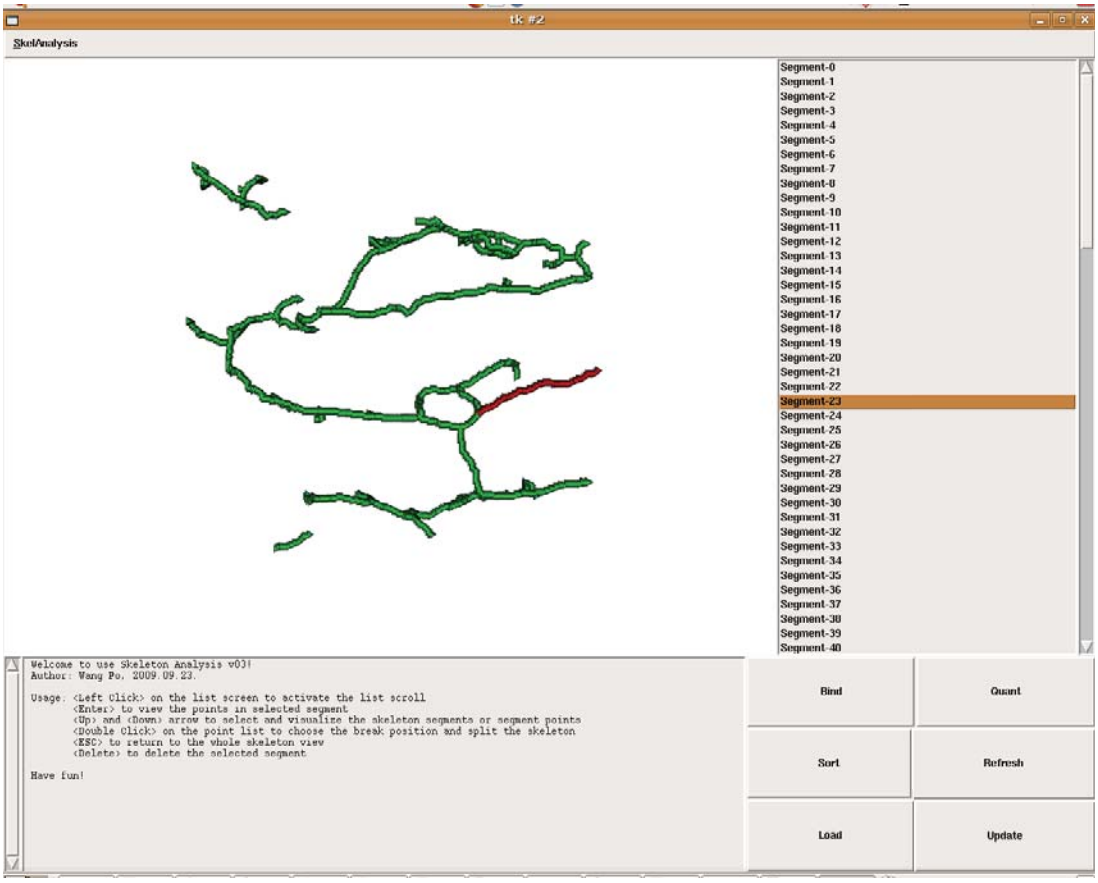

Figure 4.8: GUI for user interactive skeleton modification.

The user can load structured skeleton data from MySQL server by clicking on the 'Load' button. After successful loading, the GUI automatically rebuilds a skeleton network locally and visualizes it as a polygonal object (Figure 4.8). The GUI also generates a list of skeleton segment links on the right column (Figure 4.8). The user can select a segment by clicking on the label in the list or moving the cursor up and down. The GUI will automatically highlight the selected skeleton segment in the rendering window. The user can delete the selected segment by pressing 'Del' key. The user can also select multiple skeleton segments by 'Ctl' clicking on the segment labels and clicking on 'Bind' button to combine the selected segments.

The user can view skeleton voxels in selected segment by pressing 'Enter' key. The GUI will automatically generate a point list in the right column and visualize each skeleton voxel of the selected segment in the rendering window. The user can move the cursor

to select specific skeleton voxel which will be highlighted in the rendering window simultaneously. The user can also delete a selected skeleton voxel from the segment by pressing 'Del' key or split the segment at the selected skeleton voxel by double clicking the left mouse button on the voxel label. The user can return to the segment visualization mode by pressing 'ESC' key.

The user can upload the modified skeleton structure to or reload the skeleton from the MySQL server by clicking on the 'Update' or 'Refresh' button to save or undo the modifications.

4.6 Vessel Quantification

The vessel quantification module shares the same GUI as the user interactive modification module. It is pivotal for vessel quantification that the skeleton voxels maintain their correct sequence. However, the sequence could have been changed through combinations of skeleton segments. The user can click on 'Sort' button to do a intra-segmental sorting of skeleton voxels. The user can then click on 'Quant' button to perform vessel quantification.

4.6.1 Radius Measurement

At each skeleton voxel, the vessel radius is estimated from its 2D projection on the normal plane. The normal plane is the plane orthogonal to the local direction vector of vessel skeleton. However, direct projecting the local blood vessel volume on the normal plane may produce the partial volume effect which arises when then normal plane intersects with the discrete voxels. The partial volume effect will cause fractions of vessel voxel intensities leading to floating number intensity values in the projected image. This tends to make radius calculation inaccurate.

In order to avoid the partial volume effect, we have to project the local blood vessel volume on planes orthogonal to the x, y or z axis. For example, we can project the vessel

volume onto the xy-plane (Figure 4.9(a)). The central pixel in the projected image is the skeleton voxel where we projected the vessel volume. We can extract the connected region containing the centre pixel and count the vessel pixels as the section are in the 2D projection. Let the angle between the local vessel direction vector and the xy-plane be θ_{xy}, then we can calculate the section area of normal plane projection by Eq.4.1

$$S_{\perp}^{xy} = S_{xy} cos\theta_{xy}, \tag{4.1}$$

where S_{xy} is the area of xy-plane projection and $S_{\perp}^{xy}$ is the area of normal plane projection estimated from xy-plane projection.

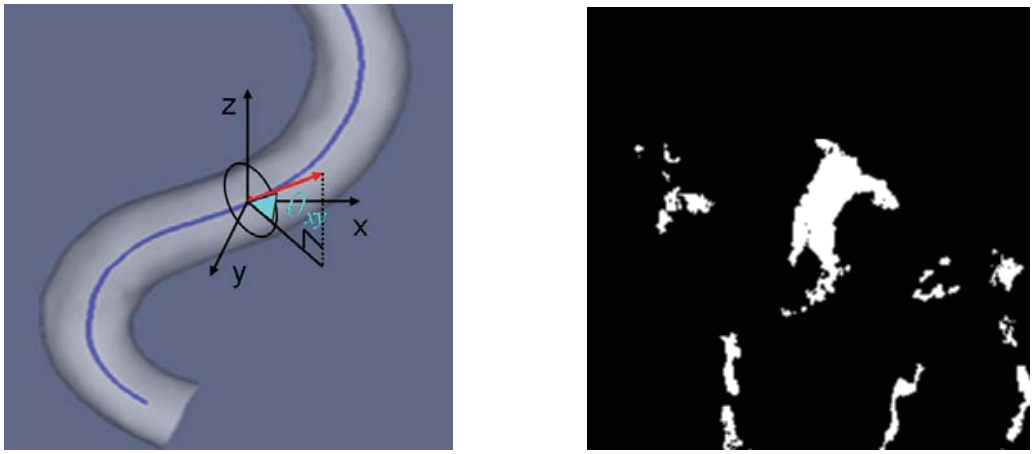

(a) projection illustration (b) example projected image

Figure 4.9: Illustration of radius measurement. (a). At each skeleton voxel, we project the vessel volume onto XY, XZ and YZ planes and calculate the vessel section radius depending on the angles between vessel direction and projection planes. (b). An example projected image.

As observed from the projected image (Figure 4.9), the vessel's shape may be far from circular. We assume that the *ex vivo* environment and imperfection of the histo-chemical staining could be the causes of the non-cylindrical vessel appearance. However, we contend that the blood vessel should be approximately cylindrical since *in vivo* the vascular pumping and pressure tend to produce a cylindrical formation. Thus we calculated the vessel radius assuming circular shape (Eq.4.2).

$$r_{\perp}^{xy} = \sqrt{\frac{S_{\perp}^{xy}}{\pi}}. \tag{4.2}$$

The unit of radius measure in this calculation is the voxel, i.e. the radius is given in terms of a number of voxels. This can, of course, be converted into micrometers by multiplying with the space dimension of a voxel. The final vessel radius measure is calculated as average of values estimated in the xy-plane , yz-plane and xz-plane projections (Eq.4.3):

$$r_{\perp} = \frac{1}{3}(r_{\perp}^{xy} + r_{\perp}^{yz} + r_{\perp}^{xz}) \tag{4.3}$$

4.6.2 Inter Branch Length Measurement

Inter-branch length is defined as the vessel segment length. At each skeleton voxel, the Euclidean distances between itself and its successor voxel is calculated and the vessel segment length is calculated by summing the Euclidean distances between pairs of subsequent skeleton voxels. This is the same as using short splines to approximate the overall curved structure, which is illustrated in Figure 4.10.

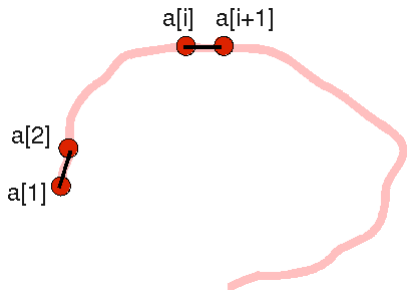

Figure 4.10: Illustration of length measurement

4.7 Tests

4.7.1 Cylinder Object Generation

To test our segmentation and quantification methods. We applied the local phase enhancement and hysteresis thresholding method to synthesize 3D noisy images and eval-

uated the segmentation and quantification errors with known ground truth. 3D cylinder objects were generated by aligning with a given orientation vector. The orientation vector was expressed using spherical coordinates (Figure 4.11).

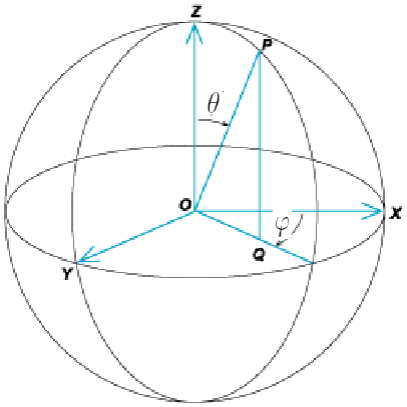

Figure 4.11: Illustration of a spherical coordinate system

In the spherical coordinate system, any space point is expressed with three coordinates, the radius r, the inclination (or elevation) angle θ, and the azimuth angle φ. For a unit vector, r=1. So the Cartesian coordinate for a unit vector $\boldsymbol{P}$ can be expressed as:

$$x = sin(\theta)cos(\varphi), \quad y = sin(\theta)sin(\varphi), \quad z = cos(\theta)$$

By varying θ between [0,π] and φ between [$-\pi$, π], the unit vector $\boldsymbol{P}$ can point to any orientation in space.

3D cylinder objects were generated for any given orientation vector. Cylinder voxels were assigned the value 1 while background voxels were assigned 0. The height of cylinder was approximately 40 voxels, the accurate value is dependent on the discrete representation of the cylinder object and can be calculated after the cylinder has been generated. The radius was fixed to be 7 voxels (Figure 4.12(a)).

We first added Gaussian blurring to the generated cylinder object. Since a Gaussian kernel is separable, Gaussian blurring was generated by convolving the cylinder image with a 1D Gaussian kernel separately along the x, y and z axes. The blurring effect is dependent on σ of Gaussian function (Figure 4.12(b)). Gaussian noise is subsequently

added to the blurred cylinder. The noise level is dependent on the mean and standard deviation of Gaussian random numbers. To avoid bias, we utilized zero-mean Gaussian distribution to generate the Gaussian noise. In this case, noise effect is solely dependent on the σ of the Gaussian distribution (Figure 4.12(c)).

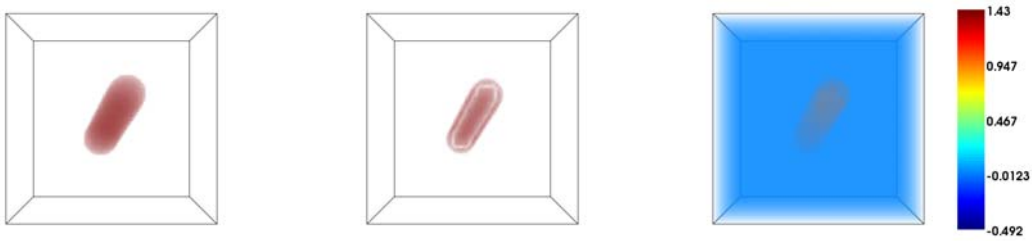

(a) Binary Cylinder (b) Blurred Cylinder (c) Noisy Cylinder

Figure 4.12: The binary cylinder was generated by setting $\theta = \pi/6$ and $\varphi = \pi/3$ where cylinder voxels were assigned 1 and background voxels were assigned 0 (a). The cylinder object was then blurred by a Gaussian kernel with $\sigma = 0.5$ (b). Zero mean Gaussian noise was subsequently added with $\sigma = 0.01$(c).

4.7.2 Measurement Error Related to Orientations

We tested our segmentation and quantification methods on cylinders with different orientations. In our experiments, the blurring σ was fixed to 0.5 and noise σ was fixed to 0.01. We applied automated hysteresis segmentation. After generation of each noisy image, we calculated the maximum intensity value (Max) and the average intensity value (Mean). The high threshold was then set equal to Max, and the low threshold was set equal to Max-0.5×(Max-Mean)(Figure 4.13).

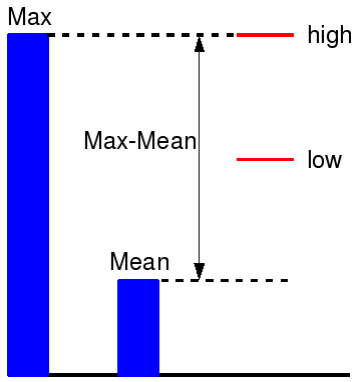

Figure 4.13: Measurement error at different levels of blurring.

We quantified the error of the automated segmentation as the ratio between the number of misclassified voxels and the number of cylinder voxels in the original binary image. The misclassified voxels were cylinder voxels misclassified as background voxels by the segmentation method or background voxels misclassified as cylinder voxels by the segmentation method.

The length measurement error was calculated as $\frac{\hat{L}-L}{L}$, where $\hat{L}$ is the measured length value and L is the ground truth length value. Similarly, the radius measurement error was defined as $\frac{\hat{R}-R}{R}$, where $\hat{R}$ is the measured radius value and R is the ground truth radius value. The relationship between segmentation error, length measurement error, radius measurement error, and the cylinder's orientation is illustrated in Figure 4.14

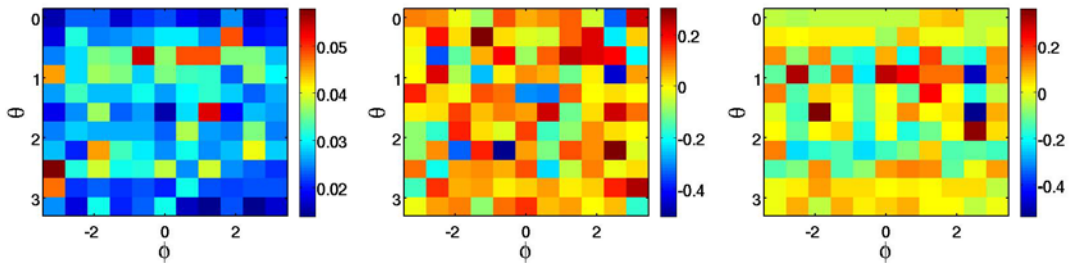

(a) Seg Error (b) Length Error (c) Radius Error

Figure 4.14: Segmentation error, length error and radius error at different inclination angles (θ) and azimuth angles (φ).

Segmentation errors were found to be small (with mean value equal to 2.81%) and orientation insensitive (with standard deviation equal to 0.86%). The distribution of

segmentation errors displays symmetry in the θ values. For cylinders whose centre lines are within the $x-y$ plane ($\theta = \pi/2$), the segmentation errors were found low. This is because when the cylinder rotates within the $x-y$ plane, the step effect in the discrete representation of the cylinder object is small in the z-direction. However, the step effect for the x and y directions still exist, which leads to variations of segmentation errors among different φ values. When the cylinder centre line lies out of the $x-y$ plane ($\theta \in (0, \pi/2), (\pi/2, \pi)$), the step effect is significant in all x, y, z directions. The segmentation errors were found to be large and sensitive to φ values. Finally, when the cylinder centre line aligns with the z-axis, the step effects in all x, y, z directions are small so the segmentation errors were found to be low when $\theta = 0$ or π. When the cylinder rotates around the z-axis, the representation of cylinder object is essentially not changed. The segmentation errors were independent of φ values, and were really the system errors related to the noisy data generation and segmentation method.

Length errors were found to be orientation sensitive (with mean value equal to 1.73% and standard deviation equal to 15.06%). However, length errors didn't exhibit symmetries to θ or φ suggesting they are random errors. Radius errors were also found orientation sensitive (with mean value 0.76%). It was found to be positively correlated with segmentation errors. This is because the radius was measured from the segmented image, thus the radius measurement accuracy is dependent on the segmentation errors.

4.7.3 Measurement Error Related to Blurring and Noise

We generated cylinders with $\theta = 0$ and $\varphi = \pi$. The cylinder object was first blurred with a Gaussian kernel of standard deviations σ from 0.25 to 2.5. Gaussian noise σ was shifted from 0.01 to 0.1. The relationship of segmentation error, radius, length measurement is illustrated in Figure 4.15.

Segmentation errors were found to increase monotonically with blurring σ and noise σ. When blurring σ and noise σ were low, segmentation errors were small. Segmentation

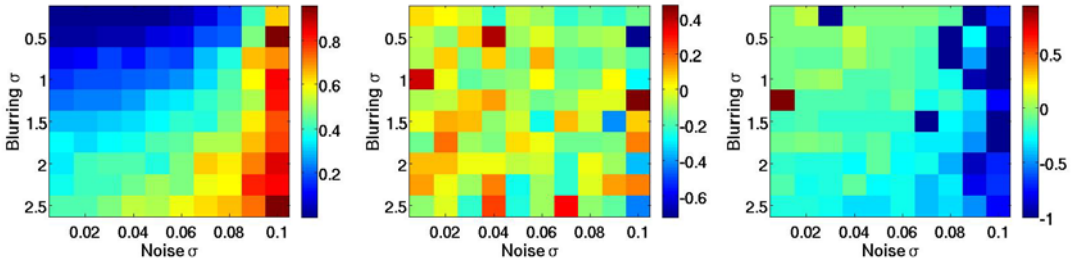

(a) Seg Error (b) Length Error (c) Radius Error

Figure 4.15: Segmentation error, length error and radius error at different bluring σ and noise σ

errors increased linearly with blurring σ and noise σ from a minimum value of 0.02849% to the maximum value of 95.84%. The high segmentation error value at high blurring and noise levels suggests that direct hysteresis thresholding becomes unreliable in this case.

Length measurement errors didn't display a consistent trend with blurring and noise σs. The mean value of the length measurement error was -5.71% and the standard deviation was 16.38%. This suggests that the length measure was unbiased but unstable with increasing blurring and noise σs.

Radius measurement errors exhibited negative correlation with segmentation errors. When segmentation errors were small, the radius measurement errors were positive, when segmentation errors were large, the radius measurement errors droped below zero. This suggests that with increasing blurring and noise level, the hysteresis thresholding tends to misclassify cylinder voxels as background voxels leading to negatively biased radius measurement.

4.7.4 Measuring Extremely Noisy Images

In this experiment, we fixed the blurring σ to be 0.5 and analyse influence of high noise level on the final segmentation, length and radius measurements. We simulated three noisy cylinder images with noise σ equal to 1, 10 and 20 respectively (Figure 4.16).

The increased noise level demands a trial-and-error process to determine the appro-

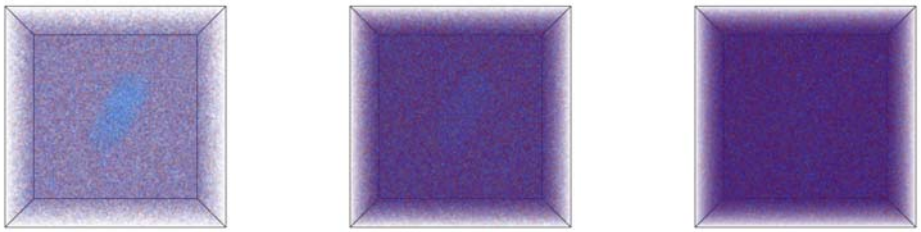

(a) σ=1 (b) σ=10 (c) σ=20

Figure 4.16: Noisy cylinder images with noise σ=1, 10, 20.

priate high and low thresholds to yield optimal segmentations. The higher the noise level (and thus the lower the SNR), the more effort-demanding the process becomes. Figure 4.17 presents the segmentation results of direct hysteresis thresholding on the noisy images. The thresholds were determined in the best effort on a trial-and-error basis using the segmentation GUI.

(a) σ=1 (b) σ=10 (c) σ=20

Figure 4.17: Optimal direct hysteresis threshold results on the noisy images.

It can be seen that in the case of a high noise level, direct hysteresis thresholding failed to yield satisfactory segmentation results. The high noisy images could be enhanced by local phase calculation. Figure 4.18 presents the corresponding local phase images of each noisy image:

Using the GUI, we tried different high threshold and low threshold values in hysteresis

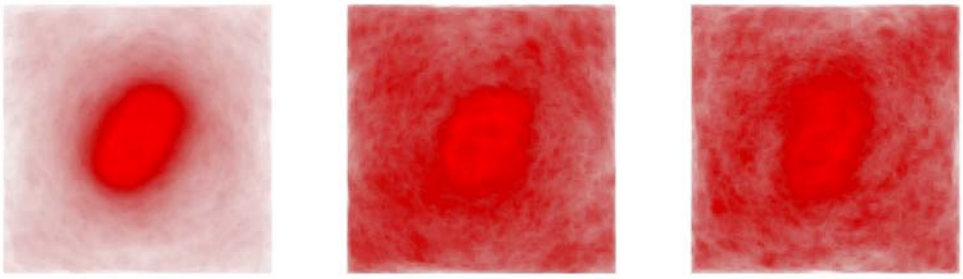

(a) σ=1 (b) σ=10 (c) σ=20

Figure 4.18: Local phase images. Local phase image for each noisy image was produced by averaging the localphase calculated with MB filtering of different scale ($\beta = 0.1$, $\alpha = 2, 2.3, 2.5$ repectively).

thresholding on the average local phase image. We obtained the optimal segmentation results based on the visual perception (Figure 4.19).

(a) σ=1 (b) σ=10 (c) σ=20

Figure 4.19: Optimal hysteresis threshold results on the average local phase image.

We carried out length and radius measurements on segments obtained by direct hysteresis thresholding on a noisy image and on the local phase enhanced image. A comparison of segmentation errors, length errors and radius errors is illustrated in Figure 4.20.

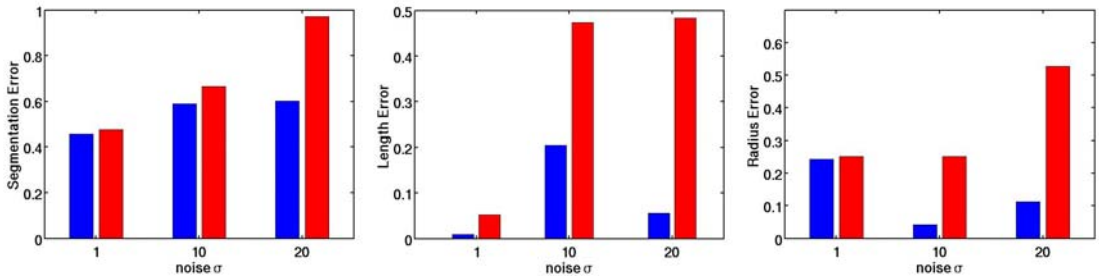

(a) Segment Error (b) Length Error (c) Radius Error

Figure 4.20: Comparison of measurement errors on direct hysteresis thresholding (red) and hysteresis thresholding on averaged local phase (blue).

From Figure 4.20, it can be seen that with increasing noise σ, direct hysteresis thresholding on the noisy image produced an increasing segmentation error which reached as high as 97.29%. In contrast, the segmentation error of hysteresis thresholding on the local phase enhanced image was constrained around 60% (the highest value was 60.08%). With increasing level of noise, the benefit of local phase enhancement in reducing segmentation error increased and became more significant.

The length measurements obtained from local phase enhanced images were also found to be superior to those obtained from noisy image. With increased noise σ, the length measurement error on direct segmentation of noisy image surged to as high as -48.29% (for illustration, we used the absolute error measure as the height of bar. The negative error indicates that the measured length value is smaller than the true length value.). In contrast the length measurement error on segmentation of local phase enhanced image was maximum of -20.56% at noise σ equal to 10. The maximum length measurement error occurs at noise $\sigma = 10$ rather than the maximum noise level of $\sigma = 20$ because the length measurement critically depends on positions of noise voxels. Since noise is added randomly, it happened that more noise voxels were attached with the cylinder surface though the noise σ was low. These noise voxels lead to the high discrepancies of measurement length to the true length value.

Radius measurement errors were also lower with local phase enhancement. When

noise σ increased from 1 to 10, radius measurement errors on segmentation of noisy image were relative stable (ca. -25%). However, when noise σ rised to 20, the radius measurement error rised as high as -52.03% (Again, negative error indicates that the measured radius value are smaller than the true radius value.). In contrast, radius measurement errors on segment of local phase enhanced image were not correlated with noise σ but were more closely related to the positions of noise voxels. This rendered a significant reduction of radius error when the noise level is high.

4.8 Summary

In this chapter, we described the various modules of a graphical user interface (GUI) developed for vessel structural analysis. Algorithms for inter-branch length measure and radius measurements have been proposed and tested on different data sets. The test results suggest that the segmentation error, length measurement error, and the radius measurement error are less affected by the orientations of blood vessels but more sensitive to blurring and the noise level of the image. For images with an extremely high noise level, segmentation, length and radius measurement become unreliable. We propose that local phase could be employed to enhance the image quality of extremely noisy data sets and compared the segmentation error, length error and radius error on segmentation of noisy image and segmentation of local phase enhanced image. We concluded that local phase enhancement on extremely noisy images could improve the reliability of hysteresis threhsolding and length, radius measurements.

Chapter 5

Quantitative Vessel Structure Analysis

5.1 Introduction

Tumour vasculature is often substantially less efficient than normal vasculature in delivering oxygen and other nutrients. Insufficient oxygen supply causes poor oxygenation in the tumour area, an effect that is known as tumour hypoxia (Jain, 2005). It has been observed clinically that hypoxia reduces radiation-induced DNA damage and so enhances a tumour's "resistance" to irradiation. This compromises the effectiveness of radiotherapy against cancer (Vaupel, 2004). In addition, inefficient tumour vascular delivery leads to failure in the take-up of drugs in the tumour region and so hypoxia also compromises the effectiveness of chemotherapy against cancer (Jain, 2005).

Tumour vessel normalization therapy has been proposed (Jain, 2005; Kerbel, 2006) to enhance tumour vessel efficacy so as to improve oxygenation in the tumour region and yield optimal responses for chemotherapy and/or radiotherapy. One strategy is to intervene directly with the tumour angiogenesis signal transduction. As described in Chapter 1, tumour angiogenesis is characterised by over-expression of proangiogenic factors, such as vascular endothelial growth factor (VEGF), which stimulates generation of new blood vessels (Weinberg, 2007). Without the regularising action of antiangiogenic factors, this results in a leaky, disorganised vasculature . Directly blocking the VEGF signal path-

way has been shown to have effect in normalizing tumour vasculature by restoring the pro/anti-angiogenic factor balance, which is evidenced by enhanced oxygenation and radio sensitivity of tumour tissues. However, this effect is only transient and vasculature redevelops into a chaotic network after a temporary period of normalization (Jain, 2001).

Since over-expression of VEGF is mediated by tumours, there should be cross-talk between VEGF expression and oncogenic signalling pathways. Therefore, tumour angiogenesis could be down regulated indirectly by the inhibition of tumorigenesis pathways. Trials aimed at normalizing the tumour vasculature by inhibiting (EGFR)-RAS-phosphatidylinositol 3-kinase (PI3K)-AKT signalling pathway have been performed (Qayum *et al.*, 2009). IRessa, an inhibitor of EGFR tyrosine kinase signaling; L-778,123, a farnesyltransferase inhibitor which blocks the RAS pathway; Nelfinavir, a protease inhibitor which down-regulates AKT signalling; and PI103, a class I PI3K inhibitor were reported with different effects in normalizing tumour vasculature (Qayum *et al.*, 2009).

In this chapter, we present methods to quantify the structure of tumour vasculature. We quantitatively evaluate the change in tumour vascular structure in response to IRessa, L-778-123 (FTI), Nelfinavir (NFV) and PI103. We confirm the results in Qayum *et al.* (2009) with statistical confidence.

5.2 Data Preparation

The microscope images of tumour blood vessels were kindly provided by Dr. Qayum, who conducted the in vivo study Qayum *et al.* (2009). Mice bearing human tumour xenografts were treated for 5 days with one of four drugs: IRessa, FTI (L-778-123), NFV (nelfinavir) and PI103. Microscope images were obtained following the protocol presented in Qayum *et al.* (2009). Microscope images were segmented using the local phase-(hysteresis) thresholding method and the vessel skeletons were obtained through modified thinning operations. In the study reported in this Chapter, we analysed three images for untreated tumour vessels, three images for FTI treated, two images for IRessa

treated, five images for NFV treated and three images for PI103 treated images. The microscope images were analysed with the GUI we described in Chapter 4. Figure 5.1 shows an example of a raw image and the vessel skeleton extracted from it.

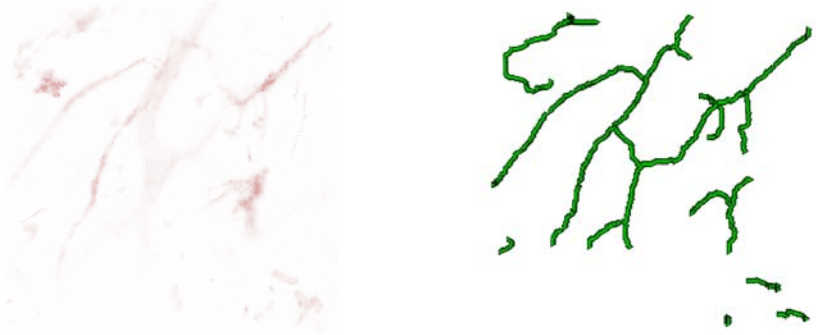

(a) raw image (b) vessel skeleton

Figure 5.1: Example microscope image (a) and corresponding vessel skeleton (b).

5.3 Radius Analysis

5.3.1 Vessel Radius Distribution Assumption

At each skeleton voxel, the vessel radius was calculated following the algorithm described in Chapter 4. Figure 5.2 shows the average values of vessel radii in each vessel sample.

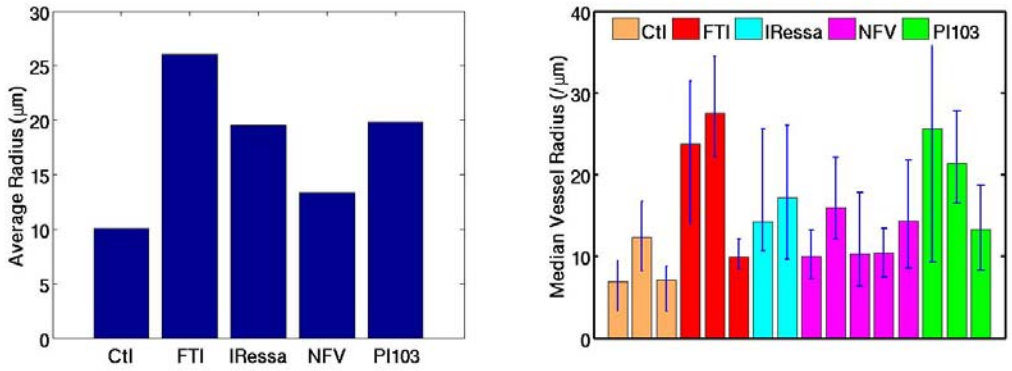

(a) Average of each drug group (b) Average of each image

Figure 5.2: Comparison of the average vessel radius of each vessel structure. In the group average (left), we used the mean value as a measure of average vessel radius of each drug treated sample; in the image average (right), we used the median value (2nd quartile) as a measure of average vessel radius of each vessel image and used the first and third quartile values as the measure of spread.

The histograms of vessel radii (Figure 5.3) indicate that the radius distribution is skewed, and so is definitely not Gaussian. As a result, the standard deviation is not suitable for describing the spread of the vessel radii. We use the arithmetic mean to describe the average radius value (Figure 5.2(a)) and the interquartile distance to describe the spread of the data (Figure 5.2(b)). We find that the average vessel radius in untreated tumour vessels is ca. 10 μm whereas the average vessel radius of drug treated tumour vessels ranges from 15 μm (NFV) to 25 μm (FTI). The spread is considered to be high because of the extreme values in the long tail of the skewed distribution.

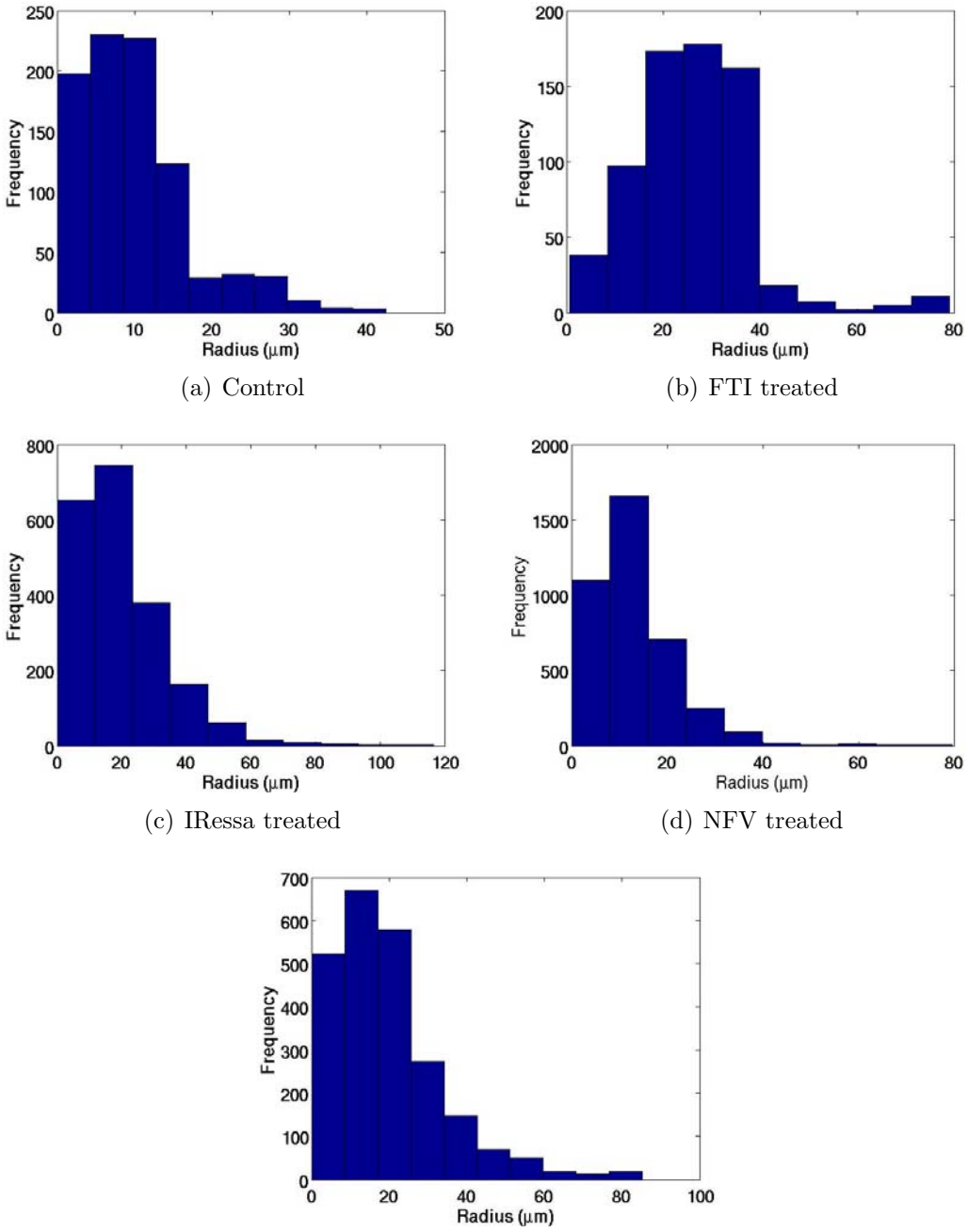

(a) Control

(b) FTI treated

(c) IRessa treated

(d) NFV treated

(e) PI103 treated

Figure 5.3: Histograms of the radius distributions in each vessel sample.

Konerding and colleagues (Konerding *et al.*, 2001) proposed that the vessel radius follows a log-normal distribution. In order to test the log-normal assumption, we calculated the logarithms of the radii in each vessel sample.

If the radius values do comply with the log-normal distribution, their logarithms should be normally distributed. For this reason, we carried out a normality test on the

logarithms of the radii and we summarise the results in (Table 5.1)

	skewness	kurtosis
Control	-1.3992	7.1228
FTI treated	-1.9553	9.4393
IRessa treated	-1.1537	5.5151
NFV treated	-1.0197	5.2441
PI103 treated	-1.2013	5.3625

Table 5.1: Skewness and kurtosis of the logarithms of radii.

Table 5.1 shows that the skewness and kurtosis of the radius logarithms are far from what one would expect for a normal distribution, for which skewness and kurtosis should equal 0 and 3. In fact, Lilliefors tests (Lilliefors, 1967) rejected the assumptions that the radii logarithms are distributed normally ($p<0.0001$). We conclude that the log-normal distribution assumption is not justified. In fact, we contend that the radii are more likely to follow a gamma distribution.

The Gamma distribution is a two parameter distribution. It is widely used in reliability, environmental, medical and other areas of statistics (Fraser *et al.*, 1997). It is derived from exponential distributions, e.g. let X_1, X_2, ..., X_k be k independently exponentially distributed random variables with same arithmetic mean θ and $S = \sum_{i=1:k} X_i$ be the sum of these random variables. Then the derived random variable S follows a gamma distribution. It has a probability density function (pdf) given in Eq.5.1

$$g(s;\theta,k) = \frac{1}{\Gamma(k)\theta^k} s^{k-1} e^{-s/\theta}, \qquad s > 0, k, \theta > 0, \tag{5.1}$$

where $\Gamma(k) = (k-1)!$ is a gamma function.

Based on this definition, $\mathrm{E(S)} = \mathrm{E}(\sum X_i) = k\mathrm{E}(X_i) = k\theta$. Though k denotes the number of exponentially distributed random variables that together form S, k is not necessarily an integer. It was found that k has a major impact on the shape of the gamma distribution probability density function curve, so it is called the "shape parameter". θ has an impact on the location of the pdf curve, it is called the "scale parameter". The

impact of different values of k and θ are illustrated graphically in Figure 5.4

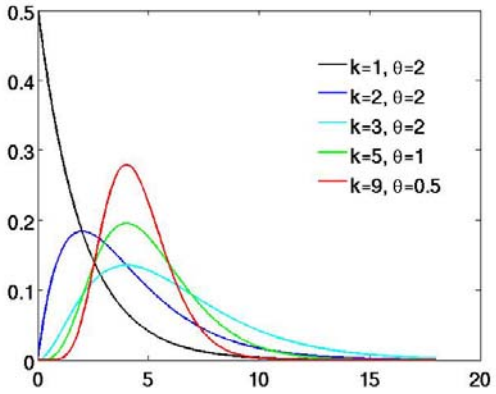

Figure 5.4: k and θ's impact on the shape of gamma pdf curve

We calculated the parameters of the best fitting log-normal and gamma distributions of vessel radii using the maximum likelihood method provided in Matlab® (R2008a). We list the estimated parameters in Table 5.2. The pdfs of the best fitting log-normal and gamma distributions and the histograms of the data are shown graphically in Figure 5.5.

	μ	σ	k	θ
Control	2.01546	0.881464	1.86355	5.39065
FTI treated	3.1163	0.624835	3.62341	7.19591
IRessa treated	2.68062	0.86467	1.87087	10.4298
NFV treated	2.35866	0.751173	2.30179	5.7988
PI103 treated	2.67773	0.902549	1.76988	11.1918

Table 5.2: Optimized parameters of log-normal and gamma distribution.

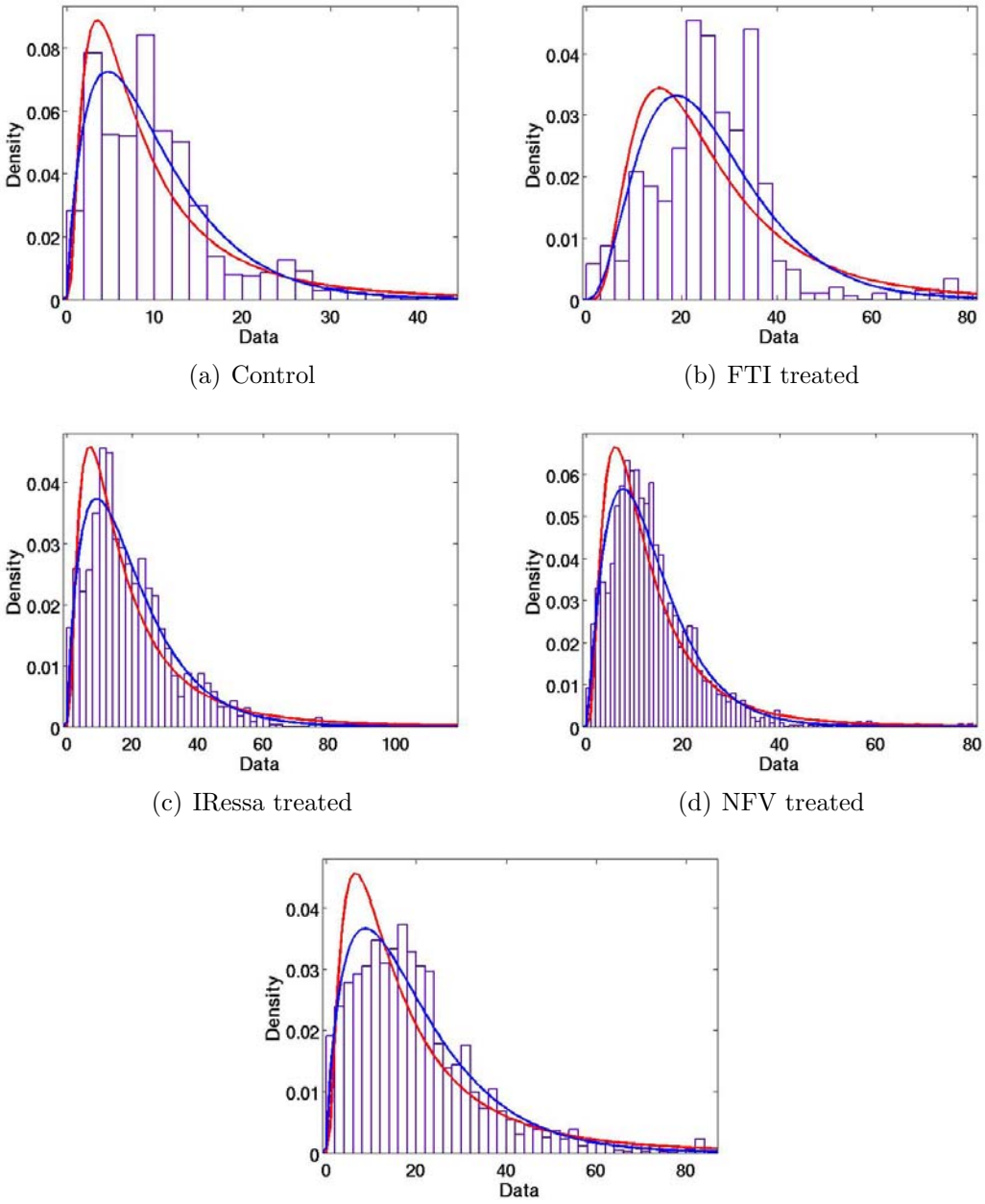

(a) Control (b) FTI treated

(c) IRessa treated (d) NFV treated

(e) PI103 treated

Figure 5.5: Comparison of the log-normal fitting (red) and gamma fitting (blue) of the radius distribution.

In order to quantitatively compare the log-normal and gamma fittings, we first calculate the Kaplan-Meier estimate of the cumulative distribution function (cdf) of the observed data. Since this cumulative distribution is derived directly from the observed data, it is also called the empirical cdf of the data. This cdf will serve as ground-truth of the distribution characteristics of the observed data. We then calculate the correspond-

ing cdfs for the best fitting log-normal and gamma distributions and plot the three cdfs in Figure 5.6

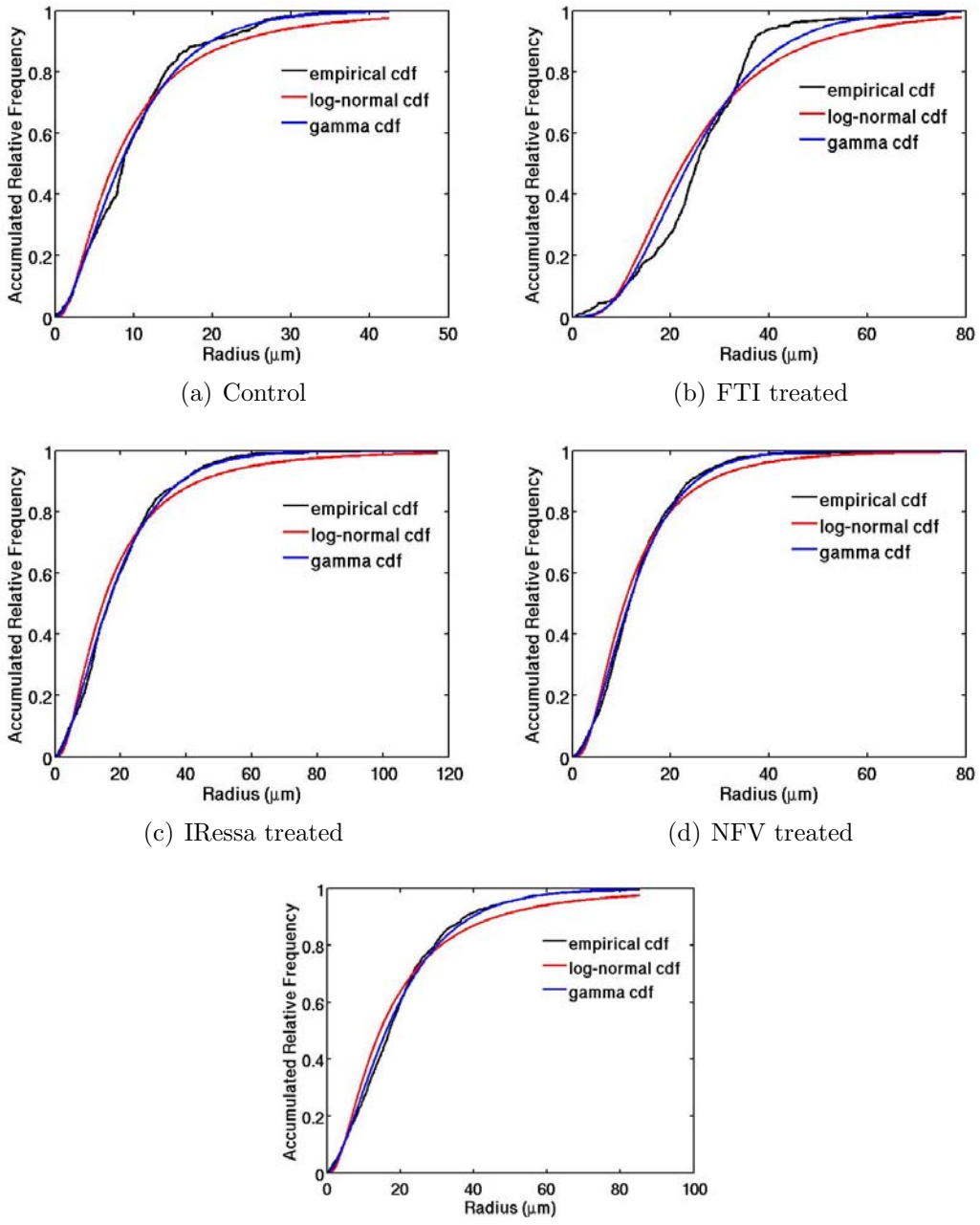

(a) Control (b) FTI treated

(c) IRessa treated (d) NFV treated

(e) PI103 treated

Figure 5.6: Comparison of empirical cdf (black) and log-normal fitting distribution cdf (red) and gamma fitting distribution cdf (blue).

The discrepancies between the fitted cdf and data cdf can be quantified as the sum of squared errors (SSE) at each sampling point. We list the SSE of the best fitting log-normal and gamma distributions in Table 5.3.

	Sample Size	SSE_{logn}	SSE_{gamma}
Control	886	1.4894	0.3510
FTI treated	691	4.7723	2.3878
IRessa treated	2030	2.51	0.2936
NFV treated	3848	5.0204	0.8878
PI103 treated	2361	4.8343	0.7218

Table 5.3: Total SSE of log-normal fitting cdf and gamma fitting cdf compared with the data's empirical cdf.

From Table 5.3, it is clear that the SSE of gamma fitting is considerably smaller than the corresponding SSE of log-normal fitting. However, SSEs cannot be compared directly across different drugs because of the different sizes of the sampling points. A smaller SSE indicates that the cdf generated by the best fitting gamma distribution more closely approximates the data's cdf. This further argues that the gamma distribution better fits the shape of data's distribution.

5.3.2 Statistical Inference

Inferences on the gamma distribution have been researched in the past few decades because of the importance of the gamma model in environmental and biomedical studies. Wei-Kei Shiue and Lee J.Bain proposed a procedure for comparing the arithmetic means of two gamma distributed samples (Shiue *et al.*, 1988). Their approach involves the χ^2 and F distributions.

The χ^2 distribution is defined by normally distributed random variables. Let the random variable S be the sum of squares of k different independent standard normal random variables. Then S would follow χ^2 distribution with k degrees of freedom, indicated as $S \sim \chi^2(k)$. The shape of χ^2 distribution is illustrated in Figure 5.7.

The F distribution is defined by χ^2 distributed random variables. If $S_1 \sim \chi^2(k_1)$

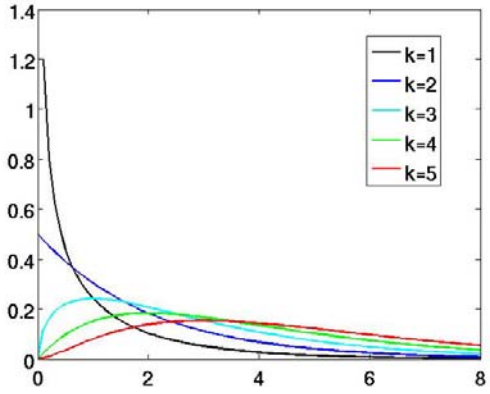

Figure 5.7: Illustration of χ^2 distributions with different degree of freedom

and $S_2 \sim \chi^2(k_2)$ are two independently distributed random variables, then their ratio $R = \frac{S_1/k_1}{S_2/k_2}$ is an F-distributed random variable. The F distribution is a member of the two-parameter family of continuous probability distributions. R can be denoted $R \sim F(k_1, k_2)$, in which case k_1, k_2 are called the degrees of freedom. The shape of F distribution is illustrated in Figure 5.8

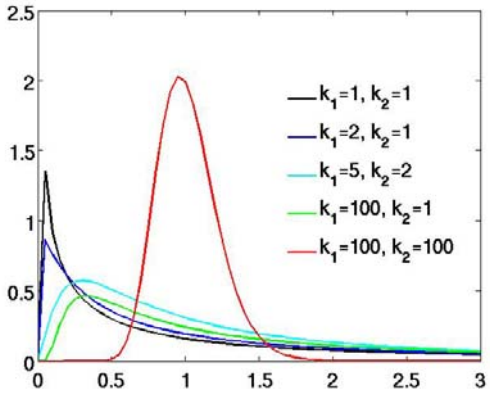

Figure 5.8: Illustration of F distributions with different degree of freedom

Shiue *et al.* (1988) first pointed out that, if $X_1, X_2 \ldots X_n$ denote n observations of a gamma distributed random variable with scale parameter θ, and shape parameter k, then the random variable $\frac{2n\bar{X}}{\theta}$ follows a χ^2 distribution with 2nk degrees of freedom. That is, $\frac{2n\bar{X}}{\theta} \sim \chi^2(2nk)$. Then for two gamma distributed samples S_1, S_2, we know from the definition of the F-distribution that

$$\frac{2n_1\bar{S}_1/2n_1\theta_1k_1}{2n_2\bar{S}_2/2n_2\theta_2k_2} \sim F(2n_1k_1, 2n_2k_2), \tag{5.2}$$

$$\frac{\bar{S}_1/\mu_1}{\bar{S}_2/\mu_2} \sim F(2n_1k_1, 2n_2k_2), \tag{5.3}$$

where $\mu_1 = k_1\theta_1$, $\mu_2 = k_2\theta_2$ are expectations of arithmetic means of sample S_1,S_2 respectively. The approximate α-significance level test of H_0: $\mu_1 = \mu_2$ against H_a: $\mu_2 > \mu_1$ is provided by rejecting H_0 if the inequality (Eq.5.4) holds:

$$\frac{\bar{S}_1}{\bar{S}_2} < F_\beta(2n_1E(k_1), 2n_2E(k_2)), \tag{5.4}$$

where β is the significance level of the test on the F-distribution corresponding the significance level (α) of the test on gamma distribution. $E(k_1)$,$E(k_2)$ are the estimates of the scale parameters of S_1, S_2. We estimated the corresponding β value for each α level based on Monte Carlo simulations for different combinations of n_1,n_2,k_1,k_2 and α; the results are listed in Figure 5.9.

From Figure 5.9, we observe that except for small k_1, k_2 values (<1), the significance level is approximately constant over k_1 and k_2. That is

$$P_3(k_1, c, \beta_1, n_1, n_2) \approx P_3(\infty, \infty, \beta_1, n_1, n_2). \tag{5.5}$$

It was proved in (Shiue *et al.*, 1988), that except for large k_1 when n_2 is very small ($\leqslant 5$) and much less than n_1, the significance level can be approximated by omitting the influence of n_2 as shown in Eq.5.6

$$P_3(\infty, \infty, \beta_1, n_1, n_2) \approx P_1(\infty, \beta_1, n_1). \tag{5.6}$$

This conclusion is convenient since we can use a simpler table to obtain the corresponding β value. We constructed a table of β values for different α and n_1, the results of which are shown in Figure 5.10.

Values of $P_3(\kappa_1, c, \beta, n_1, n_2)$, $c = \kappa_2 / \kappa_1$

			κ_1								κ_1				
n_1	n_2	c	.0	.1	1.0	4..	∞	n_1	n_2	c	.0	.1	1.0	4..	∞
			β=.01								β=.10				
5	5	1	.056	.04	.05	.05	.036	5	5	1	.175	.14	.15	.16	.142
		4	.069	.05	.04	.04	.040			4	.207	.16	.15	.15	.147
		∞	.073	.057	.053	.057	.053			∞	.220	.178	.161	.167	.158
5	10	1	.065	.05	.04	.04	.031	5	10	1	.200	.16	.14	.14	.136
		4	.071	.05	.05	.05	.042			4	.216	.17	.16	.15	.148
		∞	.073	.057	.053	.057	.053			∞	.220	.178	.161	.167	.158
5	20	1	.070	.05	.05	.04	.034	5	20	1	.213	.16	.16	.15	.140
		4	.073	.05	.05	.05	.046			4	.219	.17	.16	.16	.152
		∞	.073	.057	.053	.057	.053			∞	.220	.178	.161	.167	.158
10	5	1	.024	.02	.02	.03	.031	10	5	1	.118	.11	.13	.13	.136
		4	.030	.02	.02	.03	.025			4	.141	.12	.13	.13	.127
		∞	.033	.027	.028	.028	.027			∞	.154	.133	.126	.132	.128
10	10	1	.028	.02	.03	.03	.020	10	10	1	.137	.12	.12	.13	.120
		4	.032	.02	.02	.02	.022			4	.150	.12	.12	.12	.122
		∞	.033	.027	.028	.028	.027			∞	.154	.133	.126	.132	.128
10	20	1	.031	.02	.02	.02	.019	10	20	1	.148	.12	.12	.12	.117
		4	.033	.02	.02	.02	.024			4	.154	.13	.12	.12	.123
		∞	.033	.027	.028	.028	.027			∞	.154	.133	.126	.132	.128
20	5	1	.014	.01	.02	.03	.034	20	5	1	.094	.11	.13	.13	.140
		4	.017	.01	.02	.02	.022			4	.110	.11	.12	.12	.124
		∞	.019	.017	.017	.019	.018			∞	.126	.115	.110	.117	.113
20	10	1	.016	.01	.02	.02	.019	20	10	1	.110	.11	.11	.12	.117
		4	.018	.01	.02	.02	.016			4	.120	.11	.11	.11	.113
		∞	.019	.017	.017	.019	.018			∞	.126	.115	.110	.117	.113
20	20	1	.018	.02	.02	.02	.014	20	20	1	.119	.11	.11	.11	.110
		4	.019	.02	.02	.02	.016			4	.124	.11	.11	.11	.111
		∞	.019	.017	.017	.019	.018			∞	.126	.115	.110	.117	.113

Figure 5.9: β values for different combinations of n_1,n_2,k_1,k_2 and α, reproduced from Shiue *et al.* (1988).

	α						
N	.005	.01	.025	.050	.075	.100	.250
5	.0000	.0000	.0010	.0086	.0234	.0432	.2038
10	.0003	.0015	.0086	.0267	.0486	.0724	.2294
20	.0017	.0046	.0159	.0380	.0619	.0866	.2403
40	.0030	.0070	.0203	.0440	.0685	.0934	.2453
∞	.0050	.0100	.0250	.0500	.0750	.1000	.2500

Figure 5.10: β values for different combinations of n_1 and α, reproduced from Shiue *et al.* (1988).

As our data sample satisfied the approximation assumptions[1], we can use the β value from Figure.5.10 and Eq.5.4 to draw statistical inferences. We compared the means of drug treated vessel radii (S_2) with the control vessel radii (S_1) at 5% significance level with H_0: $\mu_1 = \mu_2$ against H_a: $\mu_2 > \mu_1$. However, the author estimated $E(k)$ based on the approximation formula proposed by Greenwood & Durand (1960) as Eq.5.7

$$\begin{aligned} E(k) &= (0.5000876 + 0.1648852M - 0.0544274M^2)/M, && 0 \leqslant M \leqslant 0.5772, \\ &= \frac{8.898919 + 9.059950M + 0.9775373M^2}{M(17.79728 + 11.968477M + M^2)}, && 0.5772 \leqslant M \leqslant 17, \\ &= 1/M, && M > 17. \end{aligned} \tag{5.7}$$

where $M = ln(\bar{S}/\tilde{S})$ and $\bar{S}$, $\tilde{S}$ denote the arithmetic mean and geometric mean respectively.

In order to check if $E(k)$ estimated by the maximum likelihood methods provided by Matlab® (R2008a) is within the acceptable discrepancy from the $E(k)$ used by the author in producing Figure 5.10, we compared the $E(k)$ estimated by both methods, the results of which are listed in Table 5.4

	M	$E(k)_{auth}$	$E(k)_{mat}$
Ctl	0.2917	1.8646	1.86355
FTI	0.1443	3.6262	3.62341
IRessa	0.2905	1.8720	1.87087
NFV	0.2327	2.3034	2.30179
PI103	0.3084	1.7709	1.76988

Table 5.4: Comparison of estimated k value with the method suggested by Greenwood & Durand (1960) ($E(k)_{auth}$) and the method provided by Matlab® ($E(k)_{mat}$).

From Table.5.4, the values of k estimated by the two methods are close to each other. We used the k value estimated using Matlab® (R2008a) as the basis of the

[1]In reality, the radii at one site on the blood vessel may be conditionally dependent on the radii of its neighbouring sites. However, in order to develop an intuitive statistical analysis framework, we have made the assumption here that the radius values at each site on the blood vessels are independent variables. This assumption of independence also applies to analysis of other geometrical metrics in this Chapter and the 2D vascular map generation discussed in Chapter 7. The characterisation of the conditional dependency between each parameter remains future work as will be described in Chapter 8.

inferences we drew. So n_1 is fixed as the radii sample size of the control vessel, $n_1 = 886$, $E(k_1)$ is estimated by maximum likelihood method, $E(k_1) = 1.86355$ and $\bar{S_1} = 2.0155$ ($2n_1E(k_1) = 3302.2$) and β was determined from Fig 5.10 to be 0.05 at the 5% significance level. We summarize the rest of the test parameters in Table 5.5.

	$E(k_2)$	n_2	$2n_2E(k_2)$	$\bar{S_1}/\bar{S_2}$	F_β	H_0
FTI treated	3.62341	691	5007.6	0.6467	0.9490	Rejected
IRessa treated	1.87087	2030	7595.7	0.7519	0.9524	Rejected
NFV treated	2.30179	3848	17715	0.8545	0.9565	Rejected
PI103 treated	1.76988	2361	8357.4	0.7527	0.9530	Rejected

Table 5.5: Parameters in conducting gamma inferences.

As shown in Table 5.5, for all comparisons between the drug treated vessel radii and the control vessel radii, $\frac{\bar{S_1}}{\bar{S_2}} < F_\beta(2n_1E(k_1), 2n_2E(k_2))$. According to Eq.5.4, H_0 was rejected and H_a was accepted at the 5% significance level. That is to say, the drug treated vessel have, on average, significantly larger radii than the control vessels at the 5% significance level.

Based on Figure 5.2, we wanted to further rank the effects of FTI, IRessa, NFV, and PI103 on the vessel radii. Following a similar principle, we have carried out hypothesis testing on each pair of radius data and concluded that $R_{FTI} > R_{PI103}, R_{IRessa} > R_{NFV} > R_{Ctl}$ at the 5% significance level. That is to say that FTI is significantly more effective at increasing the vessel radii than PI103 and IRessa. PI103 and IRessa are significantly more effective at increasing the vessel radii than NFV (at 5% level).

5.3.3 Conclusion

The sum of squared errors suggests that the gamma distribution better fits the distribution of the vessel radii than log-normal distribution does. This may provide some insight into the angiogenesis process. Since the gamma distribution is the sum distribution of exponential distributions, it is used primarily to model the time elapsed for an upcoming event. Considered in the context of angiogenesis, the growth of blood vessels is affected

by the concentration of various signalling molecules. The waiting time can be modelled as the distance of vessel loci to the source of these signal molecules. Indeed, the vessel radii can be viewed as an indicator of the equilibrium states between pro- and antiangiogenic factors[2].

Our quantitative radius analysis suggests that all vessel normalizing drugs have significant effects in dilating the blood vessel radii. As reviewed by Jain (1988), vessel diameter is a dominant parameter in regulating blood flow. As vessel diameters increases, the blood flow volume also increases within a unit period. Thus dilating the vessel radii can improve the tumour vessel delivery capacity. This in turn ameliorates the tumour tissue's micro-environment and inhibits tumour growth[3].

5.4 Inter-branch Length Analysis

5.4.1 Measurement of Inter-branch Lengths

We calculated the inter-branch lengths on the sample images following the algorithm described in Chapter 4. A comparison of the average inter-branch length among different vessel samples is presented in Figure 5.11

[2]Admittedly, in reality, tumour angiogenesis is a very complicated process. The characterisation of tumour vessel geometries require more sample data to validate and other angiogenesis factors may need to be considered.

[3]The increased blood flow could also simulate tumour growth. The total effect of tumour vessel normalization is still under investigation (McDonald & Baluk, 2002).

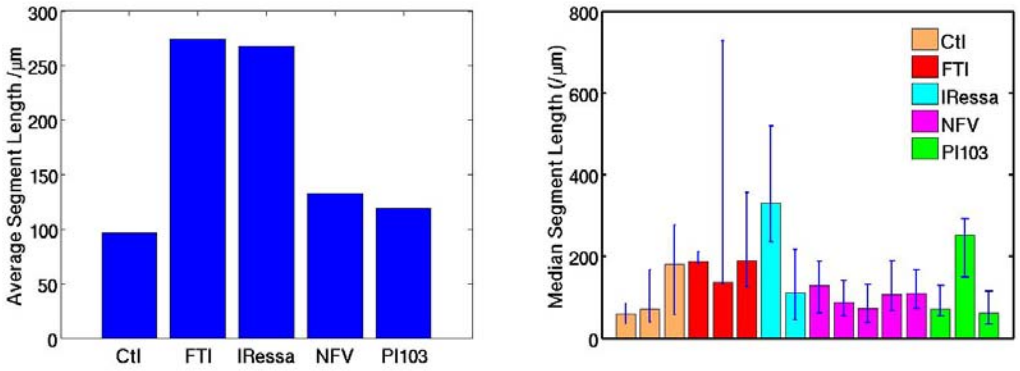

(a) Average of each drug group (b) Average of each image

Figure 5.11: Comparison of average segment length of each vessel structure. In the group average (left), we used the mean value as a measure of average segment length of each drug treated sample; in the image average (right), we used the median value (2nd quartile) as measure of average segment length of each vessel image and used the first and third quartile values as the measure of spread.

We found that the distribution of inter-branch lengths is also skewed (Figure 5.12). So we used the arithmetic mean to describe the average inter-branch length and consider the interquartile distance as a measure of spread. It has been observed that tumour vessels have an average inter-branch length of ca.100μm. FTI and IRessa treated vessels have an average inter-branch length between 250 and 280 μm, considerably longer than the untreated tumour vessels. NFV and PI103 treated vessel average inter-branch lengths lie between 120 and 140 μm, only slightly longer than the untreated vessel inter-branch length. The spread is also seen to be high due to the skewed shape of the data's distribution (Figure 5.12).

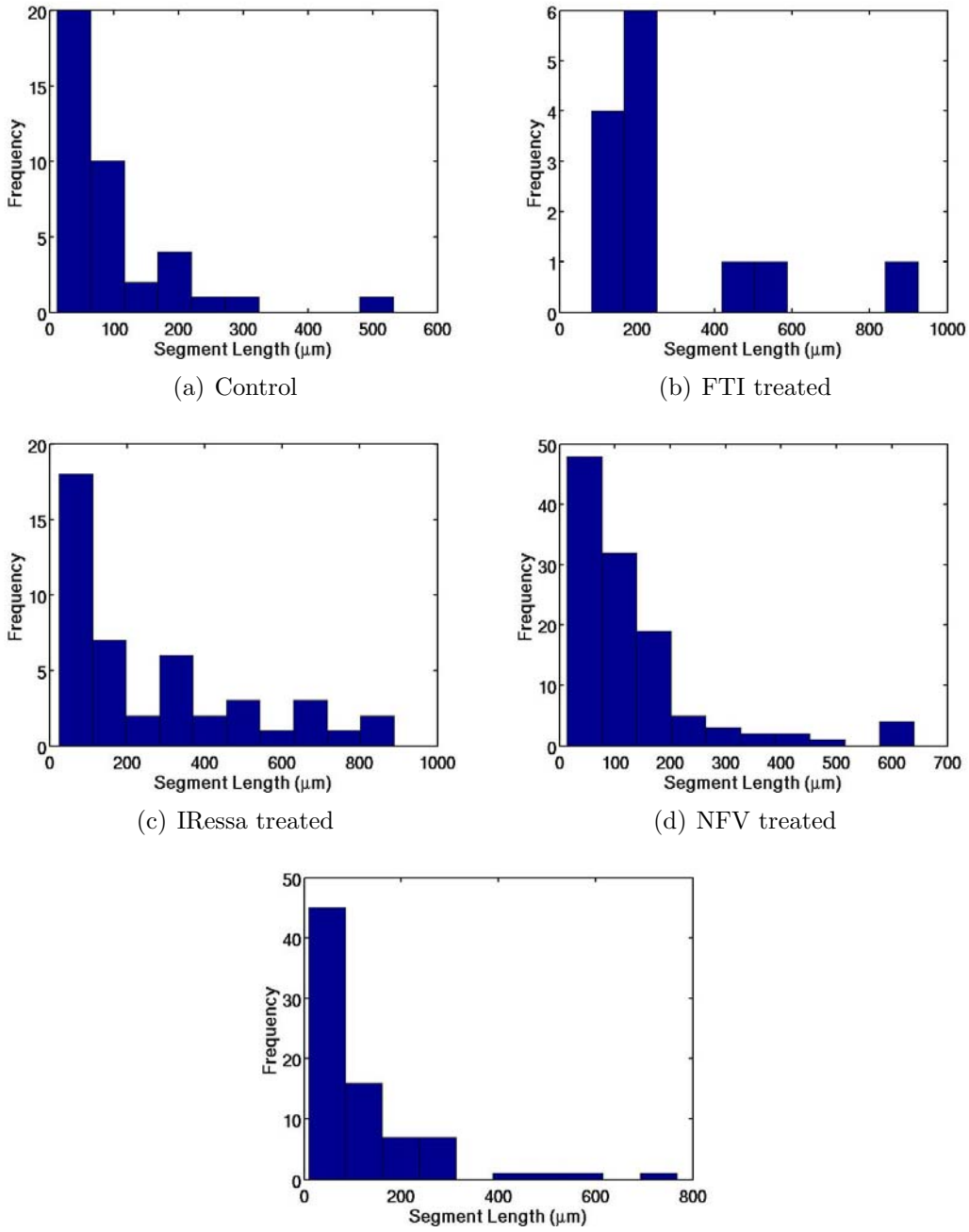

(a) Control

(b) FTI treated

(c) IRessa treated

(d) NFV treated

(e) PI103 treated

Figure 5.12: Histograms of segment lengths in each vessel sample.

5.4.2 Distribution Assumption and Statitical Inference

The histograms in Figure 5.12 resemble the log-normal distribution and many researchers assume the inter-branch lengths are distributed log-normally (Konerding *et al.*, 2001). As before, in order to examine this assumption, we plot the histograms of logarithms of

inter-branch lengths in Figure 5.13

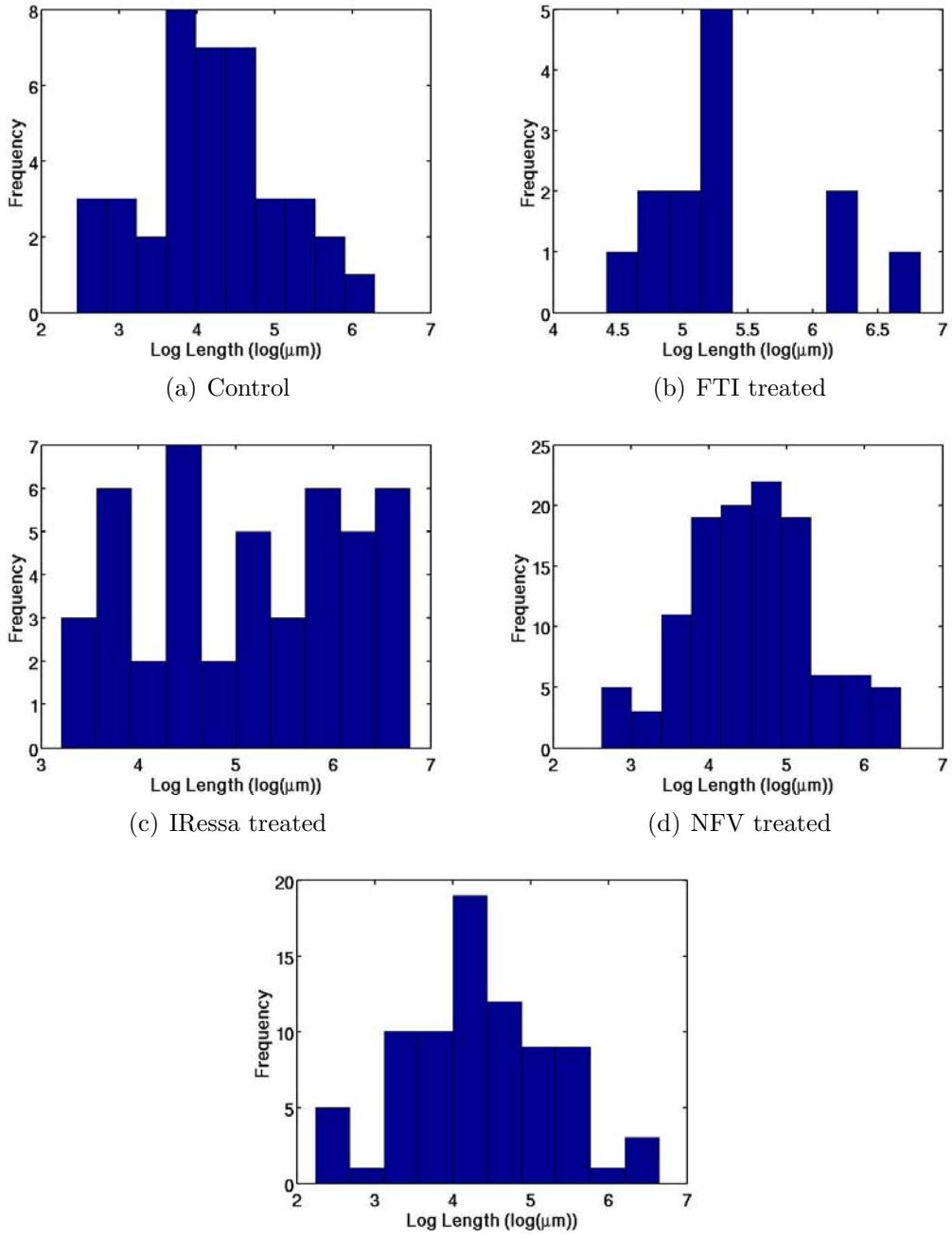

(a) Control

(b) FTI treated

(c) IRessa treated

(d) NFV treated

(e) PI103 treated

Figure 5.13: Histograms of segment length logarithms in each vessel sample.

From the shape of length logarithms' histograms, the distributions are indeed approximately Gaussian. To test the normality assumption quantitatively, we calculated the skewness and kurtosis of the logarithms distribution of each vessel sample and summarize the results in Table 5.6.

	skewness	kurtosis
Control	0.1169	2.6880
FTI treated	0.8710	2.9348
IRessa treated	-0.1277	1.7747
NFV treated	0.1258	2.8494
PI103 treated	0.0255	2.7484

Table 5.6: Skewness and kurtosis of logarithms of vessel segment lengths.

From Table 5.6, the skewness and kurtosis values of each vessel sample are close to those of a normally distributed parameter (skewness = 0, kurtosis = 3). We assume therefore that the logarithms of the vessel segment lengths follow a normal distribution. We plot the average and standard deviation of the inter-branch length logarithms in Figure 5.14.

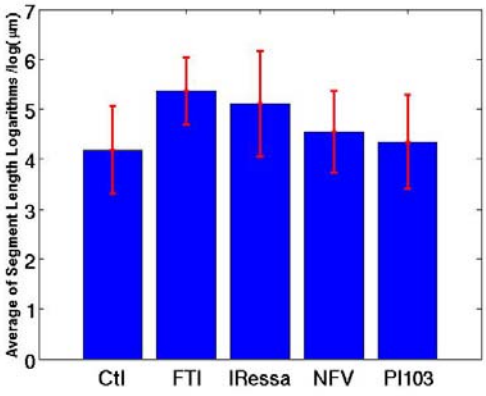

Figure 5.14: Comparison of average inter-branch length logarithms of each vessel structure.

In Figure 5.14, we can see that the high inter-data spread of length measurements is indeed caused by the skewed distribution they follow. After transforming the length data to their logarithms, the spread drops to an acceptable level because the logarithms follow a symmetric distribution. Based on the normal distribution (and equal variance)

assumption, we carried out a t-test to test the hypothesis H_0: treated vessel average segment length logarithm $\leq$ control (untreated) vessel average segment length logarithm. The t-test results are summarized in Table 5.7

	t value	sd	df	p value
FTI treated	4.43	0.8328	50	2.5716e-5
IRessa treated	4.30	0.9802	82	2.3047e-5
NFV treated	2.3757	0.8317	153	0.0094
PI103 treated	0.9070	0.9203	116	0.1831

Table 5.7: Parameters for t-test.

The null hypothesis (H_0) is rejected in FTI, IRessa and NFV treated vessel samples at the 5% significance level[4], which means that these drug-treated vessel samples have significantly longer segments than the control (untreated) vessel samples (p<0.01). However, for the PI103 treated vessel, no significant difference in segment length was observed (p=0.1831).

We further confirmed that $L_{FTI} > L_{NFV}$(p<0.0005), $L_{IRessa} > L_{NFV}$(p<0.0005), However $L_{FTI} > L_{IRessa}$ (p=0.2055) and $L_{NFV} > L_{PI103}$ (p=0.0559) cannot be accepted at 5% level. We may conclude that, based on the vessel samples we analysed, FTI and IRessa are significantly more effective at elongating tumour vessels than NFV and PI103.

5.4.3 Conclusion

FTI, IRessa and NFV are found to have significant effects in elongating the inter-branch vessel lengths at the 5% significance level. The longer inter-branch lengths are evidence of decreased branching frequency. Branching implies a change in blood flow direction, whereby energy loss is inevitable. Energy losses in blood flow are reflected in a reduced flow speed. Slower blood flow implies that the blood volume passing through a blood vessel per unit time is smaller, and so we have lower vessel delivery efficiency. In turn,

[4]Strictly, significance level in log-normal distribution inferences should be converted from the significance level in the transformed normal distribution through Monte-Carlo simulations. However, as we found in last section, when the sample size becomes large the significance level of inferences on original data and transformed data can be treated as equivalent.

by elongating inter branch lengths, these drugs improve the tumour vessel delivery and benefit tumour management.

Although PI103 failed to show a significant effect at the 5% level, it produces similar effects on the inter-branch lengths to the other drugs. The consistency in these drugs' effects on the inter-branch lengths supports the reliability of experimental data and our analytical methods.

5.5 Tortuosity

5.5.1 Definition of Tortuosity

Tortuosity is a parameter that aims to describe how meandering or non-straight a curve is. Though there have been several attempts to quantify tortuosity, no definition is yet widely accepted. Here we present the results for two tortuosity measures on the vessel segments: the first is the arc-chord ratio, which is based on Euclidean geometry; the second is that we developed based on multiple linear regression.

Arc-chord ratio

In the arc-chord ratio, one calculates the ratio between the total length of the curve and the Euclidean distance between its two ends. Intuitively, the more tortuous the curve, the larger will be the arc-chord ratio. Evidently, a straight line has a arc-chord ratio equal to 1, whereas a closed circle has an arc-chord approaches to infinity. However, in order to avoid infinity, we calculate the chord-arc ratio of each vessel segment, using the formulation given in Eq.5.8

$$\tau = \frac{C}{L}, \tag{5.8}$$

where C is the Euclidean distance between two terminals and L denotes the total length of curve. Figure 5.15 shows graphically the definition of chord-arc ratio.

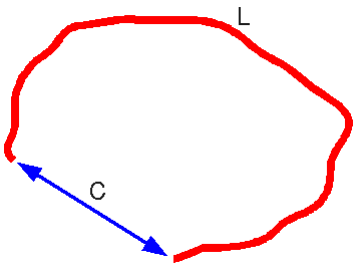

Figure 5.15: Illustration of chord-arc ratio.

We calculated the chord-arc ratio following Eq.5.8 for every skeleton segment and plot the histogram in Figure 5.16.

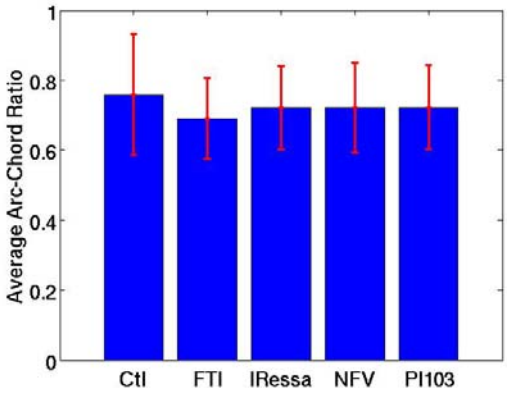

Figure 5.16: Comparisons of chord-arc ratios of each vessel structure.

Figure 5.16 suggests that the chord-arc ratio is not able to differentiate between the drug-treated and untreated vessel samples. There are several explanations for this result. First, the chord-ratio is not directly based on the shape measure, but is implied from length measures. Given the relatively high error level in length measurement (Chapter 4), the ratio calculated by two length measurements can yield errors that accumulate to such a high level that it erodes the differences of tortuosity between treated and untreated vessel samples. Second, we have observed that in each vessel sample, in which there is a substantial number of short segments, giving the same weight to each segment (by simple arithmetic averaging) ignores the importance of longer segments in the overall structure. That is to say, a vasculature with long straight vessels mixing with short curved vessels should be superior to that with short straight vessels mixing with long curved vessels.

However, since the chord-arc ratio is derived from the segment length measure, it is not straightforward to apply length weighting to it.

Statistical Measure

R^2: Linearity Measure

We proposed a statistical shape measure to evaluate vessel tortuosity. For one skeleton segment, the x-coordinates, y-coordinates and z-coordinates generate three datasets X, Y and Z, respectively. To measure the linearity of one skeleton segment, i.e. how straight it is, it is equivalent to assessing whether X, Y and Z have linear correlations. Put mathematically, if several points fall in one straight line, their coordinates X, Y, Z should satisfy the following linear relationship (Eq.5.9):

$$\alpha X + \beta Y + \gamma Z + \delta = 0, \tag{5.9}$$

where α, β, γ and δ are constants. Eq.5.9 could be reformulated in the form of a multiple linear regression problem: (Eq.5.10)

$$Z' = \alpha' X + \beta' Y + \delta' \tag{5.10}$$

notice that α', β' and δ' are new constant parameters that are not necessarily equal to α, β and δ. At each point, Eq.5.10 gives a prediction of Z' based on the linear relationship. The error between observations Z and the predictions Z' are called residuals as defined in Eq.5.11

$$\varepsilon_i = Z_i - Z'_i. \tag{5.11}$$

Because ε_i could be either positive (zero) or negative, the sum of squares (Residual Sum of Squares, SS_{err}) is often used to quantify the distance between observations and predictions. (Eq.5.12)

$$SS_{err} \equiv \sum_i \varepsilon_i^2. \tag{5.12}$$

In fact, the coefficients in Eq.5.10, α', β' and δ', are determined so that the distance between observation and predictions is minimized. (Least Squared Regression, LSR. Eq.5.13)

$$\{\alpha', \beta', \delta'\} = min_{\{\alpha', \beta', \delta'\}} \sum_i \varepsilon_i^2. \tag{5.13}$$

The variance measure, which is proportional to the real variance, of observations (Eq.5.14) is called the total variance (also, the total sum of squares, SS_{total}):

$$SS_{tot} \equiv \sum_i (Z_i - \bar{Z})^2, \tag{5.14}$$

where $\bar{Z}$ is the mean value of Z.

SS_{err} could be viewed as the variance that can not be accounted by the linear model, it is thus called the unexplained variance. Finally, the explained variance, also called the regression sum of squares (SS_{reg}), is obtained by subtracting the unexplained variance from the total variance (Eq.5.15):

$$\begin{aligned} SS_{reg} &= SS_{tot} - SS_{err}, \\ &= \sum_i (Z_i - \bar{Z})^2 - \sum_i (Z_i - Z_i')^2, \\ &= \sum_i (Z_i' - \bar{Z}')^2, \end{aligned} \tag{5.15}$$

where $\bar{Z}'$ is the mean value of predictions Z'. In multiple linear regression R^2 is used to assess the fitness of linear approximation to the underlying datasets. Intuitively, it is defined as the ratio between explained variance and the total variance. (Eq.5.16)

$$\begin{aligned} R^2 &\equiv \frac{SS_{reg}}{SS_{tot}}, \\ &= 1 - \frac{SS_{err}}{SS_{tot}}. \end{aligned} \tag{5.16}$$

To avoid zero SS_{tot}, in each skeleton segment we selected the axis along which the coordinates have the largest variation to be the dependent variable and considered the remaining two axis coordinates as independent variables. We used least squares regression (LSR) to calculate the regression parameters and calculated R^2 as defined in Eq.5.16. We present the R^2s of each blood vessel structure as in Figure 5.17

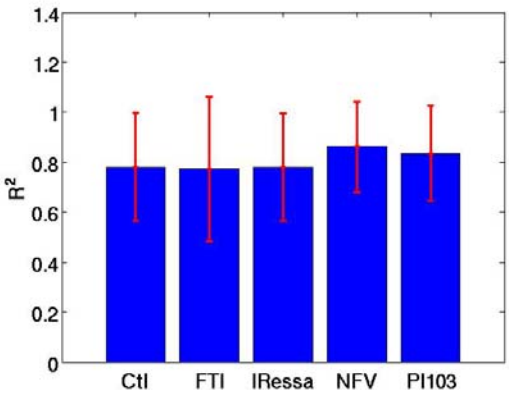

Figure 5.17: Comparisons of R^2 of each vessel structure.

From Figure 5.17, the difference in the R^2 values is unexpected. One reason might be that among the skeleton segments, there are some short curved segments present together with the long straight segments. Evidently, assigning the same weights to each segment ignores their impact on the overall vascular structure. We propose that the length-weighted average should better characterise the overall structures of blood vessels and serve as a more suitable metric to quantify vessel tortuosity. We defined the adjusted R^2 as in Eq.5.17

$$R^2_{adj} \equiv \sum_i \frac{R_i^2 L_i}{\sum_i L_i}, \tag{5.17}$$

where R_i^2 and L_i represent R^2 and length of each skeleton segments. A comparison between the adjusted R^2 values for each vascular structure is presented in Figure 5.18

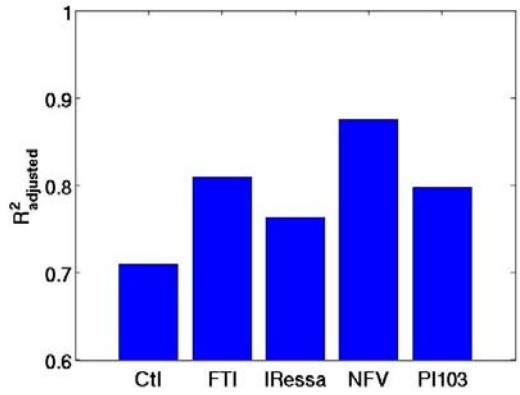

Figure 5.18: Comparisons of adjusted R^2 of each vessel structure.

As can be seen in Figure 5.18, the drug's effect in reducing the vascular tortuosity is quite evident, as the adjusted R^2s are higher than the untreated control vessel. Since R^2 quantifies the linearity relationship of x, y, z coordinates, higher values indicate that the segment is closer to a straight line, which means less tortuous. However, the adjusted R^2 is a global measure, which makes statistical analysis impractical. Borrowing from the concept of the moving average, we carried out multiple regression analyses on every 5 consecutive skeleton voxels. Since these R^2 values are calculated on (roughly) the same length of skeleton segments, their statistics should be comparable between different data sets. The results of these "moving average" R^2 values are presented in Figure 5.19.

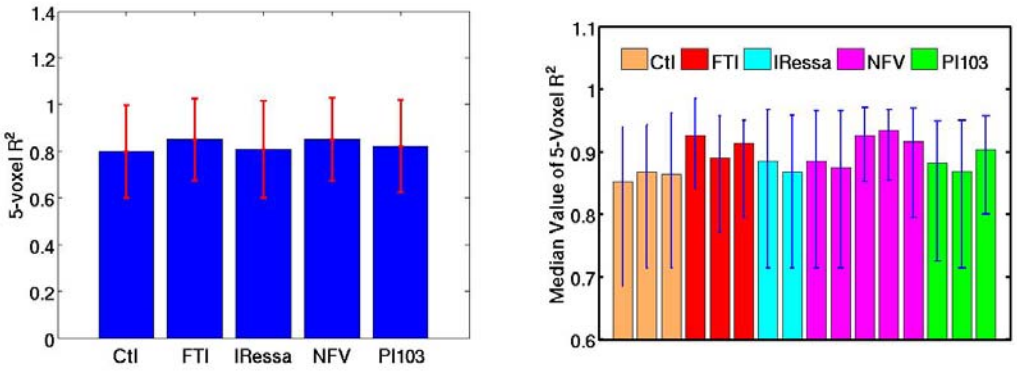

(a) Average of each drug group

(b) Average of each image

Figure 5.19: Comparison of average 5-voxel R^2 of each vessel structure. In the group average (left), we used the mean value as measure of average 5-voxel R^2 of each drug treated sample; in the image average (right), we used the median value (2nd quartile) as measure of average 5-voxel R^2 of each vessel image and used the first and third quartile values as the measure of spread.

To show the distribution shape of 5-voxel R^2 for each sample set, we drew the histograms of 5-voxel R^2 in Figure 5.20.

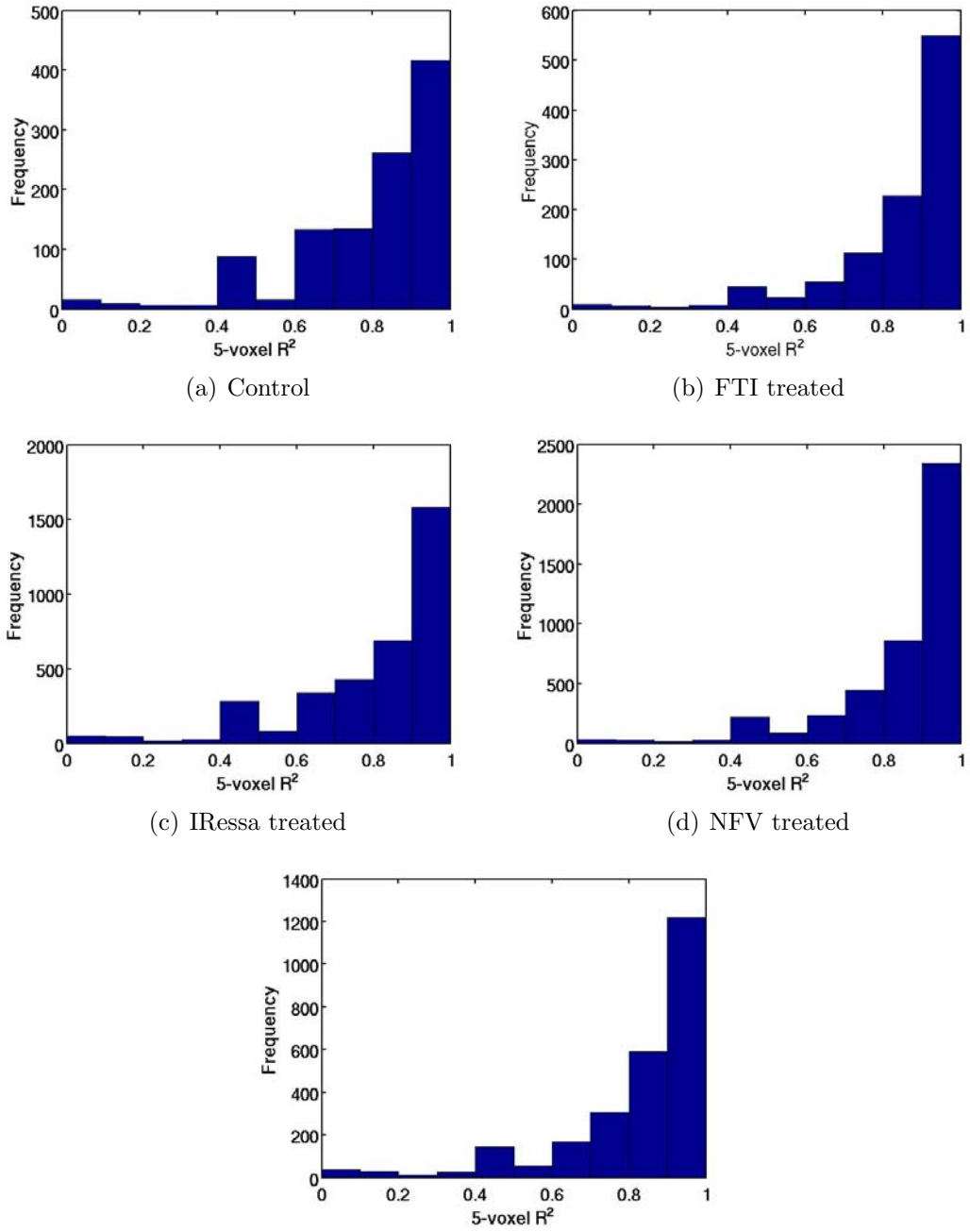

(a) Control

(b) FTI treated

(c) IRessa treated

(d) NFV treated

(e) PI103 treated

Figure 5.20: Histograms of the 5-voxel R^2 distribution in each blood vessel sample.

Tortuosity definition

Since $R^2 \in [0,1]$ and measures the linearity of vessel segment, we set $T = 1 - R^2$. Clearly, T is also in [0,1] but is negatively correlated with R^2, and so we use T to measure a vessel's tortuosity. In fact, based on the definitions of R^2 (Eq.5.16), T is the ratio between the total residual squares and the total data variance. (Eq.5.18)

$$T = 1 - R^2 = \frac{SS_{err}}{SS_{tot}} \tag{5.18}$$

Based on the adjusted R^2 and 5-voxel R^2 we calculated the corresponding T values according to Eq.5.18. We present the average measure and spread measure of T in Figure 5.21.

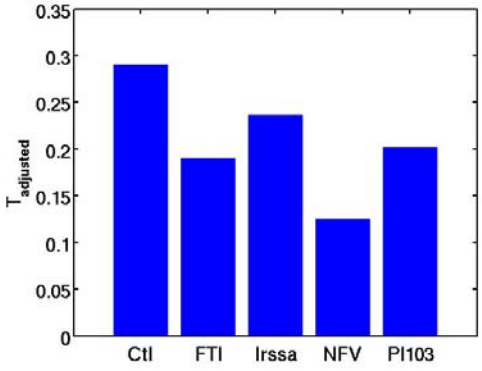

(a) Adjusted T

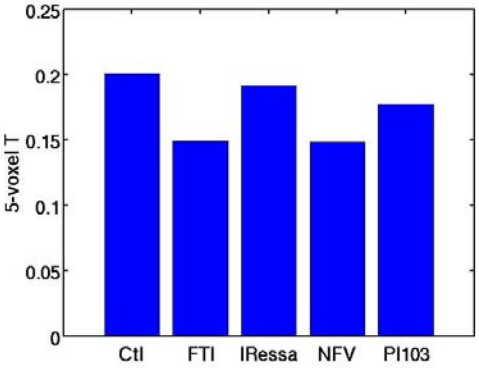

(b) Average of each drug group

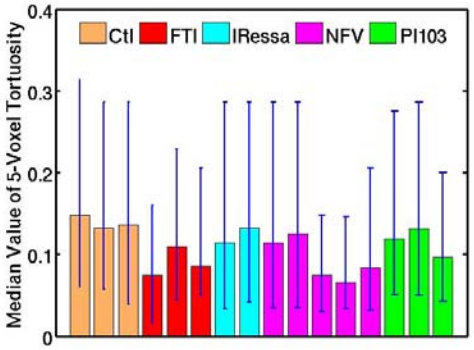

(c) Average of each image

Figure 5.21: Adjusted T and 5-voxel T values

5.5.2 Distribution Assumption and Statistical Inference

We found that the exponential distribution fits closest to the distribution of the data, as shown in Figure 5.22.

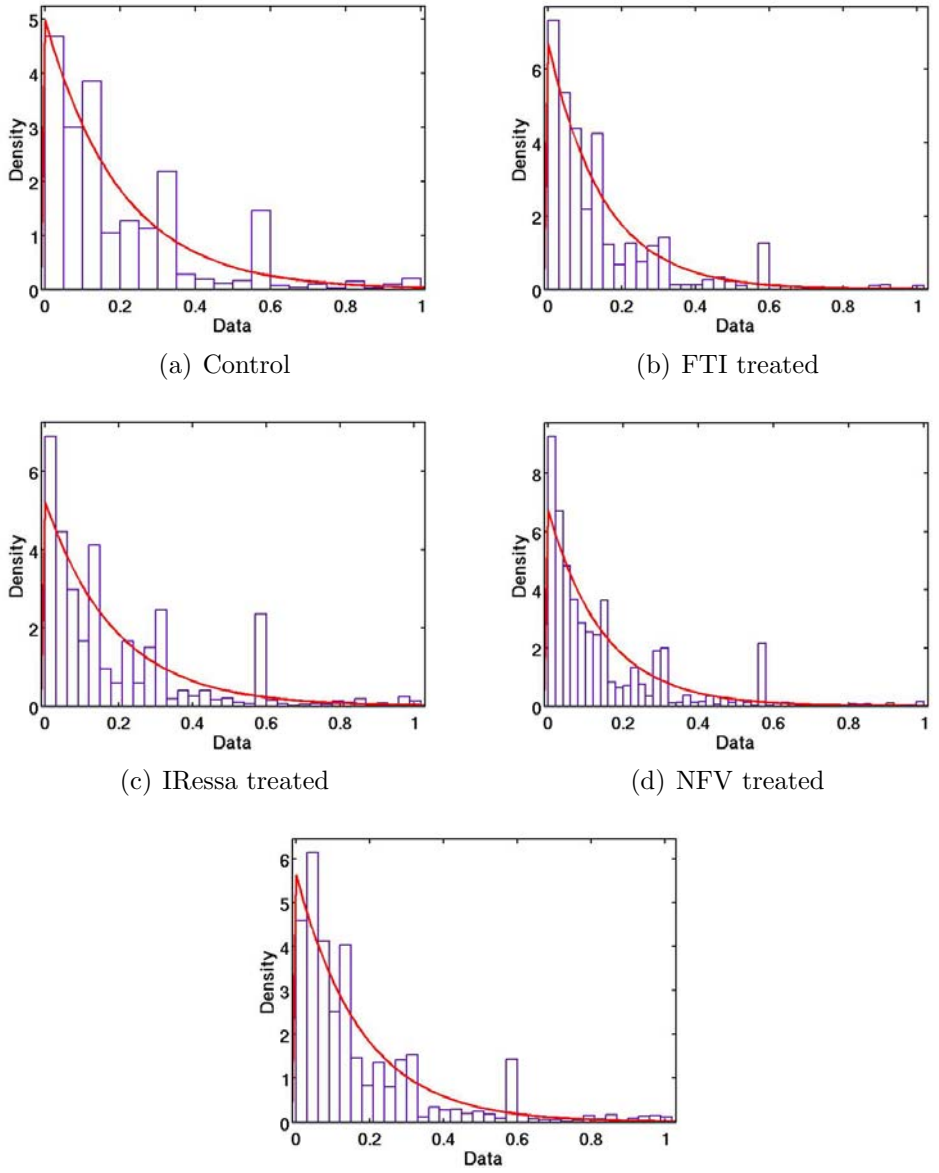

(a) Control (b) FTI treated

(c) IRessa treated (d) NFV treated

(e) PI103 treated

Figure 5.22: Exponetial fitting of T's distribution.

The exponential distribution is another widely used continuous distribution. Its pdf is written as: (Eq.5.19)

$$f(s;\lambda) = \lambda e^{-\lambda s}, \qquad s \geqslant 0. \tag{5.19}$$

where λ is the only parameter required to specify an exponential distribution. It is easily to prove that $E(s) = 1/\lambda$. The exponential distribution is derived based on the Poisson

process. In fact, the time between two Poisson events obeys an exponential distribution. Since the Poisson process has been used widely to model physical, biomedical and environmental processes, it is not surprising that the exponential distribution is also broadly utilized to fit data from biological observations. The shapes of exponential distribution given different λ values are shown in Figure 5.23:

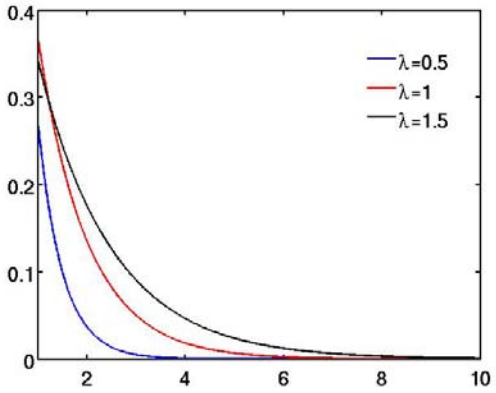

Figure 5.23: Illustration of exponential distributions with different values of λ.

As stated above, the gamma distribution is derived from exponential distribution(s). In fact, the exponential distribution can be viewed as a special case of a gamma distribution in which the shape parameter k equals 1 and the scale parameter θ equals to $1/\lambda$. In this case, it can be proved that Eq.5.1 and Eq.5.19 are equivalent to each other. This means we can use the gamma inference procedure to draw inferences from an exponential distribution. We first compared the mean value of S of drug treated vessels with those of untreated (control) vessels. H_0:$S_{control} = S_{treated}$ and H_a:$S_{control} > S_{treated}$. We fix n_2 as the control sample's size, $n_2 = 1087$. Since k is the same throughout all vessel samples, which equals to 1, $2n_2k = 2174$. λ_2 is estimated by the likelihood maximization method, so $\theta_2 = 1/\lambda_2 = 0.200758$ which is also the arithmetic average of $S_{control}$ ($\bar{S}_2 = 0.200758$). We listed the testing parameter and conclusion in Table 5.8

	n_1	$2n_1E(k_1)$	$\bar{S}_1/\bar{S}_2$	F_β	H_0
FTI treated	1038	2076	0.7425	0.9311	Rejected
IRessa treated	3533	7066	0.9544	0.9450	-
NFV treated	4292	8584	0.7388	0.9462	Rejected
PI103 treated	2585	5170	0.8807	0.9427	Rejected

Table 5.8: Inference parameters for exponential distribution

From Table 5.8 we conclude that all the drugs we have considered to date, with the exception of IRessa(p=0.09) have a significant effect in reducing S at the 5% level. Based on Figure 5.21(a), we wanted to test if $S_{FTI}, S_{NFV} < S_{PI103} < S_{IRessa}$. We have conducted pairwise hypothesis tests on the tortuosity data and concluded that S_{FTI} and S_{NFV} are significantly smaller than S_{PI103} which is further significantly smaller than S_{IRessa} at 5% significance level. To state this more straightforwardly, FTI and NFV are significantly more effective at reducing tumour blood vessel tortuosity than PI103. PI103 is further significantly more effective at reducing tumour blood vessel tortuosity than IRessa (at 5% level).

5.5.3 Conclusion

FTI, NFV and PI103 are found to have significant effects in reducing tumour vessel tortuosity at the 5% level. The lower tortuosity the vessel segment has, the less the degree of change in the blood flow direction during its passage through the vessel segment. As stated above, a change in the direction of blood flow will lead to a slowing of the blood flow speed. Thus by reducing tumour vessel tortuosity, these drugs improved the tumour vessel delivery.

Although IRessa didn't show significant effects in reducing tumour vessel tortuosity at 5% level, it presents the potential of reducing in tumour vessel tortuosity. The consistency in the results of all the tested drugs with respect to vessel tortuosity further supports the reliability of experimental data and our analytical methods.

5.6 Branch Angles

5.6.1 Measurement of Branch Angles

We examined the branch angles in each vessel sample. In most cases (including the vessel samples we are evaluating) the vascular structure has the form of a binary tree. This means that at each branch point, one main vessel (parent) branches into two sub-trees (children) (Figure 5.24):

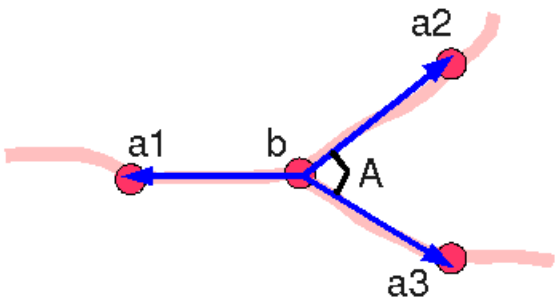

Figure 5.24: Illustration of the branching angle calculation.

At a branch point, nearby blood vessels generate three angles. We denote the smallest angle A as the branching angle and the vessels generating this angle as child vessel segments. (Figure 5.24, $\vec{ba_2}$,$\vec{ba_3}$). In our implementation, we denote by a_1, a_2, a_3 the skeleton voxels which are 5 voxels away from the branch point voxel. Then we use three vectors $\vec{ba_1}$, $\vec{ba_2}$ and $\vec{ba_3}$ to approximate the local direction of each skeleton segment. The branch angle is then determined by Eq.5.20

$$A = min\{acos(\frac{\vec{ba_1} \cdot \vec{ba_2}}{\|\vec{ba_1}\|\|\vec{ba_2}\|}), acos(\frac{\vec{ba_1} \cdot \vec{ba_3}}{\|\vec{ba_1}\|\|\vec{ba_3}\|}), acos(\frac{\vec{ba_2} \cdot \vec{ba_3}}{\|\vec{ba_2}\|\|\vec{ba_3}\|})\}, \tag{5.20}$$

where $\cdot$ denotes the vector inner product, $\|\cdot\|$ denotes the vector norm and $acos$ represents the inverse trigonometric cosine function. The average branching angles and their standard deviations are summarized in Figure 5.25

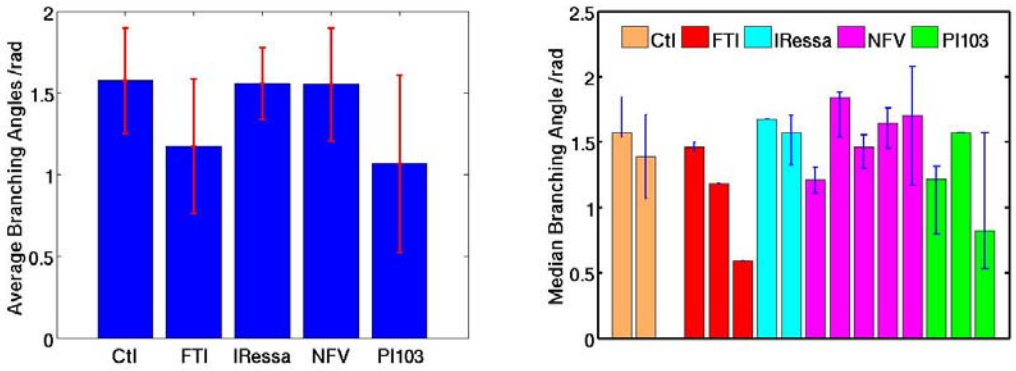

(a) Average of each drug group

(b) Average of each image

Figure 5.25: Comparison of average branch angles of each vessel structure. In the group average (left), we used the mean value as measure of average branch angles of each drug treated sample; in the image average (right), we used the median value (2nd quartile) as measure of average branch angles of each vessel image and used the first and third quartile values as the measure of spread.

To appreciate the distribution, we have plotted the histograms of branch angles in each vessel sample in Figure 5.26

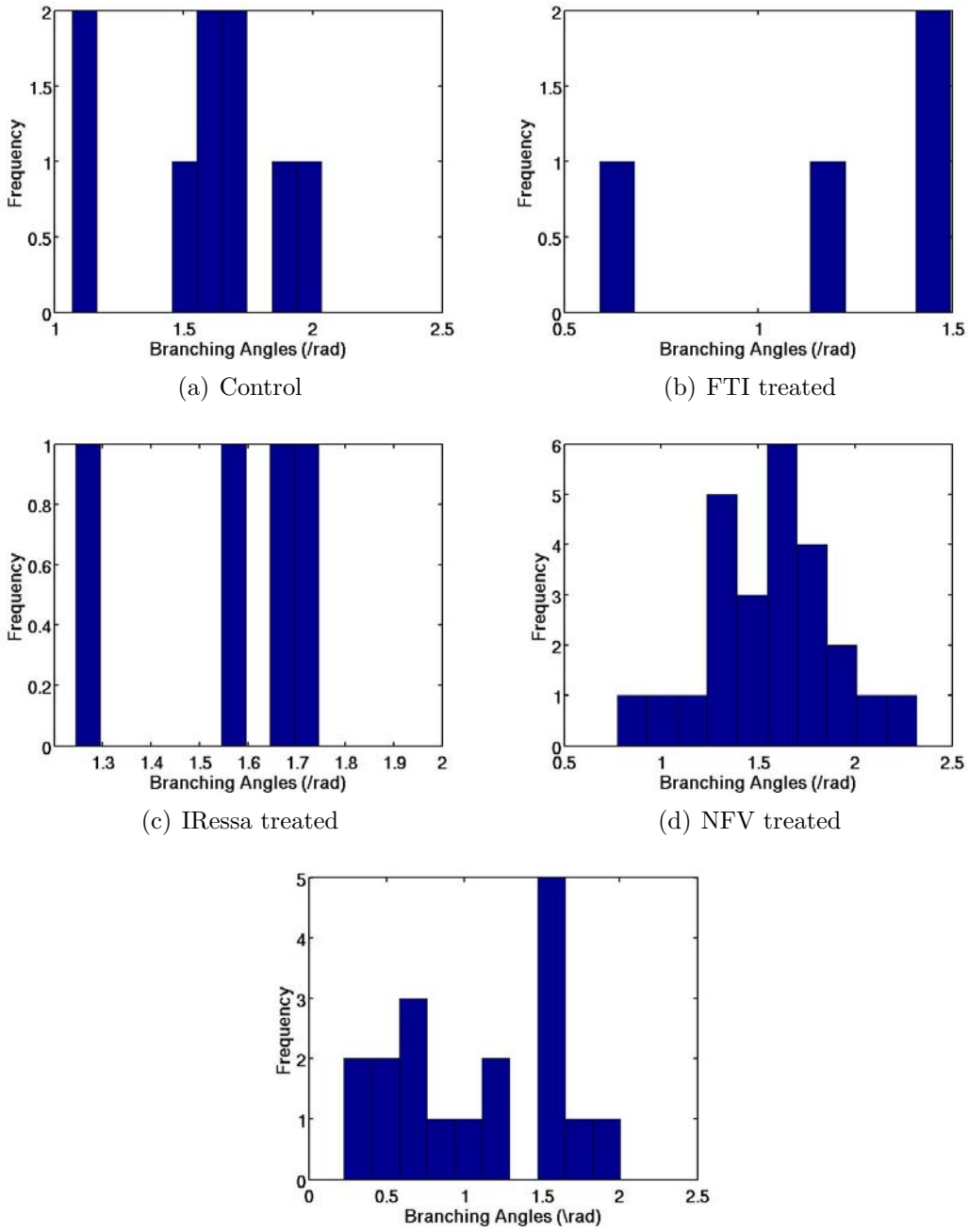

(a) Control (b) FTI treated

(c) IRessa treated (d) NFV treated

(e) PI103 treated

Figure 5.26: Histograms of branching angles.

5.6.2 Distribution Assumption and Statistical Inference

For the control sample, FTI treated sample and IRessa treated sample the distribution of branch angles is difficult to characterize due to small sample size. For samples of larger size, such as the NFV treated sample and PI103 treated sample, the distribution

of branch angles is approximately Gaussian. We list the skewness and kurtosis of each sample distribution in Table 5.9 and propose the branch angles can be assumed normally distributed.

	skewness	kurtosis
Control	-0.4183	2.2324
FTI treated	-0.8166	2.0197
Iressa treated	-0.8129	2.0605
NFV treated	-0.0916	2.9360
PI103 treated	-0.0221	1.7148

Table 5.9: Skewness and kurtosis of branch angles

Assuming normal distribution and equal variance, we carried out single tail t-tests to compare the average branch angle in drug treated vessels and in untreated (control) vessel samples; the t-tail results are listed in Table 5.10

	t-value	sd	df	p value
FTI treated	-1.9157	0.3496	11	0.0409
IRessa treated	-0.0926	0.2992	11	0.4640
NFV treated	-0.1772	0.3409	32	0.4302
PI103 treated	-2.5731	0.4842	25	0.0082

Table 5.10: Parameters for t-test

The t-test results show that FTI and PI103 have significant effect in reducing the branch angles (at the 5% level), whereas IRessa and NFV do not have a significant effect in reducing the branch angles.

5.6.3 Conclusion

FTI and PI103 are found to be effective in reducing the branch angles at the 5% significance level. When a branching event occurs in blood flow, a smaller branch angle implies a smaller change of flow direction. Since greater change of flow directions will cause greater energy loss, which is reflected in a greater slowing of the flow speed, by reducing branch angles, vessel delivery efficiency is improved.

As with inter-branch lengths and tortuosity, although IRessa and NFV fail to show

effectiveness in reducing branch angles at the 5% level, tumour vessels treated by these two drugs reveal a trend of reduced branch angles. This consistency in branch angle effects further supports the reliability of biological experiments and our analytical methods.

5.7 Summary

To summarize the results we report in this Chapter, we list below the effects of FTI, IRessa, NFV and PI103 with respect to normalizing vascular structure (increasing vessel average radius, segment lengths and reducing vessel turtuosity and branch angles) in Figure 5.27:

	Radius	Length	Tortuosity	Branch Angle
FTI	+	+	+	+
IRessa	+	+		
NFV	+	+	+	
PI103	+		+	+

Figure 5.27: Summary of drug effects in normalizing vascular structure. Effects are shown at 5% significance level. Radii, inter branch lengths, tortuosity and branch angles were measured in a fully automated manner based on vessel segments and skeletons.

We believe these metrics characterise geometries of vascular networks and have relationship with the hydrodynamics of the blood flow, which further relates to vessel delivery. Thus, quantification of these metrics can serve as indicative parameters of vessel functionality. Explanation of the different responses of tumour vasculature to FTI, IRessa, NFV and PI103, however, requires further understanding of the EGFR-RAS-PI3K-AKT pathway.

Chapter 6

Spatio-temporal Modelling

6.1 Introduction

6.1.1 Dynamic PET and Time Activity Curve

Depending on the acquisition protocol, a PET image can be acquired either in static or in dynamic mode. In static PET, data are collected over a fixed length of time, typically 20 minutes for FDG-PET. The reconstructed image represents the integrated PET signal value during the acquisition period (Figure 6.1). Static PET shows the *in vivo* distribution of tracer, from which the physiological status in the scanned tissue can be deduced. In dynamic PET, however, data are collected from a sequence of dynamic time frames[1]. Dynamic PET provides information about how the PET signal, e.g. the concentration of tracer in the scanned tissue, changes through time.

The standardization of the PET signal to tracer concentration can be achieved either through semi quantitative assays or from reference regions of interest (ROIs). Other ways to quantify the PET signal include percent injected dose per gram of tissue (%ID/g tissue) and SUV (the standardized uptake value) which take the tissue density, injected tracer dose and subject weight (surface area) into consideration. The curve which represents the signal (or percent injected dose per gram of tissue or SUV) versus time in an ROI, a so called tissue Time Activity Curve (TAC), presents the dynamic change of radioactivity

[1]The duration of dynamic time frames varies in different scans, one example dynamic time frame sequence may be 6 frames of 15 seconds each, 3 frames of 60 seconds each, 5 frames of 300 seconds each and 6 frames of 900 seconds each.

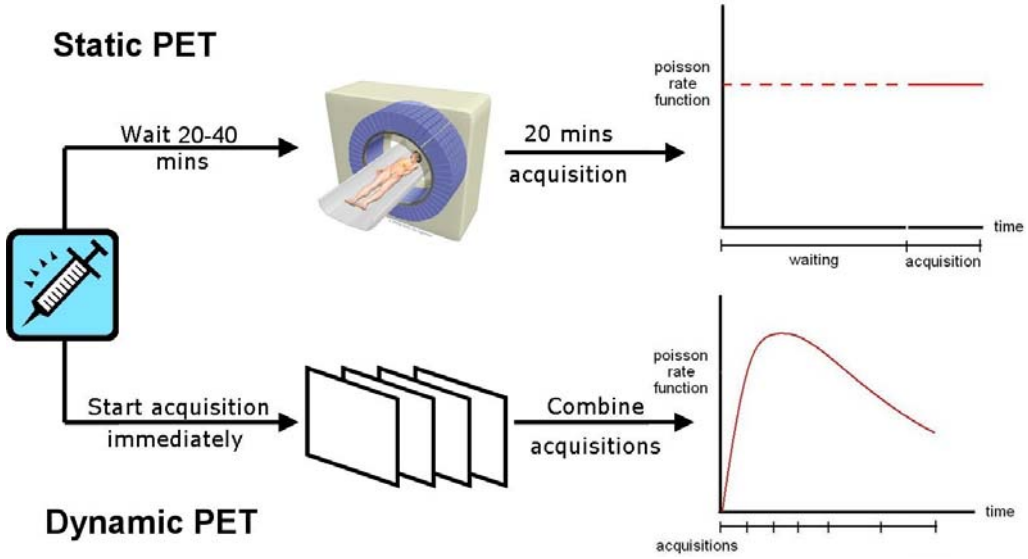

Figure 6.1: Comparison between static and dynamic PET acquisition. Image credit: Andy McLennan, with permission.

(tracer concentration) in that region (Figure 6.2).

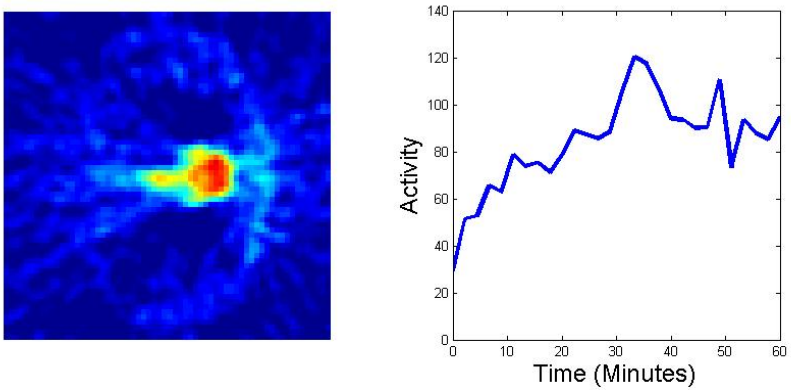

Figure 6.2: The clinical dynamic PET data was acquired from SMI in Oxford, UK. The data was acquired as part of a FDG radiotracer clinical trial to assess the effects of including (or excluding) a course of chemotherapy together with pre-op short-course radiotherapy. The image shown right is for a slice through the patient, representing detection events which occurred between 30 and 33 minutes (of a 60 minute scan). The time activity curve (TAC, shown left) is measured from the centre of the hot region.

In our research we have focused on [^{18}F] Fmiso ([18-F]fluoromisonidazole) (Figure 6.3), a PET tracer that is used increasingly, particularly pre-clinically, to detect hypoxia which is a commonly feature of solid tumours. In such tissues, the cancerous cells proliferate more rapidly than the vasculature, and the oxygen concentration is substantially lower than the normal level. Fmiso is a fluorinated misonidazole analogue which can undergo

an oxygen-reversible single electron reduction in hypoxic environments, forming reactive oxygen radicals that subsequently bind covalently to cellular macromolecules (e.g. DNA and proteins). Thus, the higher the concentration of Fmiso, the lower the oxygen concentration and the more likely the tumour is to be malignant (Koh *et al.*, 1992).

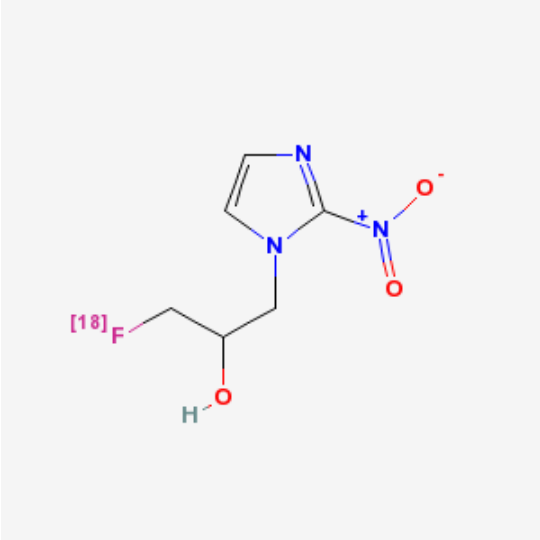

Figure 6.3: Molecular structure of Fmiso, from NIH's MICAD database.

Since Fmiso-PET images regions of hypoxia, which are frequently observed in cancer, it has been widely used in clinics to detect cancer or to evaluate the effects of chemo- and radio-therapies. Several mathematical models, e.g. distributive models (Luxon & Forker, 1982) and compartment models (Gunn *et al.*, 2001), are utilized to extract the tracer's pharmacokinetic parameters from the tissue time activity curves (TAC), which represent the temporally-varying signal at a given location. These kinetics provide information about the enzymatic activities of the cells which can be used to differentiate cancerous cells from normal cells.

6.1.2 Compartment Models

Compartment models are the most commonly used model to describe a tracer's distribution process *in vivo* and to parameterize the TAC in order to quantitatively evaluate the physiological status of the scanned tissue. Compartment models classify the tracer

in vivo into different pools (compartments) according to their biochemical states. The underlying metabolic process or biological transport process of tracer can be modelled by the inter-compartment mass exchange processes. In this way, compartment models can be used to relate the macro signal (TAC which is the temporal evolution of tracer's distribution) to the fundamental biological processes (Figure 6.4).

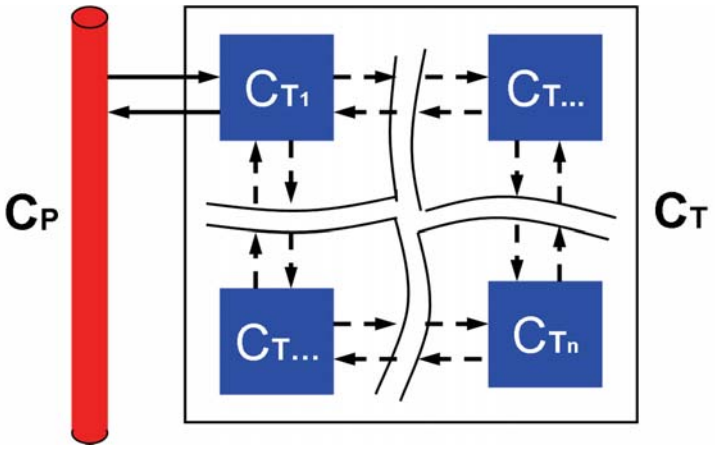

Figure 6.4: Generalized tissue compartment model, reproduced from Gunn *et al.* (2001).

Such a compartment model leads to a set of coupled ordinary differential equations (ODEs) of the following forms:

$$\dot{\mathbf{x}}(t) = A\mathbf{x}(t) + B\mathbf{u}(t) \tag{6.1}$$

$$\mathbf{y}(t) = C\mathbf{x}(t) + D\mathbf{u}(t) \tag{6.2}$$

$$\mathbf{x}(0) = \mathbf{x}_0, \tag{6.3}$$

where $\mathbf{x}(t)$ is a p-vector of state variables, $\mathbf{y}(t)$ is a q-vector of observations, $\mathbf{u}(t)$ is an r-vector of input functions, $\mathbf{A}$ is the $(p \times p)$ state transition matrix, $\mathbf{B}$ is the $(p \times r)$ input matrix, $\mathbf{C}$ is the $(q \times p)$ observation matrix, $\mathbf{D}$ is the $(q \times r)$ feedthrough matrix, and $\mathbf{x}_0$ is a p-vector representing the initial conditions. The state transition matrix $\mathbf{A}$ takes the form of a diagonally dominant matrix with non-positive diagonal elements and non-negative off diagonal elements. In PET, $\mathbf{A}$ is made up of simple combinations of the rate constants denoting the transfer of material between compartments; $\mathbf{B}$ is typically

just the delivery of the tracer to the tissue; **C** is a vector of 1's, which implies that the observation is the sum of all the compartments; and **D** contains the blood volume fraction, V_B. The input, $\mathbf{u}(t)$, contains the plasma parent and whole blood time courses, and the observation (or output), $\mathbf{y}(t)$, corresponds to the tomographic PET signal. The equations of Eq.6.1-6.3 can easily be solved, for example using the Laplace transform, and the concentration of each compartment can be expressed as convolutions with the concentration in related compartments [2].

Inter-compartment mass exchange rates are essential to derive physiological conclusions from TAC analysis. By mapping the key rates of different spatial regions in tissue, one can plot a parametric map such as Figure 6.5. A parametric map is a rather simple way to view the spatial variance of a PET signal.

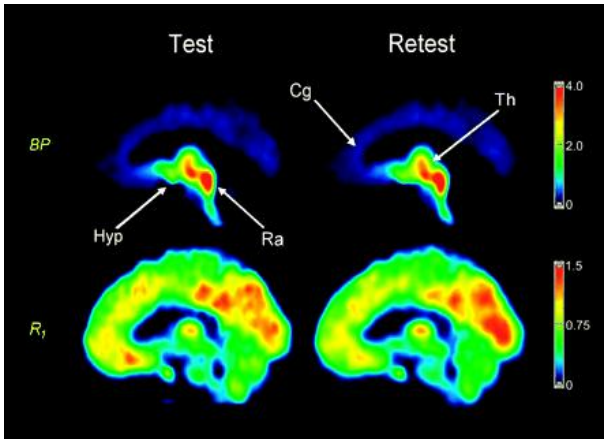

Figure 6.5: Test (left column) and retest (right column) parametric images of BP (binding potential, top row) and R1 (relative tracer delivery, bottom row) of a representative subject. Th = thalamus; Ra = raphe; Hyp = hypothalamus; Cg = cingulate gyrus. Retrieved from Kim *et al.* (2006) without permission

An image set of a dynamic PET scan is actually a 4D spatio-temporal matrix I, each slice 3D PET image provides spatial information which corresponds to $\frac{\partial I}{\partial s}$ (where s denotes space); the time activity curve actually extracts the temporal information corresponding to $\frac{\partial I}{\partial t}$ (where t denotes time). For temporal information, compartment models have been developed to explain the temporal variances based on biochemical mechanisms.

[2] Ultimately, they are related to the plasma input function $\mathbf{u}(t)$, which can be either directly measured from blood sampling or indirectly estimated from reference tissues.

For spatial information, to our knowledge, no modelling techniques has been developed to correlate the spatial variation with biochemical mechanisms. Furthermore, we think it may be beneficial to consider both temporal and spatial information simultaneously (i.e. $\frac{\partial^2 I}{\partial t \partial s}$). The parametric map is an tool to intuitively illustrate the spatio-temporal information though, it doesn't build a quantitative relationship between the spatio-temporal variances of PET signals with the underlying biochemical processes. In comparison, our work aims to quantitatively correlate the spatio-temporal variances of PET signals with the spatial information (e.g. vascular geometry) and temporal information (e.g. tracer pharmacokinetics) of the underlying biological system. Our model uses the idea of compartment models to study the mass exchange between tracers in different states (or locations). However, by considering spatial variations, our model leads to a series of partial differential equations (PDEs), which is a major difference from conventional compartment modelling. Although our approach described in this Chapter is only conceptual, we believe it could be developed in the future as a tool to extract both spatial (i.e. micro vascular geometry) and temporal (i.e. tracer pharmacokinetics) information of the scanned organism from clinical PET images..

6.1.3 Fmiso Modelling in Literature

Thorwarth et al, 2005

Thorwarth analysed dynamic [^{18}F]-Fmiso PET patient data and developed a 2-tissue compartment model to quantify hypoxia in human head-and-neck tumours (Figure 6.6):

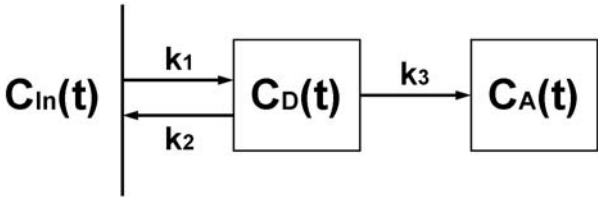

Figure 6.6: Thorwarth's compartment model consisting of a diffusive and an accumulative compartment. The input function $C_{In}(t)$ comprises the tracer concentration in the blood and in the interstitial space close to the vessels, reproduced from Thorwarth *et al.* (2005).

Thorwarth clustered Fmiso molecules according to their dynamic states; that is, a compartment that corresponds to plasma in which the tracer flows (perfusive); a compartment which represents tracer that can move freely in space (diffusive); and a compartment which represents tracer that is trapped inside the cells (accumulative). k_1, k_2 and k_3 are the inter-compartment mass exchange rates. With the compartment model shown in Figure 6.6, the following differential equations may be straightforwardly derived:

$$\frac{d}{dt}C_D(t) = k_1 C_{In}(t) - (k_2 + k_3)C_D(t), \tag{6.4}$$

$$\frac{d}{dt}C_A(t) = k_3 C_D(t), \tag{6.5}$$

where C_D(t) and C_A(t) are the basis functions for the diffusive and the accumulative compartments respectively. These equations may be solved to give:

$$\begin{aligned} C_D(t) &= e^{-(k_2+k_3)t} \otimes k_1 C_{In}(t) \\ &= k_1 \int_0^t e^{-(k_2+k_3)(t-\tau)} C_{In}(\tau) d\tau \end{aligned} \tag{6.6}$$

and

$$\begin{aligned} C_A(t) &= k_3 \otimes C_D(t), \\ &= \frac{k_1 k_3}{k_2 + k_3} \int_0^t (1 - e^{-(k_2+k_3)(t-\tau)}) C_{In}(\tau) d\tau, \end{aligned} \tag{6.7}$$

where the k_i (i=1,2,3) are the respective rate constants and $\otimes$ denotes convolution. Thorwarth expressed the total measured PET signal S(t) using a linear combination of the basis functions (Eq.6.6 and 6.7) and the input function $C_{In}(t)$:

$$\begin{aligned} S(t) &= \omega_0 C_{In}(t) + \omega_D C_D(t) + \omega_A C_A(t), \\ &= \omega_0 C_{In}(t) + \omega_D k_1 \int_0^t e^{-(k_2+k_3)(t-\tau)} C_{In}(\tau) d\tau, \\ &\quad + \omega_A \frac{k_1 k_3}{k_2 + k_3} \int_0^t (1 - e^{-(k_2+k_3)(t-\tau)}) C_{In}(\tau) d\tau. \end{aligned} \tag{6.8}$$

Here ω_D and ω_A are the relative weights of the compartments. Thorwarth proposed that they correspond to the relative contribution of each compartment to the total signal formation process. Thorwarth further pointed out that the weighted parameters correspond, if properly normalized, to the volume fractions that are occupied by these compartments. For the sake of clarity, Thorwarth defined:

$$\begin{aligned} \tilde{\omega_D} &= \omega_D k_1, \\ \tilde{k_3} &= k_2 + k_3, \\ \tilde{\omega_A} &= \omega_A k_1 k_3 / \tilde{k_3}. \end{aligned}$$

The final equation for the PET signal then reads:

$$S(t) = \omega_0 C_{In}(t) + \tilde{\omega_D} \int_0^t e^{-\tilde{k_3}(1-\tau)} C_{In}(\tau) d\tau + \tilde{\omega_A} \int_0^t (1 - e^{-\tilde{k_3}(t-\tau)}) C_{In}(\tau) d\tau. \tag{6.9}$$

This model has been fitted to different time activity curves observed in head and neck cancers of different stages. It is found that this 2-tissue compartment model is capable of reproducing the very different shapes of TACs of different cancer cases (Figure 6.7).

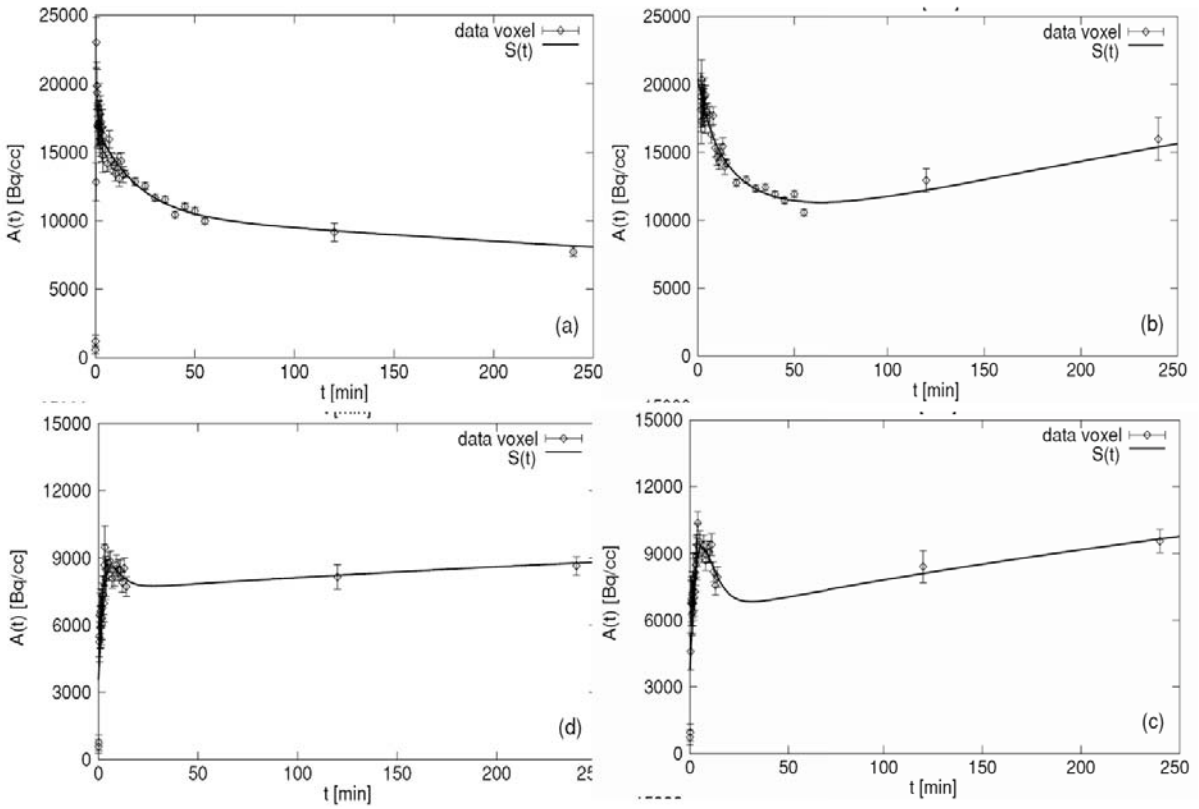

Figure 6.7: Fits of Eq.6.9 to different characteristic time-activity data curves corresponding to tumour areas with increasingly deficient vasculature. (a) Well perfused tumour area. (b) Tissue area with diffusion limited hypoxia. (c) Diffusion limited and structural hypoxia. (d) Hypoxic/necrotic area. Retrieved from Thorwarth *et al.* (2005), without permission.

Thorwarth also studied the $(\omega_0,\tilde{\omega_A k_3})$ scatter plot. Thorwarth compared the $(\omega_0,\tilde{\omega_A k_3})$ scatter plot of two patients. In patient 1, a large fraction of the tumour volume has relatively high levels of perfusion together with rather small concentration of hypoxia. In contrast, patient 2 exhibits very low perfusion values for the whole tumour, and also a high degree of hypoxia (Figure 6.8). Thorwarth pointed out that well-perfused tumour areas usually display larger ω_0 and smaller $\omega_A k_3$ values whereas hypoxic tumour area often has smaller ω_0 and larger $\omega_A k_3$ values extracted from the corresponding TACs.

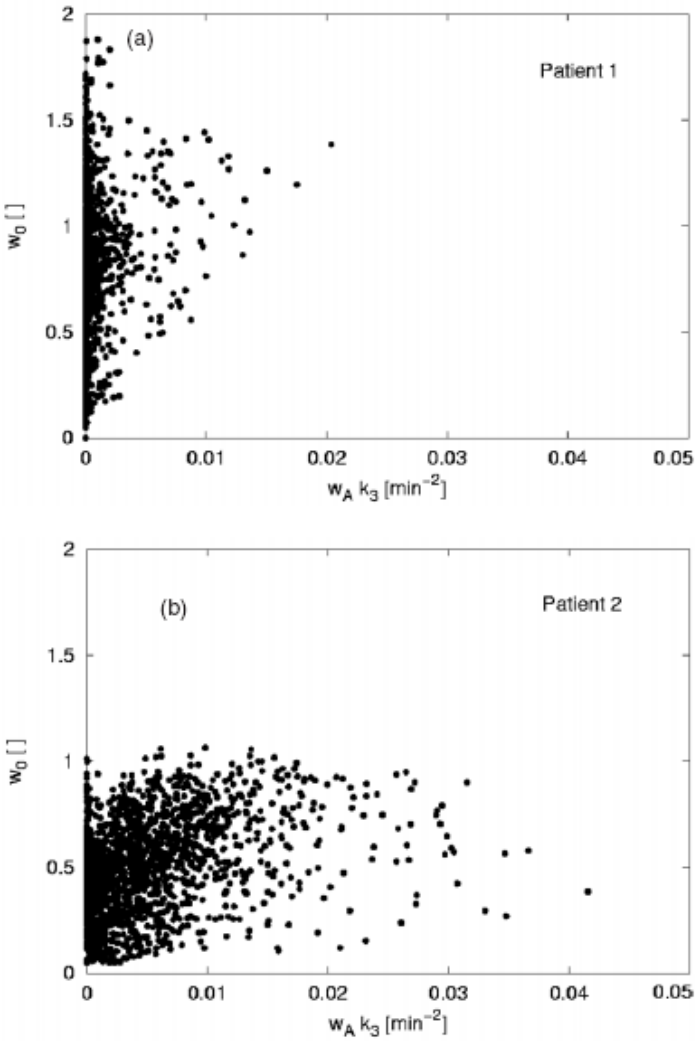

Figure 6.8: Scatter plots for two patients. Above: patient 1 shows a quite well-perfused and only moderately hypoxic tumour. Below: patient 2 in contrast has a badly-perfused and severely hypoxic tumour. Retrieved from Thorwarth *et al.* (2005), without permission.

Thorwarth's work has shown that Fmiso dynamic PET time activity curves can be modelled using a 2-tissue compartment model. Among the parameters obtained through curve fitting, ω_0 and $\tilde{\omega_A k_3}$ are found relevant to the different stages of head and neck cancer. In fact, ω_0 corresponds to the blood vessel volume as pointed out by Thorwarth. It accounts for the changes in the tumour vessel geometry. $\tilde{\omega_A k_3}$ is affected by the kinetics of inter-compartment Fmiso mass exchange. It is interesting to relate these kinetics to the physiological parameters of a tumour cell's microenvironment. In this way, a model could be developed to estimate biochemical parameters from PET time activity curves.

Because k_1, k_2 are more related to blood vessel membrane physiology and to the physicochemical properties of Fmiso, they are not explicitly modelled in conventional compartment models (and in our model). The compound redox reaction kinetics, k_3, however, is jointly determined by the chemical properties of Fmiso and the microenvironment of the cells. For this reason, research in Fmiso compartment modelling has been focused on formulating k_3. Various k_3 formulae have been proposed previously, here we present the relevant works that have inspired our model.

Casciari et al, 1995

Casciari and colleagues analysed Fmiso cellular bioreduction in order to relate cellular oxygen concentration to the cellular Fmiso reaction rate constant, κ_A (Casciari *et al.*, 1995). This provided a theoretical connection between Fmiso PET signal intensity and the *in vivo* physiological parameter, oxygen concentration.

Casciari and colleagues summarized the schematic model of the simplified nitroimidazole (RNO_2) bioreduction reactions:

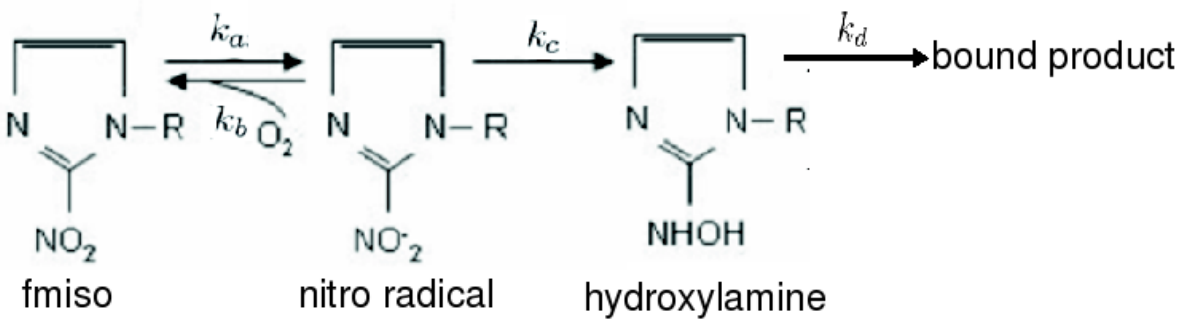

Figure 6.9: In the simplified reaction Fmiso is reduced to nitro radicals which can be further reduced to hydroxylamine derivatives in the absence of oxygen. Hydroxylamine derivatives can bind with macromolecules such as DNA, RNA and proteins. The unbound hydroxylamine derivatives can diffuse outside the cell, adapted from Casciari *et al.* (1995).

Casciari noted that the key cellular reactions of Fmiso involve the reduction of the NO_2 group to reactive intermediates. Briefly, Fmiso is reduced to the nitro radical in a one-electron reaction that can be reversed by oxygen. This oxygen-concentration-dependent reversible reaction is key to Fmiso's trapping process in cells. If oxygen

supply is reduced, the nitroradical will be further reduced to form reactive hydroxylamine derivatives. These hydroxylamine derivatives can bind to cellular macromolecules such as DNAs and proteins. This binding process is thought to be non-reversible and leads to an oxygen-dependent accumulation of radioactivity in cells.

Using mass conservation laws, the differential equations determining the cellular concentration of the nitro radical (C_{nr}), hydroxylamine reactive intermediate (C_{ri}) and the bound product (C_{bp}) can be written in terms of the extra-cellular Fmiso concentration (C_E) and the kinetic constants defined in Figure 6.9

$$\text{Nitro radical} \quad : \quad \frac{dC_{nr}}{dt} = k_a C_E - (k_b O + k_c) C_{nr}, \tag{6.10}$$

$$\text{Hydroxylamine} \quad : \quad \frac{dC_{ri}}{dt} = k_c C_{nr} - k_d C_{ri}, \tag{6.11}$$

$$\text{Bound product} \quad : \quad \frac{dC_{bp}}{dt} = k_d C_{ri}, \tag{6.12}$$

where O is the concentration of oxygen, and k_a, k_b, k_c, and k_d are first-order reaction rate constants. Casciari expressed C_{nr} and C_{ri} in terms of C_E, based on the assumption of quasi-steady-state: the nitro radical and the hydroxylamine reactive intermediates are assumed not to accumulate in the cell due to their short cellular half-lives. The hydroxylamine has a half-life of one to five minutes, while the other reactive intermediates have half-lives of less than one second. The error induced by using the quasi steady state assumption, when compared to the rigorous solutions of Eqs 6.10-6.12 was claimed to be less than 5% (Casciari *et al.*, 1995).

This assumption allows the derivatives in Eqs.6.10 and 6.11 to be set equal to zero. The solutions for C_{nr} and C_{ri} are then:

$$C_{nr} = \frac{k_a}{(k_b O + k_c)} C_E, \tag{6.13}$$

$$C_{ri} = \frac{k_a k_c}{k_d (k_b O + k_c)} C_E. \tag{6.14}$$

Substituting Eqs.6.13 and 6.14 into Eq.6.12 gives the rates of formation of bound products in terms of the extra-cellular Fmiso concentration:

$$\text{Bound product}: \frac{dC_{bp}}{dt} = \frac{k_a k_c'}{(O + k_c')} C_E, \tag{6.15}$$

where $k_c' = k_c/k_b$. Having obtained the rate of formation of bound and diffusible products in terms of the excellular Fmiso concentration, Casciari defined the global Fmiso reaction rate constant, κ_A (which corresponds to k_3 in Thorwarth's compartment model), so that the product of κ_A with C_E yields the rate of Fmiso reaction in the cell:

$$\kappa_A(k_3) = \frac{k_a k_c'}{O + k_c'}. \tag{6.16}$$

In Casciari's formulation, k_3 is expressed as a combination of reaction kinetics (k_a, k_b, k_c) and local oxygen concentration. The chemical kinetics will not change in different biological environmental conditions and can be treated as constants. For this reason, k_3 is uniquely affected by the oxygen concentration. When the oxygen level is low (i.e. in hypoxic tumours), k_3 is big, Fmiso is relatively more easily trapped in tumour cells. This is consistent with the fact that Fmiso can indicate hypoxic regions. However, Casciari's formula is based on normal cellular biology which does not account for the necrosis effect in severely hypoxic environments as observed in multi cellular spheroids. Since intracellular trapping of Fmiso demands active enzymes, it may be impeded when cells lose viability in a necrosis state (Kelly, 2007). Thus in order to apply Casciari's model into hypoxic scenarios one should consider the impact of necrosis on the cellular Fmiso reactions.

Kelly, 2007

Kelly considered that in the chemical reactions of Fmiso (shown in Figure 6.9), the kinetics are related to enzyme activities. Under extremely hypoxic circumstances, cells may die from oxygen deprivation (a process called necrosis). In this case, Fmiso cannot be

trapped in these cells since the relevant enzymes are no longer available. Kelly assumed, in the absence of other evidence, that the proportion of viable cells has the dependence on local oxygen tension similar to the curve showed in Figure 6.10.

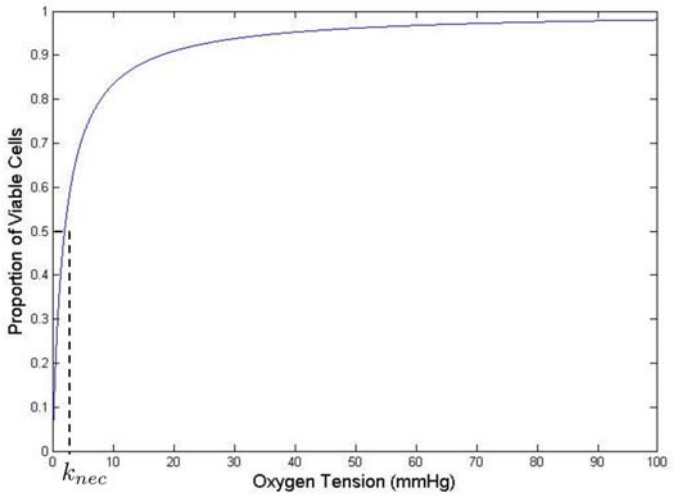

Figure 6.10: The proportion of viable cells depends on local oxygen tension: when cells are in normoxic state (i.e. the oxygen concentration is high enough), almost all cells are viable; when cells are in hypoxic state (i.e. the oxygen concentration is low), the proportion of viable cell drops when oxygen tension drops. The point where the proportion of viable cell is zero indicates the cell has died out from hypoxia (necrosis).

Kelly introduced a factor $\frac{O}{O+k_{nec}}$ to describe this effect, where k_{nec} denotes the oxygen tension where only half of the cell population is viable. By incorporating the factor into the kinetic rates in Casciari's fmiso global reaction rate Eq.6.16, we get:

$$\kappa_A = \left(\frac{k_a k_c'}{O + k_c'}\right)\left(\frac{O}{O + k_{nec}}\right). \tag{6.17}$$

Kelly validated the necrosis factor in Fmiso's global reaction using the data of Gross and colleagues (Gross *et al.*, 1995). Gross focused on Fmiso's analogue, misonidazole, which is a drug having exactly the same chemical structure as Fmiso except for the ^{18}F labelling. The result can be totally adopted in Fmiso's case. In this experiment (Gross *et al.*, 1995), multicellular spheroids derived from a mouse mammary carcinoma cell line were first incubated in complete medium with 50 μmol/l misonidazole (10 mg/l) for 90 min. The misonidazole was labelled with tritium on the side chain (445 μCi/mg) and

was evaluated with conventional auto radiography using the dipping technique. Grain density distributions were quantified in equatorial sections by a technique described by Franko and Chapman (Franko & Chapman, 1982). The number of grains per μm^2 was utilized as a measurement of the misonidazole concentration. Values of oxygen partial pressure (pO_2) were determined with recessed-type micro electrodes characterized by a sampling volume of less than one cell. Measured oxygen and misonidazole concentration in spheroids were plotted in Figure 6.11:

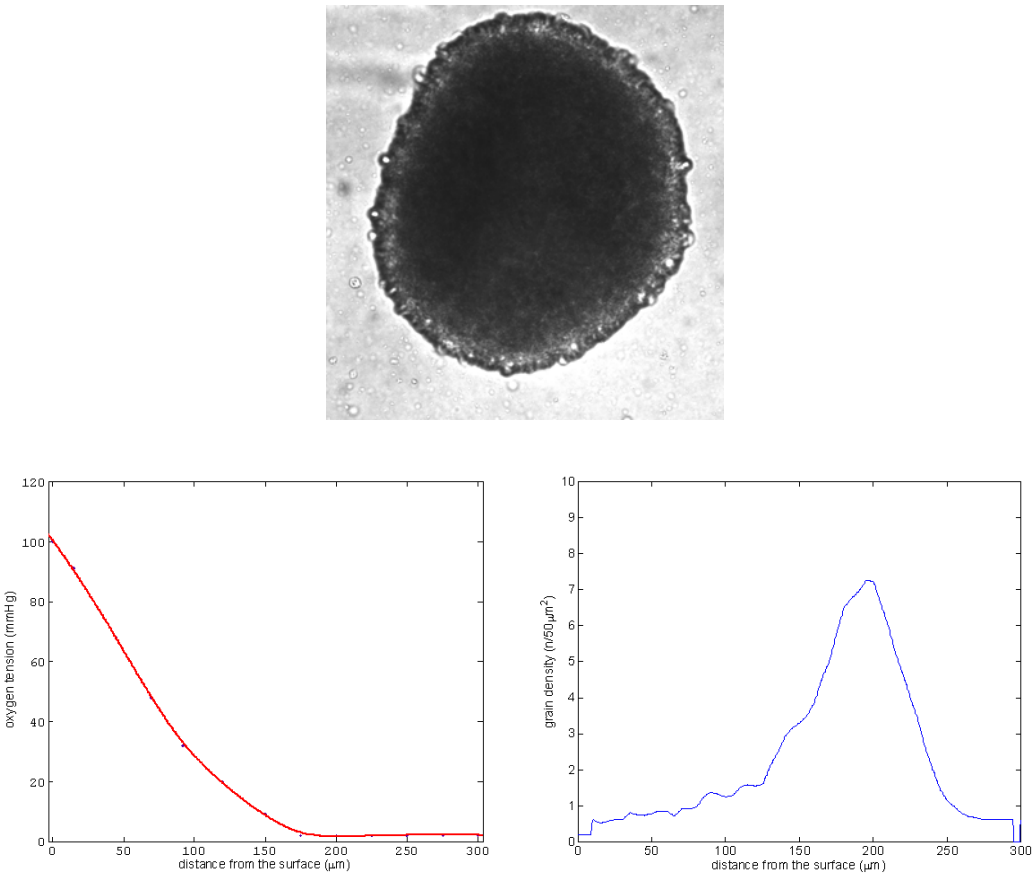

Figure 6.11: Upper: a microscopic image of multicellular spheroid, courtesy of Dr. Catherine Kelly. Lower: Gross' data of oxygen distribution (left) and intra-cellular trapped misonidazole distribution (right) measured in multicellular spheroids, reproduced from Gross *et al.* (1995).

As Fmiso's binding kinetics are dependent on oxygen concentration, so the oxygen distribution within the spheroid is first studied. Kelly assumed, in a multicellular spheroid like Figure 6.11, oxygen is supplied at the surface and diffuses towards the spheroid centre (core). From surface to centre, oxygen is also consumed by the cells throughout

the passage. The amount of oxygen available to a spheroid depends on its surface area ($4\pi r^2$), the diffusion coefficient of oxygen (D_{O_2}), and the concentration gradient (dc/dr). The amount consumed is dependent on the volume of viable cells. If a spheroid has no necrotic core, then the consumption rate is proportional to the total volume of the sphere ($\frac{4}{3}\pi r^3$) and the consumption rate per unit volume (q). Kelly considered that in multicellular spheroids, there is often a necrotic core where the cells have already died from lack of oxygen. In such a case, the consumption rate is proportional only to the volume of the viable rim of cells, i.e. $\frac{4}{3}\pi(r^3 - r'^3)$, where r' represents the radius of the necrotic core. To estimate the average consumption in this spheroid, we consider that the spheroid is of radius r_0 with the radius r_0 with the necrotic core having radius r'. By setting supply equal to consumption we obtain:

$$4\pi r^2 D_O \frac{dO}{dr} = \frac{4}{3}\pi q(r^3 - r'^3), \tag{6.18}$$

where D_O is the diffusion coefficient of oxygen inside the spheroid, q denotes the consumption rate of oxygen per unit volume, and r' is the radius of the necrotic core. By solving Eq.6.18, the analytical oxygen distribution function through the spheroid is obtained:

$$O = \frac{q}{3D_O}\left[\frac{r^2}{2} + \frac{r'^3}{r}\right] - \frac{q}{D_O}\left[\frac{r'^2}{2}\right]. \tag{6.19}$$

Exploiting the rotational symmetry of the spheroid, a model that describes the distribution of Fmiso in one dimensional space is then developed based on the three compartment diagram (Figure.6.12):

Figure 6.12: Fmiso's distribution within one dimensional space.

Following the schematic model showed in Figure 6.12, Kelly has constructed the following partial differential equation (Eq.6.20):

$$\frac{\partial M}{\partial t} = M_s - \left(\frac{k_a k_c'}{O + k_c'}\right)\left(\frac{O}{O + k_{nec}}\right) M + D_M \nabla^2 M, \tag{6.20}$$

where M is the concentration of misonidazole, M_s (mM/s) is the local supply from the outside and D_M is the diffusion coefficient of misonidazole in tissue (cm^2/s).

By solving Eq.6.20 numerically, Kelly's model is able to reproduce Gross' data (Figure 6.13):

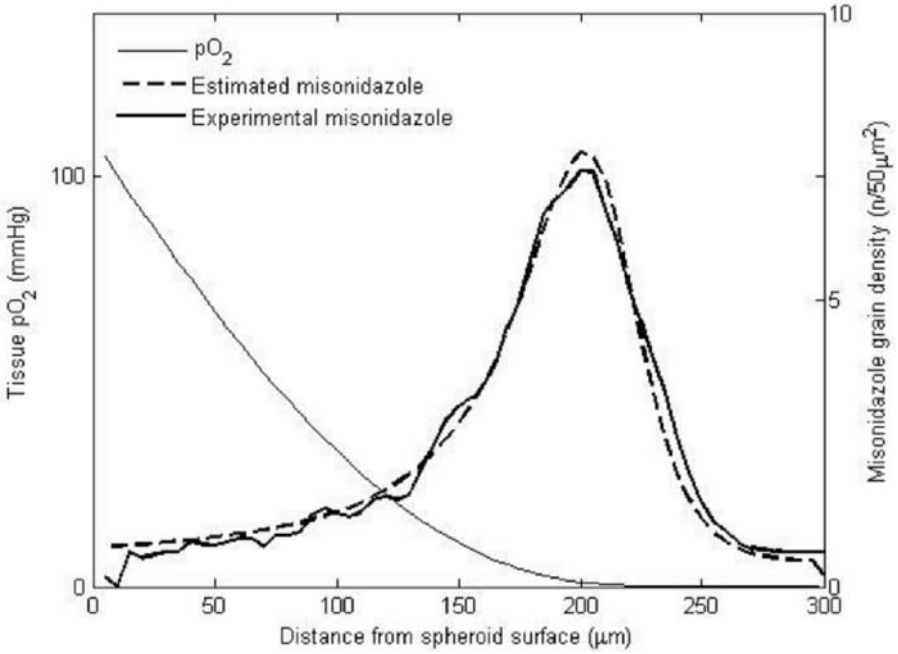

Figure 6.13: Comparison of the data produced by Kelly's model and data from Gross' experiments. Parameters: k_1=0.008s^{-1}, k_3'=1.8mmHg, k_{nec}=0.6mmHg, Medium Concentration 0.6 grains/μm^2, reprinted from Kelly (2007).

Kelly's model produced similar misonidazole distribution curves as in Gross' experiment. However, the discrepancy between the oxygen distribution predicted by the model and that measured is found to be relatively high. Kelly's model takes spatial variance into consideration by introducing a diffusion part in Eq.6.20. However, Kelly used one single partial differential equation to depict the spatiotemporal evolution of Fmiso and validated this model on Gross' data. We propose that, unlike in Kelly's model, it would be clearer to consider Fmiso in each compartment separately and to write partial differential equations to depict the spatiotemporal evolution of Fmiso in each compartment.

After the wash-out procedure, Gross' data actually corresponds to the concentration of misonidazole that is trapped inside the cell (i.e. the static compartment). So it is suitable to only validate the model depicting Fmiso concentration variations in the static compartment on Gross' data.

Meanwhile, Kelly also proposed a modelling framework for Fmiso modelling (Figure 6.14). In this framework, tumour vascularity is considered. This considers for the first time the vascular structure in modelling the Fmiso distribution. This framework consists of three models. First, an oxygen model predicts the distribution of oxygen at steady state on a given vascularity. Second, a Fmiso global reaction rate model calculates k_3 values at each point in space. Finally, the Fmiso model predicts the distribution of Fmiso through the PET scanning period.

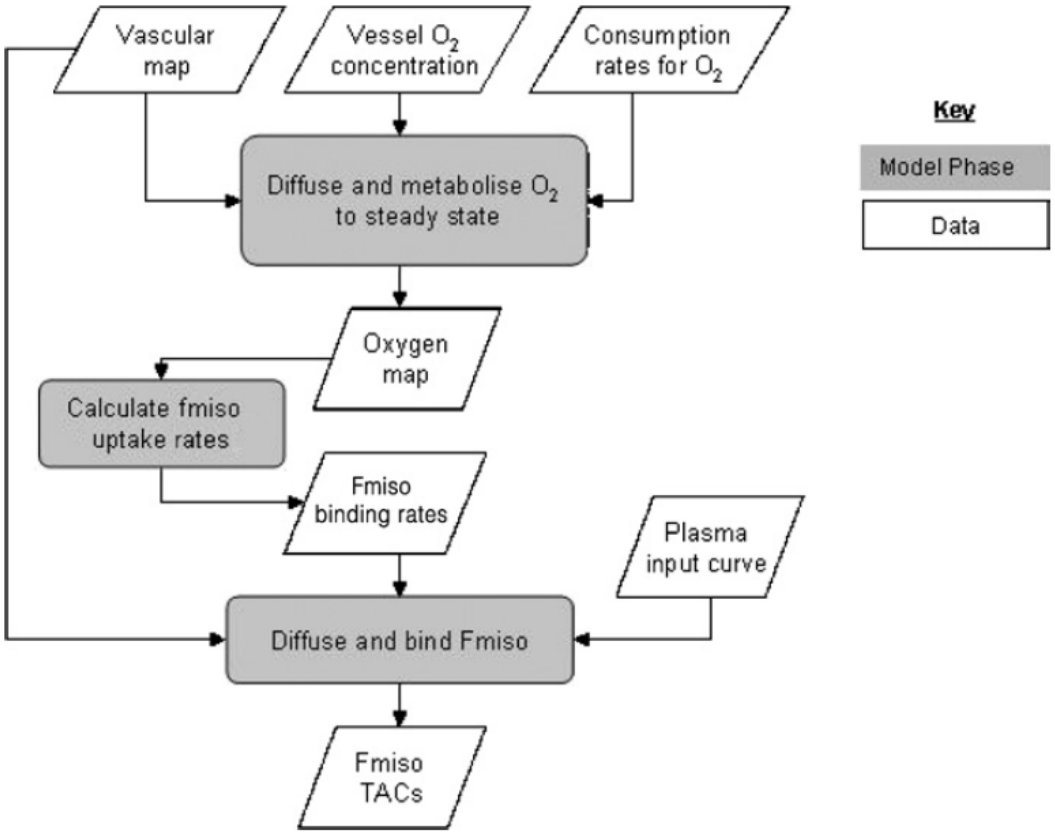

Figure 6.14: Model framework. This model consists of three parts (marked grey), oxygen distribution modelling, Fmiso binding kinetics modelling and Fmiso distribution modelling. Reprinted from Kelly & Brady (2006).

6.2 Spatio-temporal Modelling

Following Kelly's framework, we have developed a hybrid spatio-temporal oxygen and Fmiso model.

6.2.1 Oxygen Model

Our oxygen model is extended from conventional compartment models. *In vivo*, oxygen is transported through blood vessels. Some articles point out that abnormal vasculature is one of the causes that can lead to hypoxia in tumourous tissue (Fenton *et al.*, 1999). Being a gas, oxygen can pass from the blood vessels freely, so the plasma and extracellular space can be simplified into a single compartment. Oxygen is then consumed by viable cells. This process can be modelled as oxygen being irreversibly trapped inside the cell through a series of enzymatic reactions. The *in vivo* oxygen transportation can be thus described with the diagram showed in Figure 6.15:

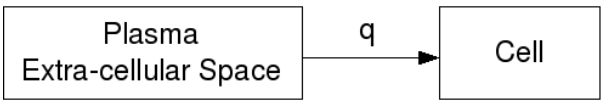

Figure 6.15: Oxygen's transportation can also be described with compartment model.

We take the spatial variance of oxygen's distributing into consideration in our model and model the oxygen delivery process by the differential equation stated in Eq.6.21:

$$\frac{\partial}{\partial t}O_{PE}(\mathbf{x},t) = O_{PE}(t) + D_{O_2}\nabla^2 O_{PE}(\mathbf{x},t) - qO_{PE}(\mathbf{x},t), \tag{6.21}$$

where $O_{PE}(\mathbf{x},t)$ denotes the oxygen concentration in the plasma-extracellular space compartment, and is a function of time and space. q is the cellular oxygen consumption rate. Kelly assumed this to be constant, and used a value published in the literature. However, the values of oxygen consumption rate are normally measured in a normal state, i.e. normoxic. In the case where the oxygen concentration is reducing, the cellular oxygen consumption rate is unlikely to remain constant. Consider the cellular oxygen

consumption process as one simplified enzymatic reaction:

$$E + O_2 \rightleftharpoons EO_2 \rightarrow E + P, \tag{6.22}$$

where E stands for enzymes and P stands for reaction products. The consumption rate of oxygen can be expressed using the Michaelis-Menten kinetics:

$$q = \frac{dO}{dt} = \frac{V_{max}O}{K_m + O}, \tag{6.23}$$

where V_{max} denotes the maximum oxygen consumption rate and K_m denotes the oxygen partial pressure when the oxygen consumption is half of the maximum rate. The kinetics q is found to have the following shape under different values of substrate (oxygen) concentration (Figure 6.16):

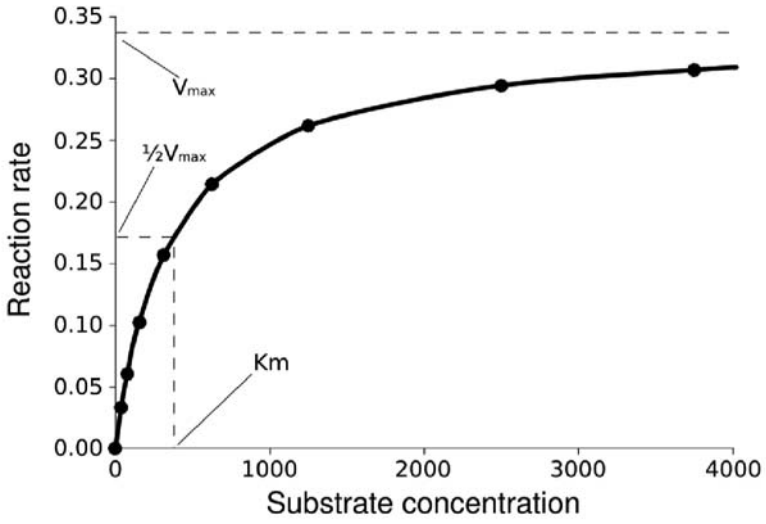

Figure 6.16: Michaelis-Menten curve of oxygen consumption. The reaction rate denotes the cellular oxygen consumption rate, substrate concentration denotes the concentration of oxygen, V_{max} denotes the maximum oxygen consumption rate and K_m denotes the oxygen partial pressure when the oxygen consumption is half of the maximum rate.

We argue that modelling oxygen consumption rate as a function of oxygen concentration (Eq.6.23) better describes the oxygen reaction mechanism and thus should have superior explanatory power for the experimental data. We fitted our oxygen model to Gross' spheroid data. In fact, substituting Eq.6.23 for q in Eq.6.18, we obtain Eq.6.24:

$$4\pi r^2 D_{O_2} \frac{dO}{dr} = \frac{4\pi}{3}\left(\frac{V_{max}O}{O+K_m}\right)(r^3 - r'^3). \tag{6.24}$$

By rearranging Eq.6.24, we find:

$$3D_{O_2}\left(1+\frac{K_m}{O}\right)dO = \frac{V_{max}}{r^2}(r^3 - r'^3)dr. \tag{6.25}$$

Integrating both sides, we get:

$$O + K_m lnO = \frac{V_{max}}{3D_{O_2}}(\frac{r^2}{2} + \frac{r'3}{r} + C). \tag{6.26}$$

The left side of Eq.6.26 can be approximated by a power function aO^b, where a,b are determined by K_m. Thus Eq.6.26 can be simplified to:

$$O = \left(\frac{V_{max}}{3aD_{O_2}}\right)^{(1/b)}\left(\frac{r^2}{2} + \frac{r'^3}{r} + C\right)^{(1/b)}, \tag{6.27}$$

where C is constant and is determined by r'.

We assumed the Michaelis constant for oxygen consumption (K_m) to be equal to 8mmHg and calculated a and b to be 5.77 and 0.7011 respectively ($R^2 = 0.9947$). We set $r' = 50\mu m$, $k = 0.6mmHg$ and $D = 2000\mu m^2/s$ as suggested by Kelly (2007). V_{max} was determined in the least square approximation process to be 20.3578 mmHg/s. Substituting parameter values, we get the following equation:

$$O = 0; r \in [0, 50], \tag{6.28}$$

$$= 2.466 \times 10^{-5}(\frac{r^2}{2} + \frac{125000}{r} - 3750)^{1.4192}; r \in [50, 300]. \tag{6.29}$$

The fitting of the oxygen distribution calculated from Kelly's model and from the modified model are compared in Figure 6.17.

Figure 6.17 shows that the modified oxygen model fits more closely to the experimental data (sum of squared errors: 0.36) compared with Kelly's model (sum of squared errors: 64.15). Note, however, that the parameter values assumed in our model still need to be further confirmed based on biological experiments.

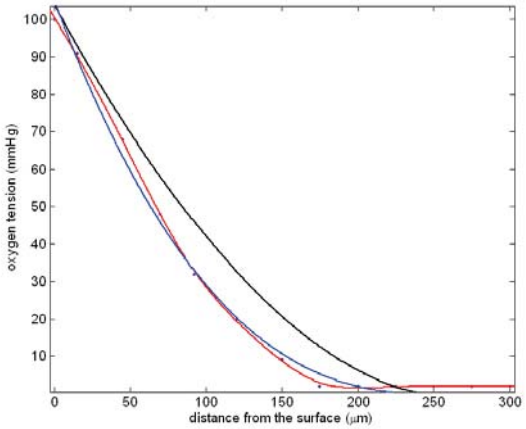

Figure 6.17: Comparison of Kelly's oxygen curve and oxygen curve generated by Eq.6.29 with Gross' data, red: Gross' data; blue: generated oxygen curve; black: Kelly's oxygen curve.

6.2.2 Fmiso Model

The distribution of Fmiso depends on both the vascular geometry and on the oxygen distribution. Similar to the case of oxygen distribution, Fmiso is transported by the blood vessels, however, it diffuses across the vessel's membrane at a rate denoted by k_1 together with a reflux rate denoted by k_2. The cellular reactions of Fmiso trap the radioactive isotope ^{18}F inside the cell. This process is irreversible and the kinetics is denoted by k_3. The distribution process can be described in the following diagram (Figure 6.18):

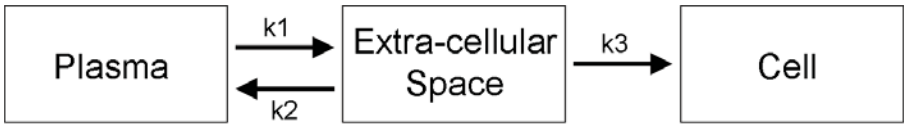

Figure 6.18: Three compartment model describing the distributing process of Fmiso.

We denote by $C_P(t)$ the concentration of Fmiso in plasma. As Fmiso perfuses with blood in plasma, we assumed that its distribution is spatially homogeneous within a specific region and consider it to be a temporal function. $C_E(\mathbf{x}, t)$ represents the concentration in extra-cellular space, we considered the spatial diffusion of Fmiso within the extra-cellular space and so $C_E(\mathbf{x}, t)$ is a spatio-temporal function. $C_C(\mathbf{x}, t)$ denotes the Fmiso concentration in cells. $C_C(\mathbf{x}, t)$ is also a spatio-temporal function since it depends

on the Fmiso concentration in the surrounding extra-cellular space. Let $V_P(\mathbf{x})$, $V_D(\mathbf{x})$ and $V_C(\mathbf{x})$ be the volumes of the corresponding compartments; these are spatial functions depending on the vascular geometry. Gathering all this together, we express the total PET signal as the sum of the amount of Fmiso within each compartment:

$$S(\mathbf{x},t) = V_P(\mathbf{x})C_P(t) + V_D(\mathbf{x})C_D(\mathbf{x},t) + V_C(\mathbf{x})C_C(t), \tag{6.30}$$

where $S(\mathbf{x},t)$ denotes the total PET signal in region of interest (ROI). Based on the three compartment model described in Figure 6.18, partial differential equations are written as Eq.6.31 and 6.32

$$\begin{aligned} \frac{\partial}{\partial t}C_E(\mathbf{x},t) &= k_1 C_P(t) - (k_2+k_3)C_E(\mathbf{x},t) + D_F\nabla^2 C_E(\mathbf{x},t), & (6.31)\\ \frac{\partial}{\partial t}C_C(\mathbf{x},t) &= k_3 C_E(\mathbf{x},t), & (6.32) \end{aligned}$$

k_1 and k_2 are related to the rates of Fmiso's diffusion across the blood vessel, they are related to blood pressure and vessels' surface areas. D_F is the diffusion coefficient of Fmiso in tumour tissues.

Like Kelly, we validated our model using Gross' data. We supposed that in Gross' experiment, the misonidazole solution concentration is sufficiently high so that misonidazole's diffusion process can be considered to be much faster than its binding process. Thus we assumed the diffusion process of misonidazole inside cell has reached a quasi-steady state. Then the distribution of misonidazole in the extra-cellular space is homogeneous, with concentration denoted by C_E. According to Eq.6.32 the trapped misonidazole concentration C_C could be expressed as:

$$\begin{aligned} C_C &= \int_0^t k_3 C_E dt, \\ &= k_3 C_E t, & (6.33) \end{aligned}$$

where t denotes the experimental period. After incubation, the unbound misonidazole was washed out before measurements. The measured misonidazole amount with the spheroid represents the amount that is trapped inside the cells. As proposed by Kelly, k_3 has the form:

$$k_3 = \left(\frac{O}{O + k_{nec}}\right)\left(\frac{k_a k_c'}{O + k_c'}\right). \tag{6.34}$$

So the experimental data can be expressed as:

$$\begin{aligned} M_C &= VC_C, \\ &= Vk_3 C_E t, \\ &= VC_E t\left(\frac{O}{O + k_{nec}}\right)\left(\frac{k_a k_c'}{O + k_c'}\right), \\ &= M_0\left(\frac{O}{O + k_{nec}}\right)\left(\frac{k_a k_c'}{O + k_c'}\right), \end{aligned} \tag{6.35}$$

where V is spheroid's volume. Since in Gross' experiment, the averaged volume V, incubation time t and C_E is constant, so M_0 is constant. The function was found very similar in shape with Gross' data (Figure 6.19).

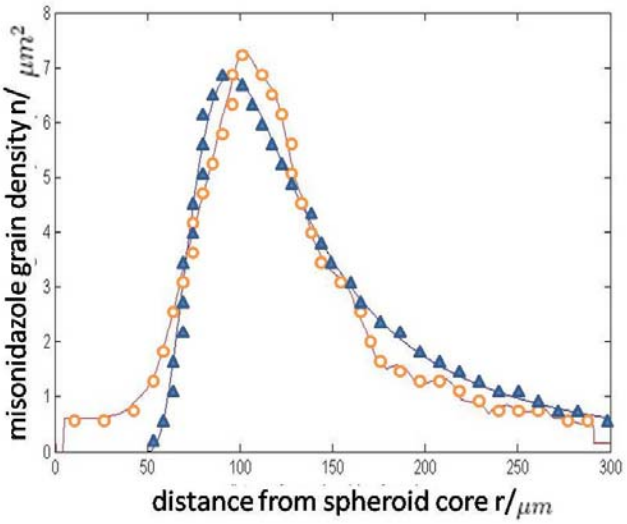

Figure 6.19: The function derived in our model has a similar shape to that of Gross' experimental data (Gross *et al.*, 1995), solid triangle: simulated data from our model (Eq.6.35); open circle: experimental data.

The main discrepancy probably corresponds to the misonidazole concentration at the sphere core area: whereas Gross' data show that there is still a low concentration of misonidazole, our simulated data predict that no misonidazole is bound in the sphere core. Possible explanations may come from the following two considerations: 1. In the simulation we assumed the 50μm area around the sphere core is necrotic core based on the oxygen data which shows that there is no oxygen available there (Figure 6.11). This assumption may be violated if cells are alive (dependent on anaerobic respiration) and can still trap misonidazole. 2. The constant concentration of Fmiso found in the multicellular spheroid core may be resulted from oxygen-independent non-specific binding of Fmiso inside cells.

6.3 Conclusion

Based on concepts of compartment models, we have developed a partial differential equation (PDE) based model that accounts for both temporal and spatial variances in oxygen and Fmiso's distribution. Compartment models are primarily developed to analyse the time activity curves recorded in dynamic PET imaging. It assumes no mass exchange between voxels in the PET images. Given low resolutions in PET images (ca.1mm), this assumption is valid. However, when time activity curves are recorded with higher resoltion imaging techniques, such as microscopes, the mass exchange between voxels should not be neglected. In these scenarios, we contend that our model has a superior explanatory power over conventional compartment models.

Chapter 7

In Silico Simulation

7.1 Introduction

The power of mathematical modelling derives not only from the capability to reproduce past processes; but also from the capability to predict phenomena under specific circumstances. Partial differential equations (PDEs) are very useful tools to describe fundamental physiochemical principles and are widely employed in mathematical models. PDEs can either be solved analytically, in which the solution is expressed in analytical forms, or numerically, in which the solution is expressed as a series of discrete numbers that (approximately) satisfy the equations.

Analytical solutions are intrinsically precise, whereas numerical solutions are often approximate. However, many partial differential equations do not have analytical solutions. Furthermore, even those that do have analytical solutions, it usually demands mathematical expertise to solve the equation and the solution formula can consist of very complicated functions, which are not very illustrative to non-mathematicians.

In contrast, a wide range of partial differential equations can easily be approximated numerically. Meanwhile, numerical solutions consist of discrete numbers, which can be readily presented visually as graphs or analysed otherwise. Though numerical solutions are only approximate, they can be made to attain any desired precision. Thus numerical methods are commonly employed to solve the PDEs in mathematical models.

The invention of programmable computers has greatly facilitated the numerical so-

lution of PDEs (which is also termed a numerical simulation). A number of numerical algorithms have been proposed which either enhance the simulation precision and speed or make the simulation process more robust.

Spatio-temporal simulation requires a considerable amount of computation. The partial differential equations will be converted into ordinary differential equations and be solved at each grid point in space. Suppose we want to simulate 10 time points on a 256× 256 grid. We have to solve $256 \times 256 \times 10 = 655360$ equations. If we want to simulate a 3D+T distribution process on a 256×256×60 grid, we have to solve $256 \times 256 \times 60 \times 10 = 39321600$ equations. However, that is only for 10 iterations. In reality, due to the convergence requirements, the time step of each iteration can be as short as 0.01 seconds. It follows that to simulate Fmiso's distributing process for 30 minutes, we need to solve $39321600 \times 1800/0.01 = 7,077,888,000,000$ equations! That would require ca. 40 days to compute on a single CPU with moderate power.

Fortunately, the computation on each grid can be executed independently. This means, instead of solving these equations serially one by one, it is possible to solve them simultaneously. This idea has been made possible thanks to the rapid developments in computer hardware, notably the multi-core CPU and GPU.

As stated above, numerical solutions can be readily analysed. One straightforward method of analysing the solutions of our spatio-temporal Fmiso distribution model is to visualize the simulated numbers. Essentially, a computerized visualization is also a simulation process. In a visualization pipeline, the data are first structured into specialized data structures which are subsequently converted into geometrical primitives. To render the images, a number of light rays are simulated to illuminate these geometrical primitives. The absorption and reflection of light are calculated based on fundamental optical physics. Finally, images are produced at some preselected observe position by composing the reflected lights at that viewpoint.

Here we briefly introduce the numerical, computational and visualization techniques

used in the Fmiso simulation.

7.1.1 Numerical Techniques

Euler method

The Euler method is very intuitive. At each x_n, we use a line to approximate the curve as illustrated in Figure 7.1, where $f(x, y)$ in this example is simply a function of x: $f(x, y) = \frac{1}{\sqrt{1-x^2}}$. The numerical approximation procedure is written as Eq.7.1

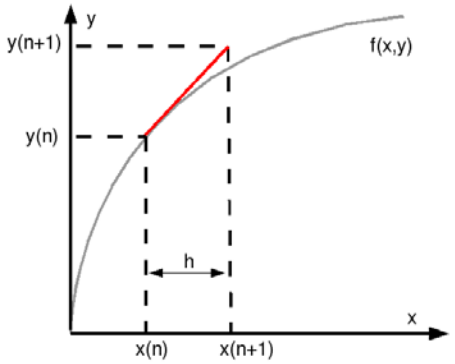

Figure 7.1: Illustration of Euler method.

$$y_{n+1} = y_n + \frac{1}{\sqrt{1 - x_n^2}} \times h \tag{7.1}$$

Because the Euler method uses the tangent at the beginning bound x_n to approximate the y value at the ending bound x_{n+1}, it is intrinsically biased. As is easily proved using a Taylor's series expansion, the precision of the Euler method is only $O(h^2)$.

Runge-Kutta method

As has been noted, the Euler method approximation is asymmetric. One simple improvement can be achieved by using the tangent at the midpoint to approximate the curve $f(x, y)$ in one sub-interval. Consider the sub-interval $[x_n, x_{n+1}]$ where $x_{n+1} = x_n + h$, the mid point of x is easy to determine as $x_m = \frac{1}{2}(x_n + x_{n+1}) = x_n + \frac{1}{2}h$. Meanwhile, suppose that y_n is also known from the previous iteration, however, y_{n+1} remains to be approximated in the current iteration. The idea of the Runge-Kutta method is to

first use Euler's method to estimate y_{n+1}. Then we can write the mid point of y as $y_m = \frac{1}{2}(y_n + y_{n+1}) = y_n + \frac{1}{2}hf(x_n, y_n)$. The tangent of curve at (x_m, y_m) is $f(x_m, y_m)$ and the value of y_{n+1} is adjusted as Eq.7.2

$$\begin{aligned} y_{n+1}^{(1)} &= y_n + hf(x_n, y_n) \\ y_{n+1} &= y_n + hf\left(\frac{x_n + x_{n+1}}{2}, \frac{y_n + y_{n+1}^{(1)}}{2}\right) \end{aligned} \tag{7.2}$$

It can again be proved using a Taylor's series expansion that the Runge-Kutta method illustrated in Eq.7.2 is a second-order approximation with error term of $O(h^3)$. In fact, the approximation of Eq.7.2 can be continued to reach increasingly higher precisions. For example if we repeat the approximation four times and calculate the weighted average of the four estimates as in Eq.7.3, we arrive at a fourth-order approximation (with error term $O(h^5)$). The procedure depicted in Eq.7.3 is thus called fourth-order Runge-Kutta method.

$$\begin{aligned} y_{n+1}^{(1)} &= y_n + hf(x_n, y_n) \\ y_{n+1}^{(2)} &= y_n + hf\left(\frac{x_n + x_{n+1}}{2}, \frac{y_n + y_{n+1}^{(1)}}{2}\right) \\ y_{n+1}^{(3)} &= y_n + hf\left(\frac{x_n + x_{n+1}}{2}, \frac{y_n + y_{n+1}^{(2)}}{2}\right) \\ y_{n+1}^{(4)} &= y_n + hf\left(\frac{x_n + x_{n+1}}{2}, \frac{y_n + y_{n+1}^{(3)}}{2}\right) \\ y_{n+1} &= \frac{1}{6}\left(y_{n+1}^{(1)} + 2 \times y_{n+1}^{(2)} + 2 \times y_{n+1}^{(3)} + y_{n+1}^{(4)}\right) \end{aligned} \tag{7.3}$$

Although Eq.7.3 is a mathematically complete description of the fourth-order Runge-Kutta method, one has to decide the step size h to use in a numerical implementation. Evidently, the precision is a function of h. The greater the step size is, the lower the precision becomes. There exists a trade-off between speed and precision, but how to determine the optimal step size h given a precision requirement? One straightforward

technique is the so called step doubling (Press *et al.*, 1995). In this method we approximate the real value $y(x+h)$ with two approaches: (1) a single step with step size h; (2) two consecutive steps with step size $\frac{1}{2}h$. As stated above, the equation of real value and approximated value with step size h could be written as Eq.7.4

$$y(x+h) = y_1 + h^5 T(5) + O(h^6), \tag{7.4}$$

where $y(x+h)$ stands for the real value at position $x+h$ while y_1 stands for the approximation with step size h and $T(5)$ stands for the 5th Taylor expansion of $y(x)$. Similarly, we can write the equation of real value and approximated value by two consecutive approximations with step size $\frac{1}{2}h$ as Eq.7.5

$$\begin{aligned} y(x+\frac{1}{2}h) &= y_2 + (\frac{1}{2}h)^5 T(5) + O(h^6) \\ y(x+h) &= y_3 + (\frac{1}{2}h)^5 T(5) + O(h^6) + (\frac{1}{2}h)^5 T(5) + O(h^6) \\ &= y_3 + \frac{1}{16}h^5 T(5) + O(h^6), \end{aligned} \tag{7.5}$$

where $y(x+\frac{1}{2}h)$ and y_2 are the real and approximated values at position $x+\frac{1}{2}h$, respectively while $y(x+h)$ and y_3 are the real value approximated values at position x+h. Notice that the error is accumulated in two approximations. By subtracting both sides in Eq.7.4 and 7.5, we can obtain Eq.7.6

$$y_3 - y_1 = \frac{15}{16}h^5 T(5) + O(h^6) \tag{7.6}$$

Press *et al.* (1995) defined $y_3 - y_1$ as the truncation error, which they denote as Δ. By doing so we can rewrite Eq.7.5 as :

$$y(x+h) = y_3 + \frac{\Delta}{15} + O(h^6) \tag{7.7}$$

So, by estimating the truncation error we reach an approximation of 5th order. The computational overhead cost is $11/8 = 1.375$. As can be seen, size doubling technique is an independent technique to reach higher precision. One additional strength of the

Runge-Kutta method is that the error estimation and step control can be embedded in the approximation procedure making it nearly twice as efficient as using size doubling technique independently (Press *et al.*, 1995). In this method, the truncate error Δ is estimated by comparing the approximation of fifth-order Runge-Kutta and fourth-order Runge-Kutta method which only requires 6 evaluations reducing the computation by a factor of 1.833 (11/6).

In the embedded fifth-order Runge-Kutta method suggested by Cash & Karp (1990), we are not evaluating the tangents at the midpoint but at a deliberately chosen set of evaluation positions (Table.7.1). The general form is given in Eq.7.8:

$$\begin{aligned}
k1 &= hf(x_n, y_n) \\
k2 &= hf(x_n + a_2 h, y_n + b_{21} k_1) \\
&\dots \\
k_6 &= hf(x_n + a_6 h, y_n + b_{61} k_1 + \ldots + b_{65} k_5) \\
y_{n+1}^{5th} &= y_n + c_1 k_1 + c_2 k_2 + c_3 k_3 + c_4 k_4 + c_5 k_5 + c_6 k_6 + O(h^6) \\
y_{n+1}^{4th} &= y_n + c'_1 k_1 + c'_2 k_2 + c'_3 k_3 + c'_4 k_4 + c'_5 k_5 + c'_6 k_6 + O(h^5),
\end{aligned} \tag{7.8}$$

where y_{n+1}^{5th} and y_{n+1}^{4th} are fifth-order and fourth-order Runge-Kutta approximations of the real value y_{n+1} respectively. The parameters are listed in Table 7.1:

i	a_i	b_{ij}					c_i	c'_i
1							$\frac{37}{378}$	$\frac{2825}{27648}$
2	$\frac{1}{5}$	$\frac{1}{5}$					0	0
3	$\frac{3}{10}$	$\frac{3}{40}$	$\frac{9}{40}$				$\frac{250}{621}$	$\frac{18575}{48384}$
4	$\frac{3}{5}$	$\frac{3}{10}$	$-\frac{9}{10}$	$\frac{6}{5}$			$\frac{125}{594}$	$\frac{13525}{55296}$
5	1	$-\frac{11}{54}$	$\frac{5}{2}$	$-\frac{70}{27}$	$\frac{35}{27}$		0	$\frac{277}{14336}$
6	$\frac{7}{8}$	$\frac{1631}{55296}$	$\frac{175}{512}$	$\frac{575}{13824}$	$\frac{44275}{110592}$	$\frac{253}{4096}$	$\frac{512}{1771}$	$\frac{1}{4}$
j		1	2	3	4	5		

Table 7.1: Cash-Karp Parameters for the Embedded Runge-Kutta Method, reproduced from Press *et al.* (1995).

The truncation error can now be estimated as Eq.7.9

$$\Delta = y_{n+1}^{5th} - y_{n+1}^{4th} = \sum_{i=1}^{6}(c_i - c_i')k_i \tag{7.9}$$

Because Δ is a function of h^5 (Eq.7.6), the step size h_1 can be adapted given level of accuracy by:

$$h_1 = h_0 \left| \frac{\Delta_1}{\Delta_0} \right|^{1/5} \tag{7.10}$$

With this property, embedded Runge-Kutta optimizes step size at each iteration to bring the truncation error below some predefined level. Compared with the Euler method, the embedded Runge-Kutta method makes symmetrical approximations and has a truncation error control mechanism, though it is more complicated to implement. As a result, both methods have received popularity among researchers of different background.

7.1.2 Computational Techniques

Parallel programming is a programming technique, in which the task is divided into several independent sub-tasks and these sub-tasks are subsequently executed on multiple processing units simultaneously. Parallel computing has become a premier speed up option with the commercial availability of multi-processor CPUs and GPUs.

CPU Parallel Programming

Based on CPU architectures (Figure 7.2), there are roughly two categories of programming interfaces of parallel computing available with C/C++. One is represented by OpenMP (Open Multi-Processing), which is based on a shared-memory multiprocessor architecture. In such an architecture, the processing units share a single memory pool, so there is no need for the processing units to exchange data. The most common example of such architecture is personal computers with multiple CPU cores. For this reason, OpenMP is very popular for parallel computing on a single machine.

Another widely used programming interface is MPI (Message Passing Interface), which is based on a distributed memory system. In such an architecture, each pro-

cessing unit has its own memory reservoir, so they are relatively independent units. The cross talk between each processing unit is essential for parallel computing on such a system. Basically, the majority of MPI classes are created to standardise the inter-processor communication protocols. Clusters are the typical systems that are built upon this architecture. For this reason, MPI is popular among institutional researchers. However, MPI can also be used on a shared memory system like PCs with multiple core CPUs.

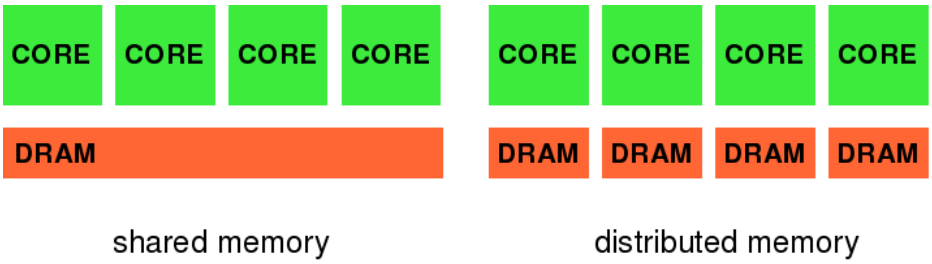

Figure 7.2: Different CPU architectures.

Since the processing units of shared memory system don't need to pass messages, parallel programs on shared memory system are generally faster than those on distributed memory systems (Chandra, 2000).

GPU Parallel Programming

Graphics processing units (GPU) are microprocessors designed primarily for computer graphics rendering. Since it is especially designed for computer graphics rendering algorithms, its structure caters for the massive parallelism and high computation intense features of these tasks. Compared with a CPU, a GPU has more transistors for data processing and fewer transistors for data caching and flow control (Nvidia, 2010) as shown in Figure 7.3.

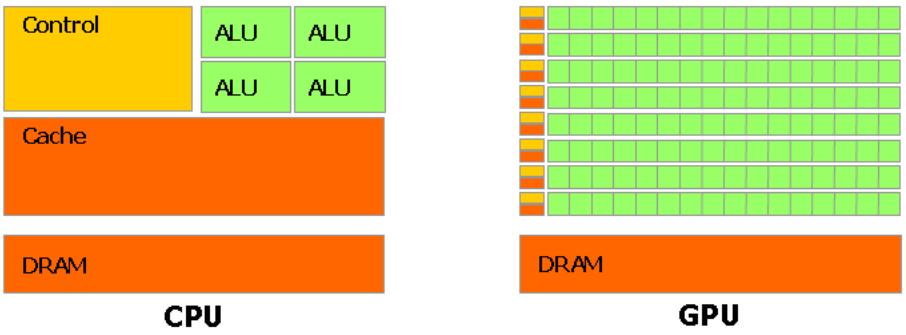

Figure 7.3: Hardware design of CPU (left) and GPU (right), reprinted from Nvidia (2010), without permission.

Because of this specialized structure design, a GPU is relatively easy to use to realize massive parallelism by clustering many processing units. Stimulated by the demands of the computer game and film industry, GPUs have experienced a much faster development in the sense of computation speed and memory bandwidth (Figure 7.4).

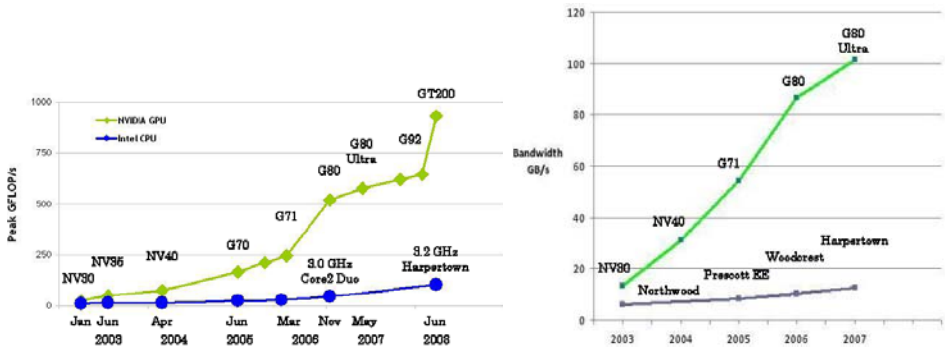

(a) Computation speed (b) Memory bandwidth

Figure 7.4: Development in computation speed (left) and memory bandwidth (right) of CPU and GPU. GT200 = Geforce GTX 280, G71 = Geforce 7900 GTX, NV35 = Geforce FX 5950 Ultra, G92 = Geforce 9800 GTX, G70 = Geforce 7800 GTX, NV30 = Geforce FX 5800, G80 = Geforce 8800 GTX, NV40 = Geforce 6800 Ultra, reprinted from Nvidia (2010), without permission.

Because GPUs enable massive parallelism, GPU applications for non-graphics computation have been sought. This has been referred as General-Purpose computation on Graphics Processing Units (GPGPU) technique. CUDA (Compute Unified Device Architecture) is a parallel programming architecture for GPUs developed by NVIDIA. It comprises a set of programming interfaces that provide connections between modern programming languages (such as C, Fortran etc.) and binary codes executable on GPUs

(Figure 7.5).

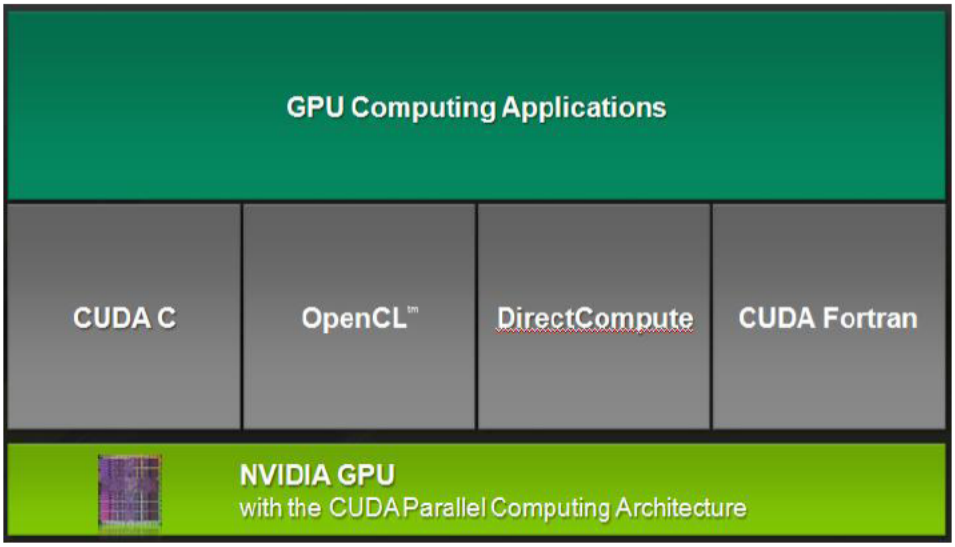

Figure 7.5: CUDA architecture for general purpose GPU computing, reprinted from Nvidia (2010), without permission.

The core of the CUDA architecture consists of three key concepts: hierarchical multi-threading, shared memories, and barrier synchronization (Nvidia, 2010). CUDA provides hierarchical thread parallelism. This enables developers to determine the organization of threads based on the structure of the data to be processed. Unlike MPI, which requires developers to split the data and send pieces of data to every CPU core, CUDA automatically divides the parallel tasks and distributes the computational burden optimally to each GPU core. This greatly simplifies coding and frees developers from optimizing task allocations on each processing unit.

CUDA enables shared memories. Shared memories are regions of memory which are accessible by all the threading tasks. Because loading data from shared memories is much faster than from global memory, enabling shared memories can greatly enhance computational efficiency.

Barrier synchronization ensures that sequential multi-threading tasks are performed in an orderly manner. By synchronizing the threading tasks, the program proceeds only when all the threads have finished computation. It is an indispensable regulation in

parallel computation when two or more multi-threading tasks need to be carried out one after another.

7.1.3 Visualization Techniques

We used VTK(Visualization Toolkit) to visualize the 3D images of oxygen and Fmiso distribution. VTK is an open source free software developed by Kitware. It consists of a C++ class library for computer graphics, image processing and visualization. It also provides interfaces to other programming languages such as Tcl/Tk, Java and Python. It has become a very popular toolkit among medical image analysis researchers.

VTK visualization pipeline

In VTK, there are two separate processes in the visualization pipeline (Figure 7.6). In the data processing pipeline, image data is represented as a variety of different data structures through different VTK readers. Various filters are available in the VTK library to modify the data's attributes. Mappers are one group of VTK classes responsible for connecting the data processing pipeline and data visualization pipeline. They transform the structured data into the formats (geometrical primitives) that are recognizable by the graphics hardware. Actors are containers of the geometrical primitives and are the visualizing objects in the visualization pipeline. Renders are algorithmic objects which coordinate all the visualization elements: lights, cameras and actors to create images. Finally, windows are widgets that display the created images.

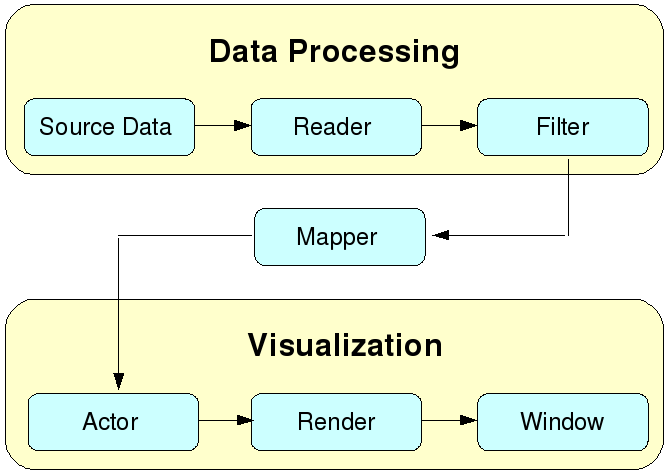

Figure 7.6: Visualiation pipeline in VTK.

Volume Rendering

Volume rendering methods visualize the whole object, including its interior structure. Data of acquired images are usually organized in grids (Figure 7.7). Each unit in the grid is called a voxel, a 1D subset of the grid is called a beam, while a 2D subset is called a slice (Figure 7.7).

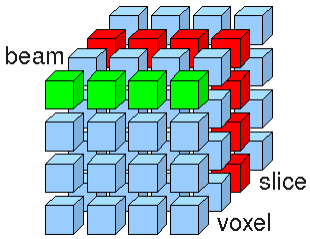

Figure 7.7: Volume dataset. The unit in the 3D grid is called a voxel (light blue), the 1D set of voxels is called a beam (light green), and 2D set of voxels is called a slice (light red).

Two volume rendering techniques have been utilized to visualize 3D volume data in our research, maximum intensity projection and volume ray casting.

In maximum intensity projection, 3D volume data is projected onto a 2D plane. The intensity of each pixel of the 2D projection is the maximum intensity of voxels aligning with the projecting rays (Figure 7.8). Maximum intensity projection assumes that human vision only perceives the voxel with the maximum intensity, which is an oversimplication; but is a method that has worked well for several kinds of medical image display, not least

computed tomography. Maximum intensity projection can not provide depth information for 3D visualization. It is thus a coarse method for 3D volume rendering. However, it is very fast to compute and useful when rendering quality is not required.

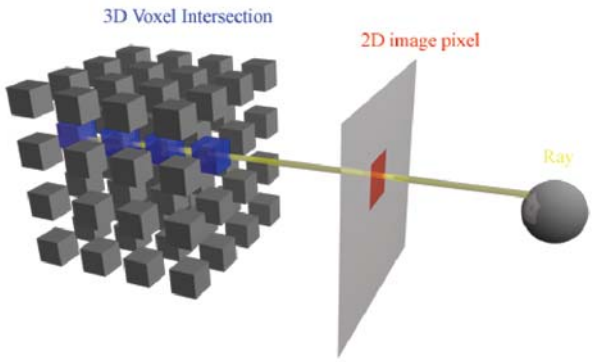

Figure 7.8: Illustration of maximum intensity projection method. The intensity of projected 2D image is determined as the maximum intensity value of voxels aligning with the projection ray, reprinted from volviz.com, without permission.

Volume ray casting is based on a similar idea to maximum intensity projection. However, pixel intensities of 2D projections are not simply determined as the maximum voxel intensity along the projection ray but are computed by considering the intensities of every voxel along the projection ray (Figure 7.9).

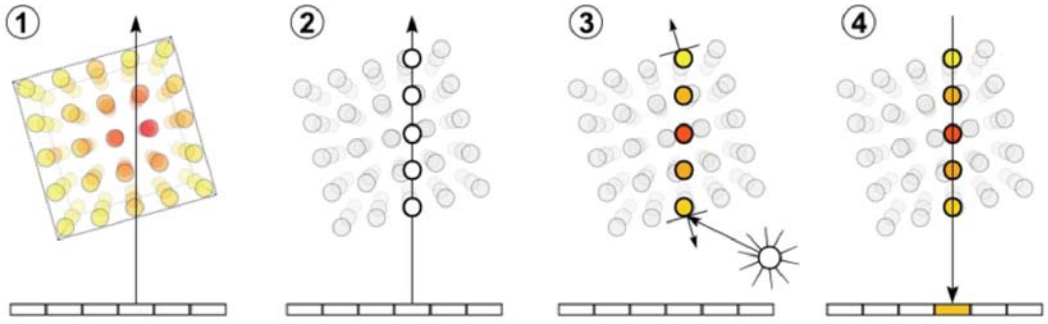

Figure 7.9: Illustration of the volume ray casting method. The intensity of the projected 2D image is determined from the composite sum of the intensities of all voxels aligned with the projection ray. Image credit: Thetawave.

Volume ray casting rendering usually consists of four major components (Ray *et al.*, 1999):

1. Ray-path calculation. Based on the position of the viewpoint, the path of the projection ray is calculated. Together with viewpoint, the paths followed by the projection rays define a complete projection geometry (i.e. projective space) that determines the 3D-2D projection.

2. Interpolation. Since the projection rays may partially pass through several voxels, the intensities along the projection rays are calculated using trilinear interpolation of the intensities of these voxels.

3. Gradient Estimation. Gradients of the intensities are next calculated. Gradient information is then used to calculate the normals of the local surfaces, which is essential for determining the reflected light direction and adding subtle textures, for example opacity and shading.

4. Compositing. The pixel intensity of the 2D projection image is calculated according to the rendering equation, based on the intensities of all the voxels along the projection ray.

Surface Rendering

Unlike volume rendering, surface rendering only renders a shape's surface. The shape's surface is usually approximated using polygons or surface splines (Schroeder & Lorenson, 1996). For example, complex surface curvatures can be approximated by a set of triangles (Figure 7.10). This triangulated data format is well suited to scanline rendering, which is a fast and accurate 3D rendering technique.

Marching cubes is a method to transform grid image data into polygonal data (Lorensen & Cline, 1987). It produces an isosurface visualization of a 3D volume. The marching cubes algorithm consists of two steps: triangle generation and local normal vector calculation. First, for every 2×2×2 voxel cube, triangular surfaces are determined so that the voxels with intensities above the isosurface value are situated on one side of the surfaces

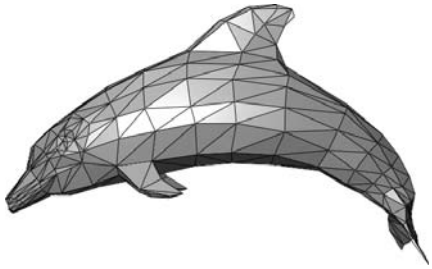

Figure 7.10: A triangular mesh network of a dolphin.

and voxels with intensities below the isosurface value are situated on the other side. Although there are $2^8 = 256$ combinations of voxel positions and states (above or below the isosurface value), only 15 unique cases are different from each other (Figure 7.11)

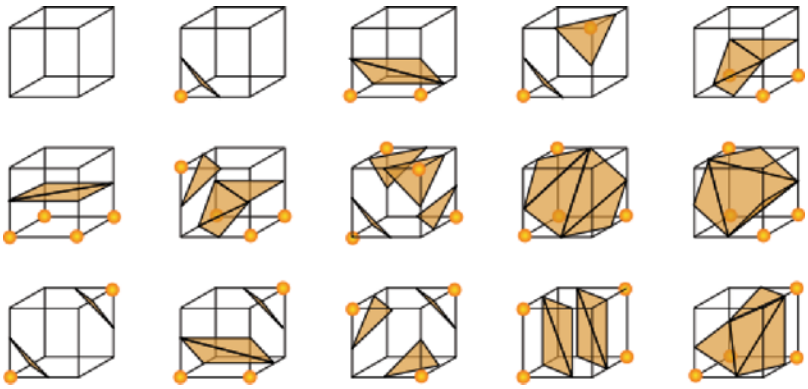

Figure 7.11: Different triangular intersection in 2×2×2 voxel cubes. The yellow vertices represents voxels with intensity above the isosurface value.

Then normal of every generated triangle is calculated via interpolation from the 8-voxel cube's normal. The normal vector is utilized to calculate light reflection, colour and shade in the following scanline rendering process.

The scanline rendering technique defines a sequence in which to load the polygonal vertices from the global memory. That is, only those vertices that intersect with the scanline are loaded. This ensures that each polygonal vertex is read only once from the global memory. Since data loading from global memory is often slow, this provides a speed up of the rendering process. Scanline rendering can be integrated with Phong shading, z-buffering algorithms and many other graphics techniques to provide fine texture information. Thus scanline rendering is a widely applied rendering technique in

computer graphics.

7.2 2D Simulation

We have implemented a 2D simulation on a synthesized 2D vasculature map. The Euler method was used in the simulation and was coded in Matlab® (R2008a).

7.2.1 2D Vascular Network Generation

As vasculature serves as the source for both oxygen and Fmiso, its geometry directly affects the spatial distributions of both oxygen and Fmiso. It has been reported that abnormal vasculature is a prominent characteristics of tumour tissues (Carmeliet & Jain, 2000; Weinberg, 2007).

In 2D, we followed Dasu and Kelly's presentation (Daşu *et al.*, 2003; Kelly, 2007) and used circles to represent blood vessels, in effect assuming that they are projections of local blood vessel volume on the orthogonal plane (Figure 7.12). The circle's diameter corresponds to the blood vessel's diameter. The closest surface-to-surface distance between two circles is defined as the inter-vessel distance.

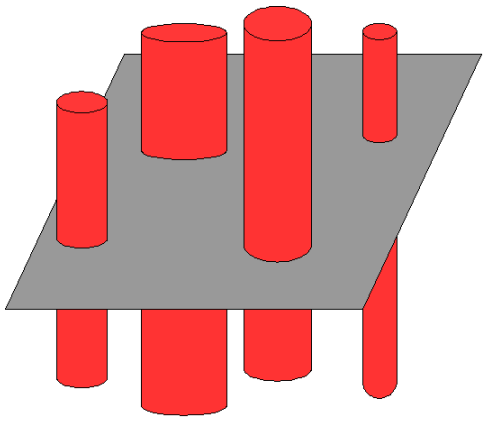

Figure 7.12: 2D vessels are represented by the projections on the orthogonal plane of the local vessel's direction.

In Chapter 5, we concluded that the tumour vessels' radii could be modelled as following a gamma distribution. On the other hand, Konerding *et al.* (2001) investigated the distribution of 3D inter vessel distances and contended that they follow log-normal

distribution. The question becomes how to place these circles so that the pairwise surface distances obey the prescribed log-normal distribution and their radii obey the prescribed gamma distribution.

Various algorithms have been developed to generate blood vessel networks. Chaplain has proposed an algorithm that generates 2D and 3D blood vessel network based on a stochastic angiogensis model (Chaplain, 2000). The obtained vessels structure is determined by the parameters of the aniogenesis model and it is hard to generate a vessel structure with desired geometry. Another approach, proposed by Szczerba, is based on a random walk algorithm and is capable of constraining the vessels' structural parameters with arbitrary probability distributions (Szczerba & Székely, 2002). However, Szczerba's method produces a continuous treelike vessel structure, which corresponds to the sagittal view of blood vessels. We found it hard to adapt Szczerba's method to generate the discrete vessel map under our vessel representation which is derived from the transverse view of the blood vessels.

Nevertheless, we adopted the idea of Szczerba's method to use a probability distribution to constrain the generation process of our 2D vascular map. We achieved this by sequentially adding one circle at each iteration. The first circle is placed at the centre of the region of interest (ROI), we denote its coordinates by (i_1,j_1). In reality, this is the blood vessel on which the screen (microscope) is focused. The radius r_1 of this circle is generated randomly from the gamma distribution with the prescribed k_r and θ_r. We then generate another random number r_2 from the prescribed gamma distribution, and assign it as the radius of the second circle we are going to place somewhere.

The first circle imposes a random field with the possibility potential defined as:

$$P(i,j) = \frac{1}{\sigma\sqrt{2\pi}} e^{-\frac{(log(d)-\mu)^2}{2\sigma^2}}, \tag{7.11}$$

where d denotes the inter-vessel surface distance which is defined as Figure 7.13

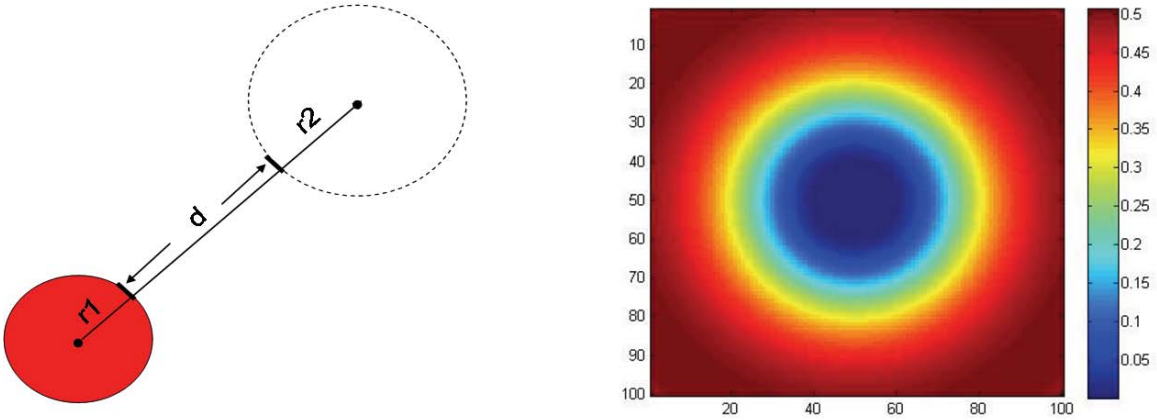

Figure 7.13: In the left figure, the first circle (coloured red) denotes the first blood vessel we placed and has a radius r_1 generated according to the prescribed gamma distribution. The second circle (with dashed line) has a radius r_2 generated with the prescribed gamma distribution, it is placed where the possibility value defined in Eq.7.11 is maximum. The inter vessel distance d is defined as the surface distance between two circles. The right figure shows the random field imposed by the first circle according to the possibility potential defined in Eq.7.11

Suppose the centre of the second circle is placed at (i_2,j_2), d is calculated as:

$$d_1 = \sqrt{(i_2 - i_1)^2 + (j_2 - j_1)^2} - r_1 - r_2. \tag{7.12}$$

Eq.7.11 is actually a function of d. For convenience, we rewrite it as:

$$P(i, j) = f(d). \tag{7.13}$$

Then i_2 and j_2 are chosen randomly from the pool of values which maximises the possibility potential function:

$$(i_2, j_2) = max_{(i_2,j_2)}\{f(d_1)\}. \tag{7.14}$$

To add the third circle, as before, we generate a random value r_3 from the prescribed gamma distribution and assign it as the radius of the third circle. Suppose the centre of the third circle is placed at (i_3, j_3), then it will add two new distances with the first and second circle (Figure 7.14).

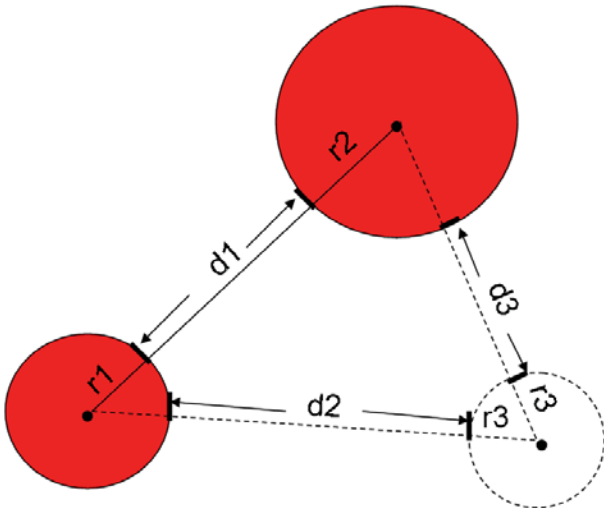

Figure 7.14: When the third circle (open circle) is added, it will generate two new distances d_2 and d_3 (dashed line) with the first and second circle. (solid circle)

As illustrated in Figure 7.14, d_2 and d_3 are calculated as:

$$d_2 = \sqrt{(i_3 - i_1)^2 + (j_3 - j_1)^2} - r_1 - r_3, \tag{7.15}$$

$$d_3 = \sqrt{(i_3 - i_2)^2 + (j_3 - j_2)^2} - r_2 - r_3. \tag{7.16}$$

Then, i_3, j_3 are determined to maximise the conditional possibility potential

$$(i_3, j_3) = max_{(i_3,j_3)}\{f(d_2, d_3)|f(d_1)\}. \tag{7.17}$$

If we define $\{D_n\}$ as the set of distances generated by the nth circle, ($\{D_1\}$=Φ, $\{D_2\}$=$\{d_1\}$,$\{D_3\}$=$\{d_2, d_3\}$,...), then Eq.7.17 can be written as:

$$(i_3, j_3) = max_{(i_3,j_3)}\{f(\{D_3\})|f(\{D_1, D_2\})\}. \tag{7.18}$$

We assume, for ease of computation, that the distances in $\{D_n\}$ ($n = 1, 2, \ldots$) are independent with each other. Under this assumption,

$$f(\{D_n\}) = \prod_{d_m \in \{D_n\}} f(d_m). \tag{7.19}$$

So Eq.7.18 can be written as:

$$(i_3, j_3) = max_{(i_3,j_3)}\{f(d_2)f(d_3)|f(d_1)\}. \tag{7.20}$$

We add the circles iteratively according to the procedure described above, i.e. we generate a random value r_n from the prescribed gamma distribution and assign it as the radius of the nth circle we are going to place somewhere denoted by (i_n,j_n), this circle will generate $(n-1)$ new distances with the current $(n-1)$ circles, denote the set of these distances by $\{D_n\}$, then i_n, j_n is picked randomly from the values that maximise the conditional possibility:

$$(i_n, j_n) = max_{(i_n,j_n)}\{f(\{D_n\}|f(\{D_1, D_2, \ldots, D_{n-1}\}))\} \tag{7.21}$$

Then the joint possibility function $f(\{D_1, D_2, \ldots, D_n\})$ is:

$$f(\{D_1, D_2, \ldots, D_n\}) = f(\{D_n|D_1, D_2, \ldots, D_{n-1}\})f(\{D_1, D_2, \ldots, D_{n-1}\}) \tag{7.22}$$

$f(\{D_1, D_2, \ldots, D_{n-1}\})$ is maximised before the nth iteration, and $f(\{D_n|D_1, D_2, \ldots, D_{n-1}\})$ is maximised at the nth iteration. So the joint possibility $f(\{D_1, D_2, \ldots, D_n\})$ is maximised, which means that the distance set $\{D_1, D_2, \ldots, D_n\}$ is closest to the prescribed log normal distribution (determined by μ and σ in Eq.7.11).

However, the conditional possibility $f(\{D_n|D_1, D_2, \ldots, D_{n-1}\})$ is not easy to calculate. In practice, we define a penalty function to regularise the the conditional possibility function. It follows that if the distances d obey a log-normal distribution, its logarithm, $\log(d)$ should conform a normal distribution, which has a percentage map as Figure 7.15

As proposed above, the distances in $\{D_n\}$ $(n = 1, 2, \ldots)$ are assumed to be mutually independent, so we can consider them separately. Let's start with the distance between the nth circle and the first vessel circle. The centre of the nth circle will be selected from the image field. For each pixel in the image field, the distance to the centre of the first vessel circle can be determined and d_i (i traverses all pixels in the image field) could be calculated by subtracting the radii r_1, r_n from these distances. d_i (and $\log d_i$) can have any value and can fall in different regions in the percentile interval. To ensure that its logarithm obeys a normal distribution conditioned by the distribution formed by

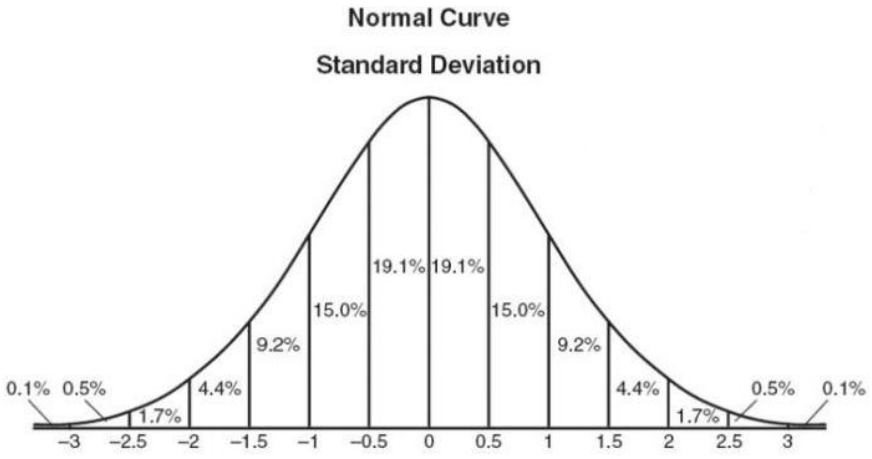

Figure 7.15: Normal distribution with percentile, the x-axis unit is σ, the origin is μ

the existing distances (i.e. those generated by the former (n-1) circles), it is natural to reward it when it falls in the interval that is less occupied and penalise it when it falls in an interval which is full or over occupied. With this in mind, we designed the following penalty function:

$$p(log(d_i)) = p(norm_{\xi_i}) - p(\xi_i). \tag{7.23}$$

We divided the normal distribution into 14 intervals as shown in Figure 7.15, and we calculated the percentages that are actually occupied by existing distances in these interval $p(\xi)$. When the value of $\log(d_i)$ falls in an interval ξ_i then we calculate the penalty function value according to Eq.7.23, i.e. the percentage in that interval under the normal distribution $p(\text{norm}_{\xi_i})$ minus the percentage currently occupied $p(\xi_i)$.

We perform the above calculation for the whole field and it yields a matrix denoted d_{n1}. Similarly, we calculate d_{n2} for distances between the nth circle and the second circle, ..., and $d_{n(n-1)}$. We measure the conditional possibility function $f(\{D_n|D_1, D_2, \ldots, D_{n-1}\}$ by summing all the matrix up, and determine (i_n,j_n) with the maximum value in this matrix. And we stop the iteration when the maximum value in this matrix falls below zero.

The steps described above can be translated into the following pseudo code:

place the first circle randomly at (i_1,j_1);

generate r_1 and r_2 from prescribed radius distribution and assign them as radius of the first and second circle;

for every (i,j) in the field **do**

if $\sqrt{(i-i_1)^2+(j-j_1)^2} - r_1 - r_2 \leq 0$ **then**

p(i,j)=$-\infty$;

else

$p(i,j) = \frac{1}{\sigma\sqrt{2\pi}} e^{-\frac{(log(\sqrt{(i-i_1)^2+(j-j_1)^2}-r_1-r_2)-\mu)^2}{2\sigma^2}}$;

end if

end for

select (i_2,j_2) randomly from the pool of values which maximize p(i,j);

place the second circle at (i_2,j_2);

generate r_3 from prescribed radius distribution and assign it as radius of the third circle;

repeat

calculate the distances of each pairs of vessels;

count the number of distances that fall within each intervals (e.g. $\mu \pm 0.5\sigma$, $\mu \pm \sigma$, $\mu \pm 1.5\sigma$, $\mu \pm 2\sigma$, $\mu \pm 2.5\sigma$, $\mu \pm 3\sigma$) of the prescribed inter vessel distance distribution;

generate r_n from prescribed radius distribution and assign it as radius of the nth circle;

for every (i,j) in the field **do**

for k=1 to n-1 **do**

calculate the potential distances with former kth circles $d_{k,i,j}$;

calculate value of p(log($d_{k,i,j}$)) (Eq. 7.23);

end for

caculate the conditional possibility potential matrix $M = \sum_{k=1}^{n-1} p(log(d_{k,i,j}))$

end for

select (i_n,j_n) randomly from the pool of values which maximize M;

place the nth circle at (i_n,j_n);

until max{ M } <0

We simulated a 2D vascular map in a 100 × 100 grid with each pixel corresponding to 2.5μm × 2.5μm area. This algorithm is found to be able to generate a vasculature map with prescribed distribution parameters (Figure 7.16):

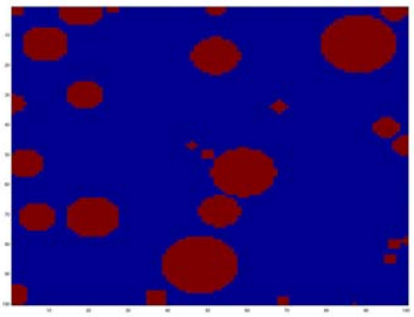

(a) Vascular map

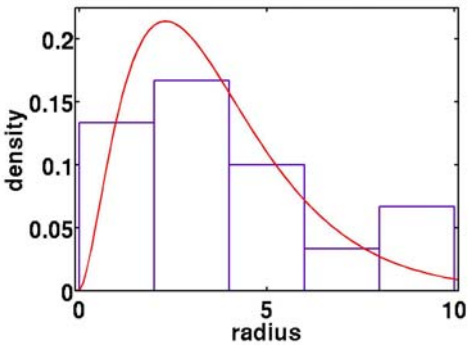

(b) Generated vessel radius

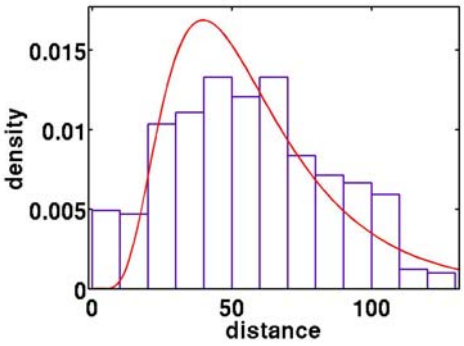

(c) Generated vessel distance

	prescribed		generated	
	μ/k	σ/θ	μ/k	σ/θ
distance	4	0.5	3.95	0.52
radius	3	1.5	2.68	1.37

(d) Parameter table

Figure 7.16: Generation of 2D vascular map.

It is shown in Figure 7.16 that our 2D blood vessel map generator can produce 2D blood vessels with radii and inter-vessel distances that approximately follow the prescribed statistical distribution.

7.2.2 2D Oxygen Map

We simulated the oxygen distribution following the spatio-temporal model we developed in Chapter 6. The parameters we used in the 2D oxygen simulation are listed in Table 7.2:

Parameter	Symbol	Value	Reference
O_2 Diffusion coefficient	D_{O_2}	$2 \times 10^{-9} m^2/s$	Tannock (1972)
Maximum O_2 consumption rate	V_{max}	15mmHg/s	Daşu *et al.* (2003)
O_2 Michaelis constant	K_m	2.5mmHg/s	Daşu *et al.* (2003)

Table 7.2: Parameters for 2D oxygen simulation in vasculated tissue.

The distribution of oxygen was simulated by solving the partial differential equations shown in Eq.7.24:

$$\frac{\partial}{\partial t} O_{PE}(s,t) = D_{O_2} \nabla^2 O_{PE}(s,t) - \left(\frac{V_{max} O}{O + K_m} \right) O_{PE}(s,t), \tag{7.24}$$

with the following boundary conditions:

$$\begin{array}{ll} O_{PE} = 40\text{mmHg}, & \text{for vascular voxels Dewhirst } \textit{et al.} \text{ (1999)} \\ & ; \\ O_{PE} \geqslant 0, & \text{for tissue voxels ;} \\ \frac{\partial}{\partial s} O_{PE}(s,t) = 0. & \text{for boundary voxels (Neumann).} \end{array}$$

We simulated the oxygen distribution on the generated 2D vascular map using the Euler method. In order to simplify notation, we use O to represent $O_{PE}(s,t)$. Eq.7.24 essentially consists of two parts: a diffusion factor D, and a consumption factor C, both of which are functions of the oxygen concentration O. So Eq.7.24 can be simplified to Eq.7.25:

$$\frac{\partial}{\partial t} O = D(O) - C(O) = f(O). \tag{7.25}$$

To implement the Euler method, we divided the simulation period T into n sub periods, each lasting for dt seconds. Within each sub-period, we calculated the spatial diffusion $D(O)$ and the oxygen consumption $C(O)$. Then the oxygen concentration at the end of $(n+1)$th period can be calculated as Eq.7.26:

$$O_{n+1} = \max(O_n + f(O_n) \times dt, 0). \tag{7.26}$$

We set $dt = 0.00075$ seconds and simulated the oxygen distributing process of 1.5 seconds (2000 iterations). The final oxygen spatial distribution and variation of average oxygen tension through time are shown in Figure 7.17

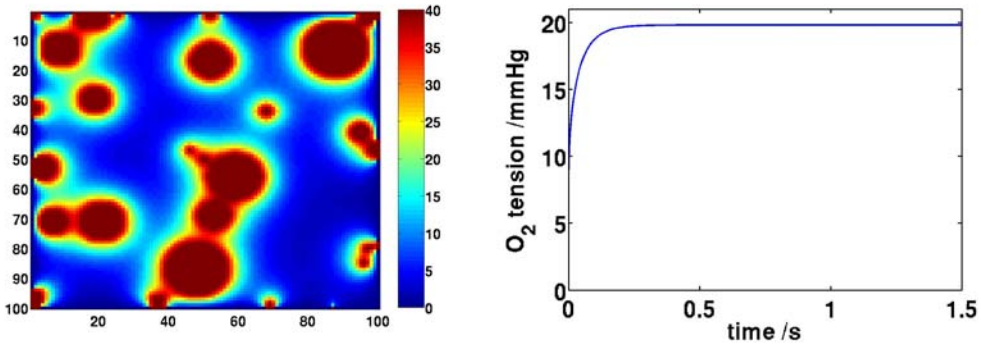

(a) Oxygen map after 1.5 seconds (b) Average O_2 tension through time

Figure 7.17: 2D oxygen map.

From Figure 7.17, it can be seen that the oxygen distribution process reaches equilibrium after ca.0.25 seconds. At equilibrium, the average tissue oxygen tension is approximately 20 mmHg.

7.2.3 2D Fmiso Map

In a similar way, we have simulated the 2D Fmiso distribution based on the spatio-temporal model we developed in Chapter 6. The Fmiso distribution process is modelled as a 2-tissue compartment model (Figure 7.18).

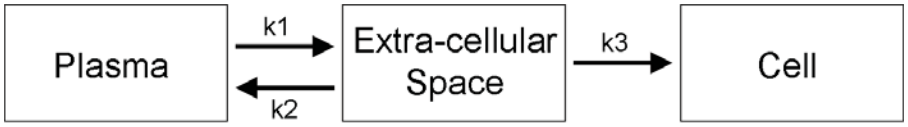

Figure 7.18: 2-tissue compartment model describing the distributing process of Fmiso

The partial differential equations describing this process are given by Eqs.7.27 and 7.28

$$\frac{\partial}{\partial t}C_E(s,t) = k_1 C_P(t) - (k_2+k_3)C_E(s,t) + D_{Fmiso}\nabla^2 C_E(s,t), \quad (7.27)$$

$$\frac{\partial}{\partial t}C_C(s,t) = k_3 C_E(s,t), \quad (7.28)$$

where C_P,C_E and C_C denote the Fmiso concentration in plasma, extra-cellular space, and cell compartment respectively. D_{Fmiso} is the diffusion coefficient of Fmiso in the tumour area. k_1 and k_2 are related to the rates of Fmiso diffusion across the blood vessel membrane. k_3 is the retention rate of Fmiso and is modelled as a function of oxygen tension.

The inter-compartment mass exchange rates k_1, k_2 and k_3 of Fmiso have been estimated in brain tumours (Bruehlmeier *et al.*, 2004). Though the transport kinetics could vary depending on the types of tumours and tissues, we assume that their values should not be dramatically different from those in brain tissue. As reported in Bruehlmeier *et al.* (2004), k_1 is in range of 0.023min^{-1} to 0.183min^{-1}; k_2 ranges from 0.036min^{-1} to 0.442min^{-1}. We performed linear regression of k_1,k_2, which is shown in Figure 7.19

It is reasonable to suppose that because of the brain blood barrier, tumour in normal tissues should have values of k_1,k_2 similar of that of meningioma, so we used $k_1 = 0.2\text{min}^{-1}(0.0033\text{s}^{-1})$ and calculated k_2 according to the regression formula to be $0.4112\text{min}^{-1}(0.0069\text{s}^{-1})$.

Bruehlmeier *et al.* (2004) also estimated the retention rates of Fmiso in cells. However, Bruehlmeier *et al.* (2004) fitted their data assuming reversible binding of Fmiso in cells.

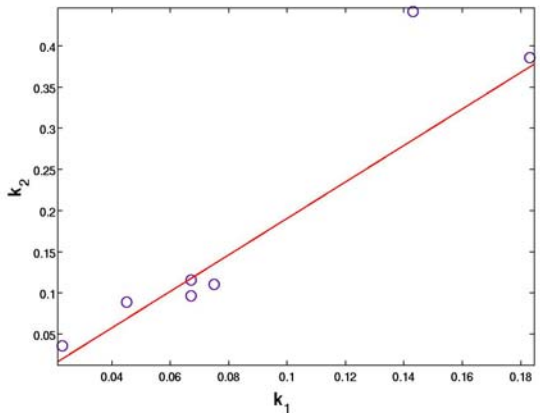

Figure 7.19: Linear regression of k_1 and k_2. k_2=2.214k_1-0.03058, R^2=0.9766.

To adapt their kinetic estimates to our assumption of irreversible binding of Fmiso, we used the difference of the on and off rates as Fmiso's irreversible binding rate in our model (k_3). Then, their estimates suggest that k_3 falls in the range of 0.001min^{-1} to 0.067min^{-1}. This range agrees with the estimates proposed by Casciari *et al.* (1995), where the author proposed that k_3 is between 0.002min^{-1}. and 0.125min^{-1}.

As we noted in the previous chapter, Casciari *et al.* (1995)'s formula did not account for the necrosis effect on cells under extremely hypoxic conditions. However, for simplicity we assume the necrosis effect in vascularised tissues is not as dominant a factor as is observed in multicellular spheroids. So we used the form proposed by Casciari:

$$k_3 = \frac{k_a k'_c}{O + k'_c}, \tag{7.29}$$

where k_a and k'_c are reaction rates of Fmiso and nitro radical, which is an intermediate product. Casciari *et al.* (1995) obtained k_a and k'_c from V79 cells grown in monolayers, which are 0.145min^{-1} and 2710 ppm respectively. We calculated k_3 based on the simulated O_2 distribution map (Figure 7.17). The parametric map of k_3 is shown in Figure 7.20.

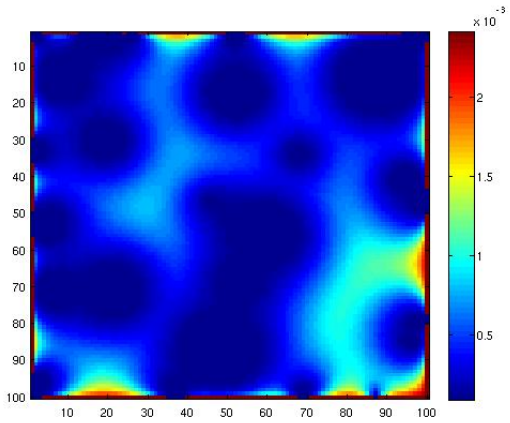

Figure 7.20: 2D k_3 parametric map.

The calculated k_3 has values between 0.0057 min^{-1} and 0.145 min^{-1} which agree with the upper and lower limits of k_3 proposed by Casciari *et al.* (1995).

We used the plasma input function as proposed by (Wang *et al.*, 2009), where the plasma input function was modelled as an analytical function:

$$CP(t) = A_0 t e^{-C_0 t} + \sum_{i=1}^{N} A_i (e^{-C_{1i} t} - e^{-C_{2i} t}), \tag{7.30}$$

where A_0's unit is $Bq/ml/min$, A_i's units are Bq/ml, and C_0, C_{1i}, C_{2i}'s units are min^{-1}.

We used the parameters suggested in Wang *et al.* (2009) and produced an input function as shown in Figure 7.21

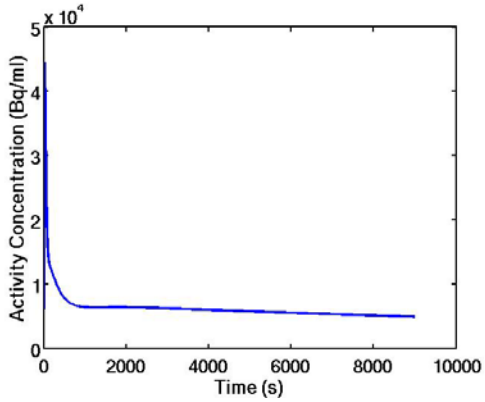

Figure 7.21: Plasma input function of Fmiso. Reproduced from Wang *et al.* (2009).

We used the Euler method to simulate the distribution process of Fmiso on the 2D vascular map following the partial differential equations Eq.7.27 and 7.28. Depending on their positions, the pixels in the simulation grid are divided into three categories (Figure 7.22):

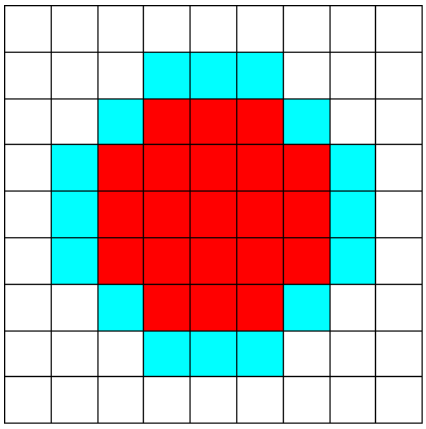

Figure 7.22: The simulation grid.

1. The red area denotes the blood vessel,with the tracer's concentration given by(Eq.7.31):

$$CP(t) = A_0 t e^{-C_0 t} + \sum_{i=1}^{N} A_i (e^{-C_{1i} t} - e^{-C_{2i} t}). \tag{7.31}$$

2. The blue area denotes the tissue area which is directly adjacent to the blood vessel. For these voxels, there is mass exchange with the blood vessel, so the concentration of tracer is expressed as Eq.7.32

$$\begin{aligned} \frac{\partial C_{E,t}}{\partial t} &= (k_1 C_{P,t} - k_2 C_{E,t} + D_{Fmiso} \nabla^2 C_{E,t} - k_3 C_{E,t}), \\ C_{E,t+1} &= \max(C_{E,t} + \frac{\partial C_{E,t}}{\partial t} \times dt, 0), \\ \frac{\partial C_{C,t}}{\partial t} &= k_3 C_{E,t}, \\ C_{C,t+1} &= \max(C_{C,t} + \frac{\partial C_{E,t}}{\partial t} \times dt, 0), \end{aligned} \tag{7.32}$$

where k_1, k_2 are the efflux and influx rates of Fmiso across the blood vessel membrane, and k_3 is the retention rate of Fmiso that is modelled as a function of oxygen.

3. The remaining area (white pixels) is normal tissue where the tracer's concentration is related only to the diffusion and cellular retention, so can be expressed as Eq.7.33:

$$\begin{aligned}
\frac{\partial C_{E,t}}{\partial t} &= D_{Fmiso}\nabla^2 C_{E,t} - k_3 C_{E,t}, \\
C_{E,t+1} &= \max(C_{E,t} + \frac{\partial C_{E,t}}{\partial t} \times dt, 0), \\
\frac{\partial C_{C,t}}{\partial t} &= k_3 C_{E,t}, \\
C_{C,t+1} &= \max(C_{C,t} + \frac{\partial C_{E,t}}{\partial t} \times dt, 0).
\end{aligned} \tag{7.33}$$

We assumed that the tumour tissue density ρ_T is 1.05g/ml (DeVries *et al.*, 2003) and chose the time step at each iteration to be 0.001 seconds. We simulated Fmiso's distributing process for 30 minutes in Matlab® (R2008a).

The temporal variations of trapped Fmiso and the diffusible Fmiso concentration are plotted as time activity curves (Figure 7.23(a), (b)). The total Fmiso concentration is the area weighted sum of plasma, trapped and diffusible Fmiso concentrations. The total Fmiso time activity curve (TAC) is plotted as temporal variations of total Fmiso concentration (Figure 7.23(c)).

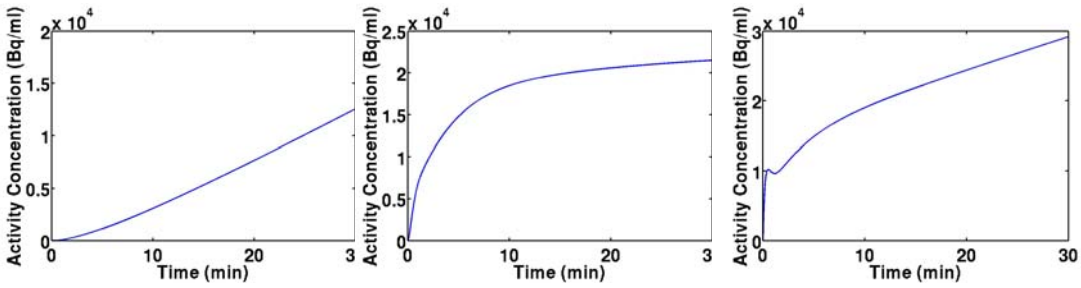

(a) C_A (b) C_E (c) TAC

Figure 7.23: Time activity curves of trapped Fmiso (a), diffusible Fmiso (b) and total Fmiso (c). The total Fmiso concentration is the area weighted sum of C_P,C_A and C_E.

The spatial distributions of trapped Fmiso and diffusible Fmiso 30 minutes after injection are shown in Figure 7.24(a) and (b). We assigned each vessel pixel with the plasma Fmiso concentration at 30 minute and obtained the total Fmiso spatial distribution map by summing the distributions of trapped, diffusible and plasma Fmiso (Figure 7.24(c)).

Note the concentrations of Fmiso in the distribution map are described in terms of Bq per pixel.

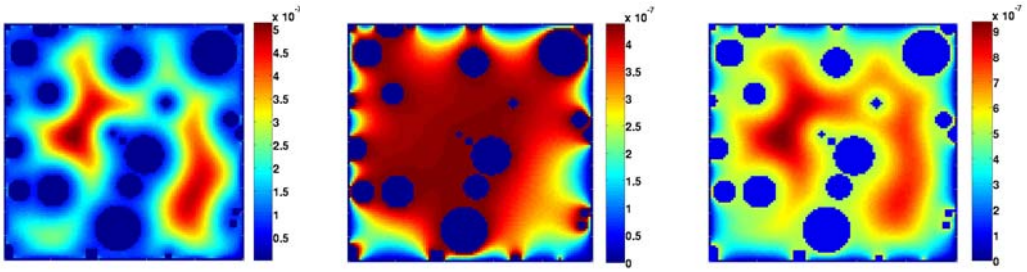

(a) C_A (b) C_E (c) Spatial distribution of Fmiso

Figure 7.24: Time activity curves of trapped Fmiso (a), diffusible Fmiso (b) and total Fmiso (c). The total Fmiso concentration is the area weighted sum of C_P,C_A and C_E.

7.3 3D Simulation

7.3.1 3D Oxygen Simulation

The 3D blood vessels were segmented using the methods that form part of the GUI developed in Chapter 4. We implemented oxygen simulation on the 3D vessel map shown in Figure 7.25:

Figure 7.25: Visualization of the 3D vessel map using maximum intensity projection method.

The distribution process of oxygen is simulated by solving the partial differential

equations shown in Eq.7.34

$$\frac{\partial}{\partial t}O_{PE}(s,t) = D_{O_2}\nabla^2 O_{PE}(s,t) - \left(\frac{V_{max}O}{O+K_m}\right)O_{PE}(s,t), \tag{7.34}$$

with the following boundary conditions:

$O_{PE} = 40mmHg,$	for vascular voxels (Dewhirst *et al.*, 1999);
$O_{PE} \geqslant 0,$	for tissue voxels;
$\frac{\partial}{\partial s}O_{PE}(s,t) = 0.$	for boundary voxels (Neumann).

We implemented the Runge-Kutta method with adaptive step size control. The fifth order Runge-Kutta methods for oxygen simulation can be written as Eq.7.35-7.40:

$$O_{n+1}^{(1)} = \max(O_n + dt \times f(O_n), 0) \tag{7.35}$$

$$O_{n+1}^{(2)} = \max(O_n + dt \times f((1-b_{21})O_n + b_{21}O_{n+1}^{(1)}), 0) \tag{7.36}$$

$$\ldots \tag{7.37}$$

$$O_{n+1}^{(6)} = \max(O_n + dt \times f((1-\sum b_{6j})O_n + \sum b_{6j}O_{n+1}^{(j)}), 0) \tag{7.38}$$

$$O_{n+1}^{5th} = (1-\sum c_i)O_n + \sum c_i O_{n+1}^{(i)} \tag{7.39}$$

$$O_{n+1}^{4th} = (1-\sum c_i^*)O_n + \sum c_i^* O_{n+1}^{(i)}, \tag{7.40}$$

where the interpolation parameters have the values listed in Table 7.1

We simulated the oxygen distribution and visualized the result using the volume ray casting method (Figure 7.26).

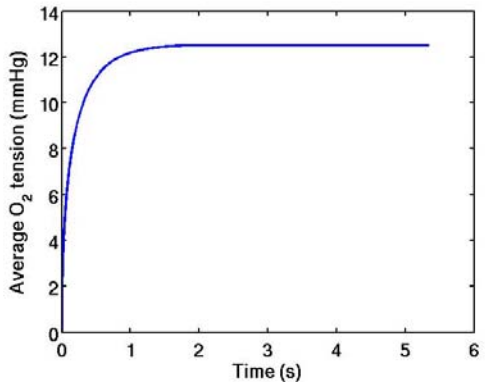

(a) Average O_2 tension

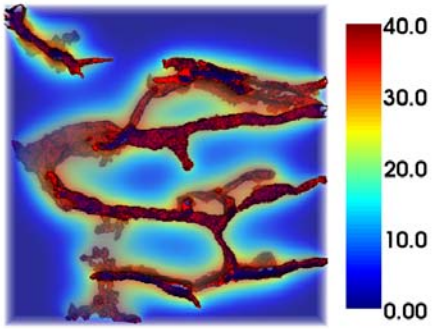

(b) Final O_2 distribution

Figure 7.26: Average O_2 tension and the final distribution of oxygen. The 3D spatial distribution of oxygen is visualized using the volume ray casting method.

Figure 7.26 shows that the oxygen distribution process reaches equilibrium after 2 seconds, and the average oxygen tension in the tumour region is 12.5127 mmHg (std: 11.8170 mmHg). We observed that the oxygen tension is approximately 0mmHg at the image boundaries because of the longer distance from the blood vessel. We consider that for *in vivo* simulation, tumour vessels should not be treated in isolation with its neighbouring regions. Instead, we assume that the neighbouring region has a similar vessel structure, which gives a similar average oxygen tension at equilibrium. Thus we impose:

$$O_{PE} = max(O_{PE}, 12.5127\text{mmHg}) \qquad \text{for boundary voxels,} \tag{7.41}$$

and once more simulated the oxygen distribution process. We present the results in Figure 7.27:

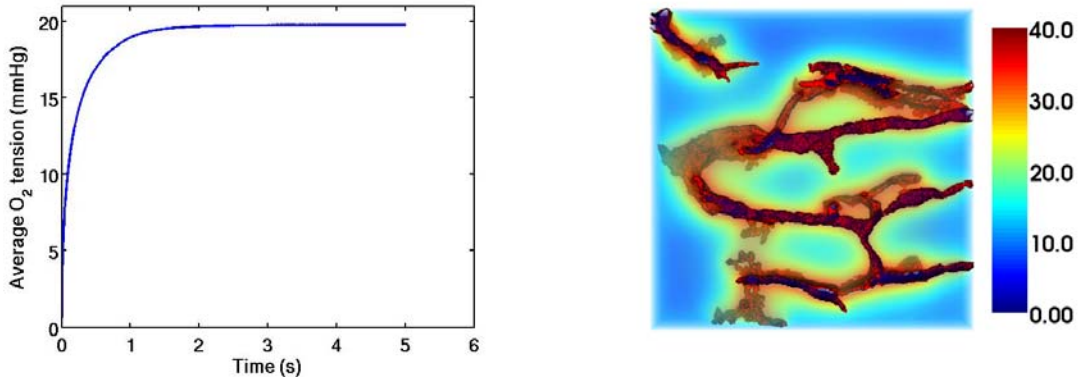

(a) Average O_2 tension (b) Final O_2 distribution

Figure 7.27: Average O_2 tension and the final distribution of oxygen. The 3D spatial distribution of oxygen is visualized with volume ray casting method.

Figure 7.27 shows that the oxygen distribution process reaches equilibrium after 2 seconds, the average oxygen tension in the tumour tissue is 19.7625 mmHg (std: 8.6635 mmHg) which is close to the values measured experimentally (Bussink *et al.*, 2000). We consider that this supports the realism of oxygen delivery *in vivo* and use it to calculate the Fmiso binding kinetics.

We have compared the Euler method and adaptive step control Runge-Kutta method on CPU (Intel® Core™ 2 processor duo, 2.4GHz) and GPU (Nvidia® GeForce® 9400M). We simulated the oxygen distributing process for 0.2 seconds and compared the computation time of each method in Figure 7.28.

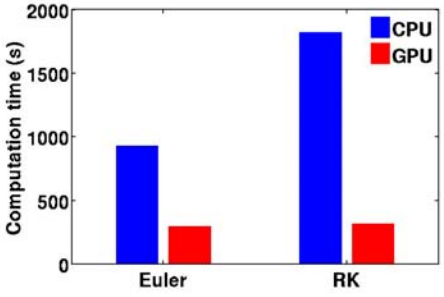

Figure 7.28: Comparison of computation time.

From Figure 7.28 it is seen that the parallel implementation on a GPU is much faster than the serial implementation on a CPU. It should be noted that the Nvidia®

GeForce® 9400M is only a moderate speed GPU which only incorporates 16 processing cores. It is worth mentioning that the current Nvidia's "fastest" graphics processor Nvidia® GeForce® GTX 480 contains 480 processing cores and only costs ca.$500, which gives the potential for further acceleration of GPU parallel computing in work such as this.

The adaptive step control Runge-Kutta method requires a longer time to compute than the Euler method on both the CPU and GPU implementations. This is because the step length of the Euler method was set to be 0.004 seconds, which was determined from implementations of the Runge-Kutta method. With a similar step length, the Runge-Kutta method does not outperform the Euler method because more computation steps are executed at each iteration in the adaptive step control Runge-Kutta method. However, it is difficult to determine the optimal step length in the Euler method without prior knowledge. In contrast, the adaptive step control Runge-Kutta method can automatically determine the step lengths to ensure the truncation errors within the required precision (Figure 7.29).

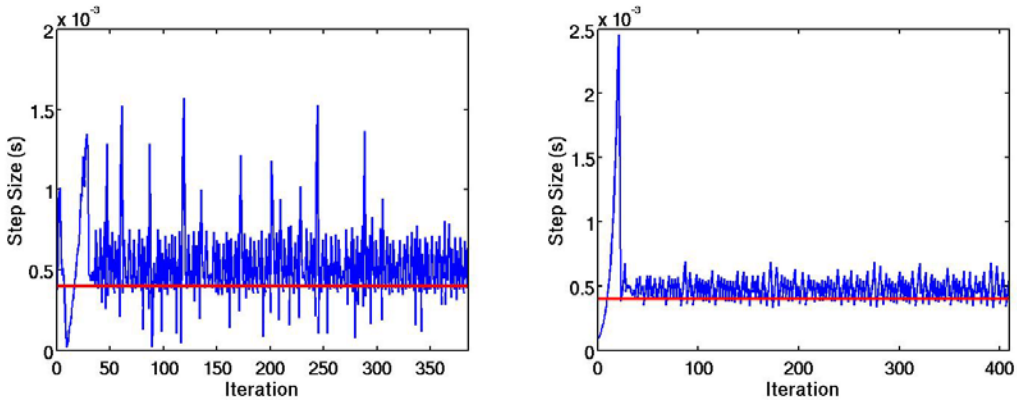

(a) CPU (b) GPU

Figure 7.29: Comparison of step size of embedded Runge-Kutta method (blue) with that of Euler method (red) in CPU (C) and GPU (CUDA) implementations.

The numerical accuracy of each implementation is compared in Figure 7.30

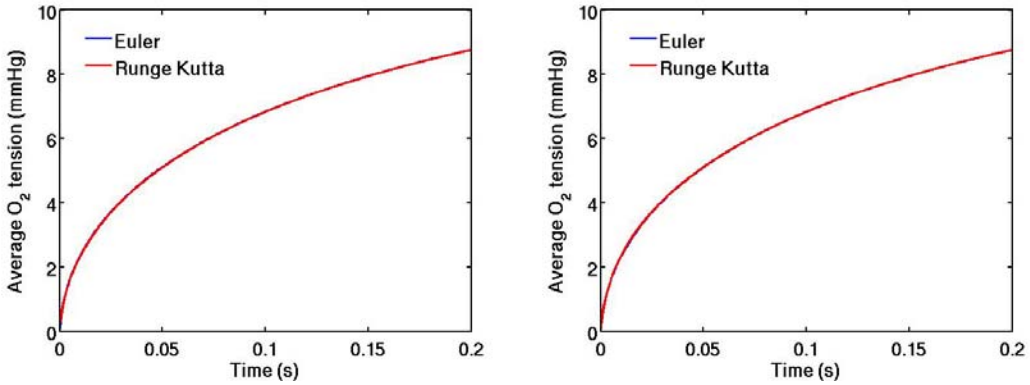

(a) CPU (b) GPU

Figure 7.30: Comparison of numerical accuracy.

It has been found that simulation results are very close to each other with different implementations. In 2D simulations, the step length was assigned a small enough value to ensure that the truncation error is not so large as to diverge the simulation iterations. The under-estimated step length will lead to an increased number of iterations. This has not been a critical problem in the 2D simulation. However, the computational burden required for 3D simulation rises dramatically compared with 2D. It can save much computation time if an optimized step length is chosen at each iteration. Thus we found adaptive step control Runge-Kutta suitable for our 3D simulations. Given the substantial reduction of computation time with the parallel method, we chose to implement the 3D Fmiso simulation using the adaptive step control Runge-Kutta in parallel on the GPU.

7.3.2 3D Fmiso Simulation

The PDEs describing the distribution process of Fmiso are written as Eq.7.42,7.43:

$$\frac{\partial}{\partial t}C_E(s,t) = k_1 C_P(t) - (k_2+k_3)C_E(s,t) + D_{Fmiso}\nabla^2 C_E(s,t), \quad (7.42)$$

$$\frac{\partial}{\partial t}C_C(s,t) = k_3 C_E(s,t), \quad (7.43)$$

with boundary conditions depicted as follows:

$C_P(t) = A_0 te^{-C_0 t} + \sum_{i=1}^{N} A_i(e^{-C_{1i}t} - e^{-C_{2i}t})$, for vascular voxels (Wang *et al.*, 2009);
$C_E(s,t) \geqslant 0, C_C(s,t) \geqslant 0$, for tissue voxels;
$\frac{\partial}{\partial s} O_{PE}(s,t) = 0$, for boundary voxels (Neumann).

The parameters used in the 3D Fmiso simulation are listed in Table 7.3

Parameter	Symbol	Value	Reference
Fmiso vessel outflux permeability	k_1	$0.0033ml \cdot s^{-1} \cdot g^{-1}$	Bruehlmeier *et al.* (2004)
Fmiso vessel influx permeability	k_2	$0.0069s^{-1}$	Bruehlmeier *et al.* (2004)
Fmiso reaction kinetics	k_a	$0.0024s^{-1}$	Casciari *et al.* (1995)
Fmiso reaction kinetics	k_c'	2710ppm	Casciari *et al.* (1995)
Tumour tissue density	ρ_T	1.05 g/ml	DeVries *et al.* (2003)
Fmiso diffusion coefficients	D_{Fmiso}	$5 \times 10^{-11} m^2/s$	Cowan *et al.* (1996)
Plasma Fmiso in put function	C_P	-	Wang *et al.* (2009)

Table 7.3: Parameters for the3D Fmiso simulation in vascularised tissue.

We calculated k_3 based on the simulated O_2 distribution map as in Figure 7.27. The parametric map of k_3 is presented in Figure 7.31

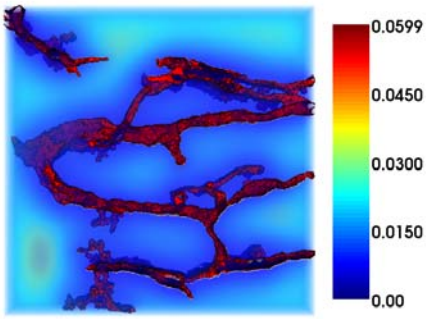

Figure 7.31: Parametric map of k_3, visualized with volume ray casting method.

Our simulated k_3 values are between 0.0057 min^{-1} and 0.0599 min^{-1}, which agrees with the upper and lower limits of k_3 proposed by Casciari *et al.* (1995).

We used an adaptive step control Runge-Kutta method in the 3D Fmiso simulation. Since $\frac{\partial C_{C,t}}{\partial t}$ is a function of C_E (thus the truncation error of C_C also depends on C_E), we can only consider the truncation error of $C_{E,t}$ during the Runge-Kutta method. Following the same space discretization scheme as in the 2D Fmiso simulation, the adaptive step control Runge-Kutta method is described as follows:

1. With blood vessel voxels, Fmiso's concentration is determined by the plasma input function proposed by Wang *et al.* (2009):

$$C_P(t) = A_0 t e^{-C_0 t} + \sum_{i=1}^{N} A_i (e^{-C_{1i} t} - e^{-C_{2i} t}), \tag{7.44}$$

where A_0's unit is $Bq/ml/min$, A_i's units are Bq/ml, and C_0, C_{1i}, C_{2i}'s units are min^{-1} and we used the parameteres suggested in Wang *et al.* (2009)

2. With vessel adjacent tissue voxels. There is mass exchange between blood vessel voxels. The Runge Kutta iteration equations are written as:

$$\begin{aligned}
\frac{\partial C_{E,t}}{\partial t} &= (k_1 C_{P,t} - k_2 C_{E,t} + D_{Fmiso} \nabla^2 C_{E,t} - k_3 C_{E,t}) = f(C_{E,t}), \\
C^{(1)}_{E,t+1} &= \max(C_{E,t} + dt f(C_{E,t}), 0), \\
C^{(2)}_{E,t+1} &= \max(C_{E,t} + dt \times f((1 - b_{21}) C_{E,t} + b_{21} C^{(1)}_{E,t+1}), 0), \\
&\ldots, \\
C^{(6)}_{E,t+1} &= \max(C_{E,t} + dt \times f((1 - \sum b_{6j}) C_{E,t} + \sum b_{6j} C^{(j)}_{E,t+1}), 0), \\
C^{5th}_{E,t+1} &= (1 - \sum c_i) C_{E,t} + \sum c_i C^{(i)}_{E,t+1}, \qquad (7.45) \\
C^{4th}_{E,t+1} &= (1 - \sum c^*_i) C_{E,t} + \sum c^*_i C^{(i)}_{E,t+1}, \qquad (7.46) \\
C_{err,E,t+1} &= C^{5th}_{E,t+1} - C^{4th}_{E,t+1}, \qquad (7.47) \\
\frac{\partial C_{C,t}}{\partial t} &= k_3 C_{E,t}, \\
C_{C,t+1} &= \max(C_{C,t} + \frac{\partial C_{E,t}}{\partial t} \times dt, 0). \qquad (7.48)
\end{aligned}$$

3. With other tissue voxels, there is only inter-voxel mass exchange determined by the

diffusion process. The Runge-Kutta iteration equations are written as:

$$\begin{aligned}
\frac{\partial C_{E,t}}{\partial t} &= D_{Fmiso}\nabla^2 C_{E,t} - k_3 C_{E,t} = f(C_{E,t}),\\
C^{(1)}_{E,t+1} &= \max(C_{E,t} + dt \times f(C_{E,t}), 0),\\
C^{(2)}_{E,t+1} &= \max(C_{E,t} + dt \times f((1-b_{21})C_{E,t} + b_{21}C^{(1)}_{E,t+1}), 0),\\
&\ldots,\\
C^{(6)}_{E,t+1} &= \max(C_{E,t} + dt \times f((1-\sum b_{6j})C_{E,t} + \sum b_{6j}C^{(j)}_{E,t+1}), 0),\\
C^{5th}_{E,t+1} &= (1-\sum c_i)C_{E,t} + \sum c_i C^{(i)}_{E,t+1}, \qquad (7.49)\\
C^{4th}_{E,t+1} &= (1-\sum c^*_i)C_{E,t} + \sum c^*_i C^{(i)}_{E,t+1}, \qquad (7.50)\\
C_{err,E,t+1} &= C^{5th}_{E,t+1} - C^{4th}_{E,t+1}, \qquad (7.51)\\
\frac{\partial C_{C,t}}{\partial t} &= k_3 C_{E,t},\\
C_{C,t+1} &= \max(C_{C,t} + \frac{\partial C_{E,t}}{\partial t} \times dt, 0). \qquad (7.52)
\end{aligned}$$

The temporal variations of the trapped Fmiso and diffusible Fmiso concentrations are plotted as time activity curves (Figure 7.32(a), (b)). The total Fmiso concentration is the volume weighted sum of plasma, trapped and diffusible Fmiso concentrations. The total Fmiso time activity curve (TAC) is plotted as temporal variations of total Fmiso concentration (Figure 7.32(c)).

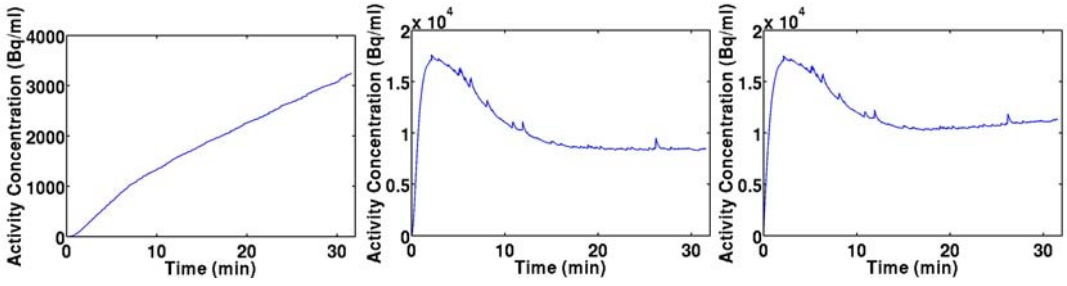

(a) C_A (b) C_E (c) TAC

Figure 7.32: Time activity curves of tapped Fmiso (a), diffusible Fmiso (b) and total Fmiso (c). The total Fmiso concentration is the volume weighted sum of C_P,C_A and C_E.

The simulated time activity curve is found not to be smooth but contains several glitches (Figure 7.32(c)). This may be caused by the max function we used in our

simulation. Max function leads to steps when Fmiso's concentration drops to negative value. These steps in space can be accumulated at some time which give rise to glitches in the simulated time activity curve.

The spatial distributions of trapped Fmiso and diffusible Fmiso at 30 minutes is shown in Figure 7.33(a) and (b). We assigned each vessel pixel with the plasma Fmiso concentration at 30 minutes and obtained the total Fmiso spatial distribution map by summing the distributions of trapped, diffusible and plasma Fmiso (Figure 7.33(c)). Note that the concentrations of Fmiso in the distribution map are described as Bq per voxel.

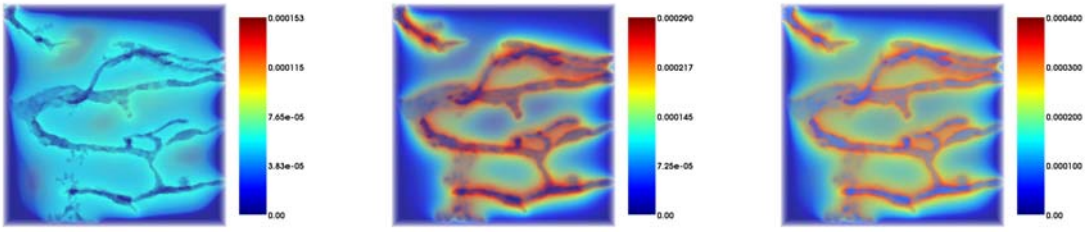

(a) C_A (b) C_E (c) Fmiso map

Figure 7.33: Spatial distribution of trapped Fmiso (a), diffusible Fmiso (b) and total Fmiso (c), all visualized with volume ray casting method.

Similar to the 3D oxygen simulation, if we consider the impact of neighbouring regions, we may impose the following boundary condition:

$$C_E(\mathbf{x}, t) = max(C_E(\mathbf{x}, t), C_E^{\text{iso}}(t)) \qquad \text{for boundary voxels,} \tag{7.53}$$

where $C_E^{\text{iso}}(t)$ is the average diffusible Fmiso concentration at time t in the simulation ignoring neighbor region effect.

With the boundary condition shown in Eq.7.53, we once again simulated the spatio-temporal distribution of Fmiso. The temporal variations of trapped Fmiso, diffusible Fmiso and total Fmiso concentration are plotted as in Figure 7.34:

As we used the simulation results in Figure 7.32(c) as boundary conditions, the glitches in Figure 7.34(c) is found to be amplified at similar temporal locations.

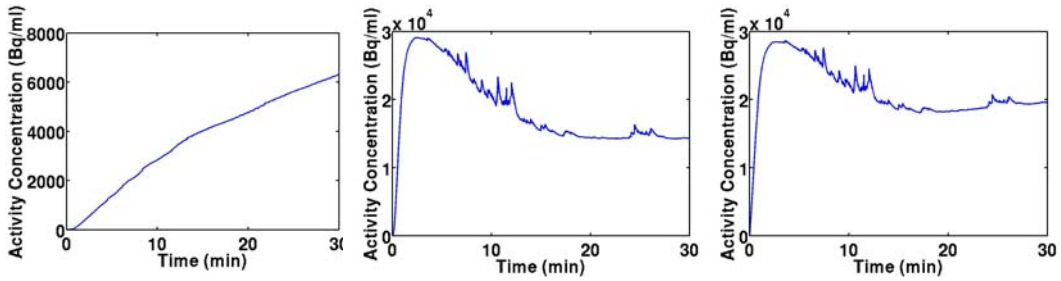

(a) C_A (b) C_E (c) TAC

Figure 7.34: Time activity curves of tapped Fmiso (a), diffusible Fmiso (b) and total Fmiso (c). The total Fmiso concentration is the volume weighted sum of C_P,C_A and C_E.

The simulated Fmiso spatial distribution map is shown in Figure 7.35. Unlike the results simulated in isolation from the neighbouring regions where concentrations of Fmiso at the boundary regions were approximately zero (Figure 7.33), Fmiso's distribution is more homogeneous when we considered the diffusion effect of neighbouring regions.

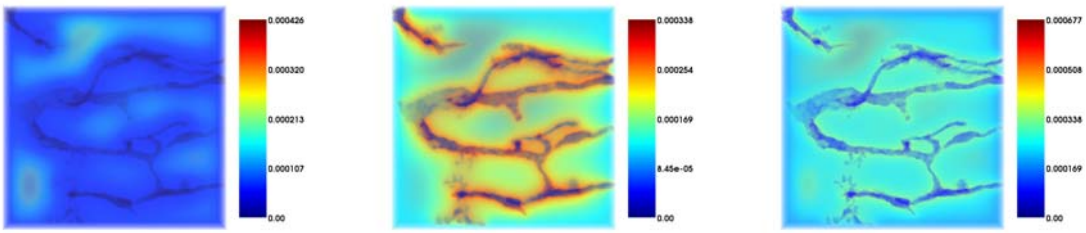

(a) C_A (b) C_E (c) Fmiso map

Figure 7.35: Spatial distribution of trapped Fmiso (a), diffusible Fmiso (b) and total Fmiso (c), all visualized with volume ray casting method.

7.4 Conclusion

The *in vivo* distributions of oxygen and Fmiso have been simulated in 2D and 3D vascular structures. The simulated Fmiso time activity curves were found to have similar shapes to those observed in Fmiso dynamic PET images and to those produced by conventional compartment models (Figure 7.36). This supports the reliability of the spatio-temporal model we developed in Chapter 6. We have implemented our simulation program using GPU technology. Though the 3D Fmiso simulation is still time consuming we believe the simulation time will be dramatically reduced when the program is executed on a more powerful GPU architecture.

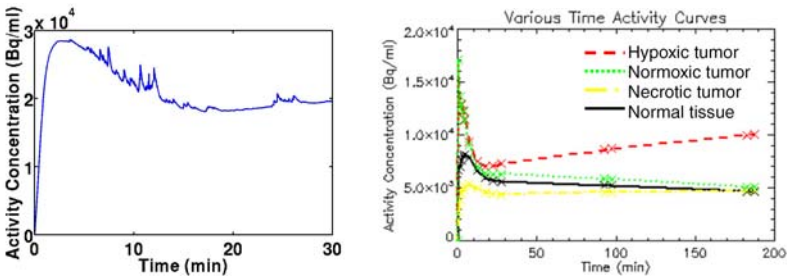

(a) (b)

Figure 7.36: Comparison of Time Activity Curves (TAC) obtained from our molecular simulation (a) and from conventional compartment models (b, reprinted from Wang *et al.* (2009), without permission). (a) and (b) are produced with the same plasma input function. The shape of TAC from our molecular simulation resembles that of hypoxic tumour in Wang's implementation. We think the discrepancies between (a) and (b) come from the different kinetic values assumed in our molecular simulation and Wang's implementation.

Chapter 8

Future Work

In this thesis, we have developed methods to analyse tumour microvessel structure based on microscope images. We proposed a set of metrics to quantitatively measure the changes to microvessel structures in response to drug treatment. Finally, we constructed a spatiotemporal model and simulated the distribution process of Fmiso on a 2D/3D microvessel map.

Based on the research described in this thesis, we believe that the following work could be accomplished in the near future:

8.1 Angiogenesis Research

As can be seen in Chapter 7, our 2D microvessel map generation algorithm is an entirely data-driven method. In other words, it generates a 2D microvessel map according to prescribed structural constraints. However, the structure of a microvessel is simply a consequence of the microvessel formation process, which itself is a result of the interplay between various angiogenic factors. Meanwhile, as we contended in Chapter 5, the distribution profiles of microvessel structural parameters also imply that these parameters are derived from some typical stochastic processes. It would be interesting to explore the biological/physiological mechanisms that have led to the specific statistics of microvessel geometry parameters.

Chaplain (2000) has developed a mathematical model of tumour induced angiogenesis. In his model, Chaplain focused on the so called *tissue response unit* which consists of epithelial cells, tumour angiogenic factors (TAF, e.g., a cytokine such as VEGF) and a matrix cell adhesion factor, fibronectin. Chaplain assumes that the interplay between these factors leads to angiogenesis around the tumour area. Chaplain denotes the endothelial cell density per unit area by n, the angiogenic factor concentration by c, and the fibronectin concentration by f. The migration of an endothelial cell is modelled by a discrete stochastic model:

$$\begin{aligned} n_{l,m,w}^{q+1} &= n_{l,m,w}^{q} P_0 + n_{l+1,m,w}^{q} P_1 + n_{l-1,m,w}^{q} P_2 + n_{l,m+1,w}^{q} P_3 && (8.1) \\ &\quad + n_{l,m-1,w}^{q} P_4 + n_{l,m,w+1}^{q} P_5 + n_{l,m,w-1}^{q} P_6, && (8.2) \end{aligned}$$

where q denotes the generation, and (l, m, w) denotes the spatial location, of an endothelial cell. P_0 is the probability of the endothelial cell to be stationary, P_1 is the probability of the endothelial moving west, P_2 moving east, P_3 north, P_4 south, P_5 up and P_6 down. Chaplain assigns another parameter P_b at each sprouting-tip to be the probability of generating a new sprout (branching). Chaplain points out that the endothelial movement probabilities P_0-P_6 are functions of local fibronectin and TAF concentration and P_b is dependent on local TAF concentration. The fibronectin and TAF's time functions are expressed as:

$$\begin{aligned} \frac{\partial f}{\partial t} &= \underbrace{\omega n}_{production} - \underbrace{\mu n f}_{binding/degradation}, && (8.3) \\ \frac{\partial c}{\partial t} &= \underbrace{-\lambda n c}_{uptake/binding}, && (8.4) \end{aligned}$$

where ω and μ denote, respectively, the production and clearance rates of fibronectin, and λ denotes the uptake rate of TAF by the endothelial cells. At any time, the space function of fibronectin is closely related to the vascular structure. Similarly, at any time

the space function of TAF is a diffusion function (whose source is the tumour cell) related to the vascular structure. Thus the endothelial migration process (Eq.8.2) is a Markov Random Process.

Chaplain has simulated tumour microvessel growth using his model. Based on the model we have developed, we can quantify the geometries of the simulated microvessel structures and then study the relationships between angiogenesis and the microvessel structure.

Meanwhile, it is possible to expand Chaplain's work to include gene regulation pathway modelling, such as the (EGFR)-RAS-phosphatidylinositol 3-kinase (PI3K)-AKT pathway. By reconciling the angiogenesis modelling and post-treatment microvessel structures, we could explore the pharmacological mechanisms of different vessel normalization drugs that act on this pathway.

8.2 Fluid Mechanics Model

As is suggested in Chapter 7, the geometry of blood vessels has an impact on the fluid mechanics of blood. Since oxygen and Fmiso are transported by the blood flow, the flow fields inside microvessels of different geometrical structures should be considered. Blood has a small Reynolds number in capillaries and blood flow is normally assumed to be laminar in micro-vessels (Manton, 2006). The 3D blood flow field in capillaries can then be simulated by solving the Navier-Stokes equations with continuity conditions (Jafari *et al.*, 2009). At bifurcations, the flow field can be simulated based on conservation laws of mass and momentum (Jafari *et al.*, 2008).

While flowing through the microvessels, the blood also osmoses from the arterioles, perfuses through the tissue, and is finally collected by the venules. In this process, Fmiso is actually carried by blood to different sites of tissues and reacts with the epithelial cells through the passage (Figure 8.1). It follows that the spatial distribution of Fmiso is actually engineered by blood perfusion rather than by the diffusion of Fmiso itself. It is

more appropriate to consider blood perfusion processes in modelling the spatiotemporal distribution of Fmiso.

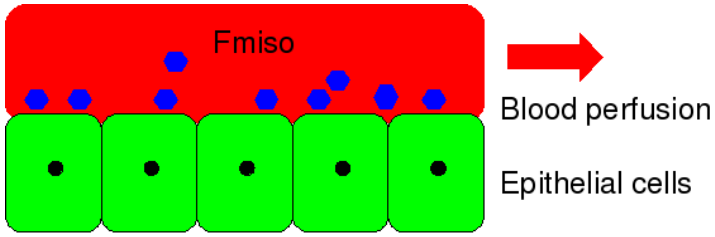

Figure 8.1: Fmiso is transported in blood perfusion to different tissue sites.

The perfusion process of blood has been studied by Pozrikidis & Farrow (2003). The extravasation flux was modelled according to Starling's law and the blood flow through the interstitium was modelled according to Darcy's law. The flow field in tissue can be constructed by solving a coupled system of integral and differential equations numerically (Pozrikidis & Farrow, 2003).

Taking into consideration the impact of blood flow, we propose a more complicated framework to model Fmiso's distribution on a given vascular structure (Figure 8.2).

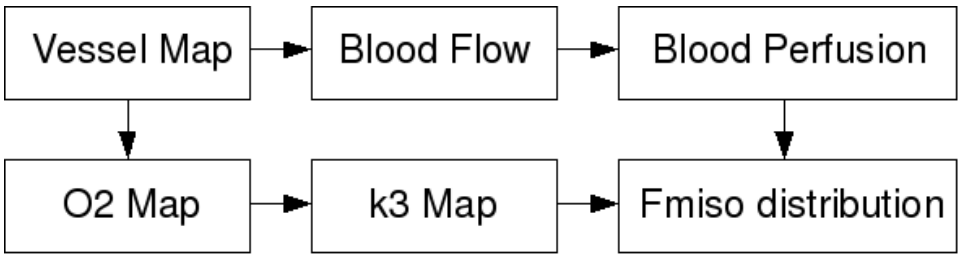

Figure 8.2: Correlate microvessel structures with PET images

For a given blood vessel map, the oxygen distribution map can be simulated based on the model we developed in Chapter 6. The oxygen concentration can then be used to calculate Fmiso's binding rates at each location based on the formulations proposed either by Casciari or Kelly. Meanwhile, the blood flow inside the blood vessels can be simulated by methods proposed by Jafari *et al.* (2008, 2009) and the blood perfusion in tissues can be simulated with methods proposed by Pozrikidis & Farrow (2003). Finally, the distribution of Fmiso can be simulated with the model we developed in Chapter

6, incorporating the blood perfusion field. We contend that this model would better describe the realistic Fmiso distribution process in spite of its mathematical complexity.

8.3 Structure vs Fmiso distribution

We have described a 2D vasculature map generation algorithm. This algorithm was shown to be capable of generating 2D vascular structures, whose radii and inter-vessel distances follow prescribed statistical distributions.

In 3D space, as the vascular structure is continuous, we could extend the algorithm proposed by Szczerba & Székely (2002) to generate a 3D blood vessel network whose structural parameters are constrained by prescribed probability distributions. With that in place we could perform Monte Carlo simulations to research the impact of individual geometrical parameters on the final Fmiso distribution. However, this is computationally expensive and would only be possible with more powerful GPUs or GPU clusters.

8.4 Tissue Scale Modelling

Our simulations have been carried out on a ROI that is on the micrometer scale. However, current PET image resolution is on the scale of millimetres. Since the PET image signal is related to tracer's concentrations, it would be interesting to construct synthetic -scale Fmiso distributions from our molecular simulations.

Shipley & Chapman (2010) have employed multiple-scale analysis method to model tissue-scale drug transport. It is based on the assumption that the macroscopic blood vessel network is formed from periodic micro-scale vascular structures (i.e. the vessel network is homogeneous). Although this may be the case in normal tissues, we consider that it is inadequate in tumour tissues where heterogeneous microvessel structures are frequently observed (Konerding *et al.*, 2001). We have proposed another approach to simulate tissue-scale Fmiso distribution which is based on Monte Carlo simulations under the assumption that the microvessel structure evolves smoothly along the distances to

the tumour centre. We believe that this method, with proper modelling, could be used to depict the tissue-scale transport of other drugs.

In a tissue-scale simulation, which has coarser resolution, our molecular simulation regions accounts only for sub-voxel volumes in the simulated image. If the time activity curves of these sub-voxel volumes could be modelled as functions of vessel geometrical parameters, we could predict the sub-voxel Fmiso concentration at each time point. Based on Monte Carlo simulations, tissue-scale Fmiso distribution maps at each time point could be constructed in similar way as mosaic pictures (Figure 8.3).

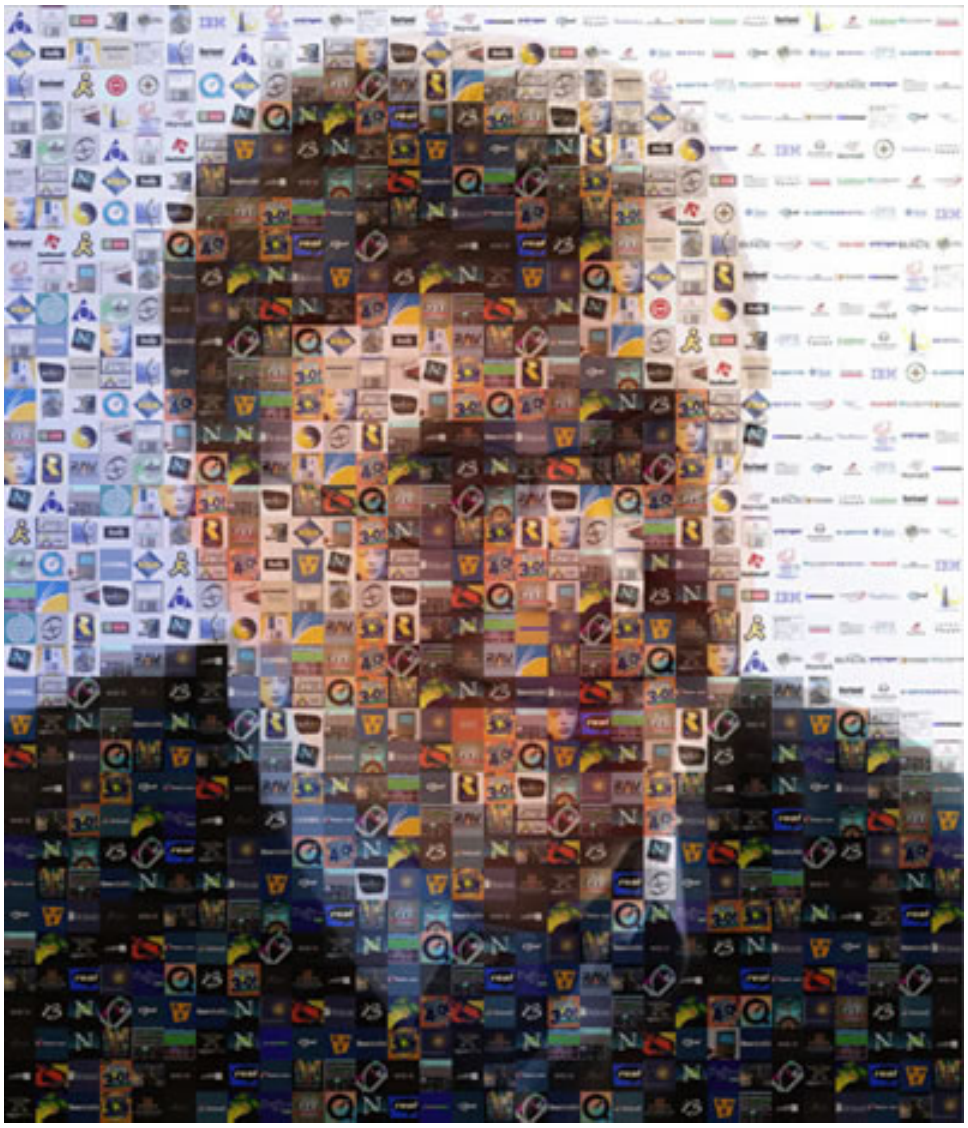

Figure 8.3: Mosaic picture of Bill Gates. Although each pixel is a small picture, a portray of Bill Gates could be perceived in larger scale.

In the tissue-scale Fmiso simulation, we contend that it is the smoothly changing microvessel structures in tumour tissues that have arrayed the sub-voxel Fmiso maps to exhibit images of the tissue-scale Fmiso map. The relationship between microvessel structure and spatiotemporal tissue-scale Fmiso distribution could be investigated. Since the PET signal is proportional to the tracer concentration, this could lead to a quantitative model from which one could infer microvessel structures from Fmiso PET images.

On the other hand, such a mathematical model could also be employed to denoise dynamic PET images. There are already attempts to use TAC models to regulate dynamic PET image reconstruction in order to reduce temporal noise. Compared with conventional TAC models, our model predicts both temporal and spatial variances of Fmiso distribution. It is hoped that our model could be used as a regulariser in dynamic PET image reconstruction algorithms to reduce noise in both spatial and temporal dimensions.

8.5 Conclusion

We believe that this thesis has laid the foundations for a simulation and experimental research network to combine biological science with mathematical modelling (Figure 8.4).

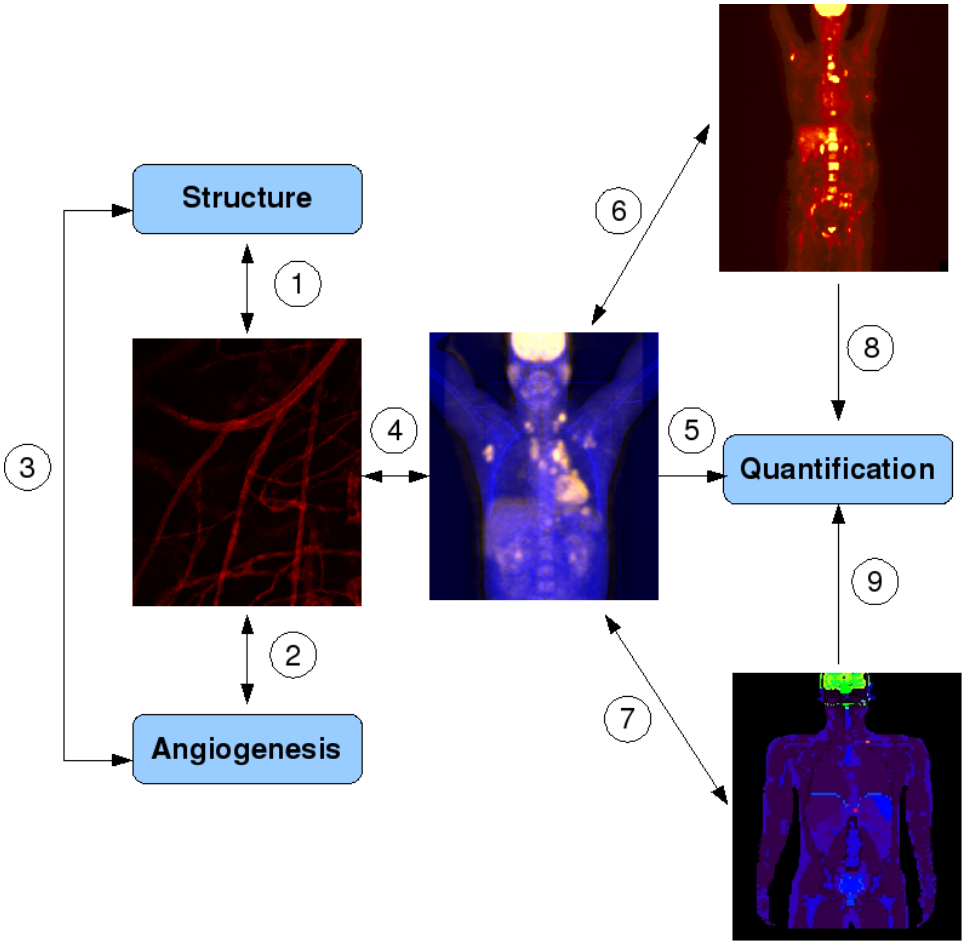

Figure 8.4: Correlate microvessel structures with PET images

The microvessel structure could be analysed quantitatively with the metrics we have proposed in this thesis. Conversely, synthetic microvessel structures can be generated with prescribed structural parameters (Figure 8.4, ①). Similarly, the microvessel map could be analysed and synthesized through angiogenesis models (Figure 8.4, ②). By comparing results of structural analysis and angiogenesis modelling it is possible to investigate the relationships between microvessel structures and angiogenic factors (Figure 8.4, ③).

With a microvessel map, we could conduct microscale or tissue scale simulations of the distribution of Fmiso and investigate the relationships between microvessel geometry and Fmiso distribution (Figure 8.4, ④). The synthesized tissue scale Fmiso distribution could be quantified with macro descriptors such as time activity curves and kinetic parameters (Figure 8.4, ⑤). At the same time the synthesized tissue scale Fmiso distribution

could be used to regularize dynamic PET image reconstruction, or be used as model to infer microvessel structures from realistic PET images (Figure 8.4, ⑥). Alternatively, the synthesized tissue scale Fmiso distribution could be fed into PET simulation programs such as SORTEO (Reilhac *et al.*, 2004) to research the correlation between microscopic vessel geometries and macroscopic PET signals (Figure 8.4, ⑦). Both realistic PET images and simulated PET images could be quantified with macro descriptors such as TAC and kinetic parameters (Figure 8.4, ⑧, ⑨).

We believe that through this network, the relationship between tumour angiogenesis process, microvessel structures and macroscopic PET signal can be researched, which will be beneficial both to clinical PET image understanding and to bench side drug development evaluations. The work described above will be the focus of our future research.

Bibliography

Abelev, G. (1971). Alpha-fetoprotein in ontogenesis and its association with malignant tumors. *Advances in cancer research*, **14**, 295.

Alivisatos, A. (1996). Semiconductor clusters, nanocrystals, and quantum dots. *Science*, **271**, 933.

Antiga, L. *et al.* (2006). VMTKVascular modeling toolkit.

Barber, P., Vojnovic, B., Ameer-Beg, S., Hodgkiss, R., Tozer, G. & Wilson, J. (2003). Semi-automated software for the three-dimensional delineation of complex vascular networks. *Journal of microscopy*, **211**, 54–62.

Boucher, Y., Baxter, L. & Jain, R. (1990). Interstitial pressure gradients in tissue-isolated and subcutaneous tumors: implications for therapy. *Cancer research*, **50**, 4478.

Bradley, J., Thorstad, W., Mutic, S., Miller, T., Dehdashti, F., Siegel, B., Bosch, W. & Bertrand, R. (2004). Impact of FDG-PET on radiation therapy volume delineation in non-small-cell lung cancer. *International journal of radiation oncology, biology, physics*, **59**, 78–86.

Bruehlmeier, M., Roelcke, U., Schubiger, P. & Ametamey, S. (2004). Assessment of hypoxia and perfusion in human brain tumors using PET with 18F-fluoromisonidazole and 15O-H2O. *Journal of Nuclear Medicine*, **45**, 1851.

Burke, W., Daly, M., Garber, J., Botkin, J., Kahn, M., Lynch, P., McTiernan, A., Offit, K., Perlman, J., Petersen, G. *et al.* (1997). Recommendations

for follow-up care of individuals with an inherited predisposition to cancer: II. BRCA1 and BRCA2. *Jama*, **277**, 997.

Bussink, J., Kaanders, J., Strik, A., Vojnovic, B. & van Der Kogel, A. (2000). Optical sensor-based oxygen tension measurements correspond with hypoxia marker binding in three human tumor xenograft lines. *Radiation research*, **154**, 547.

Cai, W., Chen, K., He, L., Cao, Q., Koong, A. & Chen, X. (2007). Quantitative PET of EGFR expression in xenograft-bearing mice using 64 Cu-labeled cetuximab, a chimeric anti-EGFR monoclonal antibody. *European Journal of Nuclear Medicine and Molecular Imaging*, **34**, 850–858.

Carmeliet, P. & Jain, R. (2000). Angiogenesis in cancer and other diseases. *Nature*, **407**, 249–257.

Casciari, J., Graham, M. & Rasey, J. (1995). A modeling approach for quantifying tumor hypoxia with [F-18] fluoromisonidazole PET time-activity data. *Medical Physics*, **22**, 1127.

Cash, J. & Karp, A. (1990). ACM Transactions on Mathematical Software. *Vol*, **16**, 201–222.

Catalona, W., Smith, D., Ratliff, T., Dodds, K., Coplen, D., Yuan, J., Petros, J. & Andriole, G. (1991). Measurement of prostate-specific antigen in serum as a screening test for prostate cancer. *New England Journal of Medicine*, **324**, 1156.

Chan, T. & Vese, L. (2001). Active contours without edges. *IEEE Transactions on image processing*, **10**, 266–277.

Chandra, R. (2000). *Parallel programming in OpenMP*. Morgan Kaufmann.

Chaplain, M. (2000). Mathematical Modelling of Angiogenesis. *Journal of Neuro-Oncology*, **50**, 37–51.

Chatterjee, D., Rufaihah, A. & Zhang, Y. (2008). Upconversion fluorescence imaging of cells and small animals using lanthanide doped nanocrystals. *Biomaterials*, **29**, 937–943.

Cornea, N., Silver, D., Yuan, X. & Balasubramanian, R. (2005). Computing hierarchical curve-skeletons of 3d objects. *The Visual Computer*, **21**, 945–955.

Cornea, N., Silver, D. & Min, P. (2007). Curve-skeleton properties, applications, and algorithms. *IEEE Transactions on Visualization and Computer Graphics*, **13**, 530–548.

Cowan, D., Hicks, K. & Wilson, W. (1996). Multicellular membranes as an in vitro model for extravascular diffusion in tumours. *The British Journal of Cancer. Supplement*, **27**, S28.

Danaei, G., Vander Hoorn, S., Lopez, A., Murray, C. & Ezzati, M. (2005). Causes of cancer in the world: comparative risk assessment of nine behavioural and environmental risk factors. *The Lancet*, **366**, 1784–1793.

Daşu, A., Toma-Daşu, I. & Karlsson, M. (2003). Theoretical simulation of tumour oxygenation and results from acute and chronic hypoxia. *Physics in medicine and biology*, **48**, 2829–2842.

Dehdashti, F., Mintun, M., Lewis, J., Bradley, J., Govindan, R., Laforest, R., Welch, M. & Siegel, B. (2003). In vivo assessment of tumor hypoxia in lung cancer with 60 Cu-ATSM. *European Journal of Nuclear Medicine and Molecular Imaging*, **30**, 844–850.

Delbeke, D. (1999). Oncological applications of FDG PET imaging: brain tumors, colorectal cancer lymphoma and melanoma. *Journal of Nuclear Medicine*, **40**, 591.

DeVries, A., Kremser, C., Hein, P., Griebel, J., Krezcy, A., Ofner, D., Pfeiffer, K., Lukas, P., Judmaier, W., Therapy, C. *et al.* (2003). Tumor microcirculation and diffusion predict therapy outcome for primary rectal carcinoma. *Int J Radiat Oncol Biol Phys*, **56**, 958–965.

Dewhirst, M., Ong, E., Braun, R., Smith, B., Klitzman, B., Evans, S. & Wilson, D. (1999). Quantification of longitudinal tissue pO2 gradients in window chamber tumours: impact on tumour hypoxia. *British journal of cancer*, **79**, 1717.

Dowling, A., Clift, R., Grobert, N., Hutton, D., Oliver, R., Oneill, O., Pethica, J., Pidgeon, N., Porritt, J., Ryan, J. *et al.* (2004). Nanoscience and nanotechnologies: opportunities and uncertainties. *London: The Royal Society & The Royal Academy of Engineering Report*.

Erasmus, J., McAdams, H., Patz Jr, E., Coleman, R., Ahuja, V. & Goodman, P. (1998). Evaluation of primary pulmonary carcinoid tumors using FDG PET. *American Journal of Roentgenology*, **170**, 1369.

Felsberg, M. & Sommer, G. (2000). A new extension of linear signal processing for estimating local properties and detecting features. *Proceedings of the DAGM 2000*, 195–202.

Fenton, B., Paoni, S., Lee, J., Koch, C. & Lord, E. (1999). Quantification of tumour vasculature and hypoxia by immunohistochemical staining and HbO2 saturation measurements. *Br J Cancer*, **79**, 464–71.

Fischman, A., Alpert, N. & Rubin, R. (2002). Pharmacokinetic imaging: a noninvasive method for determining drug distribution and action. *Clinical pharmacokinetics*, **41**, 581–602.

Fluri, F., Lyrer, P., Gratwohl, A., Raetz-Bravo, A. & Steck, A. (2007). Lead poisoning from the beauty case: Neurologic manifestations in an elderly woman. *Neurology*, **69**, 929.

Foster, J. (1978). Survival after liver resection for secondary tumors. *The American Journal of Surgery*, **135**, 389–394.

Franko, A. & Chapman, J. (1982). Binding of 14C-misonidazole to hypoxic cells in V79 spheroids. *Br J Cancer*, **45**, 694–9.

Fraser, D., Reid, N. & Wong, A. (1997). Simple and accurate inference for the mean of the gamma model. *The Canadian Journal of Statistics/La Revue Canadienne de Statistique*, **25**, 91–99.

Gao, X., Cui, Y., Levenson, R., Chung, L. & Nie, S. (2004). In vivo cancer targeting and imaging with semiconductor quantum dots. *Nature Biotechnology*, **22**, 969–976.

Gonzalez, R. & Woods, R. (2002). Digital image processing. 2002. *Publishing House of Electronics Industry*.

Green, M., Harwood, H., Barrowman, C., Rahman, P., Eggeman, A., Festry, F., Dobson, P. & Ng, T. (2007). A facile route to CdTe nanoparticles and their use in bio-labelling. *Journal of material chemistry*, **17**, 1989–1994.

Greenwood, J. & Durand, D. (1960). Aids for fitting the gamma distribution by maximum likelihood. *Technometrics*, 55–65.

Gross, M., Karbach, U., Groebe, K., Franko, A. & Mueller-Klieser, W. (1995). Calibration of misonidazole labeling by simultaneous measurement of oxygen tension and labeling density in multicellular spheroids. *Int J Cancer*, **61**, 567–73.

Gunn, R., Gunn, S. & Cunningham, V. (2001). Positron Emission Tomography Compartmental Models. *Journal of Cerebral Blood Flow & Metabolism*, **21**, 635–652.

Guo, Q., Brady, M. & Gunn, R. (2009). A Biomathematical Modeling Approach to Central Nervous System Radioligand Discovery and Development. *Journal of Nuclear Medicine*, **50**, 1715.

Han, M., Gao, X., Su, J. & Nie, S. (2001). Quantum-dot-tagged microbeads for multiplexed optical coding of biomolecules. *Nature biotechnology*, **19**, 631–635.

Hasegawa, M., Sone, S., Takashima, S., Li, F., Yang, Z., Maruyama, Y. & Watanabe, T. (2000). Growth rate of small lung cancers detected on mass CT screening. *British Journal of Radiology*, **73**, 1252.

Hendel, T., Mank, M., Schnell, B., Griesbeck, O., Borst, A. & Reiff, D. (2008). Fluorescence changes of genetic calcium indicators and OGB-1 correlated with neural activity and calcium in vivo and in vitro. *Journal of Neuroscience*, **28**, 7399.

Hilger, I., Leistner, Y., Berndt, A., Fritsche, C., Haas, K., Kosmehl, H. & Kaiser, W. (2004). Near-infrared fluorescence imaging of HER-2 protein over-expression in tumour cells. *European radiology*, **14**, 1124–1129.

Homann, H. (2007). Implementation of a 3D thinning algorithm.

Jafari, A., Mousavi, S. & Kolari, P. (2008). Numerical investigation of blood flow. Part I: In microvessel bifurcations. *Communications in Nonlinear Science and Numerical Simulation*, **13**, 1615–1626.

Jafari, A., Zamankhan, P., Mousavi, S. & Kolari, P. (2009). Numerical investigation of blood flow. Part II: In capillaries. *Communications in Nonlinear Science and Numerical Simulation*, **14**, 1396–1402.

Jaffer, F. & Weissleder, R. (2004). Seeing within: molecular imaging of the cardiovascular system. *Circulation research*, **94**, 433.

Jaffer, F. & Weissleder, R. (2005). Molecular imaging in the clinical arena. *Jama*, **293**, 855.

Jain, R. (1988). Determinants of tumor blood flow: a review. *Cancer research*, **48**, 2641.

Jain, R. (2001). Normalizing tumor vasculature with anti-angiogenic therapy: a new paradigm for combination therapy. *Nature Medicine*, **7**, 987–989.

Jain, R. (2005). Normalization of tumor vasculature: an emerging concept in antiangiogenic therapy. *Science*, **307**, 58.

Jain, R., Ellika, S., Scarpace, L., Schultz, L., Rock, J., Gutierrez, J., Patel, S., Ewing, J. & Mikkelsen, T. (2008). Quantitative estimation of permeability surface-area product in astroglial brain tumors using perfusion CT and correlation with histopathologic grade. *American Journal of Neuroradiology*, **29**, 694.

Jiang, S., Gnanasammandhan, M. & Zhang, Y. (2009). Optical imaging-guided cancer therapy with fluorescent nanoparticles. *Journal of The Royal Society Interface*.

Kalluri, R. (2003). Basement membranes: structure, assembly and role in tumour angiogenesis. *Nature Reviews Cancer*, **3**, 422–433.

Kass, M., Witkin, A. & Terzopoulos, D. (1988). Snakes: Active contour models. *International journal of computer vision*, **1**, 321–331.

Kaufmann, B. & Lindner, J. (2007). Molecular imaging with targeted contrast ultrasound. *Current opinion in biotechnology*, **18**, 11–16.

Kayser, C. & Logothetis, N. (2010). The Electrophysiological Background of the fMRI Signal. *fMRI*, 23–33.

Kelly, C. & Brady, M. (2006). A model to simulate tumour oxygenation and dynamic [18F]-Fmiso PET data. *PHYSICS IN MEDICINE AND BIOLOGY*, **51**, 5859.

Kelly, C.J. (2007). *Quantitative Modelling of Positron Emission Tomography Tracer Kinetics in Hypoxia*. Ph.D. thesis, University of Oxford.

Kerbel, R. (2006). Antiangiogenic therapy: a universal chemosensitization strategy for cancer? *Science*, **312**, 1171.

Kim, J., Ichise, M., Sangare, J. & Innis, R. (2006). PET Imaging of Serotonin Transporters with [11C] DASB: Test-Retest Reproducibility Using a Multilinear Reference Tissue Parametric Imaging Method.

Koepke, J. (2006). Molecular marker test standardization. *Cancer*, **69**, 1578–1581.

Koh, W., Rasey, J., Evans, M., Grierson, J., Lewellen, T., Graham, M., Krohn, K. & Griffin, T. (1992). Imaging of hypoxia in human tumors with [F-18] fluoromisonidazole. *International Journal of Radiation Oncology* Biology* Physics*, **22**, 199–212.

Konerding, M., Fait, E. & Gaumann, A. (2001). 3D microvascular architecture of pre-cancerous lesions and invasive carcinomas of the colon. *Br J Cancer*, **84**, 1354–62.

Kovesi, P. (1999). Image features from phase congruency. *Videre: Journal of Computer Vision Research*, **1**, 1–26.

Kron, S. & Spudich, J. (1986). Fluorescent actin filaments move on myosin fixed to a glass surface. *Proceedings of the National Academy of Sciences of the United States of America*, **83**, 6272.

Lee, T., Kashyap, R. & Chu, C. (1994). Building skeleton models via 3-D medial surface/axis thinning algorithms. *CVGIP: Graphical Models and Image Processing*, **56**, 462–478.

Li, C., Xu, C., Gui, C. & Fox, M. (2005). Level set evolution without re-initialization: A new variational formulation. In *IEEE computer society conference on computer vision and pattern recognition*, vol. 1, 430, Citeseer.

Liaw, D., Marsh, D., Li, J., Dahia, P., Wang, S., Zheng, Z., Bose, S., Call, K., Tsou, H., Peacoke, M. *et al.* (1997). Germline mutations of the PTEN gene in Cowden disease, an inherited breast and thyroid cancer syndrome. *Nature genetics*, **16**, 64–67.

Lieutier, A. (2004). Any open bounded subset of has the same homotopy type as its medial axis. *Computer-Aided Design*, **36**, 1029–1046.

Lilliefors, H. (1967). On the Kolmogorov-Smirnov test for normality with mean and variance unknown. *Journal of the American Statistical Association*, **62**, 399–402.

Lim, S., Riehn, R., Ryu, W., Khanarian, N., Tung, C., Tank, D. & Austin, R. (2006). In vivo and scanning electron microscopy imaging of up-converting nanophosphors in Caenorhabditis elegans. *Nano letters*, **6**, 169.

Lorensen, W. & Cline, H. (1987). Marching cubes: A high resolution 3D surface construction algorithm. 169.

Lovrić, J., Bazzi, H., Cuie, Y., Fortin, G., Winnik, F. & Maysinger, D. (2005). Differences in subcellular distribution and toxicity of green and red emitting CdTe quantum dots. *Journal of Molecular Medicine*, **83**, 377–385.

Luxon, B. & Forker, E. (1982). Simulation and analysis of hepatic indicator dilution curves. *American Journal of Physiology- Gastrointestinal and Liver Physiology*, **243**, 76–89.

Macdonald, G. (2008). Cecil Medicine, (Premium Edition).-. by WP Arend, JO Armitage, DR Clemmons, JM Drazen, RC Griggs and N. Larusso. *Internal Medicine Journal*, **38**, 931–932.

Manton, M. (2006). Low Reynolds number flow in slowly varying axisymmetric tubes. *Journal of Fluid Mechanics*, **49**, 451–459.

McDonald, D. & Baluk, P. (2002). Significance of blood vessel leakiness in cancer. *Cancer research*, **62**, 5381.

Mellor, M. & Brady, M. (2005). Phase mutual information as a similarity measure for registration. *Medical Image Analysis*, **9**, 330–343.

Michalet, X., Pinaud, F., Bentolila, L., Tsay, J., Doose, S., Li, J., Sundaresan, G., Wu, A., Gambhir, S. & Weiss, S. (2005). Quantum dots for live cells, in vivo imaging, and diagnostics. *Science*, **307**, 538.

Mintun, M., Raichle, M., Kilbourn, M., Wooten, G. & Welch, M. (2004). A quantitative model for the in vivo assessment of drug binding sites with positron emission tomography. *Annals of neurology*, **15**, 217–227.

Morrone, M. & Burr, D. (1988). Feature detection in human vision: A phase-dependent energy model. *Proceedings of the Royal Society of London. Series B, biological sciences*, 221–245.

Nvidia, C. (2010). *programming Guide, version 3.0*. NVIDIA Corporation.

Osher, S. & Sethian, J. (1988). Fronts propagating with curvature dependent speed: algorithms based on Hamilton-Jacobi formulations. *Journal of computational physics*.

Parkin, D., Bray, F., Ferlay, J. & Pisani, P. (2005). Global cancer statistics, 2002. *CA: a cancer journal for clinicians*, **55**, 74.

Pozrikidis, C. & Farrow, D. (2003). A model of fluid flow in solid tumors. *Annals of Biomedical Engineering*, **31**, 181–194.

Press, W., Teukolsky, S., Vetterling, W. & Flannery, B. (1995). Numerical Recipes in C. 2nd. *Cambridge University, Cambridge*.

Qayum, N., Muschel, R., Im, J., Balathasan, L., Koch, C., Patel, S., McKenna, W. & Bernhard, E. (2009). Tumor vascular changes mediated by inhibition of oncogenic signaling. *Cancer research*, **69**, 6347.

Rasey, J., Casciari, J., Hofstrand, P., Muzi, M., Graham, M. & Chin, L. (2009). Determining hypoxic fraction in a rat glioma by uptake of radiolabeled fluoromisonidazole.

Rawat, M., Singh, D., Saraf, S. & Saraf, S. (2006). Nanocarriers: promising vehicle for bioactive drugs. *Biological & pharmaceutical bulletin*, **29**, 1790–1798.

Ray, H., Pfister, H., Silver, D. & Cook, T. (1999). Ray casting architectures for volume visualization. *IEEE Transactions on Visualization and Computer Graphics*, **5**, 210–223.

Reilhac, A., Lartizien, C., Costes, N., Sans, S., Comtat, C., Gunn, R. & Evans, A. (2004). PET-SORTEO: A Monte Carlo-based simulator with high count rate capabilities. *IEEE Transactions on Nuclear Science*, **51**.

Rudin, M. & Weissleder, R. (2003). Molecular imaging in drug discovery and development. *Nature Reviews Drug Discovery*, **2**, 123–131.

Rust, M., Bates, M. & Zhuang, X. (2006). Sub-diffraction-limit imaging by stochastic optical reconstruction microscopy (STORM). *Nature methods*, **3**, 793–796.

Schroeder, W. & Lorenson, B. (1996). Visualization Toolkit: An Object-Oriented Approach to 3-D Graphics.

Shiohara, A., Hoshino, A., Hanaki, K., Suzuki, K. & Yamamoto, K. (2004). On the cyto-toxicity caused by quantum dots. *Microbiology and immunology*, **48**, 669–675.

Shipley, R. & Chapman, S. (2010). Multiscale Modelling of Fluid and Drug Transport in Vascular Tumours. *Bulletin of Mathematical Biology*, 1–28.

Shiue, W., Bain, L. & Engelhardt, M. (1988). Test of equal gamma-distribution means with unknown and unequal shape parameters. *Technometrics*, **30**, 169–174.

Souhami, R. & Moxham, J. (2002). *Textbook of medicine*. Elsevier Health Sciences.

Strauss, L., Klippel, S., Pan, L., Schoenleben, K., Haberkorn, U. & Dimitrakopoulou-Strauss, A. (2007). Assessment of quantitative FDG PET data in primary colorectal tumours: which parameters are important with respect to tumour detection? *European Journal of Nuclear Medicine and Molecular Imaging*, **34**, 868–877.

Szczerba, D. & Székely, G. (2002). Macroscopic modeling of vascular systems. *Medical Image Computing and Computer-Assisted InterventionMICCAI 2002*, 284–292.

Tannock, I. (1972). Oxygen diffusion and the distribution of cellular radiosensitivity in tumours. *British Journal of Radiology*, **45**, 515.

Taylor, J., Tofts, P., Port, R., Evelhoch, J., Knopp, M., Reddick, W., Runge, V. & Mayr, N. (1999). MR imaging of tumor microcirculation: promise for the new millenium. *Journal of Magnetic Resonance Imaging*, **10**, 903–907.

Thorwarth, D., Eschmann, S., Paulsen, F. & Alber, M. (2005). A kinetic model for dynamic [18F]-Fmiso PET data to analyse tumour hypoxia. *Physics in Medicine and Biology*, **50**, 2209.

Townley, H., Parker, A. & White-Cooper, H. (2008). Exploitation of Diatom Frustules for Nanotechnology: Tethering Active Biomolecules. *Advanced Functional Materials*, **18**, 369–374.

Vaupel, P. (2004). Tumor microenvironmental physiology and its implications for radiation oncology. In *Seminars in radiation oncology*, vol. 14, 198–206, Elsevier.

Voigt, J. (2009). Ultrasound molecular imaging. *Methods*, **48**, 92–97.

Voura, E., Jaiswal, J., Mattoussi, H. & Simon, S. (2004). Tracking metastatic tumor cell extravasation with quantum dot nanocrystals and fluorescence emission-scanning microscopy. *Nature medicine*, **10**, 993–998.

Wang, W., Georgi, J., Nehmeh, S., Narayanan, M., Paulus, T., Bal, M., O'Donoghue, J., Zanzonico, P., Schmidtlein, C., Lee, N. *et al.* (2009). Evaluation of a compartmental model for estimating tumor hypoxia. *Physics in medicine and biology*, **54**, 3083–3099.

Wang, X., Yang, L., Chen, Z. & Shin, D. (2008). Application of nanotechnology in cancer therapy and imaging. *CA: A Cancer Journal for Clinicians*, **58**, 97.

Weinberg, R. (2007). *The biology of cancer*. Garland Science New York.

Weissleder, R. (1999). Molecular Imaging: Exploring the Next Frontier1. *Radiology*, **212**, 609.

Yagi, H., Ban, T. & Goto, Y. (2009). Real-Time Observation of Amyloid Fibril Growth by Total Internal Reflection Fluorescence Microscopy. *Water and Biomolecules*, 289–299.

Yong, K. (2009). Mn-doped near-infrared quantum dots as multimodal targeted probes for pancreatic cancer imaging. *Nanotechnology*, **20**, 015102.

Zhuang, X. (2009). Nano-imaging with STORM. *Nature photonics*, **3**, 365.